InAs/InP quantum dash mode locked lasers for optical communications

Ricardo Rosales del Moral Rosales

▶ **To cite this version:**

Ricardo Rosales del Moral Rosales. InAs/InP quantum dash mode locked lasers for optical communications. Architecture, space management. Institut National des Télécommunications, 2012. English. NNT : 2012TELE0039 . tel-00923176

HAL Id: tel-00923176
https://theses.hal.science/tel-00923176

Submitted on 2 Jan 2014

HAL is a multi-disciplinary open access archive for the deposit and dissemination of scientific research documents, whether they are published or not. The documents may come from teaching and research institutions in France or abroad, or from public or private research centers.

L'archive ouverte pluridisciplinaire **HAL**, est destinée au dépôt et à la diffusion de documents scientifiques de niveau recherche, publiés ou non, émanant des établissements d'enseignement et de recherche français ou étrangers, des laboratoires publics ou privés.

THESE DE DOCTORAT CONJOINT TELECOM SUDPARIS et L'UNIVERSITE PIERRE ET MARIE CURIE PARIS 6

Spécialité : Electronique et Télécommunications
Ecole doctorale EDITE de Paris

Présentée par
Ricardo ROSALES

Pour obtenir le grade de docteur délivré par
UPMC et TELECOM SudParis

LASERS A BLOCAGE DE MODES A BASE DE BATONNETS QUANTIQUES InAs/InP POUR LES COMMUNICATIONS OPTIQUES

Soutenue le 20 Novembre 2012
devant le jury composé de :

Prof. Jean-Claude SIMON	**Professeur, Université de Rennes 1**	**Rapporteur**
Prof. Joël JACQUET	**Professeur, SUPELEC Metz**	**Rapporteur**
Prof. Georges ALQUIE	**Professeur, Université Paris 6**	**Examinateur**
Dr. Guillaume HUYET	**Senior Lecturer, Cork Institute of Technology, Irlande Senior research Scientist, Tyndall National Institute, Irlande**	**Examinateur**
Prof. Philippe GALLION	**Professeur, TELECOM ParisTech**	**Examinateur**
Dr. Abderrahim RAMDANE	**Directeur de recherche, CNRS-LPN Professeur, TELECOM SudParis**	**Directeur de thèse**
Dr. Anthony MARTINEZ	**Chargé de recherche, CNRS-LPN**	**Co-encadrant**

Thèse n° 2012TELE0039

DISSERTATION

TELECOM SUDPARIS - UNIVERSITY PIERRE ET MARIE CURIE PARIS 6

Discipline : Electronics and Telecommunications
Doctoral School : EDITE de Paris

Presented by

Ricardo ROSALES

InAs/InP QUANTUM DASH MODE LOCKED LASERS FOR OPTICAL COMMUNICATIONS

Doctoral commitee :

Prof. Jean-Claude SIMON	**Professor, Université de Rennes 1**
Prof. Joël JACQUET	**Professor, SUPELEC Metz**
Prof. Georges ALQUIE	**Professor, Université Paris 6**
Dr. Guillaume HUYET	**Senior Lecturer, Cork Institute of Technology, Irlande** **Senior research Scientist, Tyndall National Institute, Irlande**
Prof. Phiippe GALLION	**Professor, TELECOM ParisTech**
Dr. Abderrahim RAMDANE	**Research Director, CNRS-LPN** **Professor, TELECOM SudParis**
Dr. Anthony MARTINEZ	**Researcher, CNRS-LPN**

Thèse n° 2012TELE0039

Résumé

Les lasers à semi-conducteurs monolithiques à blocage de modes (*monolithic mode locked lasers*, MLL) sont des dispositifs bien adaptés à la génération d'impulsions et ont trouvé des applications dans un grand nombre de domaines, dont les communications optiques, la photonique appliquée aux micro-ondes (ou opto-hyperfréquence), l'échantillonnage optique, la biologie et la médecine. Ils ont fait l'objet de nombreuses études depuis la première démonstration d'une diode laser à semi-conducteur et présentent aujourd'hui des performances sans précédent avec des durées d'impulsions et gigue temporelle de l'ordre de quelques centaines de femto-secondes (fs) avec des fréquences de répétition au-delà de 300 GHz.

Les avancées en science des matériaux, en particulier dans le domaine de la croissance par épitaxie par jets moléculaires (*molecular beam epitaxy*, MBE), ont permis la réalisation de structures de petites dimensions telles que les puits quantiques (*quantum wells*, QW) à partir desquels des lasers hautement performants ont pu être réalisés, et qui ont contribué en particulier à l'essor des systèmes de communication par fibres optiques. Plus récemment, l'élaboration de nanostructures appelées boîtes quantiques (*quantum dots*, QD), dans lesquelles les porteurs de charges sont confinés dans les trois dimensions de l'espace, a pu été réalisée par la même technique de croissance.

Les premiers MLL passifs à base de QD ont été réalisés en 2001 [1]. Certaines propriétés attendues des lasers à QD sont en effet particulièrement intéressantes pour le régime à blocage de modes, tels que des faibles densités de courant de seuil [2] un faible facteur de couplage phase-amplitude (facteur de Henry) [3], [4], des spectres d'émission étendus [5], une dynamique de porteurs ultra-rapide [6], un faible facteur de confinement optique et une sensibilité réduite à la température [7]. Le système de matériaux InAs/GaAs, plus mature, a en particulier fait l'objet de nombreuses recherches. Les références [5], [8] présentent des revues récentes discutant de l'avantage d'utiliser des QD pour les MLL passifs et de leurs performances, pour des lasers émettant à 1,3 µm élaborés sur des substrats GaAs.

Cette thèse s'est concentrée sur l'étude des lasers à blocage de modes destinés à la fenêtre de télécommunication de 1,55 µm et dont la croissance a été réalisée sur des substrats d'InP. En général, la croissance MBE sur un substrat InP (100) donne lieu à la formation de bâtonnets quantiques (QDash), i.e., des boîtes quantiques allongées [9–11], tandis que la croissance par épitaxie en phase vapeur aux organométalliques (*metal organic vapor phase epitaxy*, MOVPE) ou par CBE (*chemical beam epitaxy*) produit de vraies boîtes avec un confinement 3D des porteurs de charge [12], [13].

Les premières démonstrations de MLL à base de QDash émettant à 1,55 µm étaient pour des dispositifs Fabry Perot (FP) qui consistaient en une seule section dépourvue d'absorbant saturable [14], [15]. Les QD obtenus par CBE permettent également d'obtenir un blocage de modes dans des dispositifs à une seule section [12] tandis que les dispositifs réalisés par croissance MOVPE présentent un comportement plus conventionnel dans le cas des MLL à deux sections où la commutation Q (*Q-switching*) ainsi que le ML ont été être observés selon les conditions de fonctionnement [13], [16].

Bien que la situation idéale, dans laquelle des QD (ou QDashes) énergétiquement isolés permettraient de développer des lasers à modulation directe présentant les caractéristiques prévues par la théorie, soit loin d'être atteinte en pratique (principalement à cause de l'élargissement inhomogène du spectre de gain), les MLL à QDash à une seule section présentent par contre un fort potentiel pour de nombreuses applications. Leurs caractéristiques représentent en effet un atout majeur par rapport aux dispositifs à base de QW généralement utilisés et sont à la base de la motivation à initier ce travail de thèse : il s'agit du spectre optique particulièrement large et plat, et du bruit de phase d'intensité réduit, des caractéristiques qui sont souvent accompagnées d'une puissance optique moyenne relativement élevée. Ces propriétés particulières pourraient offrir, dans le domaine des communications optiques, des solutions à bas coût et respectueuses de l'environnement. En effet, un spectre optique étendu comprenant un grand nombre de modes laser permettrait le développement d'une des technologies les plus prometteuses pour les réseaux optiques à haute capacité de la prochaine génération, tels que les supercanaux à multiplexage par répartition orthogonale de fréquence (*orthogonal frequency-division multiplexing*, OFDM), qui ont récemment fait l'objet de nombreuses publications [17–30]. La réduction du bruit de phase d'intensité des lasers devrait par ailleurs représenter un avantage pour des applications

futures dans les réseaux d'accès sans fil à large bande, telle que la génération d'ondes millimétriques pour la radio sur fibre (*radio over fibre,* RoF) [31–34].

Pourtant, contrairement aux dispositifs à deux sections dans lesquels le comportement ML est généralement très bien compris et contrôlé, les mécanismes physiques responsables du régime ML dans des dispositifs à une section ne sont toujours pas complètement connus, que ce soit d'un point de vue théorique ou pratique. Un des principaux objectifs de ce travail de thèse a donc consisté à apporter de nouveaux éléments permettant de mieux appréhender les aspects physiques sous-tendant le mécanisme du ML dans ces dispositifs à une section. En effet, une meilleure compréhension du comportement intrinsèque de ces dispositifs et la façon dont ils sont affectés par des facteurs externes, qui pourraient être présents dans les conditions réelles d'utilisation, est cruciale pour leur intégration dans des technologies futures. Un deuxième objectif majeur de ce travail a consisté à démontrer le potentiel d'exploitation de ces dispositifs dans différents scenarii d'applications.

Blocage de modes dans les lasers semi-conducteurs

Dans ce travail, nous avons uniquement traité la question des lasers monolithiques à blocage de modes passif, dans lesquels les mécanismes physiques principaux ont lieu dans une puce laser consistant simplement en un dispositif à une seule section. Le blocage de modes passif exploite les propriétés non-linéaires du milieu du laser. Il peut être obtenu en introduisant un absorbant saturable (*saturable absorber*, SA) dans la cavité laser, auquel cas il s'agira de lasers à blocage de modes passif à deux sections.

Blocage de modes passif dans des dispositifs à deux sections

Le principe de base responsable du régime de blocage de modes est très bien connu dans le cas de dispositifs à deux sections : l'intensité de l'onde parcourant la cavité laser sature la section de l'absorbant pendant sa propagation. L'absorbant sature plus vite que le milieu à gain créant ainsi une courte fenêtre de gain net dans laquelle les pertes de la cavité peuvent être compensées, induisant une amplification périodique du champ se propageant pendant la durée d'ouverture de la fenêtre. Après un certain nombre d'aller-retours, la situation illustrée par la Figure 0-1 peut être établie, avec la formation d'un train d'impulsions stable.

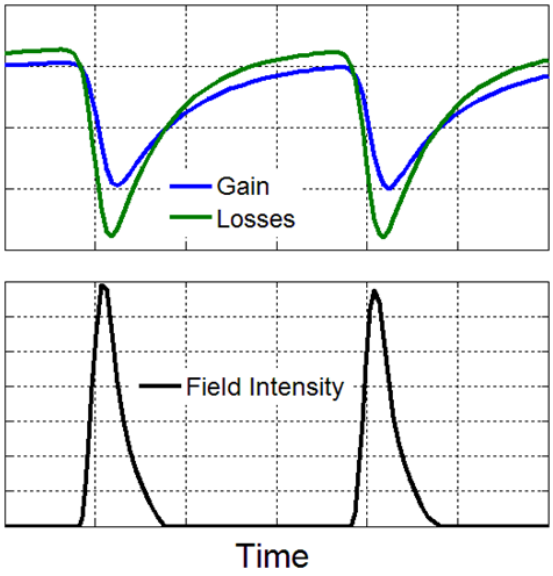

Figure 0-1 Illustration du blocage de modes d'un dispositif à deux sections avec un absorbant lentement saturable

Blocage de modes passif dans des dispositifs à une section

Le régime de blocage de modes dans les lasers semi-conducteurs peut se produire dans une configuration de laser FP simple dépourvu d'absorbant saturable. Ceci a en effet pu être mis en évidence dans les lasers semi-conducteurs massifs [35], à base de puits quantiques [36], [37], de bâtonnets quantiques [15] ou de boîtes quantiques [12], suggérant que ce régime particulier de blocage de modes ne serait pas nécessairement lié à la dimensionnalité de la couche active. Un modèle théorique complet permettant d'expliquer ce phénomène fait toujours défaut. Néanmoins, le mécanisme physique principal responsable du comportement de blocage de modes a été, dans tous les cas, attribué à un milieu à gain non-linéaire. Le mélange à quatre ondes (*four-wave mixing*, FWM) a été identifié comme étant le mécanisme essentiel jouant un rôle majeur dans ce type de régime de blocage de modes. En effet, le FWM peut conduire à un verrouillage par injection mutuelle entraînant une corrélation entre les phases des modes des cavités lasers de façon similaire à ce qui est observé dans les lasers à blocage de modes actif.

En général, la corrélation de phase entre les modes entraîne une réduction de la largeur de raie radio fréquence (RF) mais cela ne peut être le cas que s'il existe un couplage cohérent entre les modes, puisqu'une interaction incohérente mènerait à une largeur de raie RF

équivalente à deux fois celles des modes optiques. Dans les lasers semi-conducteurs, les modes peuvent interagir de façon cohérente selon deux processus : transitions interbande et intrabande [38]. Le premier implique une recombinaison électron-trou due à une modulation de la densité de porteurs (*carrier density modulation*, CDM) à la fréquence des battements des champs interagissant, c'est à dire à la fréquence des composantes de l'intensité de champs intra-cavité. Ce mécanisme est limité par le taux de relaxation interbande avec un temps de vie des porteurs caractéristique qui est typiquement de l'ordre de quelques centaines de picosecondes. Les effets intrabandes, tels que le *hole burning* spectral (Spectral Hole Burning, SHB) et l'échauffement des porteurs (*carrier heating*, CH) ont leur origine dans la modulation de la probabilité d'occupation des niveaux d'énergie et répondent dans une échelle de temps < 0,1 ps. Dans les couches actives à base de boîtes quantiques, ce type de mécanisme concerne la dispersion intrabande et représente les transitions qui ont lieu entre les états quantiques confinés ou les états dits "*bound-to-continuum*" avec des échelles de temps inférieures à 0,1 ps. Tous ces mécanismes représentent des processus non-linéaires et sont responsables du phénomène de mélange quatre ondes dans les amplificateurs et lasers optiques semi-conducteurs [38]. Ils sont gouvernés par la susceptibilité non-linéaire de troisième ordre $\chi^{(3)}$. En fait, ce paramètre peut être décomposé en contributions du CDM, du SBH et du CH. Une équation d'onde non-linéaire prenant en compte les effets FWM peut être établie :

$$\frac{\partial A_j}{\partial z} = \frac{j\omega}{2cn}\Gamma \sum_{\omega_j=\omega_k+\omega_l-\omega_m} \chi_j^{(3)}\left(\omega_j;\omega_k,\omega_l,-\omega_m\right) A_k\left(z\right) A_l\left(z\right) A_m^{*}\left(z\right) e^{-j\left(k_k+k_l-k_j-k_m\right)z} + \frac{\left(1-j\alpha_H\right)}{2}\Gamma g\left(\overline{N}\right) A_j\left(z\right)$$

$$\frac{\partial A_j}{\partial z} = \frac{j\omega}{2cn}\Gamma \sum_{\omega_j=\omega_k+\omega_l-\omega_m} \chi_j^{(3)}\left(\omega_j;\omega_k,\omega_l,-\omega_m\right) A_k\left(z\right) A_l\left(z\right) A_m^{*}\left(z\right) e^{-j\left(k_k+k_l-k_j-k_m\right)z} + \frac{\left(1-j\alpha_H\right)}{2}\left(G\left(\frac{1}{1+\sum_i \left|A_i\right|^2 / P_{sat}}\right)-\alpha\right) A_j\left(z\right) \quad (0.1)$$

avec A, ω, k, z, l'amplitude, fréquence angulaire, vecteur d'onde, axe de propagation, du champ électrique et α_H, P_{sat}, $\chi^{(3)}$ et α le facteur de couplage phase-amplitude, la

puissance de saturation du gain, la susceptibilité du troisième ordre, et les pertes linéaires intrinsèques au SOA (Semiconductor Optical Amplifier : amplificateur optique à semiconducteur). L'équation (0.1) est en accord avec l'analyse de la référence [39], et a été utilisée après quelques simplifications en combinaison avec des résultats expérimentaux sur le FWM en QDash SOA (pour déterminer la relation entre les phases stationnaires des champs équidistants injectés dans un QDash SOA.

L'efficacité du FWM dans un SOA à base de QDash ayant une longueur de 2 mm a été mesurée. Les conditions de polarisation et de puissance du signal d'entrée ont été ajustées pour exploiter le SOA dans un régime de saturation avec un gain saturé de 10 dB. La Figure 0-2 montre l'efficacité du FWM obtenue en faisant varier le désaccord de fréquence pour une fréquence de pompe fixée.

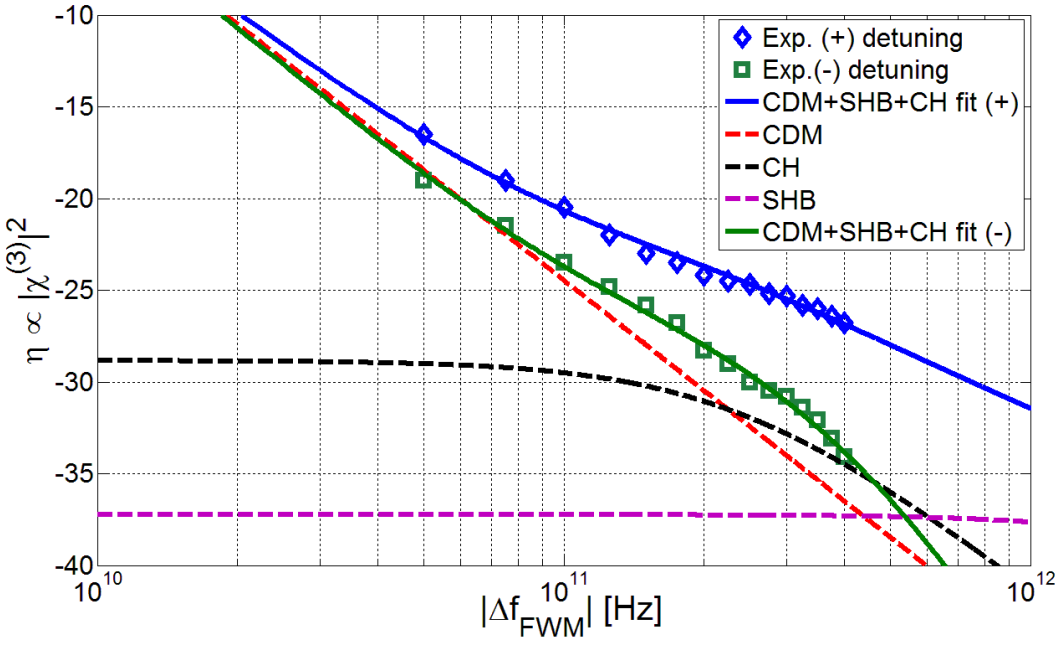

Figure 0-2. Efficacité FWM dans un SOA à base de QDash

L'efficacité du FWM s'avère être clairement asymétrique par rapport à la valeur absolue du désaccord de fréquence, une conséquence des différentes contributions de chaque processus non-linéaire impliqué. L'asymétrie est simplement due à la valeur non nulle du facteur d'élargissement des différents mécanismes non-linéaires. La décroissance de l'efficacité

atteint des valeurs minimales de ~13 dB/dec pour les SOA à base de QDash, comme précédemment décrit [40]. Afin d'identifier séparément les contributions de chaque mécanisme non-linéaire impliqué dans l'efficacité du FWM, nous avons considéré la fonction de réponse impulsionnelle complexe du SOA comme la somme des réponses associées à chaque non-linéarité. Chaque réponse en fréquence a été représentée avec l'ensemble des réponses correspondantes dans la Figure 0-2.

Nous avons trouvé des constantes de temps différentes pour les mécanismes de CDM, CH et SHB de 100 ps, 650 fs et 50 fs respectivement. Ces données sont en accord du point de vue qualitatif avec les valeurs décrites pour les SOAs à base de QD InAs sur GaAs [41].

Nous avons résolu numériquement les équations des modes couplés de (0.1) en tenant compte des valeurs mesurés dans un SOA à QDash de 2 mm de long, présentant une puissance de saturation de 1 mW, un gain net non saturé de 6300 m^{-1} et un facteur d'Henry $\alpha_H = 3$. Les conditions initiales correspondaient à un ensemble de $N = 21$ champs monochromatiques séparés de façon équidistante de 50 GHz avec 0,5 mW d'intensité. Nous avons utilisé la susceptibilité complexe estimée $\chi^{(3)}(\Delta f_{FWM})$ à $\Delta f_{FWM} = 50\text{GHz}$ et la dispersion du matériau typique des amplificateurs optiques à semi-conducteurs de $30\ \text{fs/mm/nm}$ [42]. Nous avons résolu les équations des modes couplés avec le programme Matlab en utilisant une fonction ODE45 (équation différentielle ordinaire) avec un algorithme Runge-Kutta : les résultats sont illustrés dans la Figure 0-3. Le principal résultat que nous avons obtenu à partir des simulations a été la convergence des phases des différents champs vers un état stationnaire entraînant une évolution quadratique en fonction de la fréquence. La même évolution était systématiquement obtenue lorsque les paramètres principaux étaient modifiés au cours des simulations. La diminution de la valeur absolue de $\chi^{(3)}(\Delta f_{FWM})$ a toujours eu pour conséquence un aplatissement du profil parabolique, suggérant que le FWM est l'origine principale de ce phénomène.

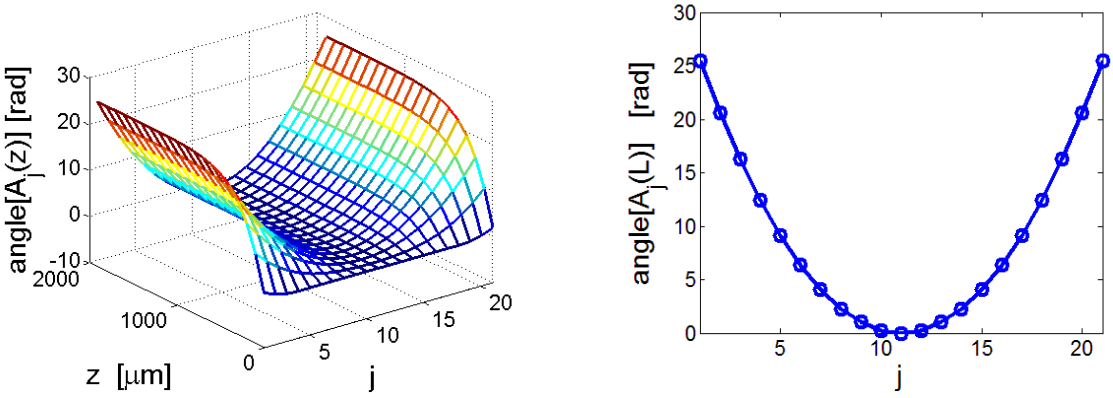

Figure 0-3. Résultats de simulations montrant l'évolution de la phase spectrale dans un SOA (j : numéro du champ ou mode dans la cavité)

Structures à QDash

Les dispositifs présentés dans cette thèse consistent en des structures à base de QDash InAs réalisées par épitaxie par jets moléculaires avec source à gaz (*gas source molecular beam epitaxy*, GSMBE) sur substrats (100) InP par le III-V lab. La hauteur et la largeur typiques des QDash sont de ~2 nm et ~20 nm respectivement. Leur longueur se situe entre 40 et 300 nm, selon les conditions de croissance, tandis que leur densité de surface varie entre 1×10^{10} et 4×10^{10} cm^{-2} [11], des résultats que nous avons pu confirmer à partir de mesures réalisées par microscopie à force atomique et par microscopie à transmission électronique (*transmission electron microscopy*, TEM) (Figure 0-4(a)).

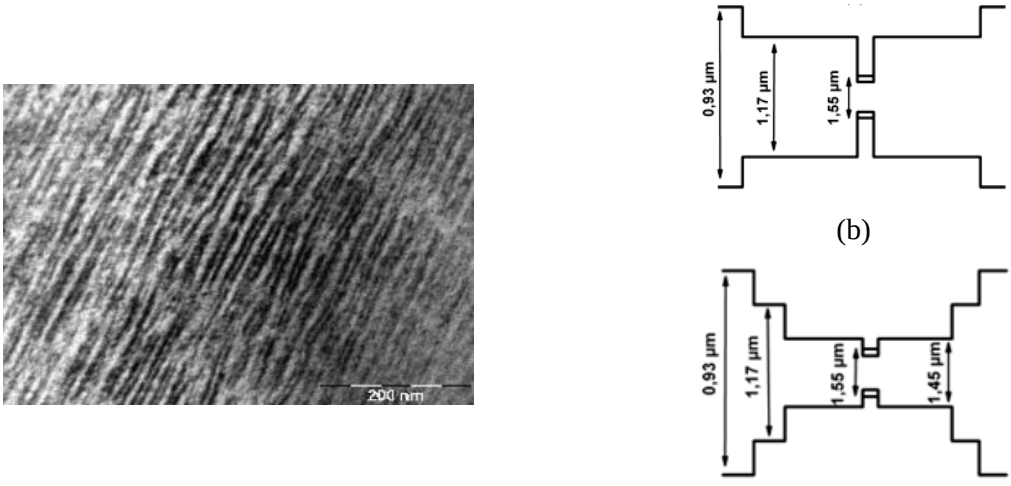

Figure 0-4. (a) Image TEM de la couche active dans le plan montrant les QDash et Diagramme de bandes des structures (b) DBAR et (c) DWELL. [11]

Fabrication de lasers

Les structures précédentes ont ensuite été utilisées dans la salle blanche du LPN pour la fabrication de lasers. Dans un premier temps, nous avons fabriqué des lasers à ruban large (*Broad Area*, BA) afin d'évaluer la qualité du matériau. En effet, ces derniers permettent de déterminer rapidement le gain modal, les pertes internes ainsi que des caractéristiques électriques importantes pour notre étude. Les mesures des caractéristiques puissance-courant (L-I) nous ont ensuite permis d'extraire la densité de courant de seuil $J_{th} = I_{th}/A$ ainsi que l'efficacité quantique différentielle η_{ext}. Le gain modal de la structure Γg_{th}, les pertes internes α_i et le seuil de densité de courant pour une longueur de cavité infinie nominale de $J_{th_{\inf}}$ ont ensuite pu être déterminés. La Figure 0-5 présente les courbes résultantes des mesures décrites ci-dessus pour une structure avec un empilement de 9 couches de type *Dash-in-the-Barrier* (DBAR). Nous avons suivi la procédure pour les cas de lasers à ruban large pour 6, 9, 12 et 15 DBAR ainsi que 6, 12 et 15 *Dash-in-the-Well* (DWELL). Le Tableau 0-1 résume les résultats obtenus.

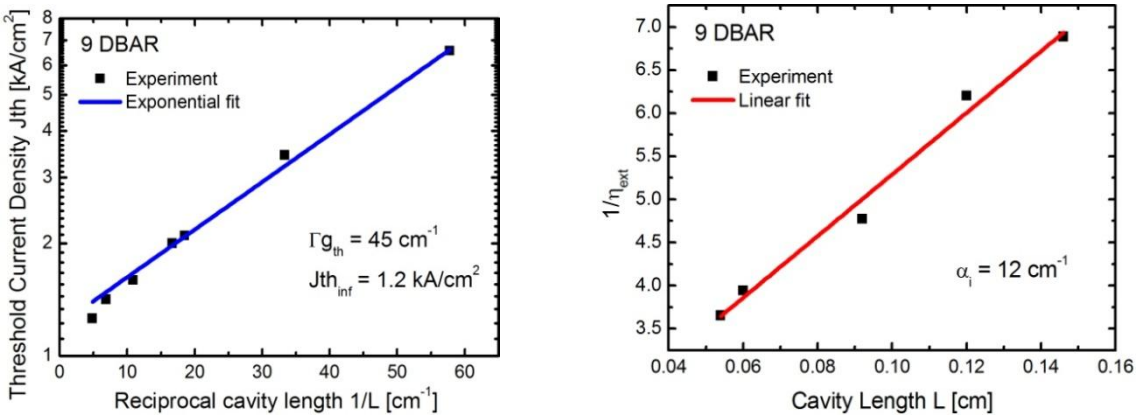

(a) (b)

Figure 0-5. (a) Densité de courant de seuil en fonction de l'inverse de la longueur de cavité (b) rendement externe en fonction de la longueur de cavité correspondant aux lasers de type 9 DBAR

N° des couches	Γ[%]	Jth_{inf} [kA/cm^2]	Γg_{th} [cm^{-1}]	α_i [cm^{-1}]
6	0,9	0,92	32,95	10,56
9	1,3	1,22	44,60	1168
12	1,8	2,01	69,83	17,92
15	2,2	2,09	56,78	18,47

(a)

N° des couches	Γ[%]	Jth_{inf} [kA/cm^2]	Γg_{th} [cm^{-1}]	α_i [cm^{-1}]
6	0,92	0,94	37	11
12	1,68	1,68	48	19
15	2,31	2,31	61	25

(b)

Tableau 0-1. Résumé des paramètres des structures pour les (a) DBAR et (b) DWELL

Le Tableau 0-1 suggère que le nombre optimal des couches implique un compromis entre un gain modal élevé et une faible valeur des pertes internes. Ces dernières semblent augmenter plus rapidement quand le nombre de couches empilées est lui même augmenté au-delà de 12, de sorte qu'il n'y ait, en pratique, plus d'intérêt, à partir de ce point, à continuer à empiler des couches. Pour le design DBAR, le cas le plus favorable semble correspondre à un empilement de 9 couches, qui donne une valeur relativement faible du $J_{th_{\inf}}$. Après avoir réalisé une évaluation systématique des différents structures et suite à des échanges réguliers avec le spécialiste de la croissance par épitaxie de III-V lab, nous avons décidé d'adopter la structure 9-DBAR comme référence pour ce travail de thèse.

Lasers de type " *shallow ridge* "

Après vérification des bonnes performances statiques de ces structures, nous avons ensuite procédé à la fabrication de lasers de type guide d'onde en arête peu profond ou « *shallow ridge* ». La Figure 0-6(a) illustre la procédure de fabrication de ces lasers. La Figure 0-6(b) montre quant à elle l'image en microscopie électronique à balayage (*scanning electron microscopy*, SEM) du dispositif final.

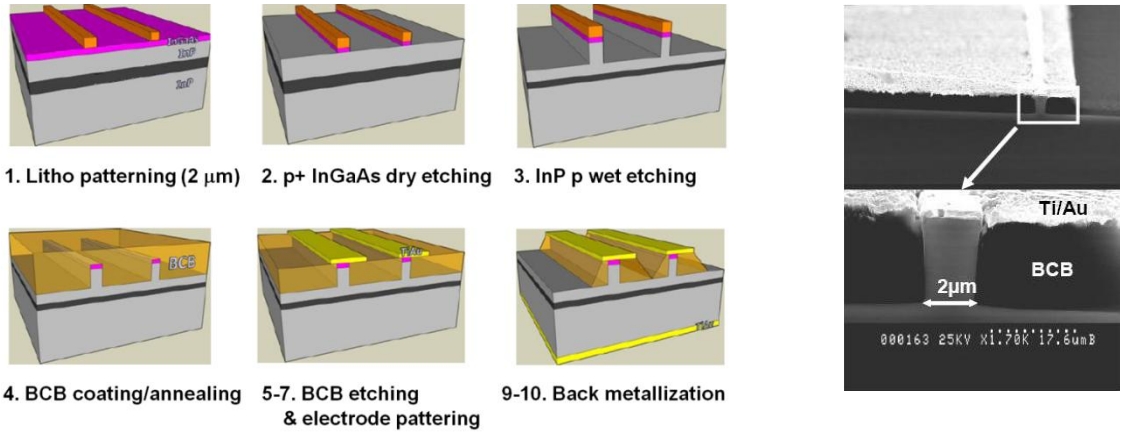

(a) (b)

Figure 0-6. (a) Etapes de fabrication de laser « *ridge* » (b) Image SEM du laser « ridge » fabriqué

Comme première étape d'évaluation des caractéristiques statiques du laser à température ambiante, les courbes L-I ont été mesurées pour des longueurs de cavité de ~ 200 μm (214 GHz) à ~2000 μm (20 GHz). Les courants de seuil obtenus ainsi que la puissance de sortie en fonction de la longueur de cavité sont illustrés dans la Figure 0-7(a) tandis que le rendement correspondant est représenté dans la Figure 0-7 (b).

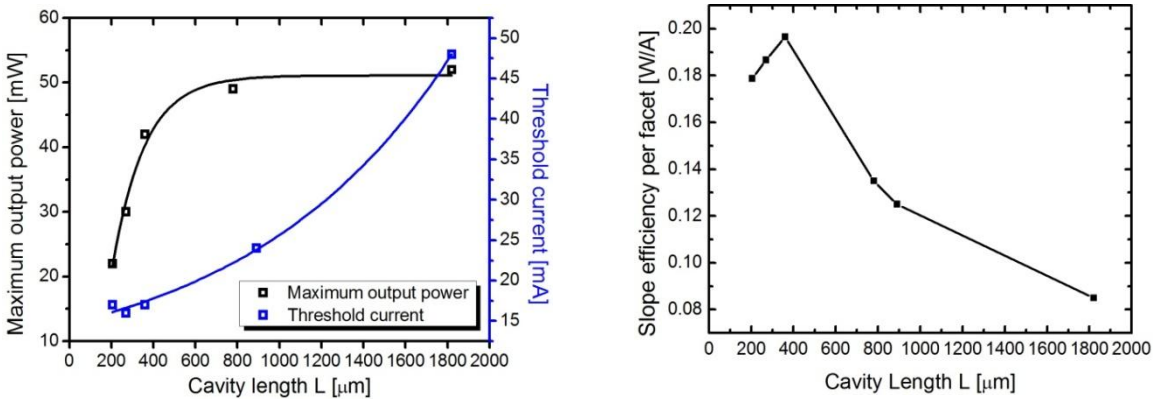

(a) (b)

Figure 0-7. (a) Puissance de sortie maximale et courant seuil, (b) rendement pour différentes longueurs de cavité de lasers « *ridge* » à une section fabriqués à température ambiante.

Blocage de modes dans des lasers QDash

Différents paramètres liés au régime de blocage de modes, tels que le spectre optique, le bruit de phase des modes et d'intensité, la gigue temporelle ainsi que les caractéristiques des impulsions ont été systématiquement analysés en fonction du courant d'injection et de la longueur de cavité dans des dispositifs à une et également deux sections.

Spectre optique

Le spectre optique a été systématiquement analysé en fonction du courant d'injection et longueur de cavité. La Figure 0-8(a) montre la largeur de l'enveloppe à mi-hauteur (*full width at half maximum*, FWHM) et la longueur d'onde au pic en fonction du courant d'injection d'un dispositif à une section de 890 μm de long.

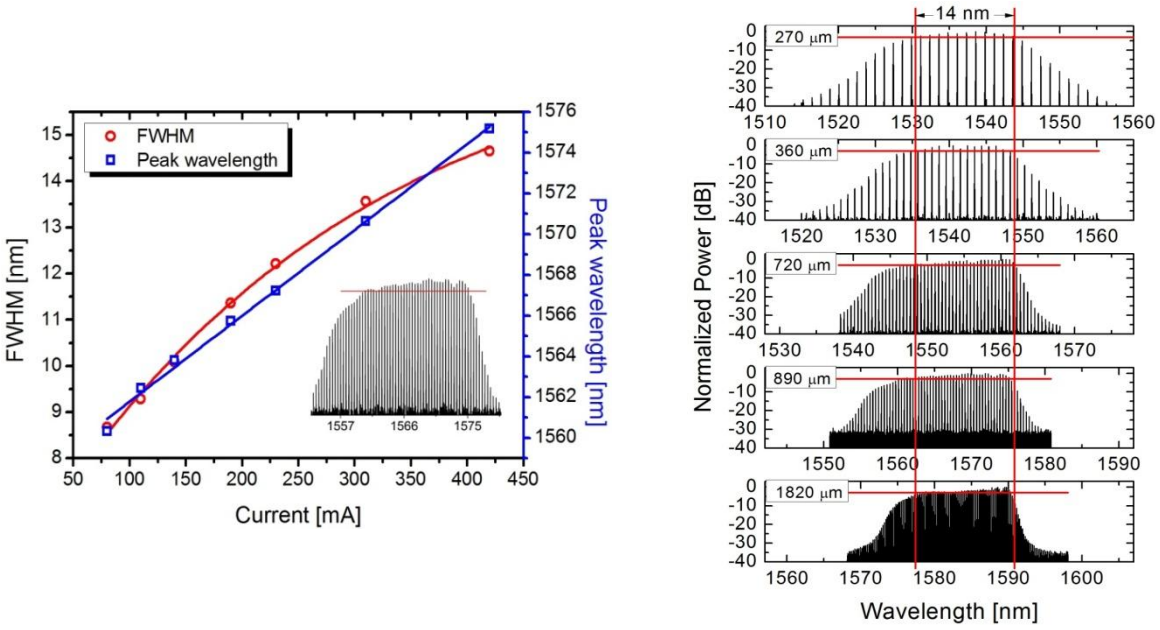

(a) (b)

Figure 0-8. (a) FWHM et longueur d'onde au pic du spectre optique en fonction du courant d'injection. Insert : spectre optique à 400 mA. (b) Spectres optiques pour des différents longueurs de cavité

Nous avons pu observer que la FHWM augmente de quelques nanomètres juste au dessus du seuil, et jusqu'à une valeur maximale de ~15 nm à des valeurs de courant d'injection élevées. Ces tendances ont été observées pour tout laser QDash FP de type DBAR indépendamment de la longueur de cavité (Figure 0-8(b)). Dans un but de comparaison, des dispositifs à deux sections issus de la même plaque ont également été étudiés. En général, la valeur maximale de FWHM qui a pu être atteinte était approximativement de 14 nm comme pour les dispositifs à une section. On peut en conclure que ce paramètre dépend du spectre de gain intrinsèque du matériau et de ses effets d'élargissement (homogènes et inhomogènes) et non d'un mécanisme ML spécifique du dispositif à une ou deux sections.

Largeur de raie RF et optique

Les largeurs de raie RF et optique représentent des paramètres très importants dans les MLL quantifiant le bruit de phase d'intensité et celui des modes longitudinaux, respectivement. La Figure 0-9(a) représente le spectre RF pour un laser 890 μm de long à une section et polarisé à 250 mA et montre une largeur de raie RF de ~ 15 kHz. La Figure 0-9(b) représente l'évolution des largeurs de raie RF ainsi que des largeurs de raie optiques d'un mode central du spectre laser, mesurées en fonction du courant d'injection.

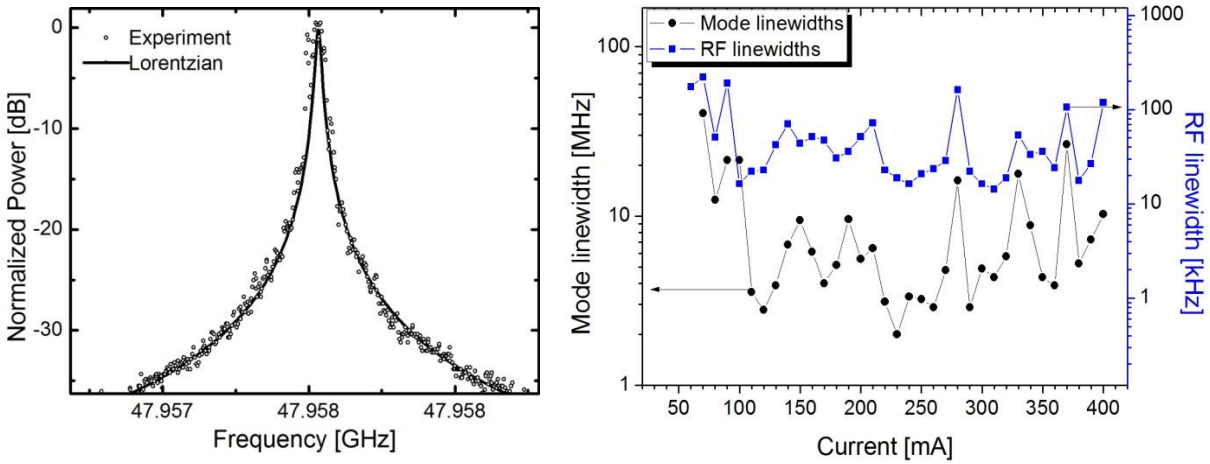

(a) (b)

Figure 0-9. (a) Spectre RF pour le dispositif de 480 μm de long à 250 mA. (b) RF et largeur de raie optique en fonction du courant d'injection

Nous pouvons observer une nette corrélation entre la largeur du mode optique et la largeur de raie RF. En effet, l'augmentation de largeur de raie du mode à des courants d'injection spécifiques se traduit par une augmentation de la largeur de raie RF correspondante. La largueur de raie RF minimale était d'environ 15 kHz à ~320 mA pour ce dispositif. La largeur de raie RF s'est révélée être la plupart du temps indépendante de la longueur de cavité, atteignant des valeurs minimales de l'ordre de 10 kHz et ce, même dans des dispositifs sans traitement spécifique des facettes.

Le spectre RF des dispositifs à deux sections a également été étudié. La Figure 0-10(a) montre les largeurs de raie RF mesurées en fonction de la tension de l'absorbant à différents courants d'injection dans la section du gain. Quand le SA a été polarisé en direct, jusqu'à la transparence, le dispositif présentait des largeurs de raie typiques de l'ordre de la dizaine de

kHz et ce, de la même façon qu'un dispositif à une section. Une augmentation abrupte de la largeur de raie juste au-dessus de 0,7 V a pu être observée pour toutes les courbes, démontrant une corrélation parfaite avec la largeur de raie optique d'un des modes centraux mesurée (Figure 0- 10(b)) comme dans le cas des dispositifs à deux sections.

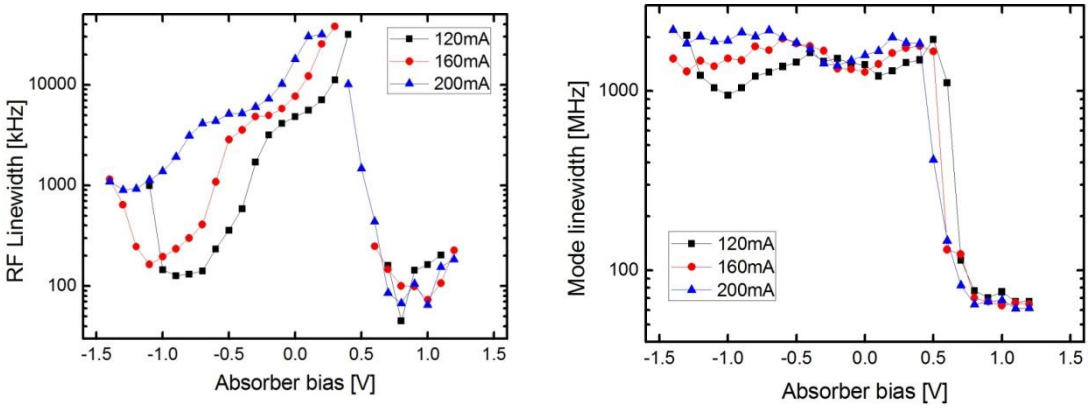

(a) (b)

Figure 0-10. (a) Largeur de raie RF et (b) largeur de mode, d'un dispositif de 890 µm à deux sections en fonction des conditions de polarisation à 120, 160 et 200 mA.

Les largeurs de raie RF étroites de l'ordre de la dizaine de kHz des lasers QDash Fabry-Perot représente un de leurs atouts majeurs. Cette caractéristique rend ces dispositifs très attractifs par rapport à leurs équivalents à base de QW qui présentent des largeurs de raie minimum de l'ordre de plusieurs dizaines ou de la centaine de kHz [36] ou des lasers *bulk* présentant des largeurs de raie de l'ordre du MHz comme mis en évidence dans la référence [11]. Un modèle théorique qui permettrait d'expliquer ce comportement, parfois attribué à un facteur de confinement plus faible des couches actives des QDash [11] fait toujours défaut. A partir des résultats expérimentaux décrits dans cette section, nous pouvons toutefois conclure qu'un faible bruit de phase des modes optiques se traduit par un faible bruit de phase d'intensité du laser. En effet, les largeurs de raies optiques des lasers FP à base de structure QW sont de l'ordre de la dizaine de MHz [36], tandis que celles de lasers de type *bulk* de l'ordre de la centaine de MHz. Cette tendance est en accord du point de vue qualitatif avec les largeurs de raies RF correspondantes dans les différents types de dispositifs. De plus, dans les trois cas, le rapport de la largeur de raie optique / largeur de raie RF est du même ordre de grandeur, ce qui signifie, en principe, que toutes les structures présentent une corrélation de phase ou,

autrement dit, une certaine forme de blocage de modes. Si le FWM est principalement responsable de la cohérence intermodale, qui se traduirait par le rapport entre les largeurs de raies optique et RF et non par la largeur de RF elle-même, le paramètre d'efficacité FWM devrait être similaire dans tous les types de dispositifs. Ceci a été confirmé pour les cas de SOA à base de QDash et *bulk* [43]. Le paramètre faisant la différence en performance ne serait pas une efficacité FWM plus importante mais plutôt une largeur de raie optique plus faible des dispositifs QD/Dash. Une des raisons de cette caractéristique pourrait être liée à un facteur d'inversion de population plus important dans les QDash/Dots. En effet, le taux d'émission spontanée diminue quand l'inversion du milieu à gain augmente. Ainsi, le fait de faire fonctionner le laser bien au-dessus du seuil doit induire un rapport taux d'émission stimulée/ taux d'émission spontanée plus important, ce qui devrait avoir pour effet de diminuer les caractéristiques du bruit. Le second aspect qui pourrait être aussi bien responsable de l'amélioration des largeurs de raies RF dans les dispositifs QDash/Dot pourrait être lié à un facteur de confinement Γ plus faible, qui induirait une inversion de population plus importante. Les valeurs obtenues pour un dispositif à couche de QD multiple (de 6 à 12 couches) sont de l'ordre de 1% tandis qu'elles se situent autour de 10% et 70% dans les dispositifs à base de MQW et *bulk*, respectivement. Ceci est corrélé à peu de choses près avec l'augmentation de la largeur de raie optique correspondante dans chaque type de laser. De plus, la réduction du facteur de confinement résulterait en une quantité plus faible d'émission spontanée couplée dans les mode laser comme précédemment décrit [36], réduisant ainsi le bruit de phase d'intensité.

Gigue temporelle et spectre optique

Il est bien connu que la gigue temporelle et la largeur de raie RF sont intimement liées au bruit de phase des modes optiques sous différents types de régimes ML [44–50]. Nous avons vu que, pour le cas particulier des dispositifs à une section, l'absence d'absorbant saturable et le gain modal élevé disponible dans les couches actives à base de QDash, ont permis de travailler avec des longueurs de cavités très courtes, compatibles avec des fréquences de répétition élevées allant jusqu'à 346 GHz [51]. A ces fréquences de répétition il est difficile de mesurer la gigue temporelle avec les techniques de photo-détection rapide communément utilisées en raison de à la bande passante limitée des photodiodes commerciales. Nous avons analytiquement et expérimentalement démontré dans ce travail que la gigue temporelle peut

être liée au spectre d'émission du laser, ce qui permet une mesure indirecte qui n'est pas limitée par la bande passante de la photodiode.

Le spectre optique $\left|E(\omega)\right|^2$ peut être calculé en prenant la fonction d'autocorrélation du champ électrique $R(\tau)$ puis sa transformée de Fourier, c.à.d.

$$\left|E(\omega)\right|^2 = \int_{-\infty}^{\infty} R(\tau) e^{-j\omega\tau} d\tau = \int_{-\infty}^{\infty} \sum_{n=1}^{N} {E_n}^2 e^{j\omega_n \tau} e^{-\frac{1}{2}\left[\mathrm{var}(\theta_c(\tau)) + \omega_r{}^2 (n-n_c)^2 \mathrm{var}(\Delta t_r(\tau)) + 2\omega_r (n-n_c)\mathrm{cov}(\theta_c(\tau), \Delta t_r(\tau))\right]} e^{-j\omega\tau} d\tau$$

$$\propto \sum_{n=1}^{N} \left\{ \left[\frac{1}{2}\Delta\omega_{\theta_c} + \frac{1}{2}{\omega_r}^2 (n-n_c)^2 D + \omega_r (n-n_c)\gamma_{\theta_c,\Delta t_r} \right]^2 + (\omega-\omega_n)^2 \right\}^{-1} \qquad (0.2)$$

avec E_n l'amplitude du champ électrique du mode longitudinal n avec $n = 1...N$ (N le numéro total de modes longitudinaux), $\theta_c(\tau)$ le bruit de phase du mode central, $\Delta t_r(\tau)$ la gigue temporelle des impulsions et D sa constante de diffusion, $\gamma_{\theta_c,\Delta t_r}$ la pente du terme de corrélation $\langle \theta_c(\tau)\Delta t_r(\tau) \rangle$ et $\Delta\omega_{\theta_c}$ la largeur de raie optique du mode central. En conséquence, le spectre optique consiste en N fonctions Lorentziennes centrées à ω_n avec une largeur de l'enveloppe à mi-hauteur (FWHM):

$$\Delta\omega_n = \Delta\omega_{min} + \omega_r^2 (n-n_{min})^2 D \qquad (0.3)$$

avec $n_{min} = n_c - \gamma_{\theta_c,\Delta t_r} / \omega_r D$, et $\Delta\omega_{min} = \Delta\omega_{\theta_c} - \gamma^2_{\theta_c,\Delta t_r} / D$. L'équation (0.3) montre que le coefficient de diffusion D affecte la largeur de raie des modes. Ainsi une estimation de la gigue temporelle est facilement accessible à partir du spectre optique en mesurant les largeurs de raie du mode atour de n_{min} [52].

On peut noter que la corrélation entre $\theta_c(t)$ et $\Delta t_r(t)$ affecte les termes d'ordre un et zéro dans l'équation (0.3). Ceci résulte en une modification de la fréquence du mode avec une largeur de raie minimum pour le cas ou les deux processus aléatoires sont statistiquement indépendants ($\gamma_{\theta_c,\Delta t_r} = 0$). Cependant, comme la valeur de D est déterminée sans ambiguïté à

partir du terme de second ordre dans l'équation(0.3), elle peut être évaluée sans connaissance préalable du niveau exact de corrélation entre $\theta_c(t)$ et $\Delta t_r(t)$.

La valeur de *D* détermine également le spectre d'intensité du $|I(\omega)|^2$, plus communément appelé spectre de radio fréquence (RF), qui peut être simplement calculé de la même façon que le spectre optique. Sans rentrer dans les détails, il correspond à la somme de $N-m$ lignes Lorentziennes centrées à $m\omega_r$ pour $m=1$ à $N-1$. A chaque valeur donnée de m, chaque raie aura des largeurs de raies FWHM identiques données par :

$$\Delta\omega_{RF_m} = m^2\omega_r^2 D = m^2\Delta\omega_{RF_1} \quad (0.4)$$

avec $\Delta\omega_{RF_1} = \omega_r^2 D$. Chaque raie correspond au battement entre une paire de modes séparés par $m\omega_r$ dans le spectre optique. Une relation entre les deux largeurs de raies de modes et celles de leurs battements, peut être établie en combinant les équations (4.9) et (4.8) pour donner :

$$\Delta\omega_n = \Delta\omega_{min} + \frac{\Delta\omega_{RF_m}}{m^2}\left(n-n_{min}\right)^2 \quad (0.5)$$

ou de façon équivalente :

$$\Delta\omega_n = \Delta\omega_{min} + \Delta\omega_{RF_1}\left(n-n_{min}\right)^2 \quad (0.6)$$

relation également obtenue et observée expérimentalement dans les travaux décrits en référence [44] pour des MLL passifs à deux sections émettant à 1,3 μm.

Une validation expérimentale des analyses théoriques décrites précédemment a été réalisée avec trois dispositifs à une section présentant des longueurs de cavité différentes. La Figure 0- 11(a) montre le spectre optique d'un laser de 1000 μm de long polarisé à 150 mA et comportant un total de $N=30$ modes. Dans un premier temps, afin de vérifier la corrélation de phase du mode et donc l'opération ML, le spectre RF de tous les $N-1=29$ battements de modes entre des paires de modes consécutifs ($m=1$), a été mesuré. La Figure 0-11(b) représente la superposition de tous ces battements. Tous les spectres de battements

correspondent très bien à des fonctions Lorentziennes. La largeur de raie moyenne du battement est $\Delta\omega_{RF_1}/2\pi = 89$ kHz avec une déviation standard de 5,3 kHz, tandis que la fréquence centrale moyenne est $\omega_r/2\pi = 39.6$ GHz avec une déviation standard de 18,2 kHz. Ces petites déviations démontrent la corrélation de la phase du mode entre tous les N modes et de plus valident les conditions du blocage de mode. La forme Lorentzienne de toutes les raies RF pour $m = 1$ confirme également que $\Delta t_r(t)$ est un processus de marche aléatoire gaussienne.

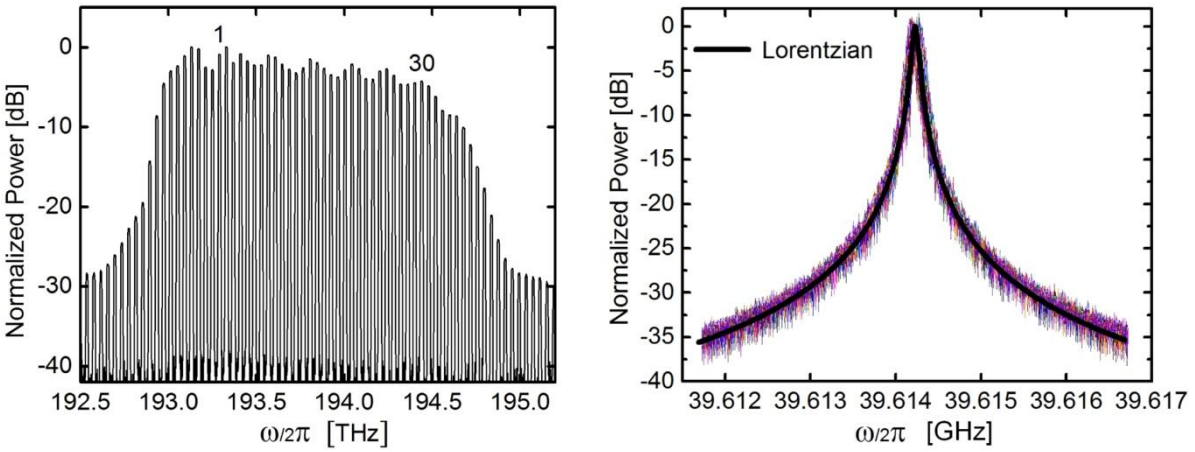

(a) (b)

Figure 0- 11. (a) Spectre optique. (b) Spectre RF des 29 modes de battement consécutifs (m = 1) d'un laser de 1000 µm de long polarisé à 150 mA. [52]

La largeur de raie de chacun des N modes du spectre optique a ensuite été mesurée par la technique d'auto-hétérodynage. Tous les spectres de battements résultant correspondent très bien aux fonctions Lorentziennes, comme illustré pour plusieurs modes dans la Figure 0-12 (a). La Figure 0-12(b) illustre les largeurs de raies mesurées en fonction du nombre de modes. La courbe continue représente une parabole $\Delta\omega_n/2\pi = 6.5 + 0.092(n-12)^2$ MHz, à partir de laquelle $\Delta\omega_{RF_1}/2\pi = 92$ kHz a été calculé avec une erreur standard de ~ 3 kHz. Ce résultat est en très bon accord avec les valeurs expérimentales des largeurs de raies mesurées pour chaque battement (Figure 0-11(b)), vérifiant l'équation (0.6).

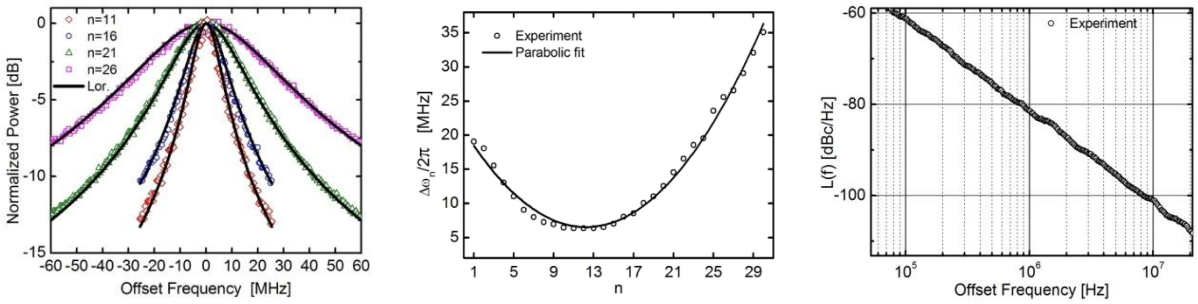

(a) (b) (c)

Figure 0-12. (a) Spectres de battement pour les modes 11, 16, 21 et 26. (b) Largeur de raie de modes en fonction du numéro de mode, (c) SSBPN, pour le laser de 1000 µm de long polarisé à 150 mA. [52]

On peut également voir que $n_{min} = 12$, ce qui correspond au numéro de mode le moins bruité avec une largeur de raie $\Delta\omega_{\theta_c} / 2\pi = 6.5$ MHz. Cette valeur devrait être celle de la largeur de raie de tous les modes en l'absence de gigue temporelle. Le coefficient de diffusion a également été calculé à partir de la fonction parabolique donnant comme valeur $D = 0.0092$ fs. Les gigues temporelles « *pulse-to-pulse* » et « *pulse-to-clock* » en partant par exemple de 1 MHz jusqu'à 20 MHz, ont ensuite été estimées à $\sigma_{pp} = 15.16$ fs et $\sigma_{pc} = 0.47$ ps, respectivement. Cette dernière est en parfait accord avec une mesure indépendante du bruit de phase SSBPN (*single side band phase noise*), comme illustré dans la Figure 0-12(c), donnant $\sigma_{pc} = 0.48$ ps, quand la même bande d'intégration est utilisée.

Phase statique et profil des impulsions

La différence de phase statique entre des modes adjacents, a été mesurée en utilisant la technique de détection hétérodyne décrite en référence [53], à partir de laquelle ont ensuite été déterminés le retard de groupe (*Group Delay*, GD), la dispersion du retard de groupe (*Group Delay Dispersion*, GDD) ainsi que la phase spectrale du champ électrique. La Figure 0-13(a) représente le GD mesuré pour un laser à une section de 890 µm de long, polarisé à 400 mA en fonction du décalage de fréquence (la fréquence de référence étant celle du mode central) pour des mesures réalisées sur 50 modes du spectre optique illustré dans la Figure 0-13(b) (encadré du haut). Un GD presque linéaire a été obtenu dont la pente a permis de déterminer la valeur du GDD à 1,3 ps^2. La Figure 0-13(b) (encadré du bas) illustre la phase

spectrale correspondante (en rouge), obtenue après intégration de la courbe de GD, montrant qu'elle présente une forme parabolique.

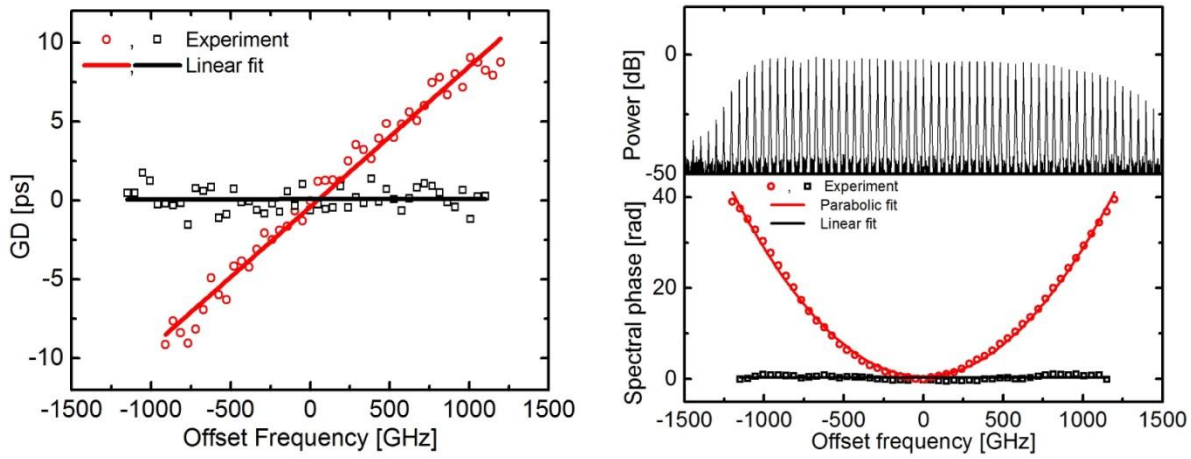

(a) (b)

Figure 0-13. (a) GD du laser de 890 µm de long à une section mesuré en sortie de laser (carrés rouges) et après 65 m de SMF (carrés noir) (b) (haut) spectre optique et (bas) phase spectrale en sortie de laser (courbe rouge) et après 65 m de SMF (courbe noir) pour un courant d'injection de 400 mA. [54]

Malgré la très bonne synchronisation des modes optiques qui se manifeste par une faible largeur de raie RF, le profil de phase spectrale parabolique montré dans la Figure 0-13(b) (bas en rouge) ne permet pas la génération d'impulsions. Pour pouvoir l'observer, l'autocorrélation de l'intensité du champ électrique (AC) a été mesurée directement à partir du laser à l'aide d'un système de détection comprenant un cristal non linéaire doubleur de fréquence (*second harmonic generation*, SHG) et un photomultiplicateur. Les résultats sont représentés par la courbe rouge dans la Figure 0-14(a). Le profil observé est presque plat indiquant l'absence d'impulsions nettes, un résultat en accord avec le profil d'intensité représenté dans la Figure 0-14(b) (courbe rouge), reconstruit à partir de la puissance et le spectre de phase mesurés.

Les mesures précédentes ont été répétées après insertion, à la sortie du laser, d'une fibre standard monomode (*single mode fiber*, SMF) introduisant -1,3 ps^2 de dispersion accumulée, censée compenser le GDD du laser de 1.3 ps^2. Les courbes noires de la Figure 0-13(a) et de la Figure 0-13(b) représentent respectivement le GD mesuré et la phase spectrale après compensation de la dispersion. Le terme de second ordre de la phase spectrale est alors

négligeable à l'extrémité de la fibre, où les modes interfèrent de façon constructive, permettant une génération d'impulsion efficace. Ceci est mis en évidence par le train d'impulsions parfait de la trace d'autocorrélation de l'intensité représenté dans la Figure 0-14(a) (courbe noire), qui a été mesuré sans utiliser aucun amplificateur optique. En fait, les largeurs d'impulsion très étroites mesurées à 600 fs après déconvolution (en supposant que l'impulsion présente une forme gaussienne) et la puissance de sortie moyenne de 40 mW correspondent à des puissances crêtes plus grandes que 1 W, ce qui représente la valeur de puissance crête la plus grande jamais obtenue avec un laser semiconducteur à blocage de modes émettant à 1,55 μm à des fréquences de répétition comparables. Le profil d'intensité du champ électrique a une fois encore été reconstruit et représenté dans la Figure 0-14(b) (courbe noire) et donne des largeurs d'impulsion de 600 fs. Ce résultat est en accord avec la trace d'autocorrélation mesurée et donne un produit largeur d'impulsion-largeur spectrale (*Time Bandwidth Product*, TBP) de 0,98.

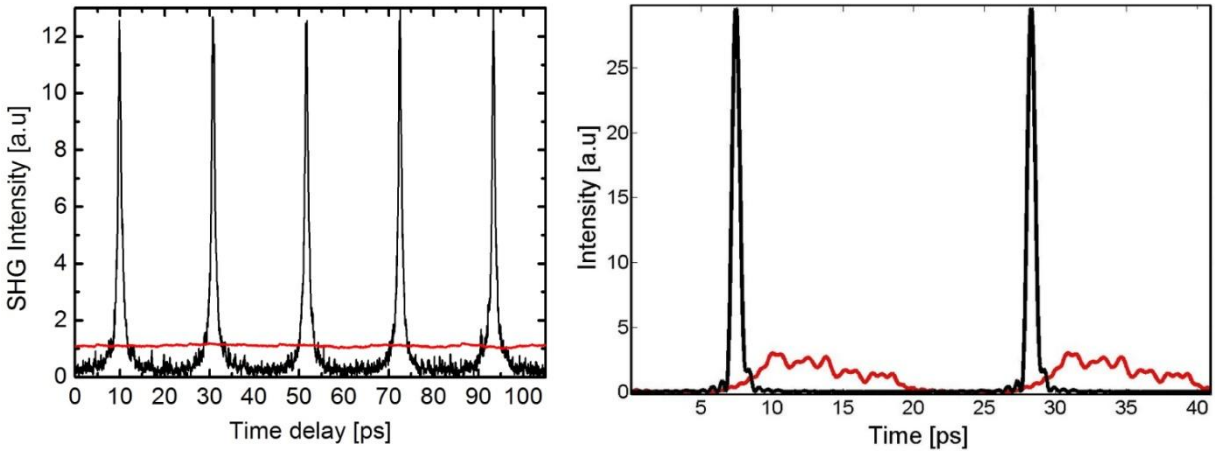

(a) (b)

Figure 0-14. (a) Trace d'autocorrélation d'intensité d'un laser de 890 μm en sortie du laser (courbe rouge) et après insertion d'une SMF de 65 m (courbe noire) (b) Intensité du champ reconstruite en sortie du laser (courbe rouge) et après 65 de SMF (courbe noire) pour un courant d'injection de 400 mA. [54]

Afin de comparer les caractéristiques de la phase stationnaire de dispositifs à une section à ceux des MLL à deux sections classiques, le GD et le GDD d'un laser à deux sections comportant un absorbant saturable, ont été mesurés. Le dispositif à deux sections provenait de la même plaque et présentait exactement la même longueur de cavité que le dispositif à une section de 48 GHz précédemment caractérisé. La section de l'absorbant saturable avait

une longueur de 60 μm et le régime ML dans ce laser a été observé quand la section était polarisée entre 0,2 et -3V en fonction du courant d'injection. A l'instar des MLL passifs classiques, les impulsions les plus courtes ont été observées pour les courants les plus faibles avec une valeur minimale de ~ 1 ps lorsqu'ont été appliqués un courant de 70 mA dans la section à gain et une tension inverse de -1,5 V à l'absorbant, donnant une puissance optique moyenne de ~ 4 mW par facette. Dans ces conditions, le GD a été directement mesuré en sortie de laser, comme illustré dans la Figure 0-15(a) et le GDD a été estimé à 0,28 ps^2.

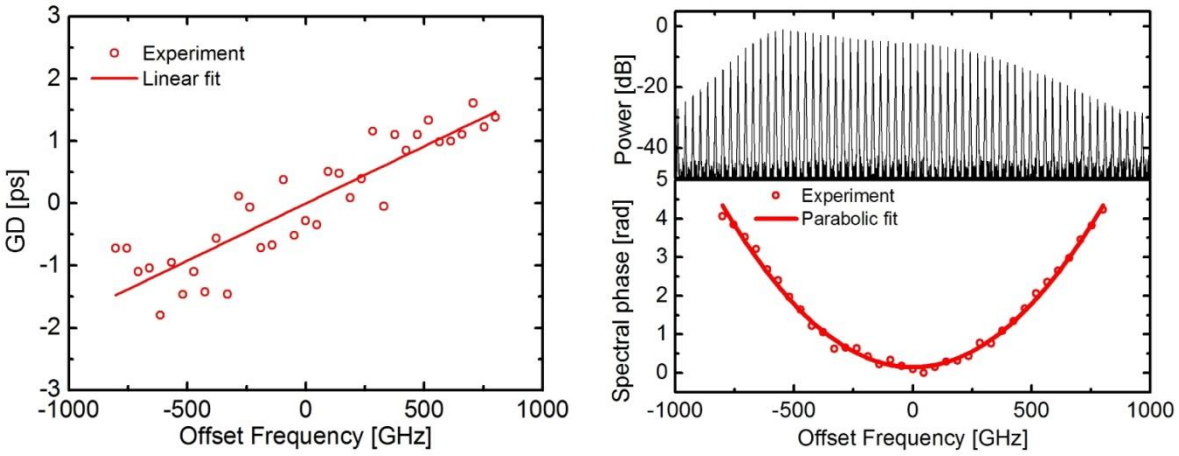

(a) (b)

Figure 0-15. (a) GD d'un laser de 890 μm de long à deux sections mesuré en sortie du laser avec (b) (haut) spectre optique et (b) (bas) profil de phase spectrale correspondant sous 70 mA de courant d'injection et une polarisation inverse appliquée de -1.5 V. [54]

Le GD et le GDD sont tous les deux plus faibles que dans les dispositifs à une sections grâce à l'absorbant saturable qui fait verrouiller les phases des modes longitudinaux de façon périodique. La faible valeur du GDD a été mise en évidence par le caractère parfait du tracé d'autocorrélation illustré dans la Figure 0-16(a), obtenu sans avoir besoin d'insérer une fibre SMF additionnelle pour compenser la dispersion et sans avoir recours à une amplification optique quelconque. Les largeurs d'impulsion ont également été mesurées à partir du champ d'intensité reconstruit (Figure 0-16(b)) et valent 1,5 ps. Le tracé d'autocorrélation présentait des impulsions plus courtes de 1,2 ps (après déconvolution) comme conséquence d'une compensation GDD du à -0,12 ps^2 de dispersion accumulée dans notre montage de mesure d'autocorrélation. Avec une largeur spectrale de 9,5 nm, le TBP de l'impulsion a été calculé à

1,7 mais pourrait être réduit à une valeur proche en limite de Fourier en compensant le GDD du laser, comme dans le cas des dispositifs à une section.

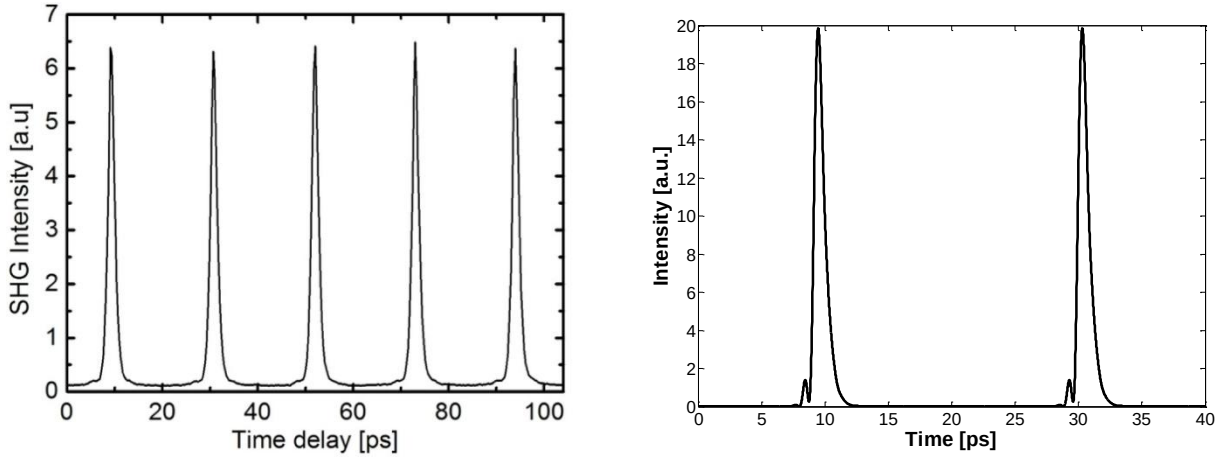

(a) (b)

Figure 0-16. (a) Autocorrélation d'intensité pour le laser de 890 μm de long à deux sections en sortie de laser et (b) profil d'intensité de champ reconstruit correspondant pour un courant d'injection de 70 mA et une polarisation inverse de -1.5 V. [54]

Radio sur fibre (RoF) pour des liens multi-Gbps sans fil

En collaboration avec Orange Labs (B. Charbonnier), nous avons réalisé des expériences de conversion par montée en fréquence (*up-conversion*) et de modulation directe pour simuler la voie descendante dans un environnement intérieur radio sur fibre (RoF) typique. Pour ce faire, nous avons utilisé l'approche de laser en blocage de modes passif en utilisation un QDash à une section, du fait de sa supériorité en termes de largeur de raie RF et de puissance optique atteignable si on le compare à son homologue à deux sections. Le laser présente une longueur de cavité de ~780 μm correspondant à une fréquence de répétition de ~55 GHz. Le spectre RF est étroit et stable dans un certain nombre de conditions de polarisation quelles que soient les fluctuations mécaniques ou vibrations techniques.

Le montage expérimental utilisé est présenté en Figure 0-17. Le signal test est compatible avec le standard IEEE802.15.3c et fonctionne jusqu'à 3 Gbps pour des applications multimédia d'intérieur. Le signal en bande de base est généré par un générateur de signaux arbitraire à deux sorties et transposé par montée en fréquence à une fréquence intermédiaire de 4,4 GHz par un mélangeur de signaux. La modulation crée deux bandes latérales autour de

la fréquence d'oscillation naturelle du laser (55.27 GHz). Deux fréquences apparaissent par transposition par montée en fréquence à partir du signal original à 4,4 GHz : la première à 50,87 GHz et la seconde à 59,67 GHz ainsi qu'un pic RF intense à 55,27 GHz. Après photodétection et un filtrage adéquat de la seconde fréquence, le signal radio transposé est prêt pour la propagation dans l'air.

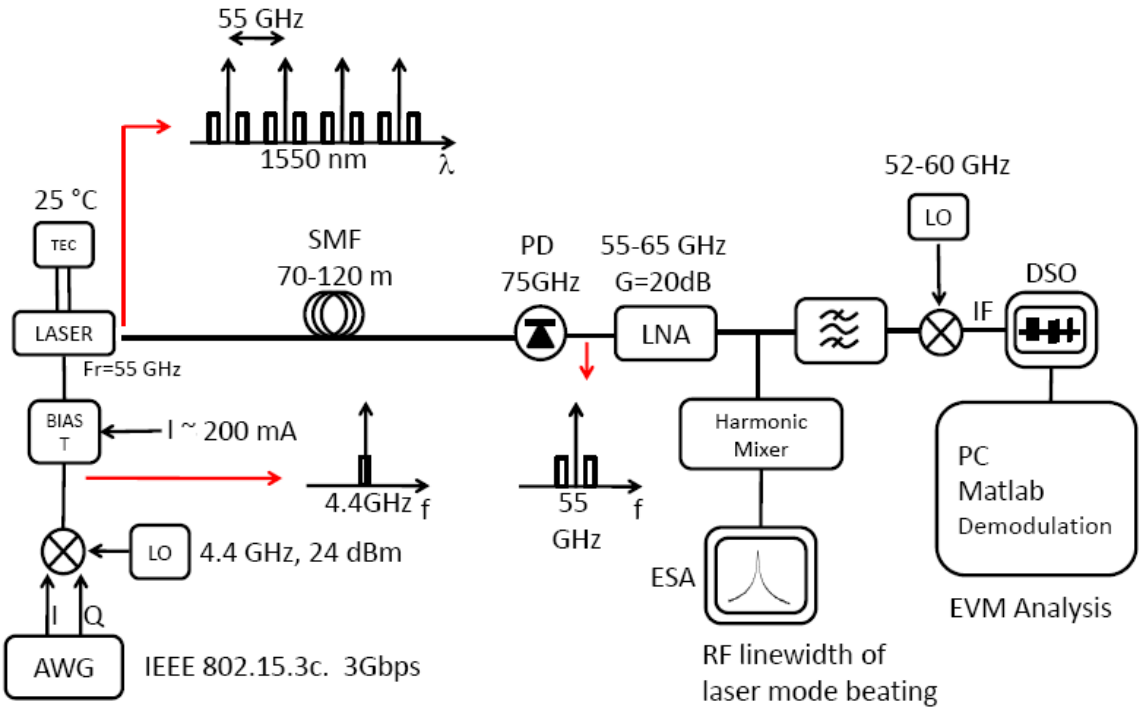

Figure 0-17. Montage pour les expériences de transmission RoF

Afin d'évaluer la qualité de ce signal, nous l'avons transposé par descente en fréquence à environ 5 GHz au moyen d'un mélangeur alimenté par un oscillateur local à 55 GHz. Le signal de fréquence intermédiaire est visualisé sur un oscilloscope numérique à échantillonnage à 40 GS/s. Pour quantifier les performances du transmetteur, nous avons mesuré le vecteur d'erreur (*error vector magnitude*, EVM). Cette mesure indique combien les points du diagramme de constellation sont loin d'un transmetteur idéal, le diagramme de constellation étant un diagramme à deux dimensions composé d'un axe dit « réel » (en phase), et d'un axe dit « imaginaire » (en quadrature). Des EVM typiques de 11 % avec un grand rapport signal sur bruit supérieur à 25 dB ont été obtenus, démontrant les grandes performances de ces composants (Fig. 2). Les expériences actuellement menées ont maintenant pour but de diminuer le bruit de phase et d'augmenter le gain différentiel du laser

dans le but d'atteindre des débits aussi élevés que 10 Gbps pour les futures applications communications sans fil d'intérieur.

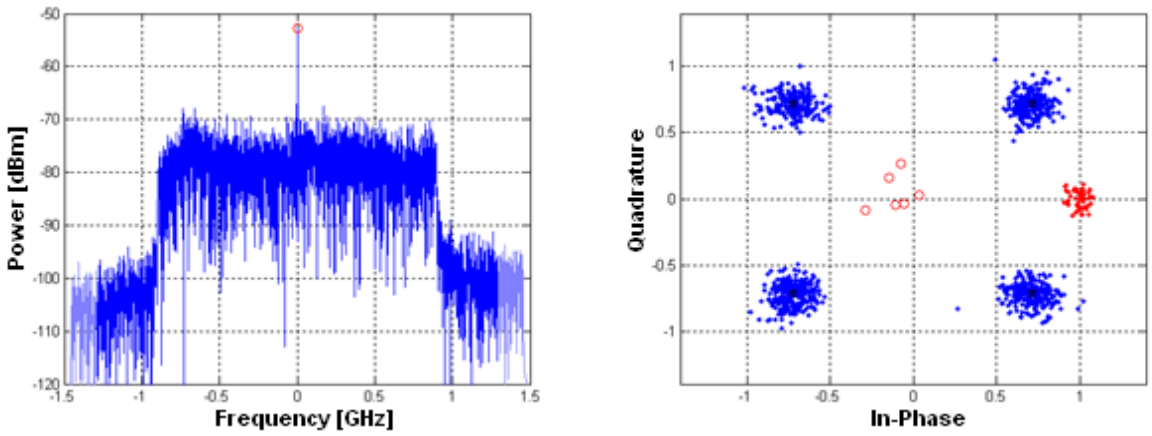

(a) (b)

Figure 0-18. (a) Spectre du signal démodulé et (b) diagramme de constellation correspondant pour l'estimation du EVM

Bien que des performances similaires donnant des valeurs de EVM ~11% ont été décrites précédemment avec la même approche [34], un certain nombre d'améliorations ont été apportées avec l'introduction d'un dispositif insensible à la rétroaction optique. En effet, les expériences précédentes utilisant des lasers QDash FP conventionnels, étaient très affectées par les effets de rétroaction optique. Cela se manifestait par un bruit de phase de la porteuse millimétrique augmenté, qui présentait au plus bas quelques dizaines de kHz de largeur de raie RF. De plus, les largeurs de raies les plus étroites et par conséquence une meilleure performance du système dans son ensemble, étaient généralement obtenues au dépend d'un désalignement intentionnel du couplage laser/ fibre pour minimiser les effets de rétroaction optique en cavité externe courte, induisant une perte de puissance RF significative et nécessitant l'emploi d'un EDFA à la sortie du laser. Dans nos expériences, nous n'avons pas eu besoin d'amplification du signal modulé, ce qui représente un avantage important en termes de coûts et de considérations pratiques.

Par ailleurs, grâce à l'insensibilité du système vis à vis des réflexions dues à la rétroaction optique, la porteuse millimétrique générée restait toujours stable sans montrer de dérive significative de la fréquence. Malgré ces améliorations importantes, les EVM obtenus

n'étaient pas diminués par rapport aux expériences précédentes, comme on aurait pu l'attendre. Nous avons attribué ce résultat aux composants RF externes présents dans le montage expérimental qui limitaient la valeur minimale de l'EVM pouvant être atteinte. Nous avons pu confirmer cette hypothèse ultérieurement en réalisant des expériences de « *back-to-back* » utilisant les montées en fréquence dans le domaine électrique : les résultats donnent un EVM de 11%, fixant la limite inférieure de la valeur que ce paramètre peut prendre.

OFDM optique pour des liens Tbps

En collaboration avec Dublin City University (groupe de Prof. L. Barry), le laser QDash 48GHz précédemment caractérisé dans la configuration à une section a été utilisé pour implémenter une transmission OFDM avec détection directe (DD-OFDM). Nous avons utilisé une transmission en bande latérale unique (SSB) selon une approche similaire à celle utilisée dans la référence [55]. Le signal SSB OFDM, qui consiste en 74 sous-porteuses, chacune étant codée par 16 QAM, a été modulé en 33 modes significatifs (ceux compris dans la largeur spectrale FWHM du spectre optique) comprenant une bande spectrale d'environ ~1,5 THz lorsqu'il a été polarisé à 300 mA. Le schéma expérimental est illustré dans la Figure 0-19 : les modes spectraux du laser QDash ont été codés avec des données OFDM en utilisant un modulateur Mach-Zehnder (MZM) et transmis à travers 25 km de SMF. Chacun des modes a été filtré individuellement puis traité en utilisant Matlab. Le graphe de la Figure 0-20 montre le diagramme de constellation pour un mode spectral donné (à 1558,55 nm) avant et après transmission. L'EVM des données *back-to-back* était de 11% et après transmission dans 25 km de SMF, de 13,4%. Le taux d'erreur binaire (*bit error rate*, BER) calculé était, quant à lui et pour les deux cas, en-dessous du seuil de $1x10^{-3}$ nécessaire pour les systèmes utilisant la correction d'erreurs sans voie de retour (FEC) (avec 7% overhead).

Le Tableau 0-2 montre les performances correspondantes aux trois modes du spectre optique, à chaque extrémité et au centre. D'habitude, la performance est dégradée vers les extrémités à cause d'une puissance plus faible par mode et probablement d'un bruit de phase plus important. Le taux de données par mode, en tenant compte du surcoût de transmission (*overhead*), était de 10 Gbps, ce qui correspondait à un débit agrégé total de 0,33 Tbps.

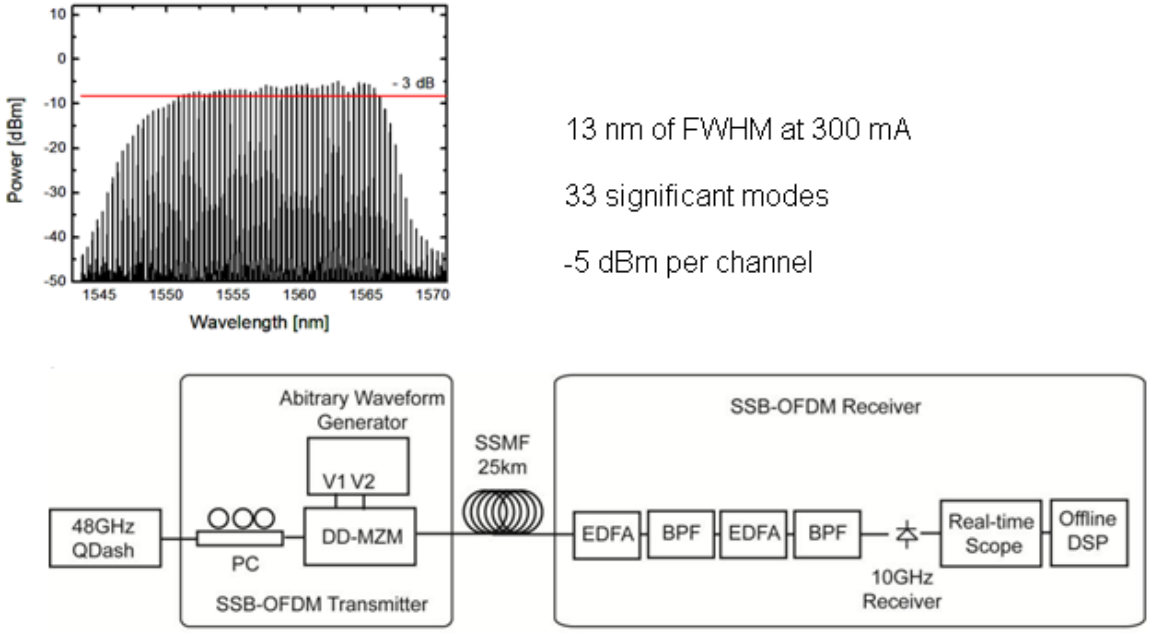

Figure 0-19. Montage pour les expériences de transmission OFDM.

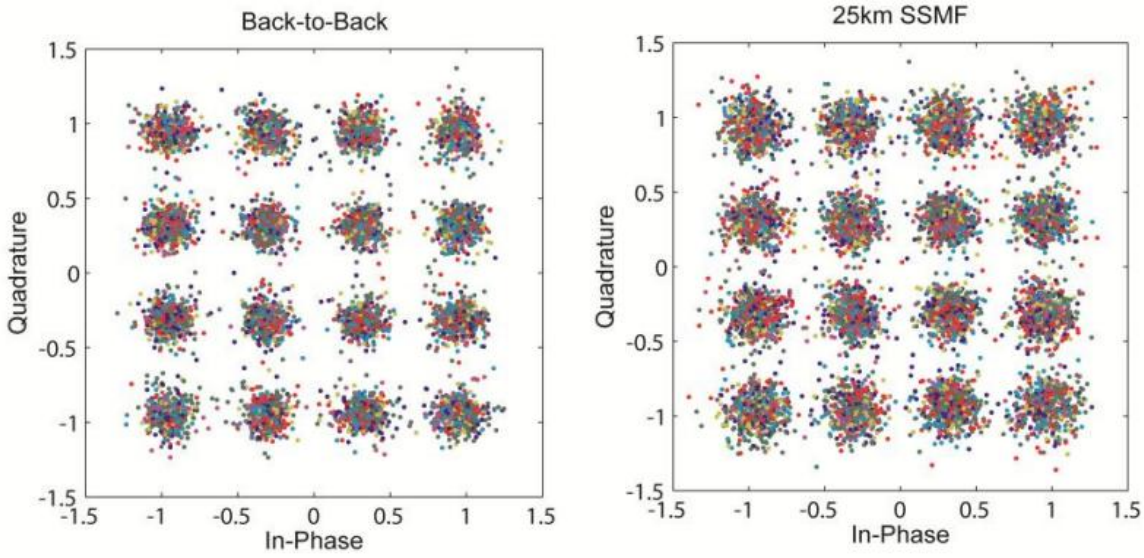

Figure 0-20. Diagrammes de constellation correspondant aux transmissions en back-to-back et après 25km de SMF.

Mode	Back to back		25 km	
(nm)	EVM (%)	BER	EVM (%)	BER
1553,55	10,96	4,9E-4	13,41	9,3E-4
1559,34	9,8	9E-5	12,7	8E-4
1566,00	10,66	4,6E-4	13,66	1,3E-3

Tableau 0-2. Performance OFDM correspondant aux trois différents modes en *back-to-back* et après transmission sur 25 km de SMF

Bien que l'efficacité spectrale obtenue de 0.22 bits/s/Hz (0.33Tbps/1.5THz) est petite par rapport à la valeur maximale de 11 bits/s/Hz trouvée dans la littérature [56], les expériences précédentes ont démontré le concept d'implémentation de supercanaux en utilisant un seul laser QDash à blocage de modes passif. Des expériences en cours, utilisant des lasers à 10 GHz, avec lesquels on prévoit un débit agrégé cinq fois plus important que celui obtenu dans les expériences précédemment décrites (soit 1,65 Tbps), pourront démontrer des transmissions Tbps en utilisant une seule source laser avec une efficacité spectrale supérieure, plus proche de celle de transmissions de type supercanaux à l'état de l'art .

Conclusion

L'optimisation de la croissance de bâtonnets quantiques InAs/InP a permis la réalisation de lasers à blocage de modes à une et deux sections présentant de très bonnes performances en termes de gain modal, de puissance moyenne, et de densités de courant de seuil.

L'identification et le contrôle des principaux phénomènes physiques limitant la performance des dispositifs ont permis démontrer des valeurs records de puissance crête, durée d'impulsion, largeur de raies RF et fréquences de répétition dans les deux types de configuration à blocage de modes passif.

Le résultat des mesures de phase spectrale dans des lasers à une section est en accord avec les données de simulation qui considéraient un mécanisme de type FWM comme étant à l'origine du régime de blocage de modes dans ce type de dispositifs. Le comportement ML

dans les lasers à deux sections s'est trouvé être gouverné par l'interaction entre le gain et la perte des effets de saturation à l'origine de nos observations expérimentales. Ces dernières ont généralement été en accord avec celles habituellement décrites pour les MLL QD plus matures basés sur le système InAs/GaAs.

Le GDD affecte la génération d'impulsions dans les dispositifs à une section. Cependant, nous avons pu montrer que ce phénomène peut être facilement compensé pour utiliser de façon efficace la bande passante spectrale etendue qui peut être atteinte dans ces structures laser, permettant ainsi des largeurs d'impulsion de l'ordre de la sub-picoseconde. En particulier, la décroissance du GDD allait de pair avec celle du courant d'injection, favorisant la formation d'impulsions bien qu'augmentant la puissance de sortie et réduisant généralement la largeur de raie RF. Ceci représente un avantage par rapport aux dispositifs classiques ML à deux sections, dans lesquels les impulsions les plus courtes sont généralement obtenues pour les courants d'injection les plus faibles et sous une polarisation inverse élevée de l'absorbant, ce qui induit des puissances de sortie moyennes plus basses et une largeur de raie RF généralement plus élevée.

Nous avons observé que la largeur de raie RF peut, en général, atteindre des valeurs très faibles, de l'ordre du kHz, plus faibles que celles obtenues dans les dispositifs à base de QW ou dans leurs homologues à deux sections. La largeur de raie RF s'est cependant trouvée sévèrement affectée par les effets de rétroaction optique, un problème clef à l'origine de la forte réduction des performances du système dans des environnements d'application pratique. Nous avons trouvé une solution monolithique simple et efficace pour supprimer presque totalement les effets de rétroaction dans les MLL QDash fabriqués (brevet en court).

Dans ce travail, une analyse théorique des spectres optique et d'intensité des lasers semi-conducteurs à blocage de modes passif a également été présentée. Celle-ci a permis d'établir des relations analytiques simples entre les largeurs de raies modales, les largeurs de raies RF et la gigue temporelle. L'utilisation de ces équations s'est montrée particulièrement intéressante à de hautes fréquences de répétition où les mesures directes du spectre RF et de la gigue temporelle sont limitées par la bande passante de la photodiode et des instruments électroniques.

Nous avons finalement montré le potentiel de lasers à blocage de modes pour des applications en radio sur fibre à ~ 60 GHz. Les paramètres importants sont la faible largeur de raie RF et la puissance RF en raison de la valeur importante de puissance moyenne accessible grâce aux structures optimisées. De meilleures performances sont également attendues grâce aux nouvelles conceptions d'hétérostructures et de lasers insensibles à la rétroaction optique.

Enfin, nous avons également réalisé des expériences de transmission OFDM avec détection directe démontrant ainsi le potentiel de ces sources comme générateur de supercanaux OFDM pour les réseaux optiques à haute capacité.

Bibliographie

[1] X. Huang, A. Stintz, H. Li, L. F. Lester, J. Cheng, and K. J. Malloy, "Passive mode-locking in 1.3 μm two-section InAs quantum dot lasers," *Applied Physics Letters*, vol. 78, no. 19, pp. 2825–2827, May 2001.

[2] M. Asada, Y. Miyamoto, and Y. Suematsu, "Gain and the threshold of three-dimensional quantum-box lasers," *IEEE Journal of Quantum Electronics*, vol. 22, no. 9, pp. 1915 – 1921, Sep. 1986.

[3] M. Willatzen, T. Tanaka, Y. Arakawa, and J. Singh, "Polarization dependence of optoelectronic properties in quantum dots and quantum wires-consequences of valence-band mixing," *IEEE Journal of Quantum Electronics*, vol. 30, no. 3, pp. 640 –653, Mar. 1994.

[4] D. Bimberg, N. Kirstaedter, N. N. Ledentsov, Z. I. Alferov, P. S. Kop'ev, and V. M. Ustinov, "InGaAs-GaAs quantum-dot lasers," *IEEE Journal of Selected Topics in Quantum Electronics*, vol. 3, no. 2, pp. 196 –205, Apr. 1997.

[5] E. U. Rafailov, M. A. Cataluna, and W. Sibbett, "Mode-locked quantum-dot lasers," *Nature Photonics*, vol. 1, no. 7, pp. 395–401, 2007.

[6] D. B. Malins, A. Gomez-Iglesias, S. J. White, W. Sibbett, A. Miller, and E. U. Rafailov, "Ultrafast electroabsorption dynamics in an InAs quantum dot saturable absorber at 1.3 μm," *Applied Physics Letters*, vol. 89, no. 17, pp. 171111–171111–3, Oct. 2006.

[7] Y. Arakawa and H. Sakaki, "Multidimensional quantum well laser and temperature dependence of its threshold current," *Applied Physics Letters*, vol. 40, no. 11, pp. 939–941, Jun. 1982.

[8] M. G. Thompson, A. R. Rae, M. Xia, R. V. Penty, and I. H. White, "InGaAs Quantum-Dot Mode-Locked Laser Diodes," *IEEE Journal of Selected Topics in Quantum Electronics*, vol. 15, no. 3, pp. 661 –672, Jun. 2009.

[9] R. H. Wang, A. Stintz, P. M. Varangis, T. C. Newell, H. Li, K. J. Malloy, and L. F. Lester, "Room-temperature operation of InAs quantum-dash lasers on InP [001]," *IEEE Photonics Technology Letters*, vol. 13, no. 8, pp. 767 –769, Aug. 2001.

[10] R. Schwertberger, D. Gold, J. P. Reithmaier, and A. Forchel, "Long-wavelength InP-based quantum-dash lasers," *IEEE Photonics Technology Letters*, vol. 14, no. 6, pp. 735 –737, Jun. 2002.

[11] F. Lelarge, B. Dagens, J. Renaudier, R. Brenot, A. Accard, F. van Dijk, D. Make, O. L. Gouezigou, J.-G. Provost, F. Poingt, J. Landreau, O. Drisse, E. Derouin, B. Rousseau,

F. Pommereau, and G.-H. Duan, “Recent Advances on InAs/InP Quantum Dash Based Semiconductor Lasers and Optical Amplifiers Operating at 1.55 mm,” *IEEE Journal of Selected Topics in Quantum Electronics*, vol. 13, no. 1, pp. 111 –124, Feb. 2007.

[12] Z. G. Lu, J. R. Liu, S. Raymond, P. J. Poole, P. J. Barrios, and D. Poitras, “312-fs pulse generation from a passive C-band InAs/InP quantum dot mode-locked laser,” *Opt Express*, vol. 16, no. 14, pp. 10835–10840, Jul. 2008.

[13] M. J. R. Heck, E. A. J. M. Bente, B. Smalbrugge, Y.-S. Oei, M. K. Smit, S. Anantathanasarn, and R. Nötzel, “Observation of Q-switching and mode-locking in two-section InAs/InP (100) quantum dot lasers around 1.55 ?m,” *Opt. Express*, vol. 15, no. 25, pp. 16292–16301, Dec. 2007.

[14] J. Renaudier, R. Brenot, B. Dagens, F. Lelarge, B. Rousseau, F. Poingt, O. Legouezigou, F. Pommereau, A. Accard, P. Gallion, and G.-H. Duan, “45 GHz self-pulsation with narrow linewidth in quantum dot Fabry-Perot semiconductor lasers at 1.5 mu;m,” *Electronics Letters*, vol. 41, no. 18, pp. 1007 – 1008, Sep. 2005.

[15] C. Gosset, K. Merghem, A. Martinez, G. Moreau, G. Patriarche, G. Aubin, A. Ramdane, J. Landreau, and F. Lelarge, “Subpicosecond pulse generation at 134 GHz using a quantum-dash-based Fabry-Perot laser emitting at 1.56 μm,” *Applied Physics Letters*, vol. 88, no. 24, pp. 241105–241105–3, Jun. 2006.

[16] M. J. R. Heck, A. Renault, E. A. J. M. Bente, Y.-S. Oei, M. K. Smit, K. S. E. Eikema, W. Ubachs, S. Anantathanasarn, and R. Notzel, “Passively Mode-Locked 4.6 and 10.5 GHz Quantum Dot Laser Diodes Around 1.55 mm With Large Operating Regime,” *IEEE Journal of Selected Topics in Quantum Electronics*, vol. 15, no. 3, pp. 634 –643, Jun. 2009.

[17] D. Hillerkuss, R. Schmogrow, T. Schellinger, M. Jordan, M. Winter, G. Huber, T. Vallaitis, R. Bonk, P. Kleinow, F. Frey, M. Roeger, S. Koenig, A. Ludwig, A. Marculescu, J. Li, M. Hoh, M. Dreschmann, J. Meyer, S. B. Ezra, N. Narkiss, B. Nebendahl, F. Parmigiani, P. Petropoulos, B. Resan, A. Oehler, K. Weingarten, T. Ellermeyer, J. Lutz, M. Moeller, M. Huebner, J. Becker, C. Koos, W. Freude, and J. Leuthold, “26 Tbit s-1 line-rate super-channel transmission utilizing all-optical fast Fourier transform processing,” *Nature Photonics*, vol. 5, no. 6, pp. 364–371, 2011.

[18] L. K. Oxenløwe, “Optical communications: Single-laser super-channel,” *Nature Photonics*, vol. 5, no. 6, pp. 329–331, 2011.

[19] S. Chandrasekhar and X. Liu, “DSP-enabled OFDM superchannel transmission,” in *Signal Processing in Photonic Communications*, 2012, p. SpTu2A.1.

[20] X. Liu, S. Chandrasekhar, X. Chen, P. Winzer, Y. Pan, B. Zhu, T. Taunay, M. Fishteyn, M. Yan, J. M. Fini, E. Monberg, and F. Dimarcello, “1.12-Tb/s 32-QAM-OFDM Superchannel with 8.6-b/s/Hz Intrachannel Spectral Efficiency and Space-Division Multiplexing with 60-b/s/Hz Aggregate Spectral Efficiency,” in *37th European Conference and Exposition on Optical Communications*, 2011, p. Th.13.B.1.

[21] D. Zou and I. B. Djordjevic, “Beyond 1Tb/s Superchannel Optical Transmission based on Polarization Multiplexed Coded-OFDM over 2300 km of SSMF,” in *Signal Processing in Photonic Communications*, 2012, p. SpTu2A.6.

[22] J. Li, M. Sjödin, M. Karlsson, and P. A. Andrekson, “Building up low-complexity spectrally-efficient Terabit superchannels by receiver-side duobinary shaping,” *Opt. Express*, vol. 20, no. 9, pp. 10271–10282, Apr. 2012.

[23] Z. He, I. Djordjevic, W. Liu, M. Luo, Q. Yang, Z. Yang, S. Yu, B. Huang, N. Chi, and W. Shieh, “Comparison of Various Bandwidth-Efficient LDPC Coding Schemes for

Tb/s Superchannel Long-haul Transmission," in *National Fiber Optic Engineers Conference*, 2012, p. JW2A.43.
[24] M. Jinno, K. Yonenaga, H. Takara, K. Shibahara, S. Yamanaka, T. Ono, T. Kawai, M. Tomizawa, and Y. Miyamoto, "Demonstration of Translucent Elastic Optical Network Based on Virtualized Elastic Regenerator," in *National Fiber Optic Engineers Conference*, 2012, p. PDP5B.6.
[25] Q. Yang, "Experimental Demonstration of Tb/s Optical Transport Network Based on CO-OFDM Superchannel with Heterogeneous ROADM Nodes Supporting Single-Fiber Bidirectional Communications," in *National Fiber Optic Engineers Conference*, 2012, p. JTh2A.47.
[26] J. Yu, Z. Dong, and N. Chi, "Generation, Transmission and Coherent Detection of 11.2 Tb/s (112x100Gb/s) Single Source Optical OFDM Superchannel," in *Optical Fiber Communication Conference*, 2011, p. PDPA6.
[27] Y.-K. Huang, E. Ip, P. N. Ji, Y. Shao, T. Wang, Y. Aono, Y. Yano, and T. Tajima, "Terabit/s Optical Superchannel with Flexible Modulation Format for Dynamic Distance/Route Transmission," in *Optical Fiber Communication Conference*, 2012, p. OM3H.4.
[28] W.-R. Peng, I. Morita, H. Takahashi, and T. Tsuritani, "Transmission of High-Speed (> 100 Gb/s) Direct-Detection Optical OFDM Superchannel," *J. Lightwave Technol.*, vol. 30, no. 12, pp. 2025–2034, Jun. 2012.
[29] X. Chen, A. Li, J. Ye, A. Al Amin, and W. Shieh, "Reception of mode-division multiplexed superchannel via few-mode compatible optical add/drop multiplexer," *Opt. Express*, vol. 20, no. 13, pp. 14302–14307, Jun. 2012.
[30] H. Griesser, K. Grobe, and J.-P. Elbers, "Quaternary Duobinary Modulation for Superchannels with Sub-Nyquist Subcarrier Spacing," in *Optical Fiber Communication Conference*, 2012, p. OTh1B.4.
[31] C. Zhang, J. Duan, J. Li, W. Hu, H. Li, H. Wu, and Z. Chen, "Bidirectional 60-GHz radio-over-fiber systems with downstream OFDMA and wavelength reuse upstream SC-FDMA," *Opt. Express*, vol. 18, no. 18, pp. 19429–19437, Aug. 2010.
[32] M.-K. Hong, Y.-Y. Won, and S.-K. Han, "Gigabit radio-over-fiber link for convergedbaseband and millimeter-wave band signaltransmission using cascaded injection-lockedFabry-Pérot laser diodes," *Opt. Express*, vol. 17, no. 10, pp. 7844–7852, May 2009.
[33] F. van Dijk, B. Charbonnier, S. Constant, A. Enard, S. Fedderwitz, S. Formont, I. F. Lealman, F. Lecoche, F. Lelarge, D. Moodie, L. Ponnampalam, C. Renaud, M. J. Robertson, A. J. Seeds, A. Sto&#x0308 andhr, and M. Weiss, "Quantum dash mode-locked lasers for millimeter wave signal generation and transmission," in *IEEE Photonics Society, 2010 23rd Annual Meeting of the*, 2010, pp. 187 –188.
[34] B. Charbonnier, F. Lecoche, M. Weis, A. Stohr, F. van Dijk, A. Enard, F. Blache, M. Goix, F. Mallecot, D. G. Moodie, A. Borghesani, and C. W. Ford, "Ultra-wideband radio-over-fiber techniques and networks," *IEEE Xplore*, 21-Mar-2010. [Online]. Available: http://ieeexplore.com/xpl/articleDetails.jsp?reload=true&arnumber=5465494. [Accessed: 23-Aug-2012].
[35] L. F. Tiemeijer, P. I. Kuindersma, P. J. A. Thijs, and G. L. J. Rikken, "Passive FM locking in InGaAsP semiconductor lasers," *IEEE Journal of Quantum Electronics*, vol. 25, no. 6, pp. 1385 –1392, Jun. 1989.

[36] K. Sato, “Optical pulse generation using fabry-Pe acute;rot lasers under continuous-wave operation,” *IEEE Journal of Selected Topics in Quantum Electronics*, vol. 9, no. 5, pp. 1288 – 1293, Oct. 2003.
[37] Y. Nomura, S. Ochi, N. Tomita, K. Akiyama, T. Isu, T. Takiguchi, and H. Higuchi, “Mode locking in Fabry-Perot semiconductor lasers,” *Phys. Rev. A*, vol. 65, no. 4, p. 043807, Mar. 2002.
[38] G. P. Agrawal, “Population pulsations and nondegenerate four-wave mixing in semiconductor lasers and amplifiers,” *J. Opt. Soc. Am. B*, vol. 5, no. 1, pp. 147–159, Jan. 1988.
[39] A. Uskov, J. Mørk, J. Mark, M. C. Tatham, and G. Sherlock, “Terahertz four-wave mixing in semiconductor optical amplifiers: Experiment and theory,” *Applied Physics Letters*, vol. 65, no. 8, pp. 944–946, Aug. 1994.
[40] A. Capua, S. O’duill, V. Mikhelashvili, G. Eisenstein, J. P. Reithmaier, A. Somers, and A. Forchel, “Cross talk free multi channel processing of 10 Gbit/s data via four wave mixing in a 1550 nm InAs/InP quantum dash amplifier,” *Opt. Express*, vol. 16, no. 23, pp. 19072–19077, Nov. 2008.
[41] T. Akiyama, O. Wada, H. Kuwatsuka, T. Simoyama, Y. Nakata, K. Mukai, M. Sugawara, and H. Ishikawa, “Nonlinear processes responsible for nondegenerate four-wave mixing in quantum-dot optical amplifiers,” *Applied Physics Letters*, vol. 77, no. 12, pp. 1753–1755, Sep. 2000.
[42] P. Runge, R. Elschner, and K. Petermann, “Chromatic Dispersion in InGaAsP Semiconductor Optical Amplifiers,” *IEEE Journal of Quantum Electronics*, vol. 46, no. 5, pp. 644 –649, May 2010.
[43] A. Martinez, J.-G. Provost, G. Aubin, R. Brenot, J. Landreau, F. Lelarge, and A. Ramdane, “Slow and fast light in quantum dot based semiconductor optical amplifiers,” *Comptes Rendus Physique*, vol. 10, no. 10, pp. 1000–1007, Dec. 2009.
[44] T. Habruseva, S. O’Donoghue, N. Rebrova, F. Kéfélian, S. P. Hegarty, and G. Huyet, “Optical linewidth of a passively mode-locked semiconductor laser,” *Opt. Lett.*, vol. 34, no. 21, pp. 3307–3309, Nov. 2009.
[45] M. J. Ablowitz, B. Ilan, and S. T. Cundiff, “Noise-induced linewidth in frequency combs,” *Opt. Lett.*, vol. 31, no. 12, pp. 1875–1877, Jun. 2006.
[46] R. Paschotta, “Noise of mode-locked lasers (Part II): timing jitter and other fluctuations,” *Applied Physics B: Lasers and Optics*, vol. 79, no. 2, pp. 163–173, 2004.
[47] R. Paschotta, A. Schlatter, S. C. Zeller, H. R. Telle, and U. Keller, “Optical phase noise and carrier-envelope offset noise of mode-locked lasers,” *Applied Physics B*, vol. 82, no. 2, pp. 265–273, Dec. 2005.
[48] J. K. Wahlstrand, J. T. Willits, C. R. Menyuk, and S. T. Cundiff, “The quantum-limited comb lineshape ofa mode-locked laser: Fundamental limitson frequency uncertainty,” *Opt. Express*, vol. 16, no. 23, pp. 18624–18630, Nov. 2008.
[49] Y. Takushima, “Linewidth of mode combs of passively and actively mode-locked semiconductor laser diodes,” 2004, vol. 5595, pp. 213–227.
[50] H. A. Haus and A. Mecozzi, “Noise of mode-locked lasers,” *IEEE Journal of Quantum Electronics*, vol. 29, no. 3, pp. 983 –996, Mar. 1993.
[51] K. Merghem, A. Akrout, A. Martinez, G. Aubin, A. Ramdane, F. Lelarge, and G.-H. Duan, “Pulse generation at 346 GHz using a passively mode locked quantum-dash-based laser at 1.55 μm,” *Applied Physics Letters*, vol. 94, no. 2, pp. 021107–021107–3, Jan. 2009.

[52] R. Rosales, K. Merghem, A. Martinez, F. Lelarge, A. Accard, and A. Ramdane, "Timing jitter from the optical spectrum in semiconductor passively mode locked lasers," *Opt. Express*, vol. 20, no. 8, pp. 9151–9160, Apr. 2012.
[53] D. A. Reid, S. G. Murdoch, and L. P. Barry, "Stepped-heterodyne optical complex spectrum analyzer," *Opt. Express*, vol. 18, no. 19, pp. 19724–19731, 2010.
[54] R. Rosales, S. G. Murdoch, R. T. Watts, K. Merghem, A. Martinez, F. Lelarge, A. Accard, L. P. Barry, and A. Ramdane, "High performance mode locking characteristics of single section quantum dash lasers," *Optics Express*, vol. 20, no. 8, p. 8649, Mar. 2012.
[55] Z. Xu, M. O?Sullivan, and R. Hui, "OFDM system implementation using compatible SSB modulation with a dual-electrode MZM," *Opt. Lett.*, vol. 35, no. 8, pp. 1221–1223, Apr. 2010.
[56] D. Qian, M.-F. Huang, E. Ip, Y.-K. Huang, Y. Shao, J. Hu, and T. Wang, "101.7-Tb/s (370×294-Gb/s) PDM-128QAM-OFDM Transmission over 3×55-km SSMF using Pilot-based Phase Noise Mitigation," in *National Fiber Optic Engineers Conference*, 2011, p. PDPB5.

Abstract

This PhD thesis focuses on the study of mode locked laser diodes based on novel optimized InAs Quantum Dash structures grown on InP substrates. It covers several important modelling aspects, the clean room processing of single and two section shallow ridge waveguide lasers, characterization of the fabricated devices and the evaluation of their performance in different application scenarios. Systematic characterization experiments and subsequent analyses have allowed to gain a much deeper comprehension of the physical mechanisms related to the mode locking regime in these devices, thus far not completely understood. This has allowed to better control most of the main physical phenomena limiting device performance, resulting in first demonstrations of record peak power, sub-picosecond pulse, low radio frequency linewidth and high repetition frequency mode locked lasers grown on InP substrates, opening the way to a vast number of potential applications in the 1.55 μm telecommunication window.

Acknowledgements

First, I would like to thank A. Ramdane and A. Martinez for their enormous support, guidance and trust they have provided me. Thanks to them I have carried out this PhD thesis with confidence and enthusiasm.

I express my gratitude to Jean-Yves Marzin and Dominique Mailly for allowing me to conduct my research work at the LPN (Laboratoire de Photonique et de Nanostructures) of the CNRS (Centre National pour la Recherche Scientifique).

I also thank the members of the doctoral committee: J. Jacquet, JC Simon, P. Gallion, G. Huyet and G. Alquie for having willingly examined and judged this PhD dissertation.

Working with K. Merghem at the LPN has been a great pleasure and I thank him for all the initial training and constant support he provided me in both clean room and laboratory environments. I owe him many of the experimental results from this thesis. I would also like to thank the members of the LPN clean room technical service who contributed directly or indirectly in the fabrication and processing of the lasers used within this work. I also thank the entire PHOTEL group and in particular G. Aubin for interesting and stimulating discussions.

I would like to acknowledge the ANR TELDOT project and all of its partners, especially to F. Lelarge from III-V lab for providing the QDash heterostructures used within this work and for very fruitful interactions throughout the course of this thesis. It was also a great pleasure working with B. Charbonnier at Orange Labs in Lannion. I owe the results from the RoF experiments in Chapter 5 to his proficiency on this subject.

I am very grateful to L. Barry and R. Watts from Dublin City University (DCU), Ireland, for our very productive collaboration that was made possible through the Ulysses scheme. I owe many of the experimental results from Chapter 4 as well as the OFDM implementation from Chapter 5 to this valuable teamwork supported by the expertise and the facilities of the DCU's Radio and Optical Communication Lab. Within the framework of this collaboration, I also had the opportunity to work with S. Murdoch from Auckland University, New Zealand, and to whom I am highly indebted for very fruitful discussions and valuable insight on

nonlinear optical phenomena. I owe him many of the experimental investigations from Chapter 4 as well as the nonlinear modelling and simulation results from Chapter 2.

Motivating interactions with other research groups have also been carried out throughout the course of this work. In this regard, I would like to thank H. T. Nguyen and C. Gosset from ParisTech as well as Y. Gottesman, Q. Zou, M. Muller and C. Lepers from Telecom SudParis.

I thank the whole IT and administrative staff of the LPN for their continuous and kind assistance which allowed me to conduct my research work in an efficient way.

Throughout my stay at the LPN, I have benefitted from the acquaintance of many people. I particularly thank my officemates A. Cattoni, E. Briones, K. Papatryfonos and C. Calo for very enjoyable and stimulating discussions as well as their friendship. I have also enjoyed the closeness from A. Giacomotti, M. Brunstein, P. Grinberg, O. Oria, D. Kazazis and J. Carimalo from the LPN as well as S. Joshi and M. Anagnosti from III-V lab.

Finally, I deeply thank all of my beloved family for their endless and unconditional support.

Contents

List of Figures

List of Tables

List of Acronyms

AC	Autocorrelation
ASE	Amplified Spontaneous Emission
AWG	Arbitrary Waveform Generator
BA	Broad Area
BER	Bit Error Rate
CBE	Chemical Beam Epitaxy
CDM	Carrier Density Modulation
CH	Carrier Heating
CO-OFDM	Coherent Detection OFDM
CW	Continuous Wave
DBAR	Dash in a Barrier
DBR	Distributed Bragg Reflector
DD-OFDM	Direct Detection OFDM
DOS	Density Of States
DSP	Digital Signal Processing
DWELL	Dash in a Well
ECL	External Cavity Laser
ESA	Electrical Spectrum Analyzer
EVM	Error Vector Magnitude
FEC	Forward Error Correction
FP	Fabry Perot
FROG	Frequency Resolved Optical Gating
FWHM	Full Width at Half Maximum
FWM	Four Wave Mixing
GD	Group Delay
GDD	Group Delay Dispersion
GSMBE	Gas Source Molecular Beam Epitaxy
GVD	Group Velocity Dispersion
LNA	Low Noise Amplifier
LO	Local Oscillator
MBE	Molecular Beam Epitaxy
ML	Mode Locking
MLL	Mode Locked Lasers
MOVPE	Metal Organic Vapor Phase Epitaxy
MZ	Mach-Zehnder
OCT	Optical Coherence Tomography
OFDM	Orthogonal Frequency Division Multiplexing

OSA	Optical Spectrum Analyzer
PL	Photoluminescence
PSD	Power Spectral Density
QAM	Quadrature Amplitude Modulation
QD	Quantum Dot
QDash	Quantum Dash
QW	Quantum Well
RF	Radio Frequency
RIN	Relative Intensity Noise
RoF	Radio over Fiber
RTS	Real Time Scope
SA	Saturable Absorber
SCH	Separate Confinement Heterostructure
SEM	Scanning Electron Microscopy
SHB	Spectral Hole Burning
SHG	Second Harmonic Generation
SMF	Single Mode Fiber
SNR	Signal to Noise Ratio
SOA	Semiconductor Optical Amplifier
SPIDER	Spectral Phase Interferometry
SSB	Single Side Band
SSBPN	Single Side Band Phase Noise
S-T	Schawlow-Tones
TBP	Time Bandwidth Product
TEM	Transmission Electron Microscopy
WDM	Wavelength Division Multiplexing

Chapter 1. Introduction

Semiconductor monolithic mode locked lasers (MLL) are very attractive devices for short pulse generation and have found applications in a vast number of fields including optical communications, microwave photonics, optical sampling, biology and medicine. They have been the subject of numerous investigations since the early demonstration of a semiconductor laser diode and achieve now unprecedented performance characteristics with pulse durations in the range of a few hundreds of femto-seconds (fs), repetition rates in excess of hundreds of GHz, and fs timing jitter.

Advances in material sciences, in particular molecular beam epitaxy (MBE) growth, has allowed the achievement of low dimensional structures including quantum wells (QW) from which high performance lasers have been fabricated, particularly contributing to the development of modern optical fiber communication systems. More recently, quantum dot (QD) nanostructures have been grown, in which the charge carriers are confined in the three spatial dimensions. This results in many remarkable properties of directly modulated QD based lasers and their investigation has witnessed a huge interest in the last decade or so [1].

The first report of a QD based passive MLL dates back to 2001 [2]. Indeed, some expected properties of QD lasers are particularly interesting for the mode locked regime, including potentially low threshold current densities [3] and linewidth enhancement factors [1], [4], broad emission spectra [5], ultrafast carrier dynamics [6], low optical confinement factors and reduced temperature sensitivity [7]. Most of the achievements have been reported for the more mature InAs/GaAs QD material system that has benefited of much attention. Recent reviews discussing the advantages of using QDs for passively MLLs and related performance are given in references [5], [8] for laser emission at 1.3 µm on GaAs substrates.

This PhD thesis concentrates on passively mode locked lasers intended for the 1.55 µm telecommunication window and grown on InP substrates. MBE growth on InP (100) usually results in the formation of quantum dashes (QDash) or elongated dots, reported by several

groups [9–11] while Metal Organic Vapor Phase Epitaxy (MOVPE) or Chemical beam Epitaxy (CBE) growth yields truly 3D confined dots [12], [13]. The first reports of QDash based MLLs emitting at 1.55 μm were for Fabry Perot (FP) devices consisting of a single gain section, devoid of a saturable absorber [14], [15]. QDs obtained by CBE also allow mode locking in single section devices [12] while devices based on MOVPE growth present a more conventional behaviour in 2-section devices where both Q-switching as well as mode locking are reported depending on operating conditions [13], [16].

Although the ideal picture of energetically isolated QDs (or QDashes) leading to the ultimate laser device with the aforementioned expected properties is still far from being achieved in practice (mainly due to inhomogeneous broadening), single section QDash lasers have experimentally shown to exhibit two main characteristics that are key in a number of potential applications, representing a clear advantage when compared to the widely employed quantum well (QW) based devices and a major motivation for this thesis work. These two characteristics are the particularly flat and broad optical spectrum and the very much reduced intensity phase noise; features that, in addition, come usually together with a relatively high optical average power in this type of devices. In order to see this, let us review some of the most relevant and recent results reporting on these particular characteristics by first focusing on monolithic mode locked lasers emitting in the 1.55 μm telecommunication window, as shown in Table 1.

Recent progress on QW based MLLs have led to significant results in terms of intensity phase noise, which can be quantified by the so-called radio frequency (RF) linewidth. In [17], this was achieved by means of a special epistructure design leading to reduced cavity losses and hence to a narrow RF linewidth of 25 kHz, the lowest value reported for a QW based MLL. By using a single QW structure design leading to a low confinement factor, similar to that typically found in QD lasers, the RF linewidth was also found to be particularly narrow in [18]. Nevertheless, the reduced phase noise in these QW based devices usually comes with comparatively low values of spectral widths and average powers, as seen in Table 1. A widely known technique to increase the average output power in QW based devices is the use of the so-called slab-coupled optical waveguides, as proposed in [19]. However, this does not seem to improve the spectral characteristics and usually comes at the expense of a very high threshold current, which is against the initiatives for future low power consuming

technologies. Moving into low dimensional based devices on InP substrates, first 2-section QD MLLs results [16], [20] were not very promising, exhibiting relatively high threshold current densities and waveguide internal losses which resulted in lower ML performance compared to those fabricated in the more mature InAs/GaAs material system intended for the 1.3 μm window. Very recently, however, two-section QDash MLLs have shown to attain remarkable performances [21] comparable to the 1.3 μm counterparts. In the single section configuration, interesting results based on QW lasers were first reported in [22] and [23], nevertheless, the spectral FWHM and the RF linewidth in these devices are generally surpassed by low dimensional QD/QDash based counterparts [12], [24] as noted from Table 1. In [25], a similar approach to that of [16] was employed for fabricating a high power QDash based device achieving optical powers in excess of 100 mW while maintaining very remarkably high-quality ML features, albeit with the typical increase in threshold current associated to this particular waveguide design. For comparison purposes, the most relevant results on passively MLLs based on InAs/GaAs are shown at the bottom of the table [26–28]. Of particular interest is the ultra low RF linewidth obtained in [26], although it should be noted that this corresponded to a packaged device in a thermoelectrically controlled case which considerably minimizes the laser intensity phase noise induced by external or environmental perturbations.

Material system and configuration	FWHM [nm]	Δf_{RF} [kHz]	Ith [mA]	Avg. P [mW]	Fr [GHz]	λ [nm]	Ref.
3 QW AlGaInAs/InP Two section	4.84	25	40	2	40	1540	[17]
5 InGaAsP QW /InP Two section	5.7	NA	600	250	4.29	1545	[19]
5 QD InAs/InP Two section	7	$2x10^3$	800	2	4.5	1530	[16]
5 QD InAs/InP Two section	~5	NA	150	~1	18.4	1560	[20]
9 InAs QDash/InP Two section	**10**	**100**	**60**	**3**	**48**	**1560**	[21]
6 InGaAsP QW /InP One section	7.92	200	6	19	100	1562	[22]
5 QD InAs/InP One section	11.6	~60	17	13	92	1540	[12]
9 InAs QDash/InP One section	**14**	**20**	**25**	**40**	**48**	**1560**	[24]
9 InAs QDash/InP One section	~10	3.2	400	100	20	1550	[25]
5 InGaAs QD/ GaAs Two section	NA	0.5	~70	~1	10	NA	[26]
5 InGaAs QD/ GaAs Two section	14	NA	25	23	21	1260	[27]
10 InGaAs QD/ GaAs Two section	5.6	NA	600	222.7	16	1260	[28]

FWHM: Full width at half maximum of the optical spectrum
I_{th}: Threshold current
Δf_{RF}: Radio Frequency Linewidth ($\propto$ intensity phase noise)
Avg. P: Average Power
Fr: Repetition Frequency
λ: Emission wavelength

Table 1. Comparative table of semiconductor passively MLLs emitting at 1.55 and 1.3 μm

Note that we did not include the pulse duration in the previous comparative analysis. This stems from the fact that a large spectral FHWM in combination with a narrow RF linewidth may enable the generation of ultra short pulses (provided the static mode phases are linearly related, cf. Chapter 2), whereas an ultra short pulse does not necessarily come together with a narrow RF linewidth, a parameter that we consider more important from a practical point of view.

Having briefly reviewed the state of the art on passively MLLs emitting in the 1.55 μm window, we are now able to recognize the potential of QDash based MLLs, particularly in its single section configuration, as they can provide a very large optical spectrum together with a reduced intensity phase noise while attaining comparatively higher average output powers. These particular features, in combination with the exceptionally simple one-section configuration and its low power consuming characteristics, may offer potentially low cost, compact and environmentally-friendly solutions for future technologies in the field of optical communications. Indeed, a wide optical spectrum comprising a large number of equally spaced and phase locked lasing modes not only may lead to ultra short optical pulses but also enable one of the most promising technologies for future high capacity optical networks such as optical Orthogonal Frequency Division Multiplexing (OFDM) superchannels, which have very recently received much attention [29–42]. A reduced phase noise of the laser intensity may, on the other hand, represent an advantage in applications such as millimeter wave generation for radio over fiber (RoF) applications [43–46] for future broadband wireless access networks. Indeed, the increase in the demand for wireless data capacity calls for the development of new technologies in the millimeter wave frequency band, which requires low noise carrier signals that may be efficiently generated by employing stable and low intensity phase noise mode locked lasers.

Yet, the physical mechanisms leading to the ML regime in single section devices still lacks a complete comprehension both from a theoretical and an experimental point of view, as opposed to the case of standard two-section devices in which the ML behaviour is generally very well understood and controlled. One of the main objectives of this thesis work is hence to provide a deeper insight into the underlying physical aspects behind the mode locking regime in single section devices that could be at the same time validated by complete and systematic characterization experiments. Indeed, key to using these devices in future

technologies is a complete knowledge of their intrinsic behaviour and the way it is affected by external factors that may be present in real implementation environments. This would allow for more efficiently exploiting their potential in the different application scenarios, which also represents a major goal of this work.

The organization of this thesis is as follows: Chapter 2 introduces the concept of mode locking both from a mathematical and a physical point of view, with a special focus on a description of the main physical mechanisms leading to the mode locked regime in single section devices. Chapter 3 highlights the potential advantages of using low dimensional QDash structures in semiconductor lasers and briefly describes the processing steps and techniques that we have used in fabricating the final devices. Chapter 4 provides a thorough characterization of the fabricated lasers in order to gain further insight into their physical behaviour and to identify the main physical phenomena that may limit system performance in the foreseen applications. In chapter 5 we employ some of the fabricated lasers for successfully demonstrating the potential of these devices in two different application scenarios, namely: radio over fiber systems for broadband wireless access and OFDM superchannels for high capacity optical networks.

Chapter 2.
Mode locking of semiconductor lasers

The objective of this chapter is to introduce the concept of mode locking both from a mathematical and a physical point of view. The main parameters associated to this regime are described together with a brief review of currently characterization techniques. Special focus is placed on the passively mode locking regime in single section devices, from which a simplified model was proposed leading to first simulation results.

2.1. Mathematical description

Let us consider the emission from a single transverse mode Fabry Perot (FP) laser with parallel mirrors, in which the cavity resonance condition results in a set of longitudinal modes ω_n, $n=1,2,3,...,N$. In a semiconductor laser under ordinary circumstances (continuous wave CW operation), these modes are only approximately equidistant due to dispersion phenomena. The frequency separations are, however, very close to a nominal round trip frequency $\Omega_{nom}=v_g/2L$, with L the FP cavity length, $v_g=c/n_g$ the group velocity, $n_g(\omega)=n_{eff}+\omega\cdot dn_{eff}/d\omega$ being the group refractive index and n_{eff} the effective refractive index seen by each propagating mode. The total number of oscillating modes N will be given by the emission spectral bandwidth which we will define by the full width at half maximum (FWHM) of the optical spectrum.

In general, the complex electric field emitted by the FP laser can be represented as:

$$E(z,t)=\Theta(x,y)\left[\sum_{n=1}^{N}E_n(t)e^{j\left[\omega_n t+\theta_n(t)+\phi_n\right]}\times U_n(z)\right]+c.c \qquad (2.1)$$

where:

E_n: Amplitude of each of the lasing modes.

$\theta_n(t)$: Time dependent phase, or optical phase noise of each mode. It results from random spontaneous emission and hence undergo a random walk process such that $\left\langle \left| \theta_n(t+T_0) - \theta_n(T_0) \right|^2 \right\rangle = D_{\theta_n} |t|$, with D_{θ_n} a diffusion coefficient.

ϕ_n: The static phase of each mode around which the modal phase noise fluctuates.

$U_n(z)$: A standing wave $\sin(k_n z)$, with k_n the wave vector associated to each mode.

$\Theta(x, y)$: The transverse mode profile, usually Gaussian.

Let us for the moment neglect the transverse dependence of the beam profile and the time dependence of the real amplitudes (as the effects of these variations are generally much less important than the phase variations), and focus on the electric field at a given position z such that it can be more easily represented as:

$$E(t) = \left[\sum_{n=1}^{N} E_n e^{j\left[\omega_n t + \theta_n(t) + \phi_n\right]} \right] + c.c \qquad (2.2)$$

The existence of mode locking (ML) can be studied by investigating the so-called relative phase Ψ [23], [47], which can be generalized for any N number of modes and written by considering the time dependent and the steady state phases separately as [24]:

$$\Psi = (2\omega_{n+1} - \omega_n - \omega_{n+2})t + 2\theta_{n+1}(t) - \theta_n(t) - \theta_{n+2}(t) + 2\phi_{n+1} - \phi_n - \phi_{n+2} \qquad (2.3)$$

for $n = 1$ to $N-2$ ($N \geq 3$). The mode locking regime corresponds to Ψ converging to a constant for all n, resulting in the following ML conditions [24]

1. $\omega_{n+1} - \omega_n = \omega_r \sim \Omega_{nom}$ (2.4)

2. $\theta_{n+1}(t) - \theta_n(t) = \Delta\theta(t)$ (2.5)

3. $2\phi_{n+1} - \phi_n - \phi_{n+2} = \Phi_n$ (2.6)

with ω_r the angular repetition frequency such that the pulse train period $T = 2\pi / \omega_r$

The previous ML conditions imply:

1. Perfectly equally separated modes, the separation being the round trip angular frequency ω_r, which is close to the nominal frequency Ω_{nom}.

2. Synchronization of consecutive time dependent phases up to some residual phase noise $\Delta\theta(t)$. We will call $\Delta\theta(t)$ the intensity phase noise, and it will be later shown to also follow random walk statistics, with $\left\langle \left| \Delta\theta(t+T_0) - \Delta\theta(T_0) \right|^2 \right\rangle = D_{\Delta\theta} |t|$, $D_{\Delta\theta}$ being a diffusion coefficient.

3. Fixed relationship between consecutive static phases. Constructive mode interference leading to pulse generation will imply $\Phi_n = 0$ for all n.

The MLL phenomenon is usually evidenced by looking at the output laser intensity $I(t)$ and its corresponding spectrum. From (2.2) we have:

$$\begin{aligned} I(t) &\propto \left| E(t) \right|^2 \\ &\propto \sum_{m=1}^{N-1} \sum_{l=1}^{N-m} 2E_{m+l}E_l \cos\left[\left(\omega_{m+l} - \omega_l \right) t + \left(\theta_{m+l}(t) - \theta_l(t) \right) + \left(\phi_{m+l} - \phi_l \right) \right] + \sum_{m=1}^{N} E_m^2 \end{aligned} \tag{2.7}$$

We can see that the laser intensity is composed of the sum of all possible beatings between modes m and l, with $m \neq l = 1, 2, 3, ..., N-1$. Its time dependent behaviour and its spectrum $\left| I(\omega) \right|^2$ will depend on how well conditions 1-3 are satisfied.

In order to illustrate the mode locking regime, temporal traces of $I(t)$ as well as the spectra of $E(t)$ and $I(t)$ have been numerically simulated for an electric field of the form as in (2.2) with $N = 21$, each mode affected by random walk phase noise. Three different cases were considered. For ease of comparison, the first ML condition was always assumed to be satisfied and the different mode amplitudes always taken as unity. Also, the ratio of $D_{\Delta\theta} / D_{\theta_{nc}}$ (n_c for central mode) was kept constant for all cases.

Case 1:

$D_{\theta_{11}} = 1\times10^{-9}$ rad/s, $D_{\Delta\theta} = 0.01D_{\theta_{11}}$, $\Phi_n = 0$ rad for all n

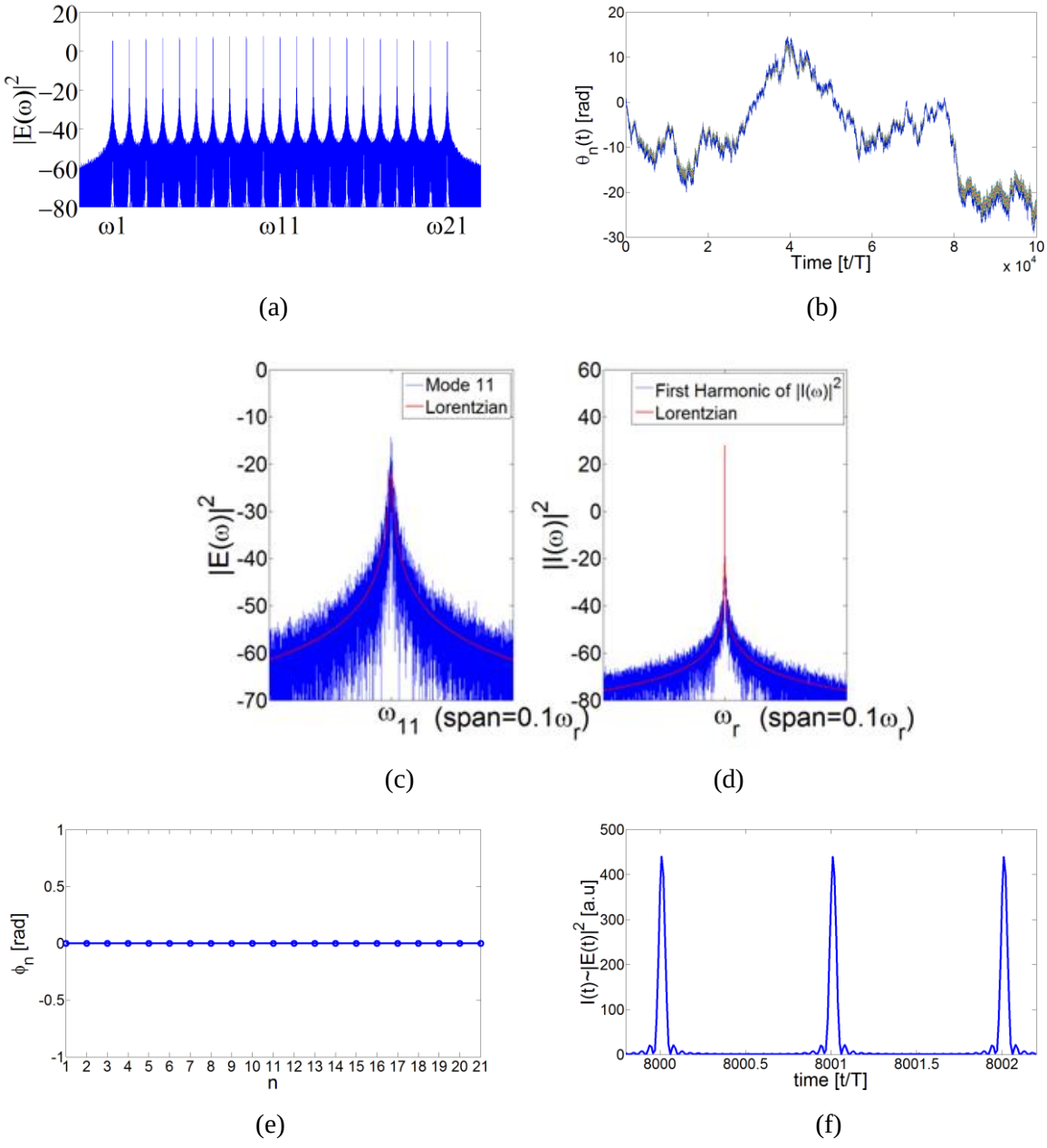

Figure 2-1(a) Optical spectrum, (b) random phases of the 21 modes, (c) zoom of the optical spectrum on mode n=11, (d) first harmonic of the intensity spectrum, (e) static phases of all 21 modes, (f) temporal trace of the laser intensity for case 1

Case 2:

$D_{\theta_{11}} = 1\times10^{-9}$ rad/s, $D_{\Delta\theta} = 0.01D_{\theta_n}$, $\Phi_n = 0.1$ rad for all n

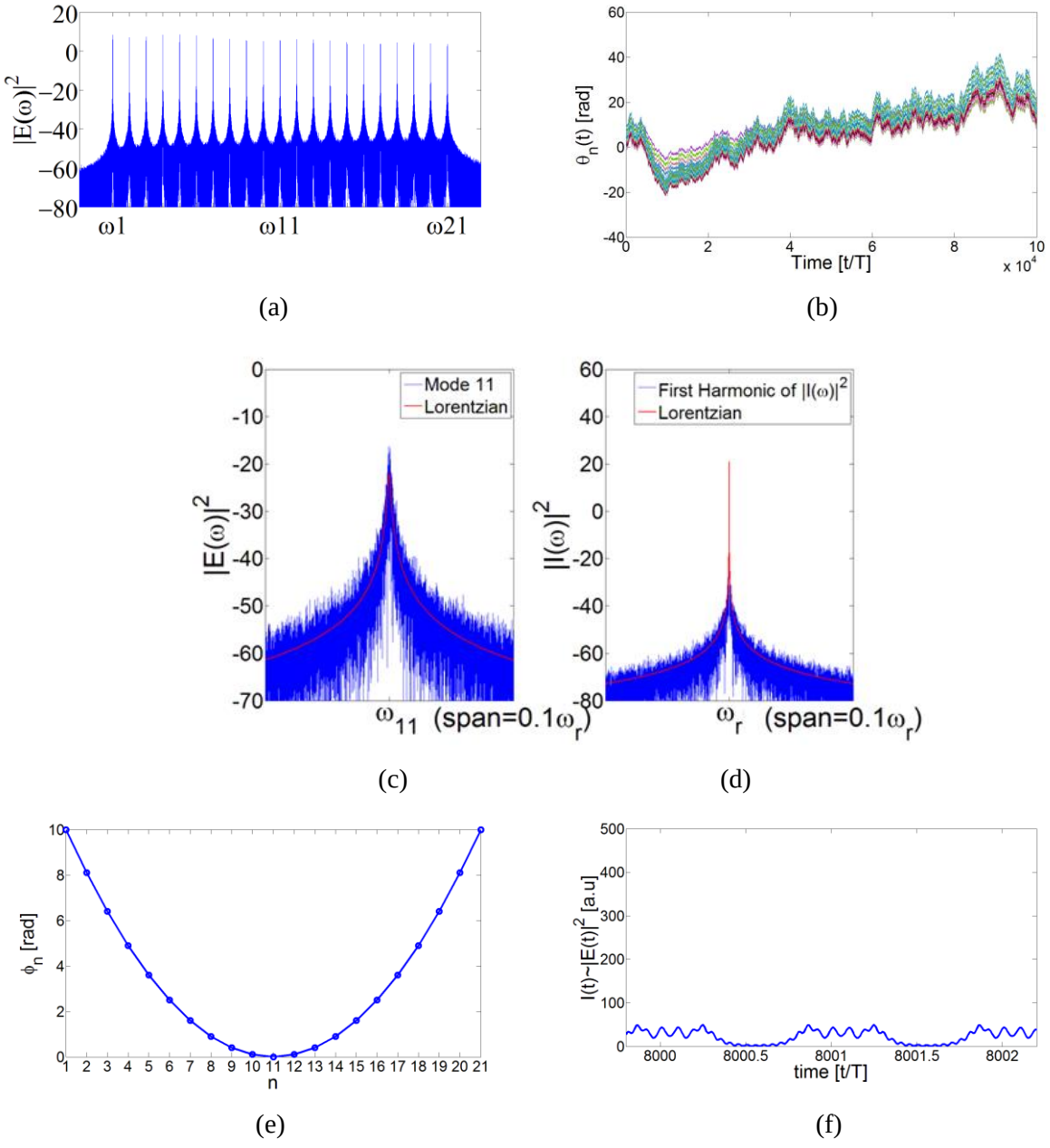

Figure 2-2(a) Optical spectrum, (b) random phases of the 21 modes, (c) zoom of the optical spectrum on mode n=11, (d) first harmonic of the intensity spectrum, (e) static phases of all 21 modes, (f) temporal trace of the laser intensity for case 2

Case 3:

$D_{\theta_{11}} = 20\times10^{-9}$ rad/s, $D_{\Delta\theta} = 0.01D_{\theta_n}$, $\Phi_n = 0$ rad for all n

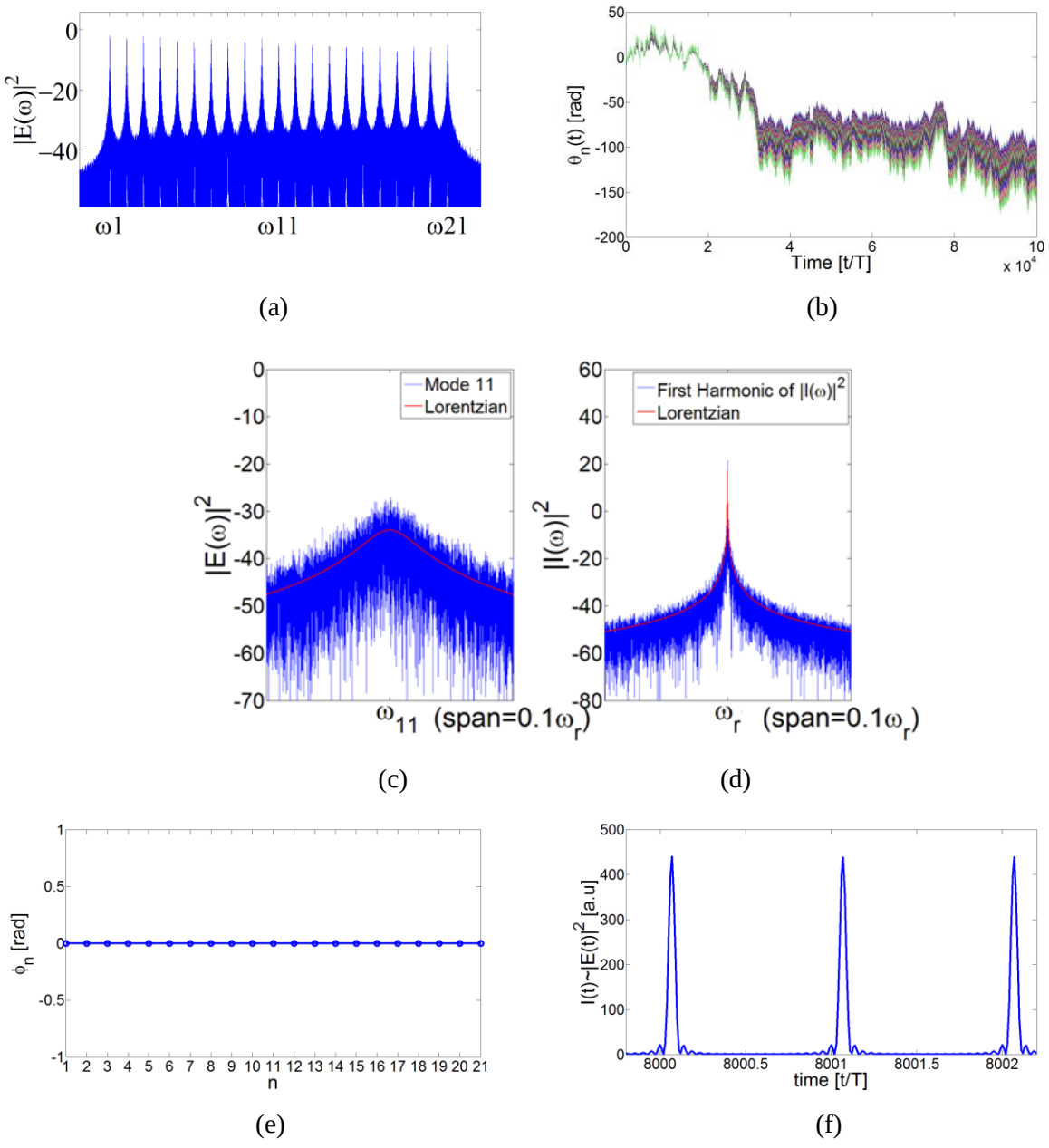

Figure 2-3(a) Optical spectrum, (b) random phases of the 21 modes, (c) zoom of the optical spectrum on mode n=11, (d) first harmonic of the intensity spectrum, (e) static phases of all 21 modes, (f) temporal trace of the laser intensity for case 3

The previous results show that:

- Synchronization of the time dependent phases leads to a reduced linewidth of the intensity spectrum compared to each of the individual mode linewidths owing to intermodal coherence.

- Even if the time dependent phases are efficiently synchronized, this condition does not necessarily lead to the formation of pulses if $\Phi_n \neq 0$. Consequently a laser may be effectively mode locked without showing any clear train of pulses (case 2).

- The amount of phase noise, be it intensity phase noise or the one from the modes themselves (provided it is coherent), does not influence the formation of pulses or its duration (see cases 1 and 3). It only affects its periodicity (timing jitter).

- Phase noise may seem to have an influence in the flatness of the optical spectrum. The higher the intensity phase noise, the more irregular the envelope of the optical spectrum appears to be (case 3).

2.2. Mode locking characteristics and characterization techniques

2.2.1. Optical spectrum

As we have seen, the optical spectrum is defined by $\left|E(\omega)\right|^2$ and is usually measured by means of commercially available optical spectrum analyzers (OSA). One of the most important parameters of a mode locked laser is the full width at half maximum (FWHM) of the optical spectrum envelope. In a semiconductor laser, this parameter is ultimately limited by the internal optical bandwidth of the gain medium (gain bandwidth) and its broadening mechanisms (homogeneous and inhomogeneous). A large internal optical gain bandwidth is usually the result of large inhomogeneous broadening, such as the one typically exhibited by quantum dot like based structures. Indeed, this property could be exploited for fabricating super luminescent light emitting diodes with very broad band emission [48] . One may hence expect a broader lasing spectra in quantum-dot based lasers than in multi quantum well (MQW) or bulk counterparts. The spectral width FWHM is often given in (nm) units but can

be easily converted to (Hz) units. The number of modes N at this FWHM will then be given by $N = 2\pi \cdot FWHM_{(Hz)} / \omega_r$.

Semiconductor MLLs usually exhibit Gaussian, hyperbolic secant and sometimes even almost rectangular shapes with very flat profiles, as in the case of QDash lasers, leading to an increased FWHM. A high spectral width is a desirable feature in MLLs as it can enable a number of applications requiring a large number of modes with equalized powers (frequency combs), such as in wavelength division multiplex (WDM) and Optical Orthogonal Frequency Division Multiplex (OFDM) systems, in which the perfectly equally spaced frequencies can be used as separate transmission channels at the transceiver. By Fourier transform analysis, larger FWHM can also result in shorter pulse durations with higher peak powers, which are also very attractive features for telecommunication and medical applications, such as Optical Coherence Tomography (OCT) for medical imaging [49].

Another important aspect of the optical spectrum is its peak wavelength, which is mainly determined by the band gap of the active layer material. In quantum dot based active layers, the band gap is highly dependent on the actual size and composition of the quantum dots, a property that can be exploited for fabricating wavelength tuneable lasers [49] which are highly desirable for most communication, instrumentation and medical applications. Particularly, for optical communication applications, one is interested in lasers emitting in the spectral ranges around 1.3 and 1.55 μm, which is typically achieved by depositing a few monolayers of InAs on GaAs and InP substrates respectively.

2.2.2. Optical phase noise and optical linewidth

The optical phase noise is determined by the instantaneous phase $\theta_n(t)$ of each of the longitudinal modes. It originates from amplified spontaneous emission (ASE) noise, which is white, and therefore it undergoes random walk-like fluctuations [50] with an associated diffusion constant D_{θ_n}. This results in a Lorentzian shape of the optical modes as shown in Figure 2-1-Figure 2-3, the width of which is proportional to D_{θ_n}. The optical phase noise can therefore be quantified by the linewidth $\Delta\omega$ of the associated Lorentzian line. Standard grating-based OSAs do not offer the resolution required for measuring the typical ~MHz linewidths exhibited by the optical modes of semiconductor lasers. Scanning filter methods

do not achieve the necessary resolution either. Consequently, heterodyne detection [51], self-heterodyne detection [52] and frequency discriminators [53] have been proposed as indirect measurement techniques for estimating the optical linewidths of narrow laser emissions.

A reduced phase noise and hence a narrow optical linewidth of the laser modes is a desirable feature for almost any foreseen application, particularly in the field of optical communications. This is particularly the case for high speed optical coherent systems, such as coherent OFDM, which usually requires very narrow linewidths for both the source and the local oscillators [54]. It will later be shown in Chapter 4 that the optical phase noise is closely related and proportional to the intensity phase noise and hence, a reduced phase noise of the optical modes can in addition lead to a reduced phase noise of the laser intensity, which represents a key requirement in microwave photonics applications, such as in radio over fiber systems. Finally, a reduced intensity phase noise can also result in low-jittered pulses, as will be explained in the following sections.

2.2.3. Intensity phase noise and RF linewidth

Insertion of the mode locking conditions into (2.7) yields the following expression for the laser intensity:

$$I(t) \propto \sum_{m=1}^{N-1} \sum_{l=1}^{N-m} 2E_{m+l}E_l \cos\left[m\omega_r t + m\Delta\theta(t) + \left(\phi_{m+l} - \phi_l\right)\right] + \sum_{m=1}^{N} E_m^2 \qquad (2.8)$$

The instantaneous phase of each of its frequency component is affected by the intensity phase noise $\Delta\theta(t)$. Originating from ASE noise, one may also expect the same type of statistics as for the optical modes with an associated diffusion constant $D_{\Delta\theta}$. Of particular interest among the MLL characteristics is the spectrum $\left|I(\omega)\right|^2$ of $I(t)$ which is often referred to as the radio frequency (RF) spectrum.

By simple inspection of (2.8), one can see that under ML regime, the RF spectrum should consist of $N-1$ lines centered at exactly $m\omega_r$, with $m=1$ to $N-1$. In the absence of phase intensity noise $\Delta\theta(t)$, the lines should correspond to Dirac delta functions, however, due to the random walk statistics of $\Delta\theta(t)$, these lines will exhibit a Lorentzian broadening, just

like each of the modes from the optical spectrum. Usually, attention is focused on the first harmonic of the RF spectrum ($m=1$), which can be seen in the temporal domain as:

$$I(t) \propto (N-1)\sum_{l=1}^{N-1} 2E_{l+1}E_l \cos\left[\omega_r t + \Delta\theta(t) + (\phi_{l+1} - \phi_l)\right] \qquad (2.9)$$

The FWHM of this spectrum corresponds to the so-called RF linewidth $\Delta\omega_{RF,1}$, which will be later shown to be proportional to $D_{\Delta\theta}$. By looking at (2.9) one can note that the RF linewidth should not be dependent of the static phase terms $(\phi_{l+1} - \phi_l)$, as it is only dependent on time fluctuations, i.e. $\Delta\theta(t)$. Consequently, one can sometimes observe narrow RF linewidths and no pulse train whatsoever as illustrated in Figure 2-2. It will be shown that the RF linewidth can also be severely affected by technical noise (e.g. mechanical vibrations, temperature fluctuations, and optical feedback, cf. Chapter 2).

The RF spectrum can be assessed by direct photodetection of the emitted light in combination with an electrical spectrum analyzer (ESA) or a real time scope (RTS) with spectral analysis functionalities. However, the limited bandwidth of currently commercially available photodiodes of ~ 100 GHz sets a limit in the maximum repetition frequency of the mode locked laser for spectral analysis. Another limitation may come from the ESA or RTS but this can be overcome through electrical down conversion techniques by mixing the laser intensity obtained after photodetection with a low noise local oscillator before spectral analysis.

2.2.4. Timing Jitter

Due to intensity phase noise $\Delta\theta(t)$, the pulse train emitted by the MLL will exhibit deviations of the pulse positions from those of a perfectly periodic pulse train. Figure 2-4 illustrates this situation which compares the laser intensity affected by timing jitter (from Figure 2-3(f)) and the laser intensity obtained by making $D_{\Delta\theta} = 0$ (without jitter).

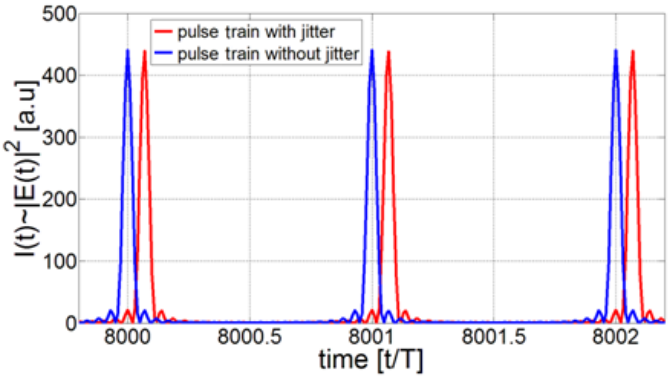

Figure 2-4. Pulse train with and without timing jitter

Two kinds of timing jitter will be considered:

- Pulse to clock timing jitter or r.m.s. integrated timing jitter: it can be assessed in the frequency domain by means of photodetection in combination with an ESA. It is measured as the power spectral density of the laser intensity phase fluctuations between two given frequencies ω_1 , $\omega_2 > 0$. The idea of this technique was originally introduced by Von der Linde [55], however, it should be noted that his model is not valid for the case of passively mode locked lasers in which the noise is fundamentally non-stationary due to the lack of a reference clock as in actively or hybrid mode locked lasers [56]. Under certain circumstances, this measurement can however give an estimate of the jitter relative to a perfect RF oscillator. This will be further discussed in Chapter 4.

- Pulse to pulse timing jitter: it refers to deviations between the temporal positions of consecutive pulses from the average pulse train period and it is usually measured by means of cross correlation techniques [57].

It will be shown in Chapter 4 that the RF linewidth, the optical linewidth of each longitudinal mode, and the timing jitter are analytically related and can provide a very useful means of jitter characterization at high repetition frequencies.

2.2.5. Static phase and pulse characteristics

The static phase ϕ_n of each mode refers to the steady state value around which the instantaneous modal phase fluctuates and will determine the pulse profile and its duration for a given spectral FWHM. From the third condition of mode locking:

$$2\phi_{n+1} - \phi_n - \phi_{n+2} = \Phi_n$$

If $\Phi_n = 0$ for all n, then there exists a linear relationship among the static phases leading to constructive interference of the optical modes. In this case, the minimum pulse for a given FWHM of the optical spectrum is obtained. Static phase relations of higher orders ($\Phi_n = \text{constant}$ or $\Phi_n = f(n)$) can give rise to destructive interference among the modes, which results in pulse broadening or intensity profiles without any clear pulse development.

If we are able to represent the electric field in the frequency domain, its associated spectral phase can in general be written as a Taylor expansion around a given frequency ω_0 as:

$$\varphi(\omega) = \varphi^{(0)} + \varphi^{(1)} \frac{\omega - \omega_0}{1!} + \varphi^{(2)} \frac{(\omega - \omega_0)^2}{2!} + \ldots$$

The group delay (GD) and the group delay dispersion (GDD) are defined as:

$$GD = \varphi^{(1)} = \frac{d\varphi(\omega)}{d\omega}$$

$$GDD = \varphi^{(2)} = \frac{d^2\varphi(\omega)}{d\omega^2}$$

We will see in Chapter 4 that generally, in a semiconductor passively mode locked laser, the GDD is approximately constant for all ω leading to a constant Φ_n for all n. Being able to measure the GD and/or the GDD can hence give us access to the static phase relation of the lasing modes. Having access to the phase as well as the amplitude of the lasing modes allows reconstructing the actual intensity profile of the mode locked laser, from which the pulse duration Δt can be determined.

Due to the limitations imposed by the electronics and the photodetector bandwidths, the minimum pulse duration that can be at present measured using the fastest commercially available photodiodes in combination with the fastest sampling oscilloscopes is about ~10 ps.

Passively semiconductor mode locked lasers based on quantum dot structures are now able to emit sub-picosecond pulses, therefore, direct detection of the laser intensity as just described is not possible. Streak cameras can now achieve sub-picosecond resolution but these devices remain extremely expensive and fragile. Intensity autocorrelation (AC) measurements through second harmonic generation (SHG) can provide femto-second resolutions and represent one of the most widely used, simple, and affordable techniques for sub-picosecond pulse characterization. However, besides being a nonlinear technique requiring high input optical peak powers, the AC trace can only give an estimate of the pulse duration when it is a well behaved one (near transform limited), otherwise leading to wrong interpretations. This is unfortunately sometimes the case as the AC trace tends to wash out any substructure in the pulse intensity, such as satellite pulses or busty profiles, for which the resulting AC trace can even approach a perfect but useless Gaussian shape. Other nonlinear techniques such as FROG (Frequency-Resolved Optical Gating) [58] or SPIDER (Spectral Phase Interferometry) [59] also exist which can be used to obtain more information on the pulses in order to overcome the ambiguities of the autocorrelation intensity. For instance, FROG is an autocorrelation measurement in which the autocorrelator output beam is spectrally resolved, so instead of just measuring the AC output energy as a function of delay, it also uses its spectrum as additional information for recovering the laser intensity profile. Yet, these techniques cannot offer complete intensity and phase characterization of the pulses or in turn they need very well characterized reference pulses in order to overcome these limitations. Linear techniques have more recently been proposed which, besides being less power stringent, can also provide complete phase-amplitude characterization [60–65]. In this work, we have made used of the simple AC technique for the cases of well behaved pulses, as it can result in fast measurement results while providing fairly good estimates of the pulse duration. We have also employed the linear technique presented in [64], which has allowed full access of the phase and amplitude of the emitted pulses, even in the cases where they had much temporal substructure, otherwise impossible to correctly characterize by the AC technique.

By simple Fourier analysis, there exists a lower limit of the minimum achievable pulse duration of the laser intensity which will be inversely proportional to the FWHM of the optical spectrum. The proportionality factor and the pulse profile are determined by the envelope shape of the optical spectrum. By applying the Fourier transform properties, the following table can be straightforwardly deduced:

OS envelope	Pulse profile	Minimum Pulse duration
Gaussian	Gaussian	$0.441/FWHM_{(Hz)}$
Hyperbolic secant squared	Hyperbolic secant squared	$0.315/FWHM_{(Hz)}$
Rectangular	Sinc squared	$0.88/FWHM_{(Hz)}$

Table 2. Minimum pulse duration and its corresponding profile for a given optical spectrum shape

The previous ideas lead to the concept of time bandwidth product (TBP). The TBP is defined as the product of the FWHM of the optical spectrum times the actual pulse duration of the laser intensity, i.e., $\left(FWHM_{(Hz)} \times \Delta t\right)$. This product is frequently used for indicating how close the emitted pulse width is to the lower limit imposed by the Fourier transform, quantifying the quality of the generated pulses and how efficiently the available spectrum is used. When the pulse duration attains its minimum value (when Φ_n=0), it is said to be transform limited. The proportionality factor in Table 2 represents the minimum value of TBP for each of the cases presented.

The TBP is often larger than the ideal minimum value from Table 2. This can result from intracavity dispersion (nonzero GDD), nonlinear chirp, or a combination of both. In the first case, dispersion itself does not modify the optical spectrum; however it has the effect of broadening the pulse, hence increasing the TBP from the transform limited value. Nonlinear chirp, on the other hand, which in general refers to a time dependence of the instantaneous frequency of the pulse, can arise in semiconductor lasers due to nonlinear self-phase modulation [66]. Indeed, a high fluctuating field intensity in the laser cavity can lead to a modulation of the carrier density N, resulting in a modulation of the laser gain $g\left(N\right)$. The

later can translate into subsequent modulations of the refractive index *n* via linewidth enhancement factor [67] $\alpha_H \propto (dn/dN)/(dg/dN)$ and finally to a phase change per unit length during propagation. While this effect, on its own, does not modify the laser intensity, it will enlarge the spectral width hence increasing the transform limited TBP value.

2.3. Mode locking mechanisms

So far we have defined the ML regime and the main features associated to it. In this section, we address the question of how this regime is actually established in semiconductor lasers. In this work we will be dealing with monolithic mode locked lasers only, in which all the main physical mechanisms leading to mode locking take place on a single laser chip, which is initially a single section FP device. There are two main ways of achieving mode locking in monolithic devices: active and passive mode locking. A combination of both techniques (hybrid mode locking) is also possible.

In active mode locking, the FP laser is driven by an external RF signal oscillating at a rate close to the nominal repetition frequency of the laser cavity, leading to a modulation of the laser gain (or losses) which creates modulation sidebands at the vicinity of each longitudinal mode. These modulation sidebands will subsequently pull the neighbouring modes forcing them to oscillate equidistantly and in synchronization, leading to the establishment of the mode locking regime. Owing to the external driving source which perfectly synchronizes the laser modes, the RF linewidth and the timing jitter of this type of MLLs are very much reduced.

Passive mode locking, on the other hand, exploits the nonlinear properties of the laser medium. This can be achieved by the introduction of a saturable absorber (SA) into the laser cavity and will be referred to as two section passively mode locking. It can also result from the intrinsic nonlinear gain of the simple FP laser, in which case it will be referred to as single section passively mode locking.

As opposed to actively mode locked lasers, monolithic passively MLLs have a number of advantages such as: compact size, ease of fabrication, low cost, low power consumption, and can in addition be direct electrically pumped, making them promising candidates for optical communication applications, particularly those presented in this work. For this reason,

passively mode locking, in both its two-section and single-section configurations, will be further discussed in the following sections.

2.3.1. Passively mode locking in two section devices

From the initial single section FP cavity, a second section can be defined by means of electrical isolation so that it can be reversed biased in order to operate as a saturable absorbing (SA) medium (cf. Chapter 3). This section is usually a small fraction (~10%) of the remaining one, which is used as the amplifying or gain medium. The main idea is to exploit the saturation dynamics of the SA for the generation of optical pulses. The duration of the pulses generated by this method in a semiconductor laser is usually much smaller than the SA recovery time. This situation is usually referred to as mode locking with a slow saturable absorber [68]. The basic principle responsible for the mode locking regime in this case is very well known: the intensity of the travelling wave inside the laser cavity saturates the absorber section during propagation. The absorber saturates faster than the gain medium therefore creating a short net gain window in which cavity losses can be compensated, leading to a periodic amplification of the travelling field for the duration of the window openings. After a number of roundtrips the situation depicted in Figure 2-5 can be established, leading to the formation of a stable pulse train. It should be noted that after a round trip passage of the pulse inside the cavity, the saturated loss must recover to its unsaturated value by radiative and non radiative decay. This process needs to be faster than the intracavity roundtrip time. In the same interval of time, the gain medium must recover slower so as to allow for the losses to be greater in such a way that no amplification can take place between two consecutive pulses.

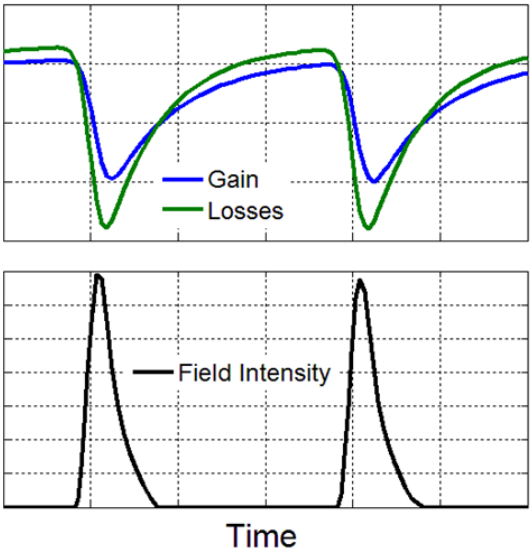

Figure 2-5. Illustration of two section passively mode locking with a slow saturable absorber

This method of generating ultra short pulses in semiconductor lasers has been known for a long time, and numerous models have already been proposed for effectively predicting their behaviour [69–74]. This has also being the case for the more recently quantum dot based devices [75–78], which basically differ from the standard initial models in that they now include carrier transport dynamics of the carriers within the quantum dots.

In general, these models are usually formulated within a time-domain approach, in which the ML regime is described as the propagation of the total optical field in both the gain and absorber sections, coupled to the corresponding rate equations for the carrier densities in each one of them. We will only present the main equations that are usually used as a departing point for describing mode locking in two section semiconductor lasers and which can be straightforwardly obtained from the Maxwell equations and from fundamental laser relations. Let us employ for instance the notation and the formulation in [74],

The field and carrier density equations in the gain section are:

$$\frac{\partial A(\tau,z)}{\partial z}=\frac{1}{2}\left(1-i\alpha_g\right)n_g(\tau,z)\,A(\tau,z)$$

$$\frac{\partial n_g(\tau,z)}{\partial t}=j_g-\gamma_g n_g(\tau,z)-n_g(\tau,z)\left|A(\tau,z)\right|^2$$

Similarly, in the absorber section:

$$\frac{\partial A(\tau,z)}{\partial z}=\frac{1}{2}\left(1-i\alpha_q\right)n_q(\tau,z)A(\tau,z)$$

$$\frac{\partial n_q(\tau,z)}{\partial t}=j_q-\gamma_q n_q(\tau,z)-sn_q(\tau,z)\left|A(\tau,z)\right|^2$$

where $\tau=t-z/v$, with v the group velocity of light (assumed the same in both sections), $A(\tau,z)=E(\tau,z)\sqrt{vg_g\Gamma_g}$, with $E(\tau,z)$, the field envelope, Γ_g the optical confinement factor , $\alpha_{g(q)}, g_{g(q)}, \gamma_{g(q)}$, the linewidth enhancement factor, the differential gain or losses, and the relaxation rates for the amplifying (*g*) and absorbing medium (*q*), $n_{g,q}(\tau,z)=g_{g,q}\Gamma_{g,q}\left[N_{g,q}(\tau,z)-N_{g,q}^{tr}\right]$, $j_g=g_g\Gamma_g J_g-\gamma_g N_g^{tr}$ and $j_q=\gamma_q N_q^{tr}$, with N and J representing carrier density and injection current respectively. The parameter $s=g_a\Gamma_q/g_g\Gamma_g$ is the ratio of the saturation intensities in the amplifying and absorbing segments.

This set of coupled differential equations can in some cases lead to self-consistent solutions of the electric field in the form of a pulse with a given profile and duration. The solution can be a stable one and the requirement for it is usually expressed as a condition for the ratio s of the saturation intensities in both media. If the stability condition does not hold, the laser may enter unstable regimes such as Q-switching, in which the pulse energy undergoes large oscillations due to dynamic instabilities owing to undamped relaxation oscillations. Regarding the pulse characteristics, one may expect that in order to decrease its duration, the absorber dynamics need to be fast, which is usually accompanied by an increased saturation intensity. However, this may be in contrast to the stability condition which in general implies a low saturation intensity of the absorber compared to that of the gain medium, requiring the saturation energy on the gain side to be increased. This can be obtained by increasing the gain in the amplifying section which can also result in a pulse with a higher peak power which may help in saturating faster the absorbing medium, in principle leading to a pulse width reduction. However, an increased in gain is usually accompanied by a faster recovery time which can result in very long trailing edges and significant broadening of the pulse. Consequently, one can see that, in general, a balanced interplay between the gain and

absorption dynamics will ultimately determine the behaviour of the two section devices in order to obtain stable and short pulses. This will be traduced by a limited bias range that can be applied to each of the ML sections.

In particular, two section mode locked lasers based on quantum dot structures have shown to present high gain saturation energies and increased differential absorption due to the reduced density of states. Furthermore, ultrafast gain recovery times owing to efficient carrier capture and relaxation in the QD states and a fast absorption recovery in reversed bias QD based structures have been measured [6], [79], [80], representing an advantage for obtaining ultra short pulses in two section devices.

2.3.2. Passively mode locking in single section devices

The mode locking regime in semiconductor lasers can also take place in the simple FP laser configuration devoid of a saturable absorber. Indeed, this has already been evidenced in bulk [81], multi quantum well [22], [23], quantum dash [15], and quantum dot [12] based semiconductor lasers, suggesting that the mode locking regime would not be particularly related to the dimensionality of the active layer. The phenomenon still lacks a full theoretical explanation. Nevertheless, the main physical mechanism responsible for the mode locking behaviour has been, in all cases, attributed to the nonlinearity of the gain medium. In particular, four-wave mixing (FWM) has mostly been identified as the mechanism playing the major role in this type of mode locking regime. Indeed, FWM can provide mutual injection locking leading to strong correlation between the phases of the laser cavity modes, similarly to the situation in actively mode locked lasers, the external RF source being replaced in this case by the internally generated signal which is formed by the beating among the laser cavity modes.

In general, phase correlation among the modes leads to a reduced RF linewidth, and this can only be the case if there exists coherent coupling between the modes, since incoherent interaction would yield RF linewidths which are twice those of the optical modes themselves. In semiconductor lasers, modes can interact coherently by two different processes: interband and intraband optical transitions [82]. The first involves electron-hole recombination due to carrier density modulation (CDM) at the beating frequencies of the interacting fields, i.e. at the frequency components of the intracavity field intensity. This mechanism is limited by the

interband relaxation rate with a characteristic carrier lifetime which is typically in the order of hundreds of picoseconds. The intraband effects, such as spectral hole burning (SHB), and carrier heating (CH), have their origin in the modulation of the occupation probability within the energy bands and respond at time scales < 1 ps. In quantum dot based active layers, this type of mechanism is referred to as intraband scattering and account for transitions occurring between confined quantum states or bound-to-continuum states, exhibiting similar time scales smaller than 0.1 ps. All these mechanisms represent nonlinear processes and are responsible for four wave mixing (FWM) phenomena in semiconductor optical amplifiers and lasers [82].

Correlation of the time dependent phases due to a FWM mechanism induced by CDM alone has being theoretically and experimentally demonstrated in a distributed Bragg reflector (DBR) semiconductor laser [83], leading to a RF linewidth reduction in this type of devices. In fact, the RF linewidth reduction has been the main indicator of mode locking in devices devoid of a saturable absorber section and, although not explicitly reported by all authors, the observation of pulses usually required some sort of external dispersion compensation. This situation recalls that depicted in Figure 2-2, in which although the instantaneous phase synchronization had been achieved, the nonlinear static phase relation did not allow for the formation of a clear train of pulses. To the authors knowledge, the static phase relation in single section devices has not theoretically been investigated although it was predicted and experimentally verified for QDash based lasers to follow a quadratic law [24]. In the following section we will attempt theoretically and by simulations, to determine the static phase relation due to FWM in a semiconductor optical amplifier (SOA), and for that we will first review some general aspects of this nonlinear phenomenon.

In general, FWM has its origin in the nonlinear nature of the propagating medium. It refers to a third order parametric process involving four different optical fields as depicted in Figure 2-6 in which the photon energy is conserved ($\hbar\omega_j + \hbar\omega_m = \hbar\omega_k + \hbar\omega_l$). Thus, the fields will interact such that $\omega_j + \omega_m = \omega_k + \omega_l$.

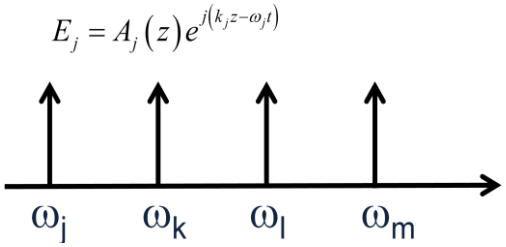

Figure 2-6. Four wave mixing interacting fields

An optical field with a sufficient intensity that propagates in a semiconductor medium will generate linear and nonlinear polarizations. The magnitudes of these polarizations will be determined by the optical susceptibilities of the medium such as $\chi^{(1)}, \chi^{(2)}, \chi^{(3)}$ etc, with $\chi^{(n)}$ being the nth order nonlinear susceptibility. FWM arises from a third order optical nonlinearity, hence we will focus our attention on $\chi^{(3)}$. The induced third order nonlinear polarization at a given frequency ω_j due to electric field interaction is given by [84]:

$$P_j^{(3)}(\omega_j) = \varepsilon_0 \sum_{\omega_j=\omega_k+\omega_l-\omega_m} \chi_j^{(3)}(\omega_j;\omega_k+\omega_l-\omega_m)E(\omega_k)E(\omega_l)E^*(\omega_m) \qquad (2.10)$$

In semiconductors lasers and amplifiers, a monochromatic field of the form $E_j = A_j(z)e^{j(k_j z-\omega_j t)}$ obeys the wave equation which follows straightforwardly from the Maxwell equations [82]:

$$\nabla^2 E - \frac{n^2}{c^2}\frac{\partial^2 E}{\partial t^2} = \frac{1}{\varepsilon_0 c^2}\frac{\partial^2 P}{\partial t^2} \qquad (2.11)$$

In this thesis, we will deal with semiconductor lasers in which only the TE mode is present. For the sake of simplicity, we will ignore spatial effects and assume infinite plane waves propagating in the *z* direction in a homogeneous medium, which allows us to replace the Laplacian operator by a spatial derivative in *z* , hence, we can write:.

$$\frac{\partial^2 E}{\partial z^2} - \frac{n^2}{c^2}\frac{\partial^2 E}{\partial t^2} = \frac{1}{\varepsilon_0 c^2}\frac{\partial^2 P}{\partial t^2} \qquad (2.12)$$

Due to the energy transfer between waves, the field amplitudes $A_j(z)$ will change as they propagate through the medium, however these variations are only significant after

propagation over distances much longer than their wavelengths, which allows us to write (2.12) in the slowly varying amplitude approximation as [84]:

$$\frac{\partial A_j}{\partial z} = \frac{j\omega}{2\varepsilon_0 cn}\Gamma P_j e^{j\left(k_j z-\omega_j t\right)} \qquad (2.13)$$

In which we have introduced the confinement factor Γ to account for the fraction of mode energy which is confined within the laser active region, outside of which $P_j = 0$.

In the presence of all fields, the total polarization is actually given by the sum of linear and nonlinear contributions. $P_j = P_j^{(1)} + P_j^{(3)}$. The linear part, associated with the saturated SOA gain, can be written as [82] :

$$P_j^{(1)} = \varepsilon_0 \chi_j^{(1)} E_j = -\varepsilon_0 \frac{nc}{\omega_j}\left(\alpha_H + j\right)\Gamma g(\overline{N})E_j \qquad (2.14)$$

where $\overline{N}$ is the static carrier density satisfying the carrier density equation:

$$\frac{dN}{dt} = \frac{I}{qV} - \frac{N}{\tau_s} - \frac{g\left(N\right)}{\hbar\omega_0}\left|E_{total}\left(t\right)\right|^2 \qquad (2.15)$$

with $q, V, \tau_s, E_{total}\left(t\right)$ the electron charge, the active volume, the carrier lifetime, and the sum of all the fields propagating within the SOA, respectively.

In fact, solution of (2.15) also results in a fluctuating carrier density at the frequency components of $I\left(t\right)$, i.e., the frequencies corresponding to the resulting beats between the different electric fields propagating in the SOA [82]. This is referred to as carrier density modulation (CDM), and will generate amplitude and index gratings which scatter the propagating fields creating additional FWM fields. Being one of the nonlinear processes responsible for FWM, its effects will be accounted for in $\chi^{(3)}$. In fact, $\chi^{(3)}$ can be decomposed into contributions from CDM, SHB and CH, as will be seen later in this section. By inserting (2.10) and (2.14) into (2.13) we obtain:

$$\frac{\partial A_j}{\partial z} = \frac{j\omega}{2cn}\Gamma \sum_{\omega_j=\omega_k+\omega_l-\omega_m} \chi_j^{(3)}\left(\omega_j;\omega_k,\omega_l,-\omega_m\right) A_k(z) A_l(z) A_m^*(z) e^{-j\left(k_k+k_l-k_j-k_m\right)z} + \frac{\left(1-j\alpha_H\right)}{2}\Gamma g\left(\overline{N}\right) A_j(z)$$

$$\frac{\partial A_j}{\partial z} = \frac{j\omega}{2cn}\Gamma \sum_{\omega_j=\omega_k+\omega_l-\omega_m} \chi_j^{(3)}\left(\omega_j;\omega_k,\omega_l,-\omega_m\right) A_k(z) A_l(z) A_m^*(z) e^{-j\left(k_k+k_l-k_j-k_m\right)z} + \frac{\left(1-j\alpha_H\right)}{2}\left(G\left(\frac{1}{1+\sum_i |A_i|^2 / P_{sat}} \right) - \alpha \right) A_j(z) \tag{2.16}$$

in which we have introduced P_{sat} and α to account for gain saturation and linear losses, respectively. Equation (2.16) is in agreement with the analysis presented in [85], and after some simplifications it will be used in combination with experimental results on FWM in QDash SOAs as a first attempt to determine the steady state phase relation between a set of equidistant fields launched into a QDash SOA.

Specifically, in QDash based semiconductor optical amplifiers, the conjugate field created by the FWM process is also a consequence of the different nonlinear polarizations arising from the various mechanisms previously described. Additionally, interaction between different dash sub-ensembles [21] mediated through a common carrier reservoir has also being identified as a nonlinear processes leading to broadband FWM in QDash based SOAs [86], [87]. The efficiency of the FWM process will be proportional to the squared absolute value of the linear combination of the third order susceptibilities $\chi^{(3)}$ of all of these contributions.

Let us consider the typical FWM efficiency experiment as in Figure 2-7. In this case $\omega_k = \omega_l$, and the FWM process is said to be nearly degenerate; hence $E_k = E_l$, and this field will be referred to as the pump signal. The FWM field is generated at $\omega_j = 2\omega_k - \omega_m$, the field at ω_m being referred to as the probe signal. The FWM efficiency η_{FWM} is defined as the signal power ratio of the FWM signal at the SOA output and the probe at the SOA intput, i.e. $\eta_{FWM} = P_{FWM}(L) / P_{probe}(0)$. This efficiency will therefore be proportional to $\left|\chi_j^{(3)}\left(\Delta f_{FWM}\right)\right|^2$,

with $\Delta f_{FWM} = \left(\omega_{pump} - \omega_{probe}\right)/2\pi$ the frequency separation between the pump and the probe, commonly referred to as the frequency detuning.

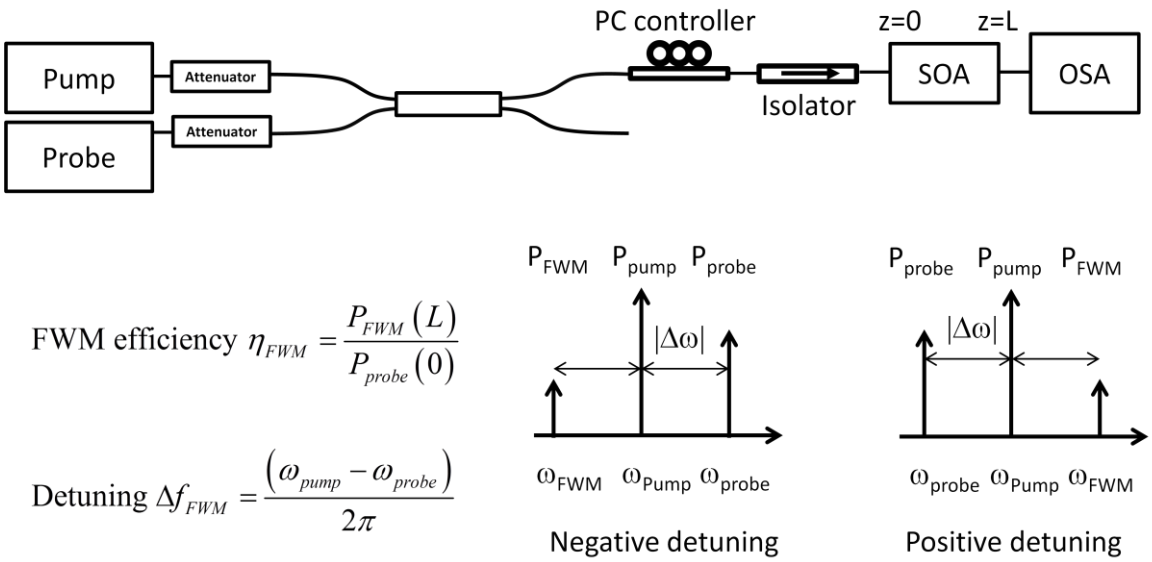

Figure 2-7. FWM efficiency set-up and related parameters

By using a setup like in Figure 2-7, the FWM efficiency in a QDash based SOA has been measured. Bias and input power conditions were set in order to operate the SOA under saturation regime with a corresponding saturated gain of 10 dB. Figure 2-8 shows the measured FWM efficiency for both positive and frequency detuning obtained by varying the probe frequency for a fixed pump field.

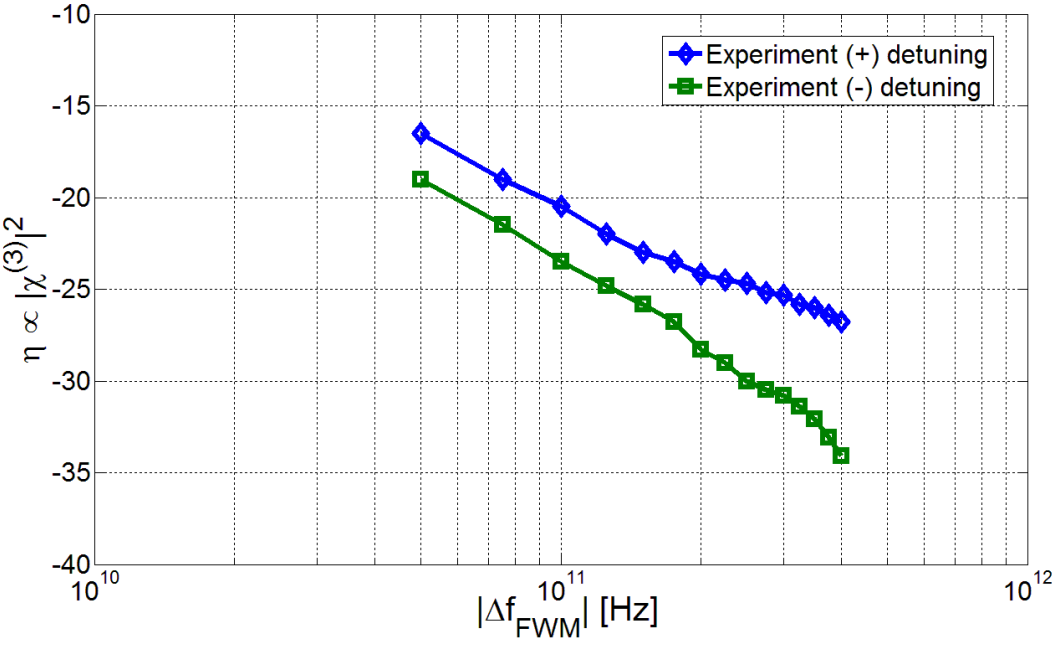

Figure 2-8. FWM efficiency in a QDash SOA (SOA length=2mm, I=250mA, saturated gain=10dB)

The FWM efficiency is clearly asymmetric with respect to zero detuning and decreases at different rates as a consequence of the different contributions of each nonlinear process involved. The FWM efficiency can attain minimum values down to ~13 dB/dec as also reported in [86] for QDash based SOAs. In order to separately identify the contributions of each nonlinear mechanism involved in the FWM efficiency, we have considered the temporal complex impulse response of the SOA to be a sum of the individual impulse responses associated to each nonlinearity, i.e.:

$$h(t) = a_{CDM}\left(i-\alpha_{CDM}\right)\exp\left(-t/\tau_{CDM}\right) + a_{SHB}\left(i-\alpha_{SHB}\right)\exp\left(-t/\tau_{SHB}\right) + a_{CH}\left(i-\alpha_{CH}\right)\exp\left(-t/\tau_{CH}\right) \quad (2.17)$$

where α (or α_H, the linewidth enhancement factor) as already introduced in section 2.2, represents the coupling of gain to index changes, τ corresponds to the dynamic time constant and a to a fitting parameter associated to each one of the nonlinear processes. The asymmetry of the FWM efficiency in Figure 2-8 with respect to zero detuning is simply due to the nonzero value of α associated to the different nonlinear responses.

The FWM efficiency will hence be proportional to the Fourier transform of the overall impulse response. By using this fact and by fitting the measured FWM efficiency data with the frequency response of (2.17), Figure 2-9 was obtained from which we have estimated the parameters of each nonlinear process, similarly to [88]. Each of the frequency responses are separately plotted together with the overall fitted responses.

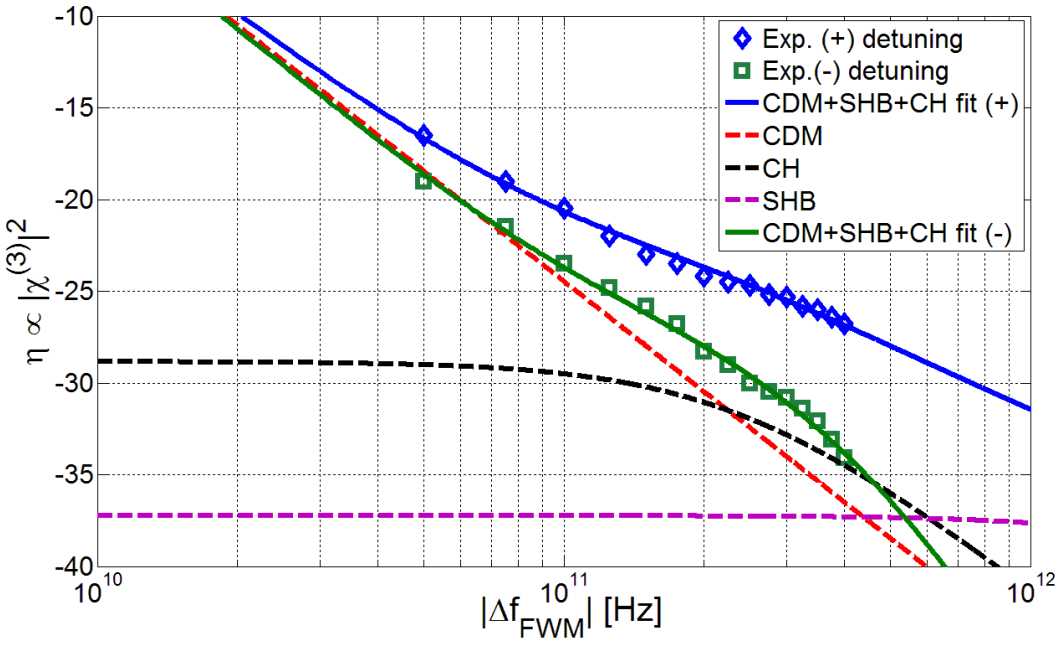

Figure 2-9. FWM efficiency in a QDash SOA for both positive and negative detuning (length=2mm, I=250mA, saturated gain=10dB) with fits of individual contributions from CDM, CH and SHB

We have found the different time constants to be 100 ps, 650 fs and 50 fs for CDM, CH and SHB mechanisms respectively, in qualitative agreement with values reported for InAs QD based SOAs [88]. We can see that the CDM contribution is dominant for a detuning below ~ 200 GHz, in agreement with [89] for an SOA under saturation regime. This prevailing CDM effect is attributed to a reduction in the population inversion owing to saturation of the gain medium which in turn decreases the carrier lifetime, resulting in a more efficient CDM mechanism. The contributions from the other two processes, however, make the overall efficiency greater than 20 dB/dec as would be the case for CDM alone and can be potentially used for broad band wavelength conversion.

We can now use the estimated value of the complex $\chi_j^{(3)}(\Delta f_{FWM})$ to numerically solve (2.16) in the case of N equidistant fields propagating in the SOA. The idea is to determine the steady state field amplitudes and phases of each field after propagation. We first simplify (2.16) by only considering the nearly degenerate FWM mechanism only as depicted in Figure 2-10, just like in the FWM efficiency experiment, which, due to pump to pump interactions, is much more efficient than the non-degenerate case. This will substantially reduce the number of equations for implementing the numeric algorithm. In this case, the phase mismatch factor becomes:

$$\Delta k_{kljm} = 2k_k - k_m - k_j = \frac{\omega_k 2n(\omega_k) - \omega_m n(\omega_m) - \omega_j n(\omega_j)}{c} \qquad (2.18)$$

which can be further simplified by using a linear approximation for $n(\omega) = n(\omega_k) + dn/d\omega(\omega - \omega_k)$, in which case:

$$\Delta k_{kljm} = \frac{d^2k}{d\omega^2}(\Delta\omega)^2 \qquad (2.19)$$

with $\Delta\omega = \omega_m - \omega_k = \omega_k - \omega_j$ corresponding to the frequency detuning while $\frac{d^2k}{d\omega^2}$ is the linear group velocity dispersion within the SOA.

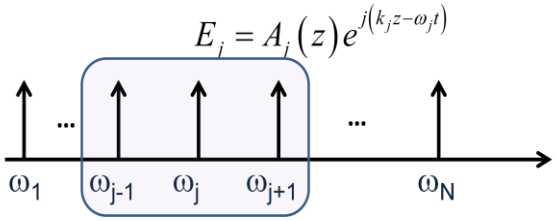

Figure 2-10. Simplified FWM interactions within an SOA taking into account the nearly degenerate case between adjacent modes only

It should be noted that an extension to interactions with non adjacent modes could also be considered. This will of course depend on the frequency separation between the fields and the effective bandwidth of the FWM process. In a semiconductor laser, the different cavity modes play the role of the interacting fields, which are typically separated from 10 to about

300 GHz depending on the laser cavity length. This separation will correspond to the frequency detuning.

We make further simplifications by adiabatically eliminating the carrier density equation, hence bypassing any transitory effects due to the non-instantaneous response of the carrier density owing to changes in the intracavity field intensity. We also follow an adiabatic approach by assuming that the electric polarization instantaneously follows the electric field, although this could be more easily justified due to the very short polarization dephasing times (<0.1 ps) compared to the photon lifetime [90]. Phase noise is not considered as we are only interested in the static phase of each mode.

It is clear that a more rigorous description of FWM in a SOA is necessary and would have to include the coupling of the mode equations with the carrier density equation in combination with carrier transport effects in the case of quantum dot based active layers. Also, the inhomogeneous gain of the active medium should be properly included in order to account for its frequency dependency. This is however outside the scope of this work and would require the collaboration with theoreticians from the field of nonlinear optics.

Being aware of the limitations in our model, we have numerically solved the coupled mode equations of (2.16) by taking into account the measured values of a 2 mm long QDash SOA presenting a saturation power of 1 mW, an unsaturated net gain of 6300 m-1, and a linewidth enhancement factor $\alpha_H = 3$. The initial conditions correspond to a set of $N = 21$ monochromatic fields equidistantly separated by 50 GHz with 0.5mW of power. We used the estimated complex susceptibility $\chi^{(3)}(\Delta f_{FWM})$ at $\Delta f_{FWM} = 50\text{GHz}$, and material dispersion commonly exhibited in semiconductor optical amplifiers around the band gap wavelength of 30 fs/mm/nm [91]. We solved the coupled mode equations with the Matlab program using an ODE45 (ordinary differential equation) function with a Runge-Kutta algorithm, the results of which are shown in Figure 2-11.

The main result of the simulations was the convergence of the different phases toward a steady state leading to a quadratic evolution as a function of frequency. The same evolution was systematically obtained when varying the main parameters in the simulations. Decreasing the absolute value of $\chi^{(3)}(\Delta f_{FWM})$ always led to a flattening of the parabolic

profile, suggesting FWM as the main responsible for the parabolic behaviour. The linewidth enhancement factor also influenced the slope of the parabola; however, it is difficult to derive conclusions on this regard at these early stages of the model.

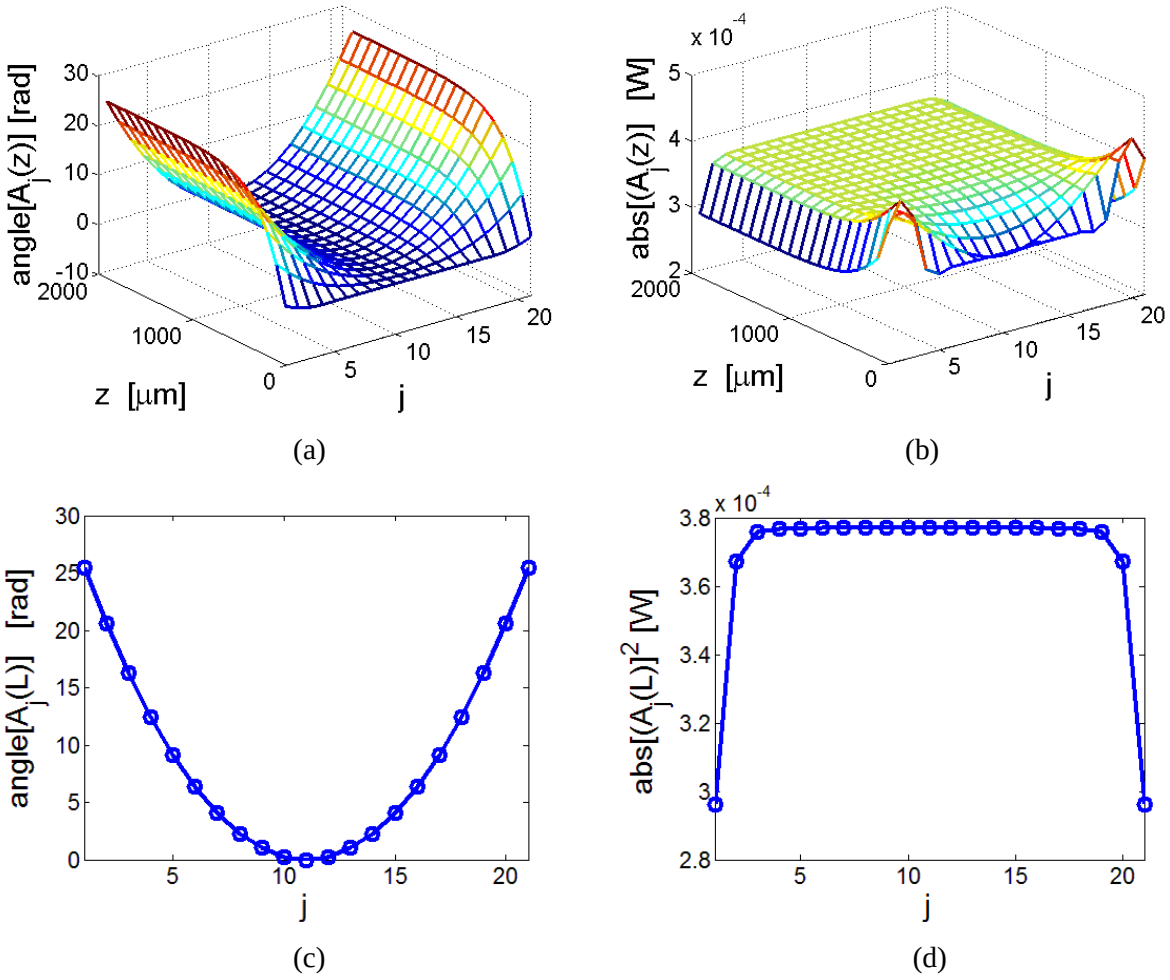

Figure 2-11 Simulation results of 21 equidistant fields propagating in a SOA (a) Phases and (b) amplitudes of each interacting field as a function of propagating distance. (c) Static phase and (d) amplitude profiles at z=L (2 mm).

In order to experimentally verify the simulation results, we have performed static phase and amplitude measurements of a set of equidistant fields after propagation through a 2 mm QDash SOA. Figure 2-12 illustrates the experimental set-up, consisting of an external cavity laser (ECL) which is externally modulated with a synthesized signal at 50 GHz by means of a

Mach-Zehnder (MZ) modulator so as to generate three equidistant optical fields at its output, serving as the input for a 2 mm QDash SOA.

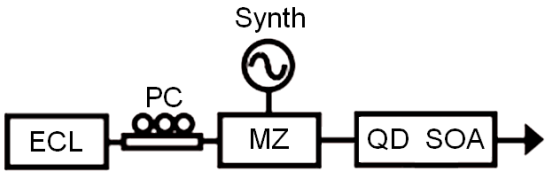

Figure 2-12. Set-up for amplitude-phase characterization at a QDash SOA output

The experiments have been carried out in collaboration with partners from Dublin City University (DCU) in Ireland and the phase measurements have been performed by using the technique described in [64] , which will be described in more detail in Chapter 4.

Figure 2-13(a) is the optical spectrum and the static spectral phase at the QDash SOA input.

Figure 2-13(b), (c) and (d) is the SOA output for increasing values of total input power of -9, 0 and 5 dBm, respectively. Firstly, we can clearly observe the generation of new FWM signals which are equidistantly separated as the input power is increased, confirming the high efficiency of the FWM process in the SOA. Secondly, the output phases are modified after propagation and this effect appears to increase with increasing the overall input power suggesting a qualitative agreement with the previous simulations.

Although the analysis presented for the passively mode locking mechanism has been based on the propagation of travelling waves in an SOA, it will be shown in Chapter 4 to be in very good qualitative agreement with experimental results in a laser configuration. Moreover, the reported model could be transformed into a laser model by applying the necessary boundary conditions. It should be noted, however, that in a FP configuration, one can expect an increase in the overall efficiency of the FWM process owing to the intracavity geometry of the laser, i.e., the newly generated FWM optical fields will be amplified by the laser gain during back and forth propagation between the reflective mirrors of the FP resonant cavity, hence the FWM fields themselves will more efficiently generate new sidebands in a cascaded fashion after interacting with the existing intracavity fields. The total spectral bandwidth over which these new fields will be created will ultimately depend on the laser broadened

gain, independently of the intermodal separation, as will be seen from experimental results in Chapter 4.

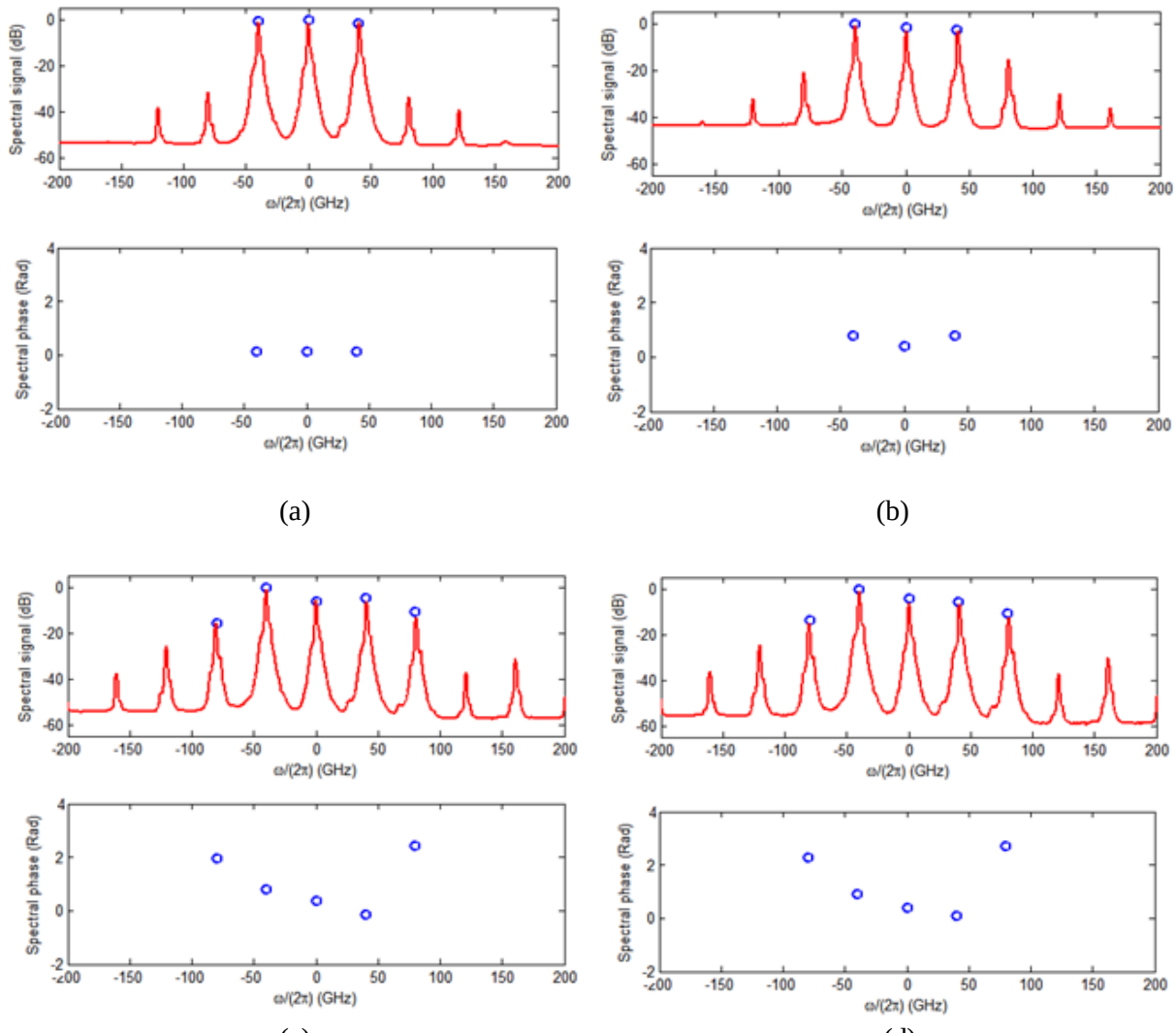

Figure 2-13. Measurements of amplitude and phase of FWM fields at the output of a QDash SOA. (a) Input signal, (b), (c), (d) corresponding output for a total input power of -9, 0 and 5 dBm respectively

Chapter 3. InAs/InP Quantum Dash structures and fabrication

This chapter introduces the underlying physical principles behind quantum dash structures in order to highlight the expected advantages for semiconductor laser-based devices. A description of the investigated quantum dash active layers is presented together with subsequent systematic characterizations that allowed for their optimization. The processing steps followed for fabricating the final devices is also summarized and first measurement results of their static characteristics are presented.

3.1. Low dimensional quantum semiconductor structures as active layers in laser devices

The reduction of the size of a semiconductor down to a small number of atomic layers significantly changes the optical and electronic properties of the structure. Indeed, the confinement of carriers (electrons or holes) down to physical dimensions which are comparable to their de Broglie wavelengths leads to quantization effects otherwise not apparent. The de Broglie wavelength of electrons in InAs at room temperature is 40 nm; hence, one may expect quantization effects to manifest in structures of a few tens of nanometers size. This results in a reduced density of states (DOS), which refers to the amount of carriers allowed at a given energy position, and is defined as the available number of states per energy per unit volume. The reduction of the structure size can be made so as to confine the carriers in one, two, or all three space dimensions, leading to two dimensional 2D (quantum well), one dimensional 1D (quantum wire) and zero dimensional 0D (quantum dot) structures, respectively, as opposed to the 3D or bulk structure in which carriers can move freely in all three dimensions. The density of states can be analytically calculated for each case and take the general forms as in Figure 3-1.

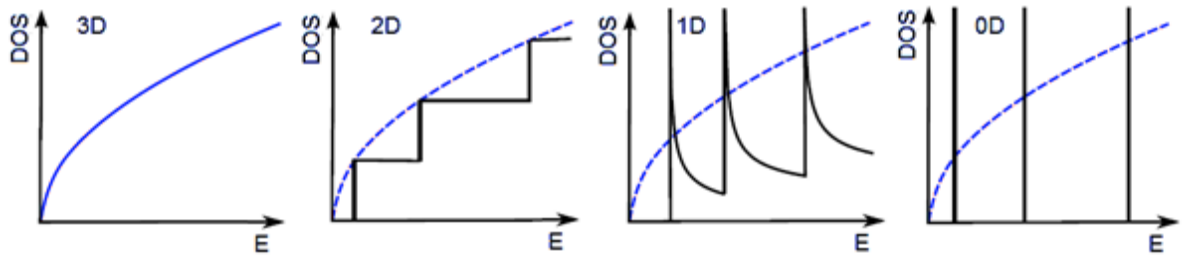

Figure 3-1. Density of states (DOS) as a function of energy E for the 3D, 2D, 1D and OD structures (Dashed line: 3D DOS for comparison purposes)

We notice that for the case of OD or quantum dots (QDs), the DOS is simply given by a series of delta functions and only depends on the number of confined levels. It has been predicted that this delta function-like DOS should lead to a number of benefits in quantum dot based lasers, such as an increase in both optical and differential gain, decrease in threshold current density, reduced temperature sensitivity [3], [7], reduced linewidth enhancement factors [1], [4], and even high modulation bandwidths [92]. Indeed, a semiconductor laser with an active region consisting of quantum dot structures would restrict the electrons and holes that are injected by electrical pumping to the energy levels where they can contribute most efficiently to the lasing process.

However, this idealistic DOS is only a theoretical result as in practice there exists at room temperature a finite distribution of energies around each level owing to two different types of physical phenomena: homogeneous and inhomogeneous broadening. The first one refers to intrinsic properties of the quantum dot due to the finite carrier lifetime in each confined energy state, as well as carrier-phonon and carrier-carrier interactions [93]. In contrast, inhomogeneous broadening is the result of a superposition of a number of transitions in a quantum dot ensemble, mainly due to a variation in the size and composition of the quantum dots which leads to different energy levels for each one of them, reducing the overall optical gain [94]. It is mainly due to this inhomogeneous broadening that the performance of QD based lasers remains limited and efforts to reduce it should be undertaken if full advantage of the theoretical predictions is to be gained.

Besides a reduced DOS, a more obvious implication of having QD structures is the reduced volume of the laser active layer. This leads to a lower optical confinement factor, which is defined as the overlap of the optical field and the active gain material, given by:

$$\Gamma = \frac{\int_{-d/2}^{d/2}\int_{-w/2}^{w/2} \left|E(x,y)\right|^2 dxdy}{\int_{-\infty}^{+\infty}\int_{-\infty}^{+\infty} \left|E(x,y)\right|^2 dxdy} \qquad (3.1)$$

where *d* and *w* are the active layer height and width respectively. This has two main consequences; one is related to the well known laser threshold condition stating that the modal optical gain must balance the total losses at the threshold current, i.e.:

$$\Gamma g(I_{th}) = \alpha_i + \frac{1}{2L}\log\left(\frac{1}{R_1 R_2}\right) \qquad (3.2)$$

with $\Gamma g(I_{th})$ the modal gain at threshold, α_i the internal losses of the structure, *L* the cavity length and $R_{1,2}$ the laser facet reflectivities. Consequently, a very low confinement factor may limit the lasing effect if the laser cavity is made too short and/or if the intrinsic optical gain *g* is small. The intrinsic optical gain will be limited, among other factors, by the dot area density in the active layer, and is usually not enough for achieving lasing if only one QD layer is used. The modal gain should thus be increased, and this is usually done by using the concept of vertically coupled quantum dots, by stacking a number of QD layers using ultra thin spacers of barrier material [95], leading to an overall increase in the optical confinement factor.

Another important parameter which is influenced by the optical confinement factor is the gain saturation of the active medium, which is defined by [66]:

$$E_{sat} = \frac{\hbar\omega A}{\Gamma dg/dN} \qquad (3.3)$$

with $\hbar\omega$ the photon energy, $A = wd$ the mode cross-section and dg/dN the differential gain. A lower confinement factor would hence increase the saturation energy which would allow maximizing the intracavity power, increasing the ratio of stimulated to amplified spontaneous emission and consequently reducing the phase noise of the lasing modes, a key parameter governing the performance of mode locked lasers. This is also in agreement with reports linking a reduced intensity phase noise with a low confinement factor of the laser active

medium [11]. In addition, higher saturation energies could prevent mode locking destabilizations due to carrier index nonlinearities which take place when the pulse energy is comparable to the saturation energy [19]. Finally, having a low confinement factor by reducing the number of QD layers would in principle increase the medium inversion, as a less number of QDs would need to deliver the same gain, just like in multi quantum well active layers [96].

As a consequence, the optimum value of confinement factor, or equivalently the number of quantum dot layers, is to be found in order to have sufficient modal gain for optimum static laser characteristics and at the same time superior laser dynamics and low noise performance.

The ultimate objective would be to achieve quantum dot based active layers with a high density of quantum dots, a reduced inhomogeneous broadening and the optimum value of overall confinement factor, while at the same time keeping the waveguide thickness sufficiently narrow in order to achieve single transverse mode operation.These considerations will be consequently taken into account when designing the final laser devices.

3.2. QDash structures

Fabrication of QD nanostructures can be achieved by several methods, the process of which is referred to as growth. Several growth techniques exist such as Metal Organic Vapor Phase Epitaxy (MOVPE) or Chemical beam Epitaxy (CBE) from which truly 3D confined dots can be obtained [12], [13]. On the other hand, Molecular Beam Epitaxy growth (MBE) on InP(100) usually results in the formation of elongated dots [9–11], also known as Quantum Dashes (QDash). The devices presented in this thesis consist of InAs QDash structures grown by Gas Source Molecular Beam Epitaxy (GSMBE) on (100) InP substrates at III-V lab. The typical dash height and width are ~2 nm and ~20 nm respectively. Their lengths lie between 40 to 300 nm, depending on growth conditions, while the surface density ranges between 1×10^{10} and 4×10^{10} cm^{-2} [11]. Figure 3-2(a) is an in-plane Transmission Electron Microscopy (TEM) image of one active layer sample.

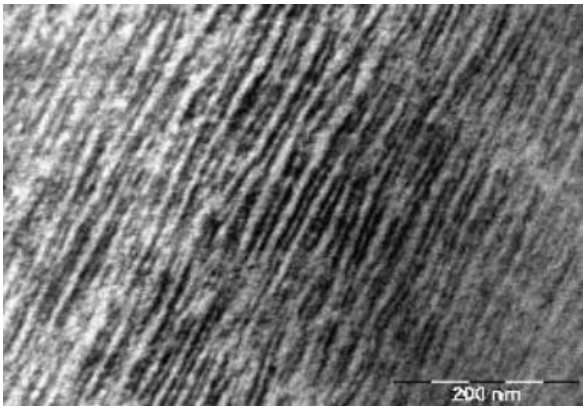

(a)

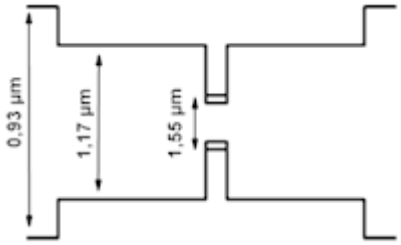

(b)

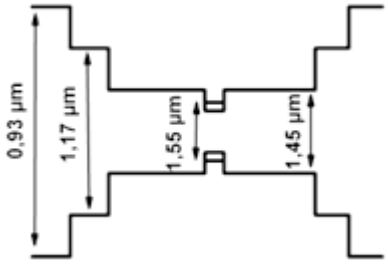

(c)

Figure 3-2. (a) TEM image of the in-plane active layer showing the QDashes or elongated dots. Band diagrams of (b) DBAR and (c) DWELL structures

Two types of structure design were investigated: dashes in a barrier (DBAR) and dashes in a well (DWELL); the schematics of their band diagrams are depicted in Figure 3-2(b) and Figure 3-2(c) respectively. The DBAR structure consists of InAs QDashes enclosed within 40-nm-thick barriers and two 80-nm-thick separate confinement heterostructure (SCH) layers. Both the barriers and the SCH are undoped and lattice-matched quaternary $Ga_{0.2}In_{0.8}As_{0.4}P_{0.6}$ layers (λg = 1.17 µm). In the DWELL structure, the QDashes are additionally embedded within 8-nm-thick QWs obtained from a lattice-matched quaternary material emitting at 1.45 µm. The barrier for the QW is again the quaternary $Ga_{0.2}In_{0.8}As_{0.4}P_{0.6}$ material with λg = 1.17 µm. The details of the complete structure in both cases are presented in Table 3.

Layer	Function	Thickness (nm)
InP	Substrate	
InP	Buffer	1000
InGaAsP 1,17	SCH	80
InGaAsP 1,17	Barrier	40
InAs	QDash	2
InGaAsP 1,17	Barrier	40
InGaAsP 1,17	SCH	80
InP	Top	100
InGaAsP 1,17	Stop-etch	35
InP	Top	30
MOVPE regrowth		
InP	Upper cladding	1500
InGaAs	Contact	300

(a)

Layer	Function	Thickness (nm)
InP	Substrate	
InP	Buffer	1000
InGaAsP 1,17	SCH	80
InGaAsP 1,17	Barrier	20
InGaAsP 1,45	QW	4
InAs	QDash	2
InGaAsP 1,45	QW	4
InGaAsP 1,17	Barrier	20
InGaAsP 1,17	SCH	80
InP	Top	100
InGaAsP 1,17	Stop-etch	35
InP	Top	30
MOVPE regrowth		
InP	Upper Cladding	1500
InGaAs	Contact	300

(b)

Table 3. Schematic description of (a) DBAR and (b) DWELL structures

As already explained in the previous section, a single layer of QD (QDash) structures would not be enough for overcoming the losses in the laser cavity, hence a stack of these layers is necessary. Growth conditions were optimized in order to keep a full width at half maximum (FWHM) of the photoluminescence (PL) spectrum almost constant when the number of stack is increased up to 15 layers, leading to a value of ~ 100 nm at room temperature [97], as illustrated in Figure 3-3(a) for a stack of 6, 9, 12 and 15 layers. This important result represents a key improvement in the efforts of reducing the inhomogeneous broadening due to QDash size and composition variations among the different layers and will allow for the

achievement of good static characteristics of the lasers processed in the next section. Figure 3-3(b) is a TEM image of the structure transversal cut for the case of a 6 layer stack and Figure 3-3(c) reflects the good quality of the resulting grown wafer, in which one can observe the uniformity of the PL intensity along the whole wafer surface.

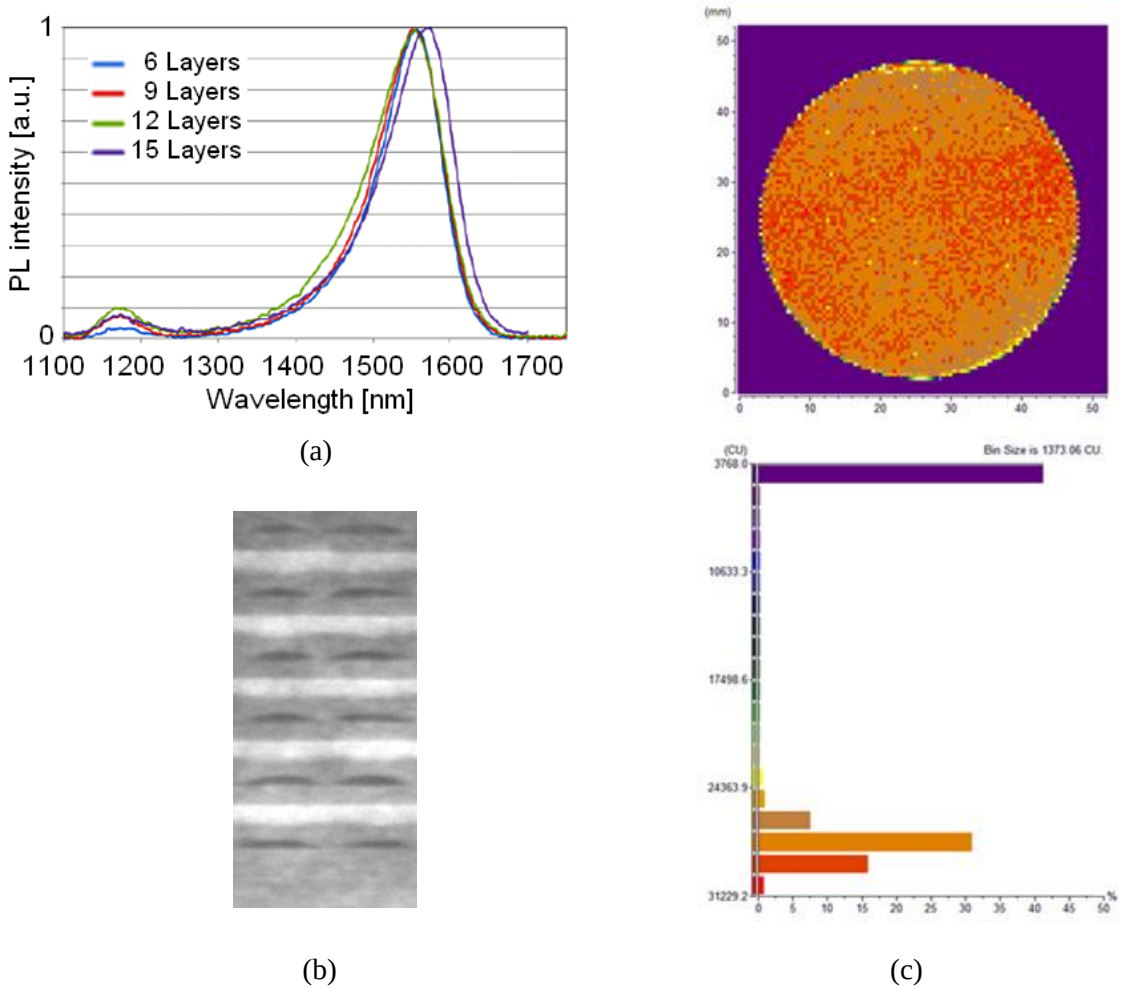

Figure 3-3. (a) Photoluminescence (PL) spectra as a function of number of stacked layers, (b) TEM image of the wafer cut view showing a stack of 6 QDash layers (c) PL intensity over the wafer surface for the wafer with a 6-layer stack.

3.3. Laser fabrication

3.3.1. Broad Area Lasers

The previous grown structures were then processed within the clean room facilities of the LPN for laser fabrication. We have first fabricated broad area (BA) lasers as a first step in

evaluating the quality of the grown active layers as it allows for rapidly determining the modal gain, internal losses as well as important electrical characteristics.

The standard procedure consisted of the following steps:

1. Wafer oxide removal
2. Lithographic pattering of 50 μm ribbons
3. Ti/Au metallization and lift-off
4. Wet etching of p-doped InGaAs ternary by using the Ti/Au ribbons as mask
5. Thinning and back metallization.

BA lasers were subsequently obtained by cleaving different cavity lengths. Measurements of the light-current (L-I) characteristics then allowed for extracting the threshold current density $J_{th} = I_{th} / A$ and the external differential quantum efficiency η_{ext} . The second parameter refers to the amount of photons-out of the laser cavity per electrons-in (input injected current) and hence is proportional to the slope of the L-I curve. The structure modal gain Γg_{th}, the internal losses α_i, and the threshold current density for a nominal infinite cavity length $J_{th_{\inf}}$ were then extracted from the following relations:

$$\ln\left(J_{th}\right) = \frac{L^{-1}}{\Gamma g_{th}} \ln\left(\frac{1}{R_1 R_2}\right) + \frac{\alpha_i}{\Gamma g_{th}} + \ln\left(J_0\right) \qquad (3.4)$$

$$\frac{1}{\eta_{ext}} = \frac{q}{\eta_i \hbar\omega}\left(1 + \frac{2\alpha_i}{\ln\left(\frac{1}{R_1 R_2}\right)} L\right) \qquad (3.5)$$

with J_0 the transparency current density, q the electron charge, $\hbar\omega$ the photon energy, and η_i the internal quantum efficiency.

Figure 3-4 shows the resulting curves from the above measurements for a 9-DBAR structure (with a stack of 9 DBAR layers), in agreement with the expected trends from (3.4) and (3.5).

We have followed the above procedure for the cases of 6, 9 12 and 15 DBAR as well as for 6, 12 and 15 DWELL broad area lasers. Table 4 summarizes the extracted data.

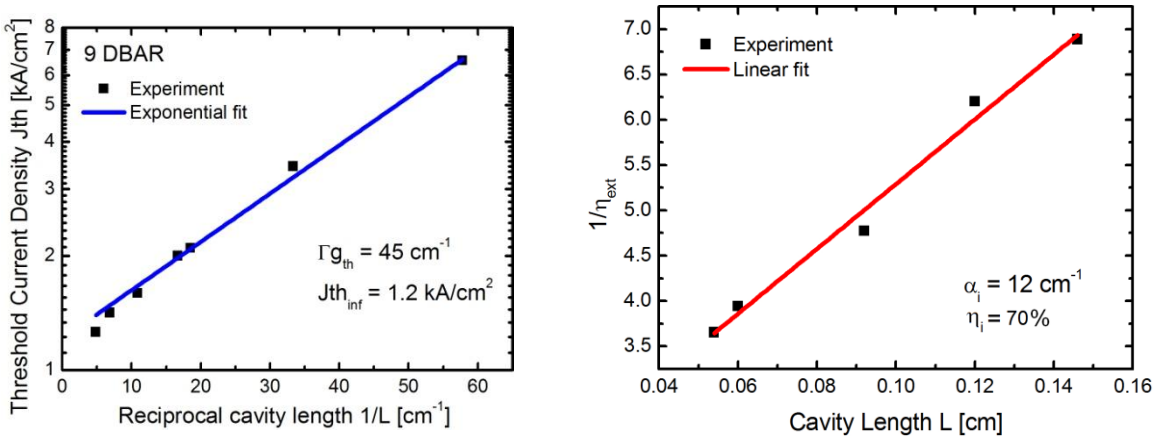

(a) (b)

Figure 3-4. (a) Threshold current density as a function of reciprocal cavity length, (b) inverse differential external quantum efficiency as a function of cavity length for the 9 DBAR BA lasers

N° of layers	Γ[%]	Jth_{inf} [kA/cm^2]	$Γg_{th}$ [cm^{-1}]	$α_i$ [cm^{-1}]
6	0.9	0.92	32.95	10.56
9	1.3	1.22	44.60	11.68
12	1.8	2.01	69.83	17.92
15	2.2	2.09	56.78	18.47

(a)

N° of layers	Γ[%]	Jth_{inf} [kA/cm^2]	$Γg_{th}$ [cm^{-1}]	$α_i$ [cm^{-1}]
6	0.92	0.94	37	11
12	1.68	1.68	48	19
15	2.31	2.31	61	25

(b)

Table 4. Summary of structure parameters for (a) the different DBAR and (b) DWELL designs

Compared to the most recent results of QDash based lasers from other research groups, the overall modal gain and losses were found to be similar to those in, for instance [98]. However, the achieved threshold current densities in our QDash lasers were significantly lower, which has also allowed us to attain lasing in much shorter devices, which is probably due to the superior homogeneity of the self-organized grown structures. From Table 4, it may

seem that the optimum number of layers involves a trade-off between a high modal gain and a small value of internal losses. The later appears to increase faster when increasing the number of stacked layers beyond twelve so that there is no practical interest in continuing stacking from that point. For the DBAR design, the most favourable case seems to correspond to a stack of 9 layers, which also yields a relatively low value of $J_{th_{\inf}}$. After systematic evaluation of the different designs followed by regular interactions with the epitaxial growers at III-V lab, we have decided to adopt the 9-DBAR structure as the reference for the next section and subsequent chapters. Although the DWELL design has also exhibited comparable performances as the DBAR, in terms of static, dynamic and mode locking characteristics, the low reproducibility of the measurements, probably due to inhomogenities during the growing process, made difficult the analysis of the characterization results and for this reason it will no longer be referenced throughout the rest of this work.

3.3.2. Shallow Ridge Lasers

After verification of the good static performance of the structures, we then proceeded to the fabrication of shallow ridge waveguide lasers. Simulations were first carried out in order to determine the waveguide dimensions so as to obtain single transverse mode operation. The maximum allowable width for this was obtained at 2µm for the case of a complete etching of the upper InP layer down to the SCH layer. Figure 3-5 shows one of these simulations using the proprietary software ALCOR developed by France Telecom/CNET, based on the beam propagation method [99], depicting the near field transverse mode profile for the previous design parameters.

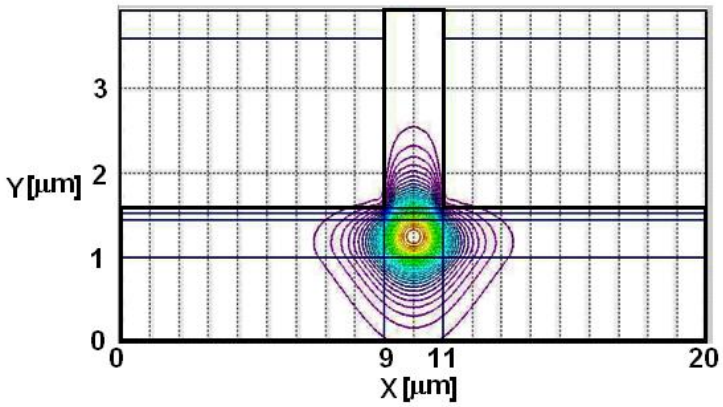

Figure 3-5. Simulation of the near field transverse mode profile for the designed ridge laser

The procedure used for the fabrication included the following steps:

1. Lithographic pattering of 2 μm ribbons.
2. Dry etching (Inductively Coupled Plasma) by using the resin as a mask and then wet etching with a $H_3PO_4/H_2O2/H_2O$ solution of the ternary p doped InGaAs.
3. InP wet etching with HCl for waveguide formation according to the crystallographic plane.
4. BCB coating and annealing for structure planarization.
5. RIE etching of BCB.
6. 80 μm lithographic pattering aligned with the 2 μm ribbon.
7. Ti/Au metallization and electrode elaboration by lift-off.
8. (For two section devices only). Addition of a second section (absorber section) by means of electrical isolation.
9. Thinning.
10. Metallization of the N side.
11. Cleaving.

The final result is a processed wafer with a series of ideally identical parallel ridges separated by 400 μm from which lasers having different cavity lengths can be obtained by simply cleaving. Figure 3-6(a) illustrates the ridge laser fabrication procedure previously described, while Figure 3-6(b) shows a scanning electron microscopy (SEM) image of the completed ridge device.

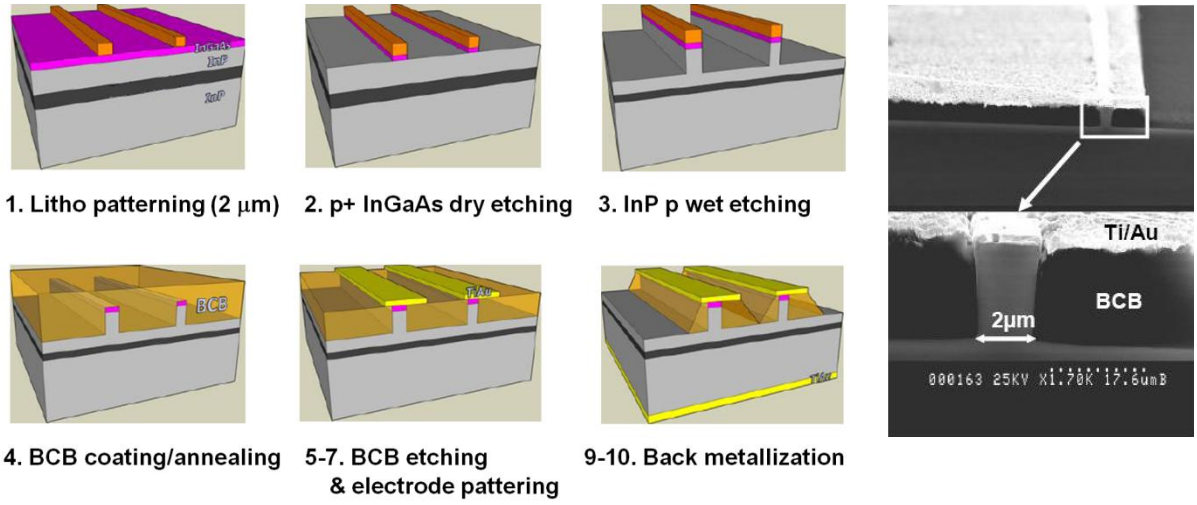

(a) (b)

Figure 3-6. (a) Ridge laser fabrication steps (b) SEM image of the fabricated ridge laser

Figure 3-7(a) shows the representation of a single fabricated ridge laser in both the single and two section configurations. In order to confirm single transverse mode operation, which is essential for high performance mode locking, the far field profile at different bias conditions above threshold was subsequently measured, showing at all times the expected single mode Gaussian profile in both the vertical and horizontal axes as shown in Figure 3-7(b). As a first step in evaluating the ridge laser static characteristics at room temperature, the L-I curves were consequently measured for cavity lengths ranging from ~200 μm (~214 GHz) up to ~2000 μm (~20 GHz). The obtained threshold currents and the maximum output power as a function of cavity length are plotted in Figure 3-8(a) together with their corresponding slope efficiencies in Figure 3-8(b). The V-I characteristics are also shown in Figure 3-8(c) exhibiting the typical 0.7 V knee voltages and from which a series resistance between 2 and 4 Ω is extracted, confirming the good quality electrical characteristics of the finalized ridge devices.

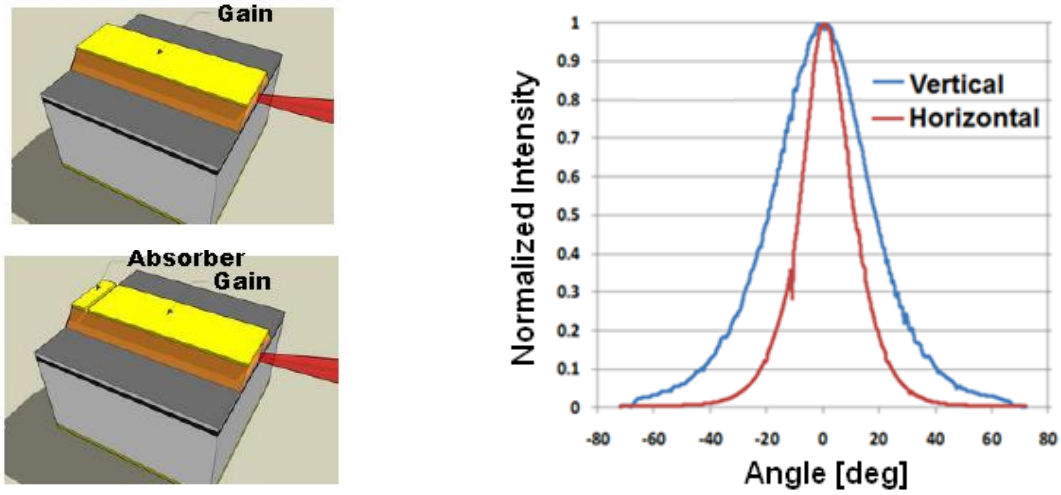

(a) (b)

Figure 3-7. (a) Schematics of the finalized ridge lasers in both the single and two section configurations and (b) far field profile above threshold, based on the 9 DBAR design at 300K

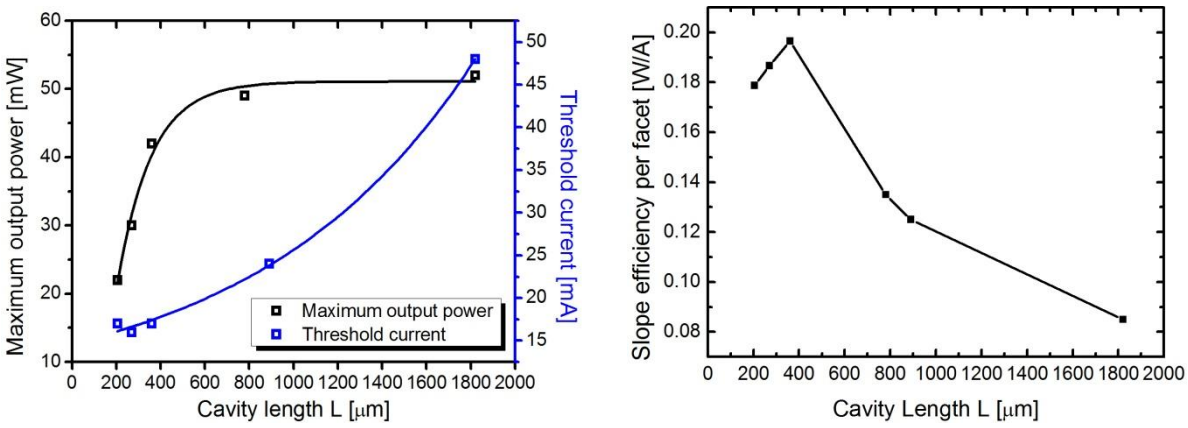

(a) (b)

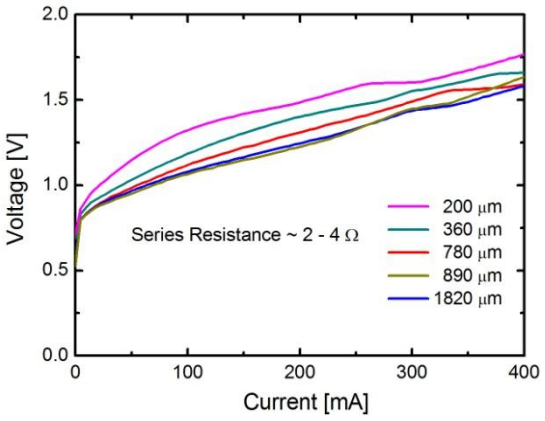

(c)

Figure 3-8. (a) Maximum output power and threshold current, (b) slope efficiencies and (c) corresponding V-I curves for different cavity lengths of the fabricated single section ridge lasers at 300K

3.3.3. Buried Stripe Ridge Lasers

Although fabricated at III-V lab, numerous measurements have in addition been performed on this type of devices, hence a brief description of the fabrication procedure is also provided in this section.

From the initial wafer before MOVPE regrowth, 2 μm ribbons are realized by dry etching by using a SiO_2 mask obtained by optical lithography. A series of these ribbons are then defined and separated by 400 μm. Once etched, the ribbons are subsequently buried by a regrowth of MOVPE followed by formation of Ti/Au electrodes by lift-off. Finally, proton implantation is performed on both sides of the ridge in order to assure lateral electrical confinement. Thinning and back metallization finalize the BRS fabrication. A TEM image of a BRS laser based on the 9-DBAR structure design is shown in Figure 3-9.

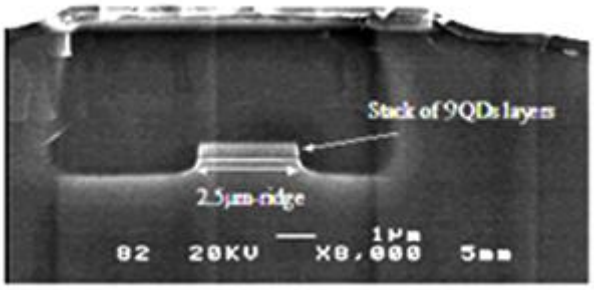

Figure 3-9. TEM image of a BRS laser based on a 9-DBAR structure design

BRS lasers have shown very similar results to the previous ridge lasers in terms of static characteristics. They present the advantage of a robust design and usually exhibit a lower beam divergence, whereas the ridge lasers can present the benefits related to the use of BCB for the planarization which may result in reduced parasitic capacitance enabling higher modulation bandwidths. Both types of fabrication designs will be used interchangeably throughout the rest of this dissertation.

Chapter 4.
Mode locking characteristics of QDash lasers

A thorough characterization of the fabricated devices in Chapter 3 is provided, with a special focus on the ML features that are critical for optimal performance in telecommunication applications, particularly those presented in Chapter 5. The idea is to investigate the intrinsic characteristics of the devices rather than providing measurement results obscured by extrinsic factors, as unfortunately sometimes presented in the literature. Systematic measurements of the ML characteristics presented in Chapter 2 will be described along with a comparison between single-section and two-section QDash MLLs. The underlying physical phenomena responsible for the experimental observations are in most cases explained. The main aspects limiting device performance are identified and practical solutions for some of them are presented. Record peak power (> 1 W) sub-picosecond pulses with kHz RF linewidths for a very large range of operating conditions were consequently obtained.

4.1. Optical Spectrum

The optical spectrum as a function of injection current was systematically investigated. Figure 4-1(a) shows the L-I curve of the 890 μm long single section device used for the characterizations. The envelope full width at half maximum (FWHM) and the peak wavelength of its optical spectrum as a function of injection current are shown in Figure 4-1(b).

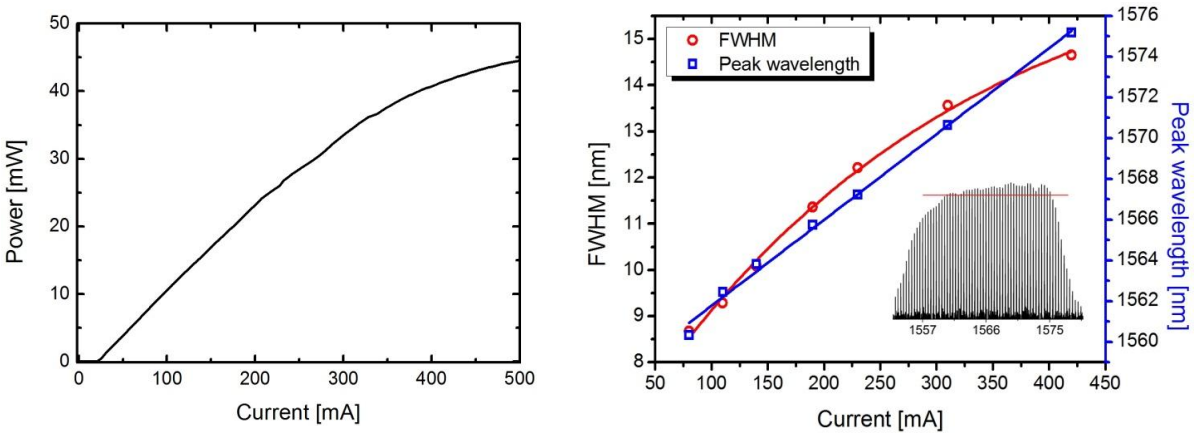

(a) (b)

Figure 4-1. (a) L-I curve of a 890 μm long single section laser, (b) FWHM and peak wavelength of the optical spectrum as a function of injection current. Inset: Optical spectrum at 400 mA

The FHWM increases from a few nanometers at threshold up to a maximum value of ~15 nm at high injection currents, after which it essentially remains constant with increasing current, similarly to the output power saturation effect observed in the L-I curve. The measured spectral broadening is most likely due to band-filling of QDash ensembles. The enlargement of the optical spectrum is also a result of the FWM effect which creates new frequency components owing to an increase in intracavity photon density at higher injection currents, as already discussed in Chapter 2 (cf. Figure 2-13). This fact is supported by the clear asymmetry typically exhibited by the optical spectrum above threshold, as seen e.g. in the inset of Figure 4-1(b), which usually reveals a faster decrease in intensity toward longer wavelengths, as opposed to the shorter wavelength components that are more efficiently created, in agreement with the higher FWM efficiency curve for the positive detuning case as depicted in Figure 2-8, which is a consequence of the nonzero linewidth enhancement factors in these devices [87]. On the other hand, higher injection currents lead to a temperature increase which results in a red shift of the emission spectrum due to the temperature induced band gap shrinkage effect. This red shift translates into a linear increase of the peak wavelength with current at a rate of ~0.04 nm/mA, as also shown in Figure 4-1(b). These are the typical trends observed for any QDash FP laser based on a DBAR design, and take place independently of its cavity length. In fact, it has been observed that the FWHM of the spectrum envelope reaches a maximum value of up to ~14 nm regardless of this parameter. This fact is illustrated in Figure 4-2(a) for five lasers with different cavity lengths processed

from the same wafer. The different spectra were measured near saturation, where their FWHM envelope becomes the widest. There is, nevertheless, an important red shift effect of the emission wavelength when increasing the cavity length, as can be seen in Figure 4-2(b). This effect is most likely due to a dependence of the gain peak wavelength on the total cavity losses, which is in turn dependent on the cavity length, just like in multi quantum well based FP lasers [100]. The fact that the envelope FWHM of the lasing spectrum is preserved means that the maximum attainable number of longitudinal modes under the spectrum envelope increases proportionally when increasing the laser cavity length. This property can be exploited in applications requiring a large number of equally spaced longitudinal modes, such as in optical OFDM, as will be discussed in Chapter 5.

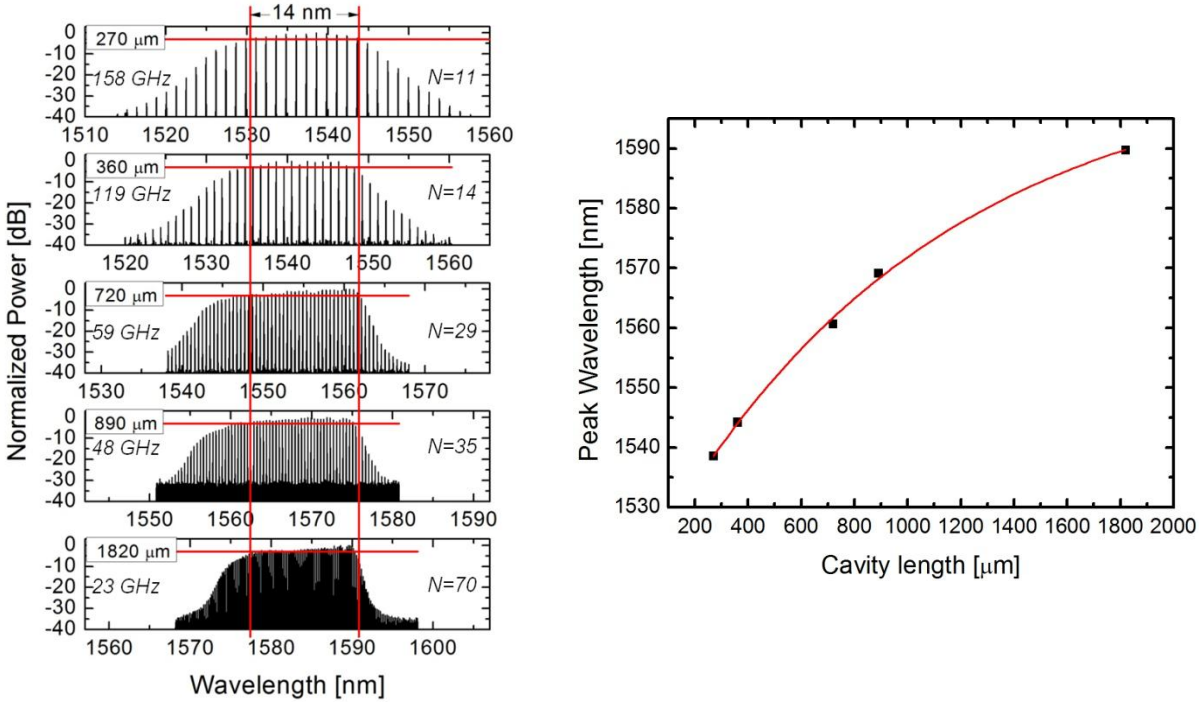

(a) (b)

Figure 4-2. (a) Optical spectrum and corresponding number of lasing modes at saturation for different cavity lengths, (b) Peak wavelength dependence on cavity length

For comparison purposes, a two section device from the same processed wafer and having the same total cavity length (890 μm) as the previous single section laser was investigated. The device now includes a 110 μm length saturable absorber (SA) section. Figure 4-3(a) shows its L-I curve in which one can identify two operating regimes as a function of absorber bias.

Above 0.7 V, where the absorber is transparent, the SA section acts as a gain medium and the device output power characteristic is similar to that of the single section device, being 0.9 V the absorber bias at which the L-I curve best matches that of the single section. Below 0.7 V one can observe the characteristic kinks in the L-I curve of two section passively MLLs. These kinks are the result of the pulses inside the cavity saturating the absorber which reduces the losses, generating higher average output powers for the same injection current. The reason why we worked on a reduced bias range was because outside of it the mode locking characteristics were lost. Figure 4-3(b) and (c) show the corresponding FWHM spectrum and the peak wavelength as a function of absorber bias for different injection currents, respectively. Above 0.7 V, both the FWHM and the peak wavelength increase with current just like in a single section device, as expected. Below 0.7 V, the FWHM and the peak wavelength now depend on the interplay between the gain and the SA dynamics. In general, the maximum attainable FWHM value is approximately 14 nm as for the single section devices, indicating that this parameter depends on the intrinsic material gain spectrum and its broadening effects (homogeneous and inhomogeneous) rather than the particular ML mechanism (single section or two section). In general, we have found that the maximum spectral FWHM in the QDash MLLs, both in its single and two section configurations, was larger than those reported for QD [12], [16], [20] or QW based devices [17], [18] on InP substrates, and it was also generally the case when compared to QDs MLLs based on the InAs/GaAs material system.

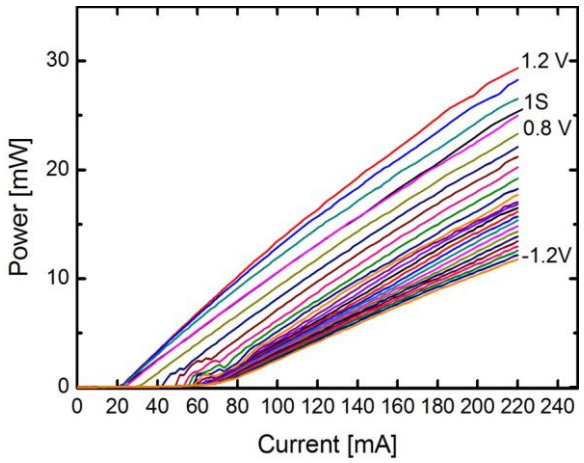

(a)

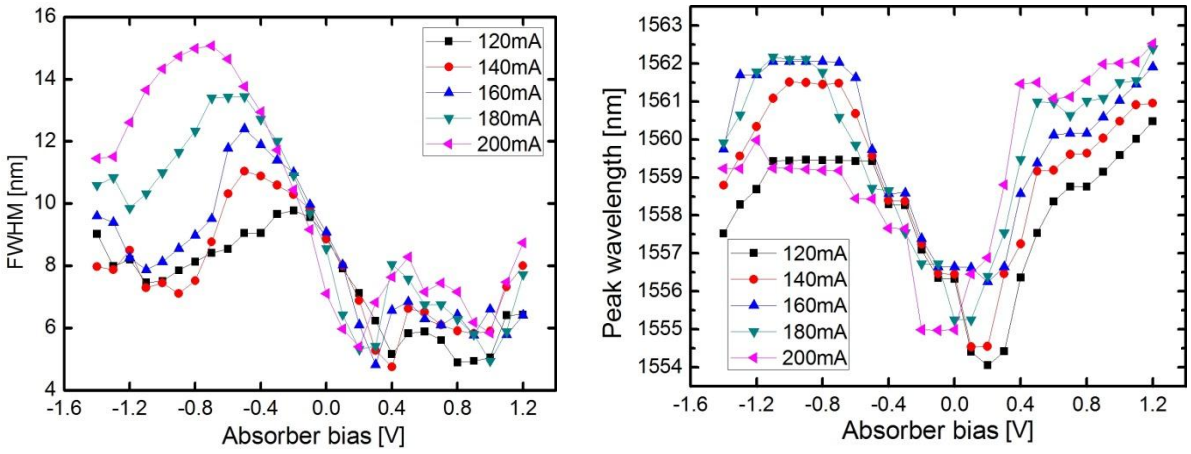

(b) (c)

Figure 4-3. (a) L-I curve of a 890 μm two section device (SA length=110 μm) and its (b) FWHM, (c) peak wavelength as a function of bias conditions

4.2. Optical phase noise and optical linewidth

Optical phase noise refers to instantaneous random fluctuations of a given laser emission or lasing mode (cf. Chapter 2). The sources of phase noise can be intrinsic or extrinsic. The intrinsic sources are related to quantum noise due to spontaneous emission. The extrinsic sources include current source noise, temperature fluctuations, vibrations and external feedback reflections into the laser cavity. In this thesis, the effect of these sources have been minimized as the lasers were mounted on temperature controlled heat sinks and were at all times operated with ultralow noise current and voltage sources on relatively stable optical tables. Feedback reflections from the near end coupling fiber have however proven to obscure the laser noise properties. This problem has been minimized throughout most characterizations by intentionally uncoupling and misaligning the emitted light into the fiber, yet the effects were still occasionally noticeable. This major source of phase noise has been investigated in detail and is described in section 4.7. In this section, and unless otherwise stated, we will nevertheless assume that the extrinsic noise was negligible compared to the intrinsic ones during the measuring time period.

If only the intrinsic noise is considered, then the phase noise will diffuse through a random walk process. This is indeed the case for the phases of the different lasing modes in a semiconductor passively mode locked laser which are, in addition, synchronized to each other

owing to the specific locking mechanism. This is a known fact for standard passively mode locked two section devices, as the saturable absorber continuously locks the mode phases together. However, for the single section case, this condition has not yet been reported. In order to verify this, the single section device of cavity length 1820 μm has been used. If the lasing modes under the FWHM envelope of its optical spectrum in Figure 4-2(a) are numbered from 1 to 74, then the temporal trace of the phases corresponding to consecutive modes 15-17 can be measured by using a setup like in Figure 4-4. The idea is to mix an ultra low noise external cavity laser (local oscillator- LO) with the lasing modes under investigation and simultaneously recording the corresponding beat signals as measured by a real time scope scope (RTS). The down-converted RF spectrum of the total acquired signal is shown in Figure 4-5, which has been previously mixed in the electrical domain with a 30 GHz local oscillator for down-conversion in order for the beat signals to be under the RT scope bandwidth (10 GHz). For instance, the QDash laser has a repetition frequency of 23 GHz, therefore it will appear at a down-converted frequency at approximately 7 GHz .

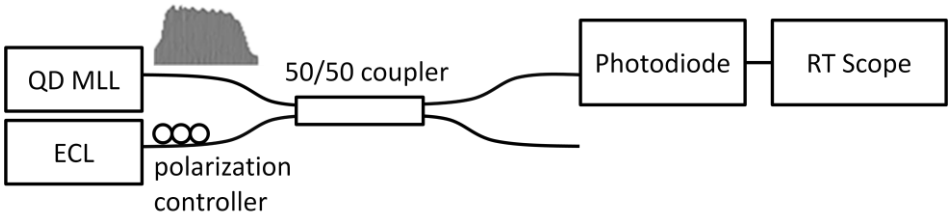

Figure 4-4. Experimental setup for instantaneous phase characterization

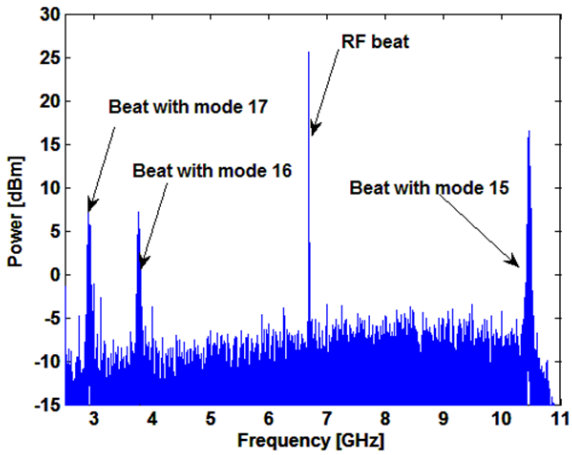

Figure 4-5. Downconverted RF spectrum of beating signals of a 1820 μm single section laser with a LO

The recovered phases are shown in Figure 4-6. The total acquisition time was ~ 3.5 μs, throughout which the instantaneous phases under study are clearly locked and undergo a random-walk like behaviour, as expected. How well all of these spectral phases are synchronized together represents one of the most important characteristics of a mode locked laser. It will be shown that the degree of synchronization, which is quantified by the RF linewidth, is dependent on the individual phase fluctuations themselves, i.e., the individual optical mode linewidths, as will be described in the following sections.

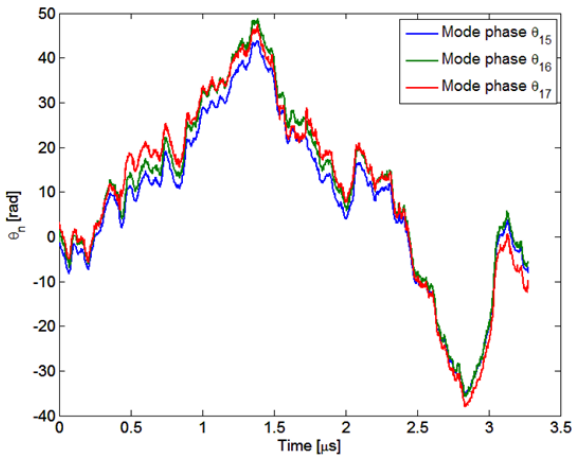

Figure 4-6. Recovered instantaneous phases θ(t) of modes 15-17 from a 1820 μm single section laser

The phase fluctuations will translate into a Lorentzian shape of the corresponding lasing mode. For the simplest case of a single mode laser such as a DFB, the linewidth of this Lorentzian is given by the well known Schawlow-Tones (S-T) formula, which only considers phase noise due to intracavity spontaneous emission. However, in a semiconductor laser, a spontaneous emission event will cause a gain change that will translate into an additional phase change owing to the linewidth enhancement factor α_H [67] which results in a modified S-T formula, a simplified version of which can be written as [90]:

$$\Delta\omega = \frac{\beta R_{sp}}{4\pi S}\left(1+\alpha_H{}^2\right) \qquad (4.1)$$

where R_{sp} is the total spontaneous emission rate , β the fraction of spontaneous emission coupled into the lasing mode, S the photon density in the lasing mode and α_H the linewidth

enhancement factor. Therefore, the S-T linewidth will typically exhibit a decrease when increasing the intracavity power. In multimode semiconductor lasers, however, the complex nonlinear mode interactions can lead to strong excess noise which can invalidate the S-T formula and the typical power dependent characteristic of the linewidth is no longer observed [101]. The S-T formula may still in some cases provide an estimate of the central mode linewidth, whereas the linewidth of the side modes will be affected and increased by timing jitter as will be seen in section 4.4. The linewidth of the optical modes has been measured by using the standard self-heterodyne technique [52] as illustrated in Figure 4-7. A given longitudinal mode is individually filtered and split into two paths. The mode frequency in one path is offset using an acousto-optic modulator. On the second path, 3 km of standard single mode fiber (SMF) is inserted to introduce a delay exceeding the coherence time of the mode light so that the combining beams interfere as if they were independent. The self beating spectrum at the ESA is then recorded for analysis.

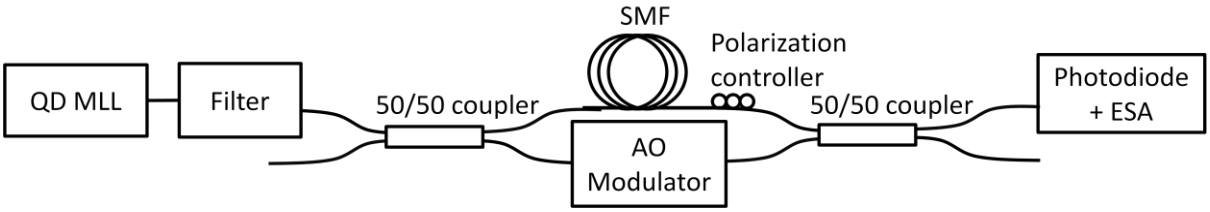

Figure 4-7. Self-heterodyne set-up for optical linewidth measurements

We first focus our attention on the 48 GHz single section device. Figure 4-8(a) shows a typical self-beating spectrum of one of the central lasing modes showing the expected Lorentzian shape, in agreement with the random walk nature of the phase noise. The spectrum is centered at the frequency shift of 160 MHz provided by the AO modulator. The measured mode linewidth (for the same mode) as a function of injection current is shown together with the device L-I curve in Figure 4-8(b).

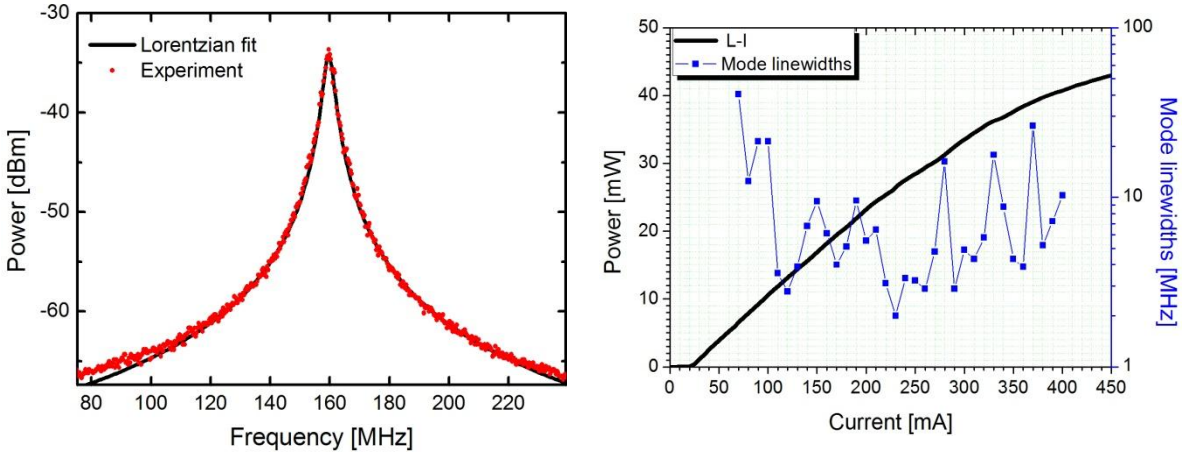

(a) (b)

Figure 4-8. Linewidth measurements of a 890 μm single section device. (a) Self-beating spectrum of an optical mode, (b) optical linewidth as a function of injection current

We can almost observe a linewidth decrease with injection current right above threshold (30 mA) up to about four times this value. This roughly agrees with the S-T trend of decreasing linewidth with increasing photon density (which is proportional to optical output power). At higher injection currents, however, the linewidth does not follow a clear tendency, exhibiting jumps at specific injection currents. It seems that the linewidth of the mode now incorporates a contribution which is power independent, i.e., the linewidth would not decrease even at very high intracavity photon densities. It was observed that this irregular dependence of linewidth on injection current is enhanced when the number of lasing modes increases, suggesting the idea of linewidth contributions due to multimode interaction. It was however later recognized and understood (cf. section 4.7) that these sudden linewidth increases with current were merely due to instabilities owing to short feedback reflections which are dependent on the coupling distance at a sub-micron scale. An increase in current would translate into a slight expansion of the laser cavity length due to temperature variations. Interestingly, it will be seen that the linewidth dependence on current was very much correlated to the corresponding RF linewidth at all times, meaning that a laser exhibiting narrow optical linewidths may as well exhibit narrow RF spectra.

Linewidth measurements throughout the whole spectrum have also been performed at a given injection current. Figure 4-9(a) shows the self-beating spectra of the lasing modes for the 890 μm laser when biased at 150 mA. Clearly, the modes have different linewidths depending on

their position in the optical spectrum. The evolution of linewidth as a function of optical frequency is shown in Figure 4-9(b) (bottom) corresponding to the optical spectrum on top. The solid line is a parabolic fit and it will be shown that this effect is induced by timing jitter.

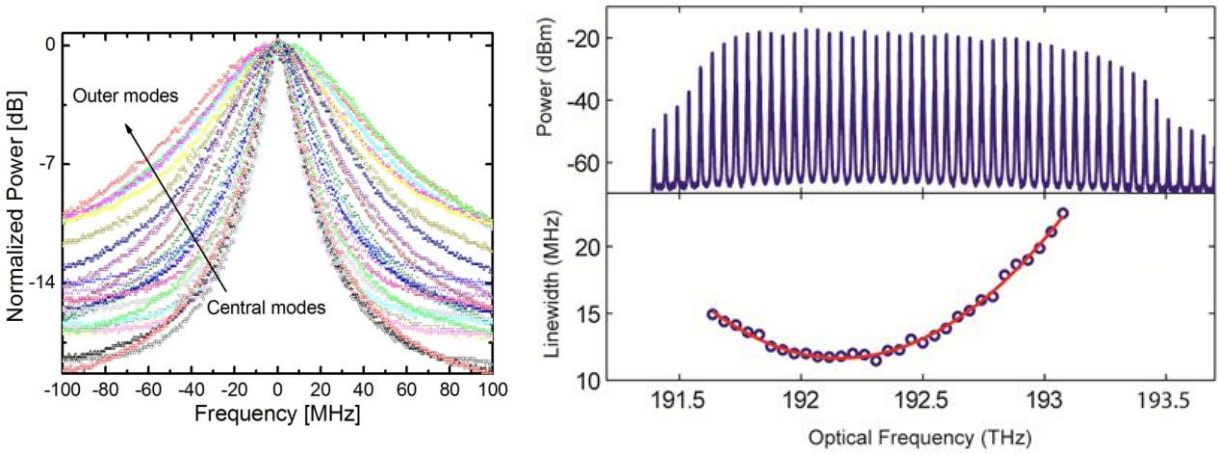

(a) (b)

Figure 4-9. Self beating spectra of a 890 μm single section device biased at 150 mA, (b) top: optical spectrum, (c) bottom: optical linewidth evolution with frequency

For comparison purposes, the two section device described previously having 890 μm of total length including a 110 μm length SA section has also been characterized. By looking at the L-I curve in Figure 4-3, one can readily see the effect of the absorber section on the output power as compared to the single section device. One hence might expect, according to the S-T formula, an increase in the optical phase noise due to a decrease in the intracavity photon density. Figure 4-10(a) shows the measured mode linewidths of a central mode as a function of absorber bias for three different injection currents. When the SA section is biased above transparency at ~ 0.7 V, the device operates as a single section device and exhibits mode linewidths of ~50 MHz, about three times wider than in the single section case in agreement with the S-T formula for a corresponding three times decrease in intracavity photon density. There is however a drastic increase in the mode linewidth when further increasing the reverse SA voltage. Figure 4-10(b) shows the normalized spectrum measured at 120 mA for illustrating this point. This severe linewidth increase cannot be completely explained by the simple S-T linewidth formula and still lacks a clear explanation. This is however in qualitative agreement with the linewidth of two section QD passively mode locked lasers based on InAs/GaAs. Several hundred MHz linewidths (up to ~ 1 GHz) have already been

reported for these type of devices [102], hence the measured ~ GHz linewidths in the two section devices may seem reasonable considering that InAs/GaAs based structures usually exhibit lower values of internal losses compared to those in the InAs/InP material system.

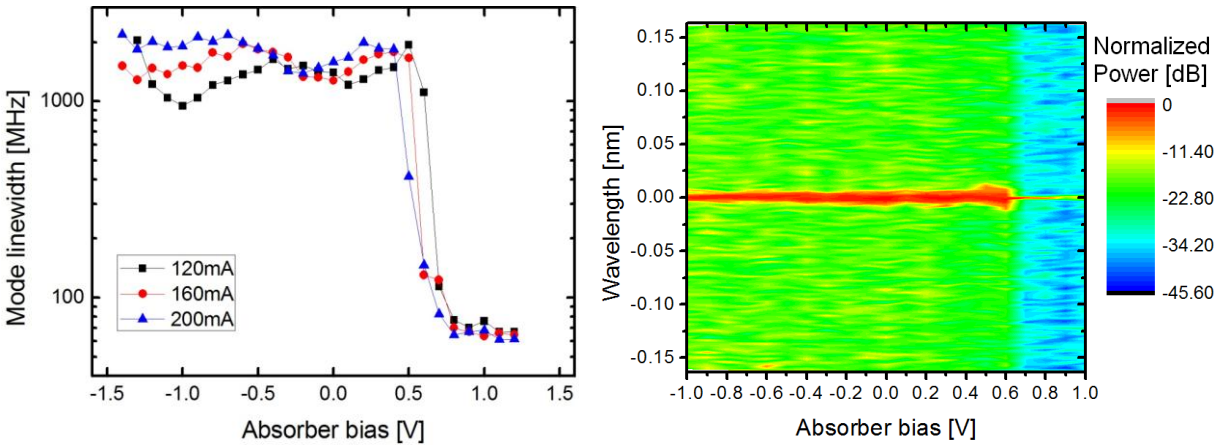

(a) (b)

Figure 4-10. Mode linewidth of the 890 μm two section device as a function of bias conditions. (b) Normalized spectrum of a central mode measured with a 5 MHz resolution OSA at 120 mA

4.3. Intensity phase noise and RF linewidth

The intensity phase noise refers to the instantaneous phase fluctuations of the laser intensity and it can be quantified by the linewidth of the first harmonic of the RF spectrum (RF linewidth) or equivalently, the linewidth of the beat signal between adjacent modes. Having its origin in the spontaneous emission noise (neglecting extrinsic noise sources), the instantaneous intensity phase noise also diffuses via a random walk process and consequently the laser intensity spectrum will also exhibit the typical Lorentzian shape just like each of the optical modes.

Let us first consider the experiment described in Figure 4-4 and Figure 4-5 used for extracting the phase noise of three consecutive modes of the 1820 μm length single section device. From the recorded data, it is also possible to extract the phase noise of the RF beat, i.e. the intensity phase noise, by simply filtering the spectrum at ~ 7 GHz. Figure 4-11 shows the extracted phase corresponding to the same interval of time as in Figure 4-5. One can readily notice the resemblance of this temporal trace with the previously extracted phases of modes 15-17. This remarkable fact suggests that the optical phase noise is actually correlated

in time to the intensity phase noise, so they are not statistically independent as commonly assumed in the literature [103–105].

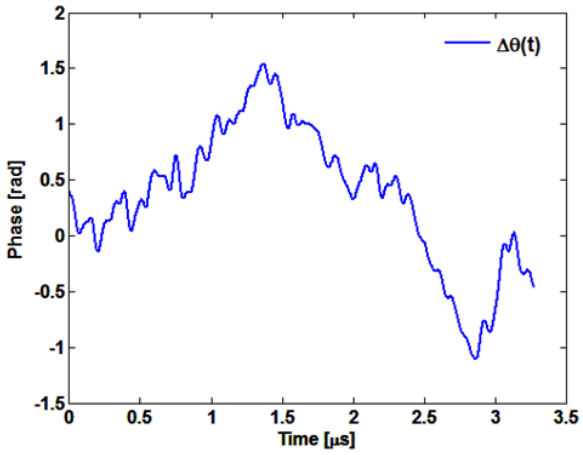

Figure 4-11. Recovered instantaneous intensity phase noise Δθ(t) from a 1820 μm single section laser

Systematic RF linewidth measurements as a function of injection current were then carried out for the 890 μm single section laser. Figure 4-12(a) is a plot of the expected Lorentzian spectrum at 250 mA showing a RF linewidth of ~ 15 kHz. Figure 4-12(b) shows the measured RF linewidths evolution with injection current together with the previously measured optical linewidths.

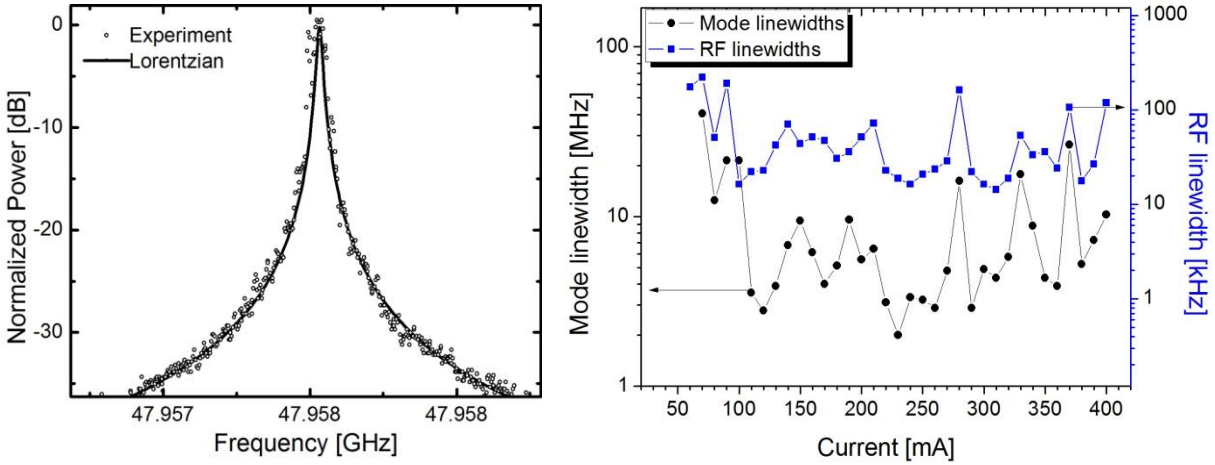

(a) (b)

Figure 4-12. (a) RF spectrum for the 890 μm device at 250 mA. (b) RF and optical linewidth vs. injection current

There is clearly a correlation between the optical mode and the RF linewidths. One can see that the enhancement in mode linewidth at specific injection currents translates into an increase in the corresponding RF linewidth. This is in fact a direct consequence of the phase noise and the intensity phase noise correlation already described. Interestingly, the ratio of the optical and the RF linewidths remains almost constant at about two orders of magnitude for all injection currents, meaning that even when the phase noise is enhanced, the phases are still synchronized so that the modes are still locked together, i.e., the laser is at all times mode locked. It should be noted, once again, that it was later understood that the sudden linewidth increases were due to instabilities owing to short feedback reflections which are dependent on the coupling distance at a sub-micron scale, as will be explained in section 4.7.

The minimum RF linewidth for this device was about 15 kHz at ~320 mA. In general, the RF linewidth was observed to be mostly independent on cavity length attaining minimum values in the order of 10 kHz even in simply as-cleaved devices devoid of any HR coatings or more complex waveguide designs. The fact that we did not observe any RF linewidth improvement with longer cavity lengths, which may have been expected due to an increase in the cavity quality factor, can be explained by arguing that the gain and loss per pass which is added to the field intensity remains the same, therefore the ratio is identical for all cavity lengths.

Besides the RF linewidth, the repetition frequency of the RF intensity also represents an important parameter among the ML characteristics. This is given by the RF frequency peak of the Lorentzian line. Generally, it would be very useful to have a narrow RF linewidth together with a fine tunability (tens to hundreds of MHz) of the repetition frequency in order to achieve the precise value required for the specific application. Figure 4-13 shows the repetition frequency of the same 890 μm device at several injection currents in order to show the general trend. Throughout the whole ML range, there appears to be an overall increase in repetition frequency with current. This frequency shift is due to material dispersion, i.e., the effective index in the propagating semiconductor medium decreases when increasing wavelength. From Figure 4-1, there is a 15 nm red shift of the optical spectrum. If we consider, for instance, propagation through the InP layers, this shift results in a change of effective refractive index of ~ 0.0015 [91], [106] when increasing the injection current from 50 mA to 400 mA. This index change can be calculated to yield a ~ 20 MHz of change in repetition frequency, which very well agrees with the curve in Figure 4-13. One hence may

only expect a few 10s of MHz of tunability for the simple FP configuration. Including a DBR section may allow to achieve an increased control of the repetition frequency owing to a more important variation in the effective cavity length which is introduced when varying the applied bias in the grating section.

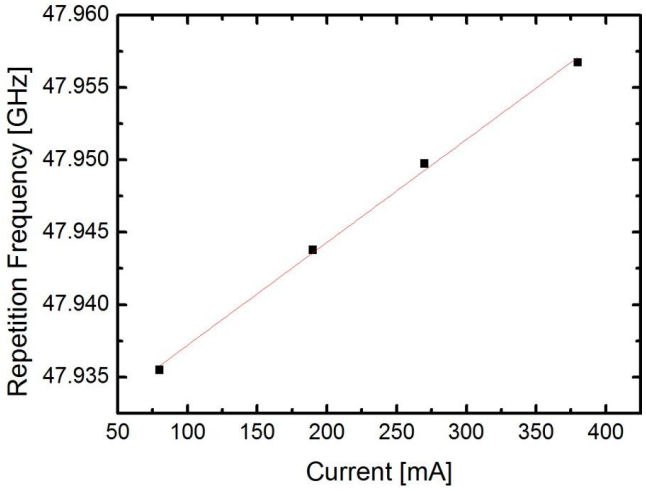

Figure 4-13. Repetition Frequency of the 890 μm device as a function of injection current

The RF spectrum of two section devices has also been investigated. The device under study is the same one used for the previous characterizations, also having a nominal repetition frequency of ~48 GHz. Figure 4-14(a) shows the measured RF linewidths as a function of absorber bias at different injection currents in the gain section. When the SA is forward bias above transparency, the device exhibits typical RF linewidths in the range of 10s of kHz, as in a single section device. There is an abrupt increase in linewidth right below 0.7 V in all curves. This is in perfect correlation with Figure 4-10(a) which now also confirms the connection of the modal phase noise to the intensity phase noise in the two section devices. Figure 4-14(b) is a mapping of the normalized RF spectrum at 120 mA which better illustrates this effect and which can be compared to Figure 4-10(b). If the SA reverse bias is further decreased, the RF linewidth starts decreasing up to an optimum value where the effects of gain and absorption balance each other for optimum mode locking. Regardless of the drastic phase noise increase in the two section devices, they can exhibit narrow RF linewidths of about 5 orders of magnitude lower with respect to their respective optical linewidths, implying a very efficient mode locking mechanism. Finally, it should be pointed

out that given the lower output powers emitted by the two section devices compared to the single section ones, the feedback level and its effects are very much reduced which is reflected by the absence of linewidth jumps as a function of bias conditions.

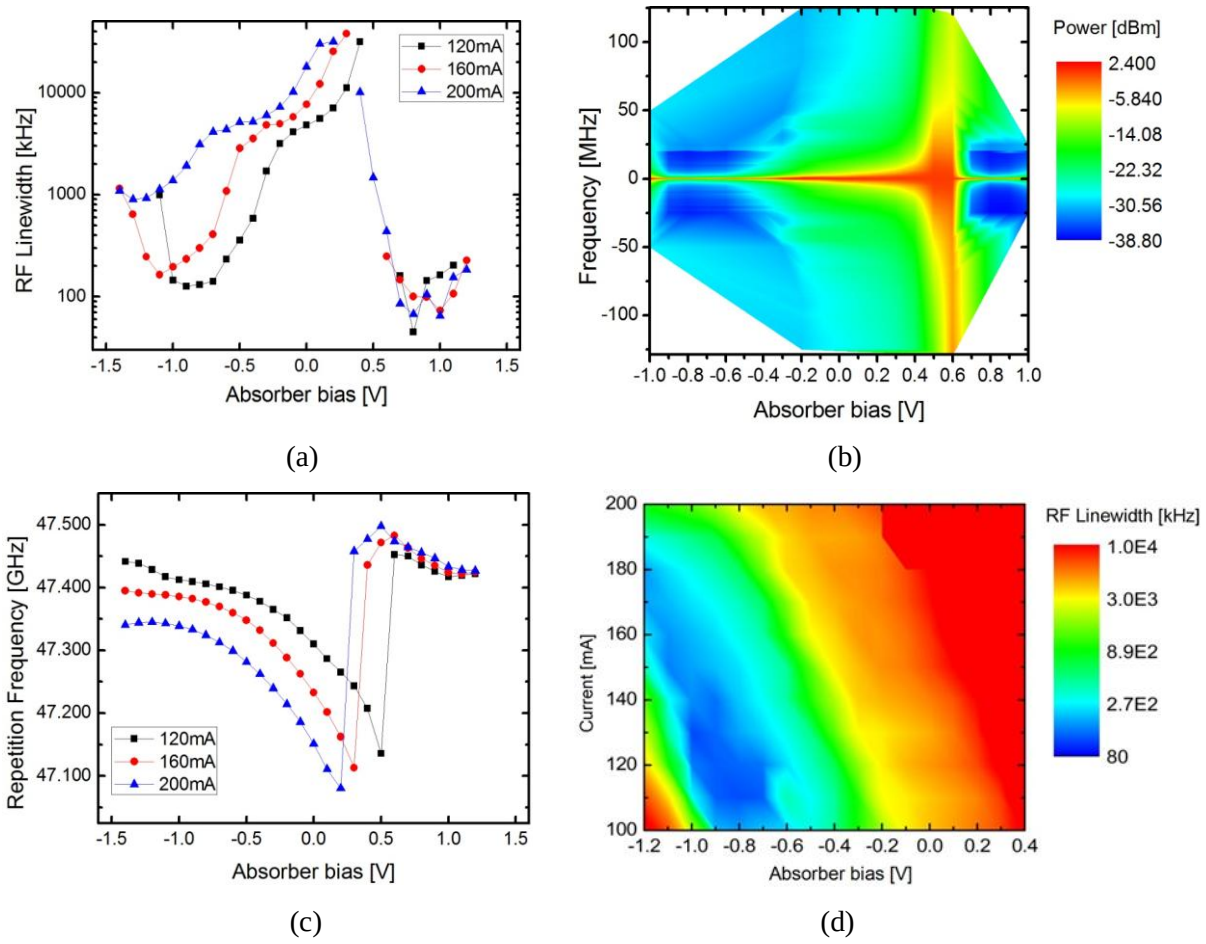

Figure 4-14. RF linewidth of the 890 μm two section device as a function of bias conditions at 120, 160 and 200 mA. (b) Normalized RF spectrum at 120 mA. (c) corresponding repetition frequency (d) RF linewidth mapping

Figure 4-14(c) shows measured repetition frequencies for this device. Once again, two distinct behaviours are observed, one corresponding to the equivalent single section device and another one corresponding to the saturable absorption regime. One can slightly distinugish a repetition frequency increase with current for a fixed absorber bias above transparency, just like in the single section devices. In the SA regime, the tunability is enhanced to about 300 MHz, one order of magnitude greater in comparison to the single section case. In this regime, the repetition frequency is now the result of an interplay between

dispersion and pulse shaping effects [107]. It should be noted, however, that even if the tunability is enhanced, the RF linewidth is not always narrow througout the whole current range. Finally, Figure 4-14(d) is a mapping of the RF linewidth as a function of bias conditions in the SA regime.

The narrow ~ kHz RF linewidths exhibited by QDash single section lasers is one of the main assets making these type of devices attractive when compared to their QW counterparts, which typically exhibit minimum RF linewidths of ~ 100s kHz or bulk based ones with ~MHz linewidths as pointed out in [11]. This fact still lacks a clear theoretical explanation and it is sometimes attributed to the lower confinement factor of QDash active layers [11]. From the experimental results described in this section, one can now conclude that a low phase noise of the optical modes translates into a low phase noise of the laser intensity, i.e., a narrow RF linewidth. Indeed, the typical optical linewidths of FP lasers based on QW structures are of 10s of MHz [22], while for the bulk type is of 100s of MHz. This trend is in qualitative agreement to the corresponding RF linewidths in the different types of devices. Moreover, in all three cases, the ratio of the optical to the RF linewidth is of the same order of magnitude, meaning that, in principle, all these structures exhibit phase correlation or, equivalently, some form of mode locking regime. If FWM was the main responsible for this intermodal coherence, which should be regarded as the ratio of the optical to the RF linewidth and not by the RF linewidth itself, then the FWM efficiency parameter would have to be similar independently of the device structure, which has in fact been confirmed in [108] for the cases of QDash and bulk based SOAs. The parameter making the difference would not be a stronger FWM efficiency but rather a lower optical linewidth of the QD/Dash devices. One of the reasons leading to this characteristic might be related to a higher population inversion factor of the ground state in QDash/Dots (provided a narrow inhomogeneous broadening is achieved). Indeed, the spontaneous emission rate reduces when increasing the inversion of the gain medium so that operating the laser far above threshold my lead to a higher ratio of stimulated to spontaneous emission, therefore reducing the noise characteristics. The second aspect that may as well be responsible for the improved RF linewidths in QDash/Dot devices may be related to the lower confinement factor, also leading to a higher inversion of the gain medium. A typical value for a multi quantum dash layer (6 to 12 layers) device is about 1% whereas in a typical multi QW is about 10% and up to 70% for

bulk, which roughly correlates to the increase in the corresponding optical linewidths in each type of laser. Additionally, the reduced confinement factor may also result in a lower amount of coupled spontaneous emission into the lasing mode as reported in [22], consequently reducing the intensity phase noise.

4.4. RF and optical linewidth relationship: an alternative approach for timing jitter characterization of high repetition rate MLLs

So far we have seen that there exists a strong correlation of the instantaneous phase of the optical modes and that of the laser intensity. In this section, we present a general formalism establishing analytical relations between the optical linewidth, the RF linewidth and the timing jitter, the latter being an important parameter in most photonics applications, including optical communications, optical sampling, microwave photonics, etc. Being directly related to the RF linewidth [109], characterization of timing jitter is commonly performed by means of an electrical spectrum analyzer (ESA) after photodetection of the laser pulse train as described in [55]. This method is however restricted to relatively low repetition frequencies due to the limited bandwidth of currently available photodiodes. Besides, the model in [55] relies on the assumption of stationary timing fluctuations which is not the case in passively MLLs [56], where the timing jitter exhibits a diffusion-like behaviour characterized by a diffusion constant. Timing jitter can also be measured by the cross correlation technique presented in [57], however the high power levels required by the second harmonic generation nonlinear crystal limit its applicability.

It is known that timing jitter and the RF linewidth are closely related to the phase noise of the optical modes under different types of ML regimes [50], [104], [105], [110–113]. In [103], an expression relating the optical mode linewidths to the linewidth of the RF spectrum was in particular obtained by using soliton perturbation theory, which is justified when the steady state pulse is closed to a soliton. This relation was later shown in [104] to be in agreement with experimental investigations on a two-section semiconductor passively MLL emitting at 1.3 μm, suggesting the possibility of timing jitter extraction from measurements of the laser modal linewidths, circumventing the limitations of the characterization methods previously described. A theoretical asymptotic analysis in [110] reveals scaling laws for the optical

linewidth as a function of mode number, depending on specific laser dynamics, also demonstrating the timing jitter to optical linewidth relation. In this section, a simple general formalism is proposed yielding an explicit expression relating the timing jitter diffusion constant to the modal linewidths of semiconductor lasers exhibiting the passively ML regime. We have seen that for the particular case of single section devices, no cavity losses are introduced by a saturable absorber and thanks to the high modal gain available in QDash based active layers, the cavity length in these lasers can be made short enough to achieve high repetition rates with reported values of up to 346 GHz [114]. This calls for a means to estimate the timing jitter which does not require pulse train direct photodetection. This is the case of the method here presented [115], [116] which readily becomes an attractive alternative.

Considering only the effects of phase fluctuations induced by quantum noise, the complex electric field in a semiconductor passively MLL can be written as (cf. Chapter 2):

$$E(t)=\left[\sum_{n=1}^{N}E_n e^{j\left[\omega_n t+\theta_n(t)+\phi_n\right]}\right]+c.c \qquad (4.2)$$

where E_n, ω_n, $\theta_n(t)$ and ϕ_n are respectively the real amplitude, angular frequency, phase noise and static phase, of each of the N longitudinal modes. Amplitude noise has been neglected since phase noise dominates close to ω_n [105]. Under ML regime, equation 2.5 holds, and the instantaneous modal phase relation can be written as:

$$\theta_n(t)=\theta_c(t)+(n-n_c)\Delta\theta(t) \qquad (4.3)$$

for $n=1$ to N, and with n_c a given mode number with corresponding phase noise $\theta_c(t)$. The complex electric field then becomes:

$$E(t)=\left[\sum_{n=1}^{N}E_n e^{j\left[\omega_n t+\theta_c(t)+(n-n_c)\Delta\theta(t)+\phi_n\right]}\right]+c.c \qquad (4.4)$$

and the laser intensity:

$$I(t) \propto \left|E(t)\right|^2 = \sum_{m=1}^{N-1}\sum_{l=1}^{N-m} 2E_{m+l}E_l \cos\left[m\omega_r t + m\Delta\theta(t) + \left(\phi_{m+l} - \phi_l\right)\right] + \sum_{m=1}^{N} E_m^2$$

$$= \sum_{m=1}^{N-1}\sum_{l=1}^{N-m} 2E_{m+l}E_l \cos\left[m\omega_r\left(t + \Delta t_r(t)\right) + \left(\phi_{m+l} - \phi_l\right)\right] + \sum_{m=1}^{N} E_m^2 \qquad (4.5)$$

with $\Delta t_r(t) = \Delta\theta(t)/\omega_r$ being the timing fluctuations in the pulse position, commonly referred to as timing jitter. It has been experimentally shown in two section QW [57] and single section QDash passively MLLs [117] through cross correlation measurements, that the variance of $\Delta t_r(t)$ grows linearly with time, which implies that timing jitter undergoes a random walk. By the central limit theorem, $\Delta t_r(t)$ is normally distributed at large t, therefore it can be described by a Gaussian random walk with zero mean and variance $\left\langle\left|\Delta t_r(t+T_0) - \Delta t_r(T_0)\right|^2\right\rangle = D|t|$, with D a diffusion coefficient. Substituting $\Delta\theta(t) = \omega_r \Delta t_r(t)$ in (4.4) yields:

$$E(t) = \left[\sum_{n=1}^{N} E_n e^{j\left[\omega_n t + \theta_c(t) + \omega_r(n-n_c)\Delta t_r(t) + \phi_n\right]}\right] + c.c \qquad (4.6)$$

The phase fluctuations in each mode, and therefore $\theta_c(t)$, are affected by amplified spontaneous emission noise and hence undergo a random walk process [50], which again for large t will be normally distributed. From(4.6), the optical spectrum $\left|E(\omega)\right|^2$ can be calculated by taking the electric field autocorrelation function $R(\tau)$ and Fourier transforming the result:

$$\left|E(\omega)\right|^2 = \int_{-\infty}^{\infty} R(\tau)e^{-j\omega\tau}d\tau = \int_{-\infty}^{\infty}\sum_{n=1}^{N} {E_n}^2 e^{j\omega_n\tau} e^{-\frac{1}{2}\left[\left\langle|\theta_c(\tau)|^2\right\rangle + \left\langle|\omega_r(n-n_c)\Delta t_r(\tau)|^2\right\rangle + 2\omega_r(n-n_c)\left\langle\theta_c(\tau)\Delta t_r(\tau)\right\rangle\right]} e^{-j\omega\tau}d\tau$$

$$\propto \sum_{n=1}^{N}\left\{\left[\frac{1}{2}\Delta\omega_{\theta_c} + \frac{1}{2}{\omega_r}^2(n-n_c)^2 D + \omega_r(n-n_c)\gamma_{\theta_c,\Delta t_r}\right]^2 + \left(\omega-\omega_n\right)^2\right\}^{-1} \qquad (4.7)$$

with $\gamma_{\theta_c,\Delta t_r}$ the slope at large t of the correlation term $\langle \theta_c(\tau)\Delta t_r(\tau)\rangle$. Consequently, the optical spectrum consists of N Lorentzian lines centered at ω_n with full width at half maximum (FWHM) linewidths:

$$\Delta\omega_n = \Delta\omega_{min} + \omega_r^2 \left(n - n_{min}\right)^2 D \quad (4.8)$$

with $n_{min} = n_c - \gamma_{\theta_c,\Delta t_r} / \omega_r D$, and $\Delta\omega_{min} = \Delta\omega_{\theta_c} - \gamma^2_{\theta_c,\Delta t_r} / D$. Equation (4.8) shows that the diffusion coefficient D affects the linewidth of the optical modes; hence, an estimation of timing jitter is readily available from the optical spectrum by measuring the mode linewidths around n_{min}. It can be noted that correlation of $\theta_c(t)$ and $\Delta t_r(t)$ affects the first and zero order terms in equation (4.8) resulting in a frequency shift of the mode with minimum linewidth relative to the case in which both random processes are statistically independent ($\gamma_{\theta_c,\Delta t_r} = 0$), which we have determined in the previous sections not to be the case. However, as the value of D is unambiguously determined from the second order term in (4.8), it can be extracted without knowledge of the exact level of correlation between $\theta_c(t)$ and $\Delta t_r(t)$.

The value of D also determines the spectrum of the laser intensity $\left|I(\omega)\right|^2$ (RF spectrum), which can be calculated straightforwardly in the same way as the optical spectrum. Skipping the details, it is found to consist of a sum of $N-m$ Lorentzian lines centered at $m\omega_r$ for $m = 1$ to $N-1$. At any given value of m, each line will have identical FWHM linewidths given by:

$$\Delta\omega_{RF_m} = m^2\omega_r^2 D = m^2 \Delta\omega_{RF_1} \quad (4.9)$$

with $\Delta\omega_{RF_1} = \omega_r^2 D$. Each line corresponds to the beating between a pair of modes separated by $m\omega_r$ in the optical spectrum. We notice that the diffusion coefficient D could be directly derived from $\Delta\omega_{RF_1}$, this is however not possible in practice at relatively high repetition frequencies due to the limited bandwidth of the photodiode. A relation between both the mode linewidths and those of their beatings can be established by combining (4.9) and (4.8) to yield:

$$\Delta\omega_n = \Delta\omega_{min} + \frac{\Delta\omega_{RF_m}}{m^2}\left(n - n_{min}\right)^2 \qquad (4.10)$$

or equivalently:

$$\Delta\omega_n = \Delta\omega_{min} + \Delta\omega_{RF_1}\left(n - n_{min}\right)^2 \qquad (4.11)$$

which was also obtained and experimentally observed in [104] for a two section passively MLL emitting at 1.3 μm.

In order to be able to quantify the timing jitter from measurements of the mode linewidths, various basic aspects are first reviewed. Timing jitter is quantified as the standard deviation σ of $\Delta t_r(t)$, hence, in a passively MLL, it will be given by:

$$\sigma = \sqrt{\left\langle \left|\Delta t_r(t)\right|^2 \right\rangle} = \sqrt{Dt} \qquad (4.12)$$

Despite the lack of convergence as $t \to \infty$, the timing jitter from pulse i at time t_i to pulse $i+N$ at time $t_i + NT_r$ can be defined. This yields:

$$\sigma(N) = \sqrt{DNT_r} \qquad (4.13)$$

For $N = 1$this gives the pulse to pulse timing jitter σ_{pp} that is sometimes used in practice. Timing jitter can also be quantified in the frequency domain as:

$$\sigma = \sqrt{\left\langle \left|\Delta t_r(t)\right|^2 \right\rangle} = \sqrt{\int_{-\infty}^{+\infty} S_{\Delta t_r}(\omega)\frac{d\omega}{2\pi}} = \sqrt{\int_{-\infty}^{+\infty} \frac{D}{\omega^2}\frac{d\omega}{2\pi}} \qquad (4.14)$$

Clearly, the power spectral density (PSD) of $\Delta t_r(t)$ does not converge as $\omega \to 0$, which is expected from the lack of convergence in the time domain as $t \to \infty$ and which is a consequence of the absence of a reference clock signal. The timing jitter can however be quantified between two given frequencies ω_1 , $\omega_2 > 0$ to yield the pulse to clock timing jitter, that is, the jitter relative to a perfect RF oscillator, also called r.m.s. integrated timing jitter:

$$\sigma_{pc} = \sqrt{\int_{\omega_1}^{\omega_2} \frac{D}{\omega^2} \frac{d\omega}{2\pi}} = \sqrt{\int_{\omega_1}^{\omega_2} \frac{\Delta\omega_{RF_1}}{\omega_r{}^2 \omega^2} \frac{d\omega}{2\pi}} \qquad (4.15)$$

The above result is related to the commonly used formula for estimating the timing jitter from the single side band phase noise of the laser intensity as measured by an ESA, or L(f). In fact, if $\Delta\omega_{RF_1} / 2 << \omega << \omega_r$, it can be approximated by [118]:

$$L(\omega) \approx \frac{\Delta\omega_{RF_1}}{2\omega^2} \qquad (4.16)$$

and by inserting this result into (4.15) we obtain the well known equation:

$$\sigma_{pc} = \frac{T}{2\pi} \sqrt{\int_{\omega_1}^{\omega_2} 2L(\omega) \frac{d\omega}{2\pi}} = \frac{T}{2\pi} \sqrt{\int_{f_1}^{f_2} 2L(f) df} \qquad (4.17)$$

which demonstrates that the value of timing jitter commonly measured in practice from L(f) can be estimated from the MLL optical spectrum.

Experimental validation of the previous theoretical analysis has been performed with three single section devices having different cavity lengths. Figure 4-15(a) shows the optical spectrum of a 1000 μm long laser when biased at 150 mA, from which a total of $N = 30$ modes have been numbered. First, in order to verify the mode phase correlation and hence ML operation, the RF spectrum of all $N - 1 = 29$ mode beatings between consecutive pairs of modes ($m = 1$) were measured. Figure 4-15(b) is a plot of the superposition of all these beatings. All beating spectra are very well fitted by Lorentzian functions. The average beating linewidth is $\Delta\omega_{RF_1} / 2\pi = 89$ kHz with a standard deviation of 5.3 kHz, while the average center frequency is $\omega_r / 2\pi = 39.6$ GHz with a standard deviation of 18.2 kHz. These small deviations demonstrate the mode phase correlation between all *N* modes and thus validate the mode locking conditions. The Lorentzian shape of all the lines in the RF spectrum for $m = 1$ also confirms that $\Delta t_r(t)$ is in fact a Gaussian random walk process.

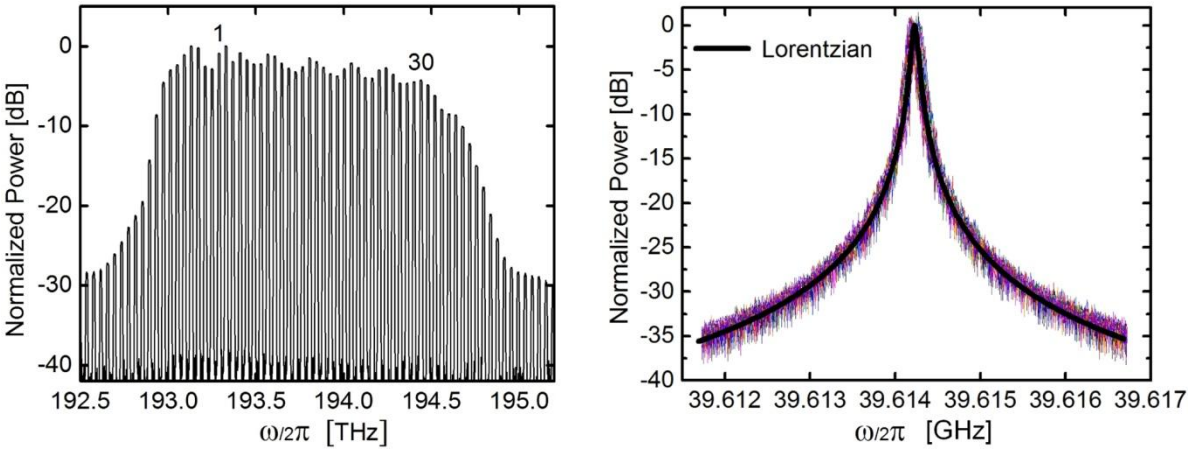

(a) (b)

Figure 4-15. (a) Optical spectrum. (b) RF spectrum of the 29 consecutive mode beatings (m = 1) of the 1000 µm laser when biased at 150 mA.

The linewidth of each of the N modes of the optical spectrum was then measured by the self-heterodyne technique, as already described in section 4.2. All the resulting self-mode beating spectra fitted very well Lorentzian functions, as can be seen in Figure 4-16(a) for several modes, confirming the Lorentzian shape of the modes as expected. Figure 4-16(b) is a plot of the measured linewidths as a function of mode number. The solid line is a parabolic fit $\Delta\omega_n / 2\pi = 6.5 + 0.092\left(n-12\right)^2$ MHz, from which $\Delta\omega_{RF_1} / 2\pi = 92$ kHz is extracted with a standard error of ~ 3 kHz, which very much agrees with the measured linewidth of each beating in Figure 4-15(b), verifying (4.11).

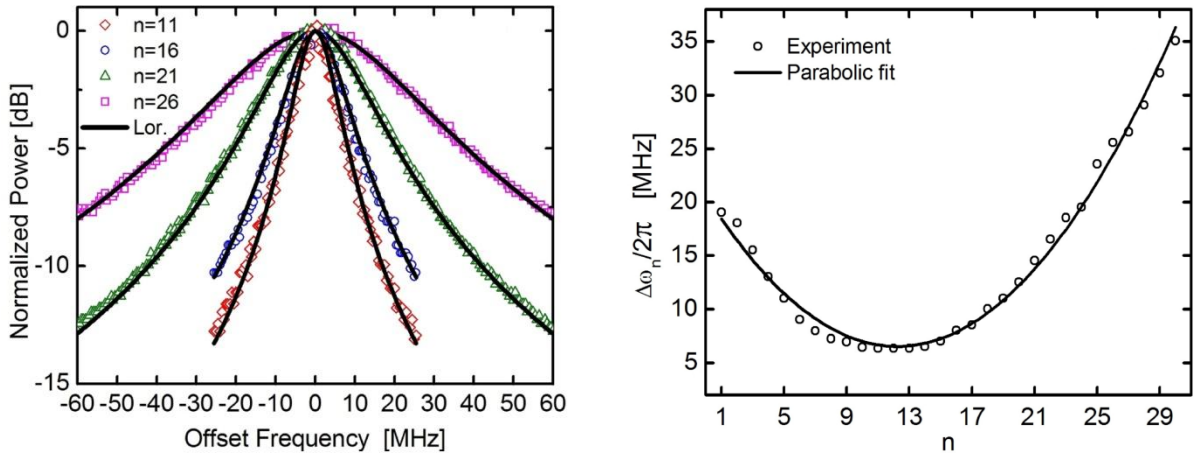

(a) (b)

Figure 4-16. (a) Self-mode beating spectra with Lorentzian fits for modes 11, 16, 21 and 26. (b) Measured mode linewidths as a function of mode number and parabolic fit for the 1000 µm laser at 150 mA.

We can also see from the fit that $n_{min} = 12$ which is the number of the less noisy mode with linewidth $\Delta\omega_{\theta_c} / 2\pi = 6.5$ MHz, and this is what the linewidth of all the modes should be in the absence of timing jitter. The diffusion coefficient is also extracted from the parabolic fit to give $D = 0.0092$ fs. By using (4.13) and (4.15), the pulse to pulse and the pulse to clock timing jitter, from e.g. 1 MHz to 20 MHz, were then estimated at $\sigma_{pp} = 15.16$ fs and $\sigma_{pc} = 0.47$ ps respectively, the latter which is in perfect agreement with an independent single side band phase noise (SSBPN) *L(f)* measurement as shown in Figure 4-17, yielding $\sigma_{pc} = 0.48$ ps when using the same integration band.

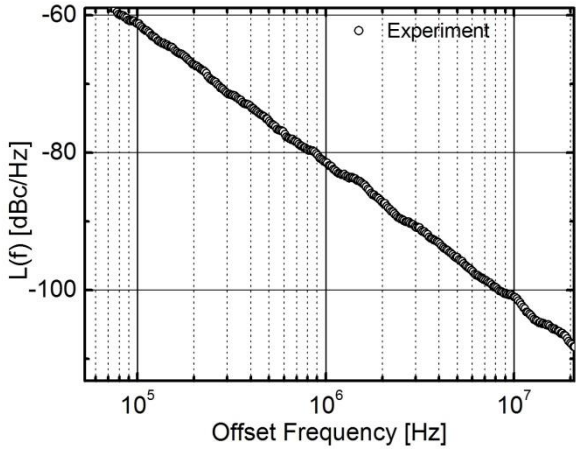

Figure 4-17. SSBPN for the 1000 μm laser at 150 mA

In order to verify equation (4.9), the linewidths of the RF spectrum for $m \geq 1$ have been measured from the laser with cavity length 3800 μm, yielding a repetition frequency $\omega_r / 2\pi = 11.2$ GHz, when biased at 200 mA. Figure 4-18(a) shows the measured RF spectra for $m = 1$ to 4, superimposed with Lorentzian fits. The inset is a plot of the full span RF spectrum from 10 to 50 GHz. Figure 4-18(b) shows the expected quadratic dependence of $\Delta\omega_{RF_m}$ on m, as evidenced by the parabolic fit $\Delta\omega_{RF_m} / 2\pi = 48.5m^2$ kHz. From this we determine $D = 0.062$ fs, $\sigma_{pp} = 74.12$ fs and from 100 kHz to 4 MHz $\sigma_{pc} = 5.61$ ps. To verify the agreement of the previous result, the *L(f)* was measured by an ESA (Figure 4-19). By integrating the measured curve from e.g. 100 kHz to 4MHz, a value of $\sigma_{pc} = 5.63$ ps was

obtained, in agreement with the previously calculated value. The *L(f)* as measured by an ESA will then yield a correct value of σ_{pc} as long as it decays at -20 dB/dec.

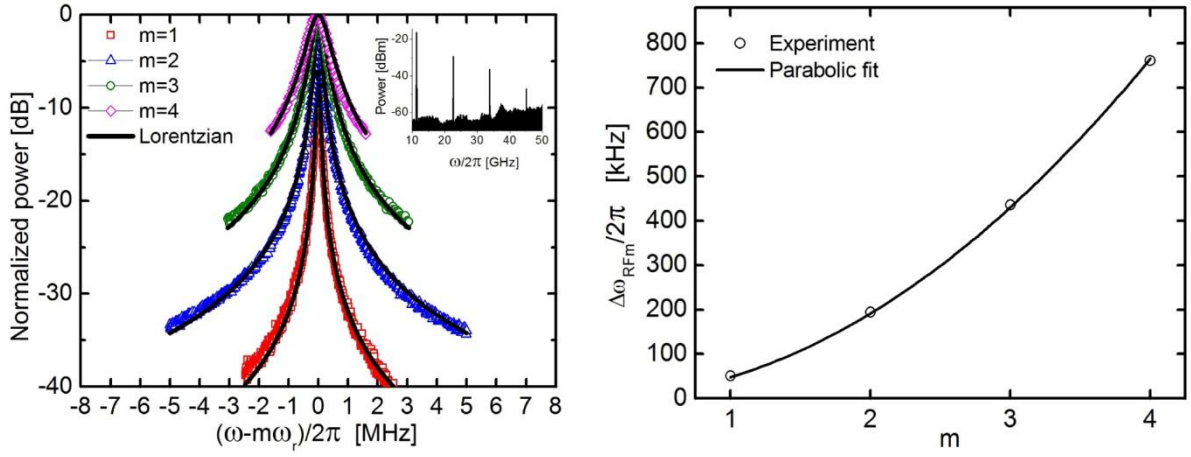

(a) (b)

Figure 4-18. (a) RF spectra for m=1 to 4 and corresponding Lorentzian fits. Inset: full span RF spectrum (b) Measured RF linewidths as a function of m with parabolic fit for the laser with cavity length 3800 μm when biased at 200 mA

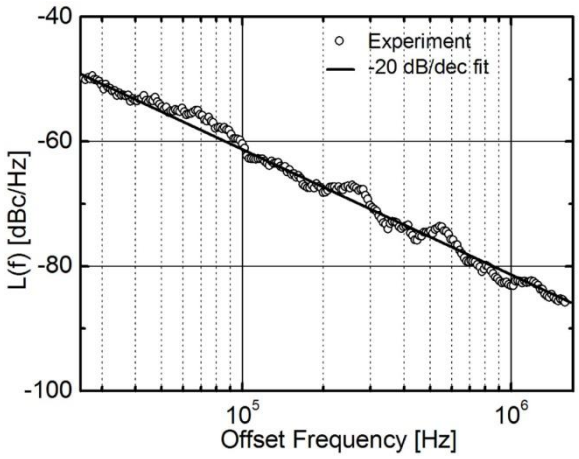

Figure 4-19. SSBPN for the 3800 μm laser at 200 mA

The experimental results in the previous section have demonstrated the validity of a method for determining the timing jitter of passively MLLs from measurements of the individual mode linewidths. We now apply this method to estimate the timing jitter and the RF linewidth of a 130 GHz single section QDash laser. ML operation in this device is evidenced by the intensity autocorrelation function of the laser as it exhibits a pulsating behaviour when biased at 300 mA, with a period corresponding to the inverse of the repetition frequency and pulse widths of ~ 850 fs having high extinction ratios, as shown in Figure 4-20(a). The

corresponding optical spectrum is shown in Figure 4-20(b) from which 13 modes have been numbered and filtered for measuring their corresponding linewidths. Figure 4-20(c) shows the mode linewidth evolution with mode number and the expected parabolic behaviour. The parabolic fit $\Delta\omega_n / 2\pi = 8.53 + 0.093(n-7)^2$ MHz gives $D = 8.76\times10^{-4}$ fs, $\sigma_{pp} = 2.6$ fs and from 16 MHz to 320 MHz $\sigma_{pc} = 51.3$ fs.

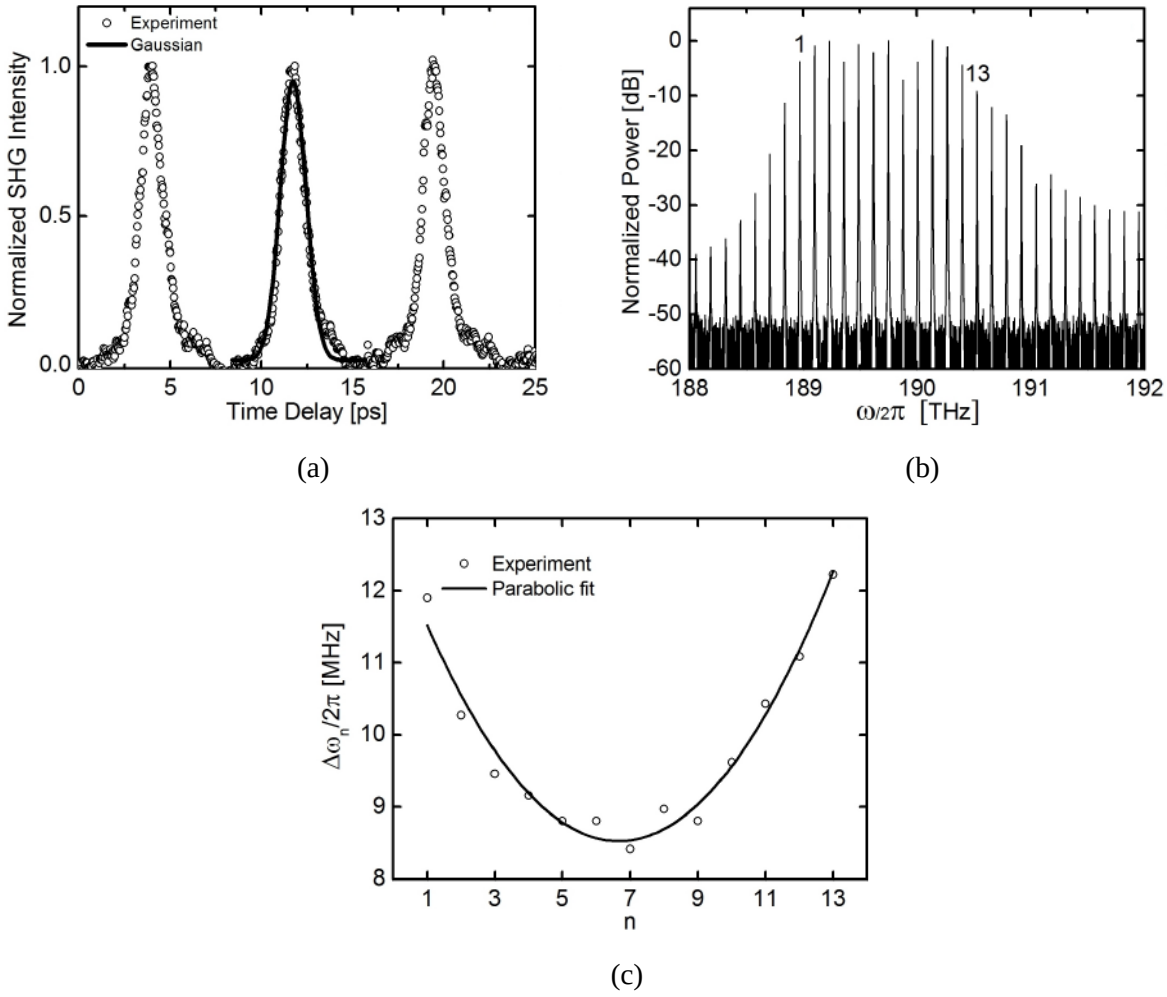

Figure 4-20. (a) Intensity autocorrelation, (b) optical spectrum, and (c) measured mode linewidths for the laser with cavity length 330 μm when biased at 300 mA

In order to evaluate the limits in repetition rate for the applicability of the proposed method, estimations of the RF linewidth as a function of measured number of modes have been performed, from which corresponding relative errors have been calculated. Figure 4-21 illustrates this for the laser with repetition rate of 40 GHz, with errors being determined

relative to the RF linewidth value directly measured from the photocurrent spectrum. This figure suggests that it is not required to perform the measurements of the entire number of available modes in order to obtain similar relative error values, which can be kept smaller than ~ 10% by measuring at least six of the available modes. This gives an idea on the maximum repetition frequency that the method could be applied to. In this example, six available modes is equivalent to performing the measurements every five modes, corresponding to a separation in frequency of ~ 200 GHz, for which an estimation of the RF linewidth with a relative error of about 11% was obtained. Hence, application of the method might be possible at repetition frequencies up to 200 GHz yielding similar relative errors provided six modes are available for linewidth measurements. Timing jitter at even higher repetition rates could however be estimated if more modes are available. A lower limit in repetition frequency for the applicability of the method is also imposed since precise linewidth measurements on multiple lines of the optical spectrum becomes more difficult as the lines become closer to each other. If the self-heterodyne technique is used, this limit will then be determined by the minimum bandwidth of commercially available optical filters of ~ 0.1 nm in order to individually separate the optical modes, setting a repetition frequency limit down to ~10 GHz. Other linewidth measurement techniques, such as the heterodyne detection with narrow linewidth reference lasers, may however be implemented, allowing a lower limit in repetition frequency depending on the specific instrumentation used.

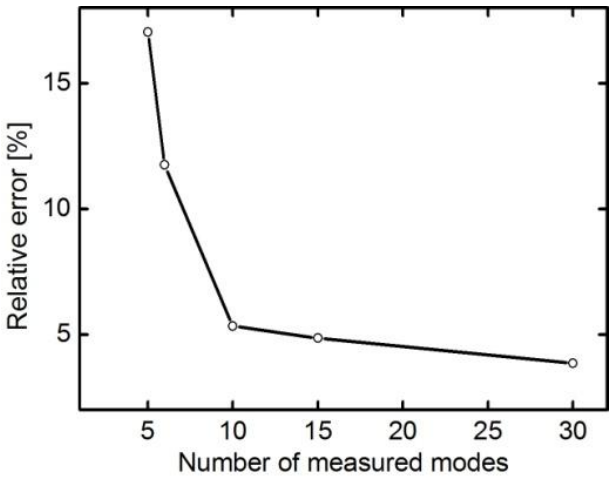

Figure 4-21.Relative error as a function of number of measured modes for the 1000 μm long laser

4.5. Coherence between non-adjacent modes

To this point we have seen that adjacent spectral modes are in general well synchronized together. This was analyzed in both the time and frequency domains. This fact resulted in the RF beat linewidth between consecutive modes being at least two orders of magnitude lower when compared to that of the optical modes themselves. In the previous section, we also have looked at the RF beat-tone linewidth of non-adjacent spectral modes out to the fourth harmonic of a 10 GHz device, which validated the theoretical result of a quadratic dependence with harmonic number. This, however, was not possible at higher repetition rates due to, once again, a limitation in the electronics bandwidth. In this section we present experimental results of a measurement technique capable of measuring the RF beat-tone linewidth of spectral modes of a passively mode locked QDash laser out to the thirty first harmonic, or a mode separation of 1.5 THz [119]. This wideband interrogation is realized through a degenerate FWM-based wavelength conversion scheme in an SOA. The following experiments have been carried out in collaboration with DCU, Ireland.

For this study we have used the single section device from the previous sections having a repetition frequency of 48 GHz (890 μm length). The setup for this technique is shown in Figure 4-22 in which the two spectral modes (at angular frequencies of ω_1 and ω_4) are filtered using a WaveShaper and are combined with two 20mW external-cavity lasers, or ECLs, (at angular frequencies of ω_2 and ω_3).

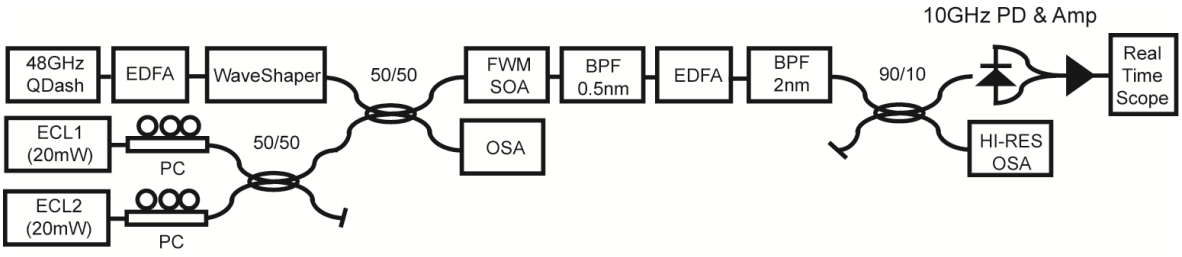

Figure 4-22. Experimental setup used to measure the RF linewidth of non-adjacent spectral modes using FWM in a nonlinear SOA and real-time detection [119].

The ECLs are used as pumps for a FWM-based wavelength converter which is implemented using an SOA (Kamelian OPB-12-15). The operating principle of the wavelength conversion is illustrated in Figure 4-23(a), where widely-space spectral modes spacing are converted down to a small frequency separation through the careful choice of the pump frequencies

which would generate two degenerate FWM mixing idlers at frequencies of $2\times\omega_2 + \omega_1$ and $2\times\omega_3 - \omega_4$ which ensures that the frequency separation of the two generated idlers is lower than 10 GHz.

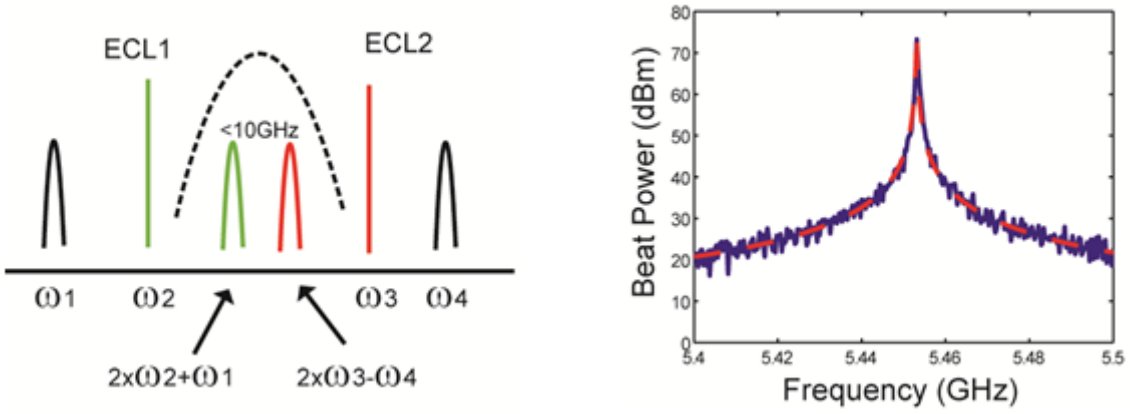

(a) (b)

Figure 4-23. (a) Dual degenerate FWM mixing scheme employed to achieve correct phase conjugation and (b) RF beat-tone linewidth measured for two ECLs and two adjacent spectral modes using the FWM technique. The dashed red line shows a Lorentzian fit [119].

It was not possible to measure the RF beat-tone linewidth of these two idlers using a fast photodiode and ESA because the limited short-term frequency stability of the two ECLs would mean the beat frequency generated by the two idlers would move by 100MHz over the minimum scan time of the ESA (around 50ms). This finite integration time therefore obscured any accurate measurement of the narrow RF beat-tone. To overcome this, we used a real-time oscilloscope to measure beat signal over a considerably shorter time window (3.2 μs, which is 128,000 samples at 40 GS/s sampling rate) than with the ESA, thereby greatly reducing the time over which the ECLs could drift in optical carrier frequency. The RF beat-tone linewidth of the non-adjacent spectral modes was determined by fitting a Lorentzian lineshape to the power spectral density of the measured temporal beat signal. There are two points worth noting about this method of wavelength conversion; first is that one cannot simply use one pump to degenerately FWM one spectral mode so that it is close to the second spectral mode. In doing this, the first mode undergoes phase conjugation and loses its coherent temporal relationship with the second spectral mode. The manifestation of this temporal incoherence is that the measured RF beat-tone linewidth is about 24MHz. This is

the sum of the optical linewidths of the two QDash spectral modes, as the RF linewidth of two incoherent oscillators is the sum of their optical linewidths. This issue is remedied by ensuring both modes are phase conjugated in a similar manner thereby maintaining their temporal phase relationship which results in the generation of a narrow frequency tone. The second note is about the minimum frequency resolution. The RF beat-tone linewidth measured using this technique has a minimum value of at least the sum of the optical linewidths of the two pump ECLs (~120 kHz each), plus the RF linewidth of the two adjacent modes (typically a few 10s of kHz). Figure 4-23(b) shows the beating spectrum between the two idlers (separated by ~5.45 GHz) after two central spectral modes undergo degenerate FWM, where the dashed red line is a Lorentzian fit to the measured data with a linewidth of 320 kHz. This dual-pump degenerate FWM conversion scheme can not accurately measure RF beat-tone linewidths less than 320kHz, but instead infers that the spectral modes exhibit excellent coherence.

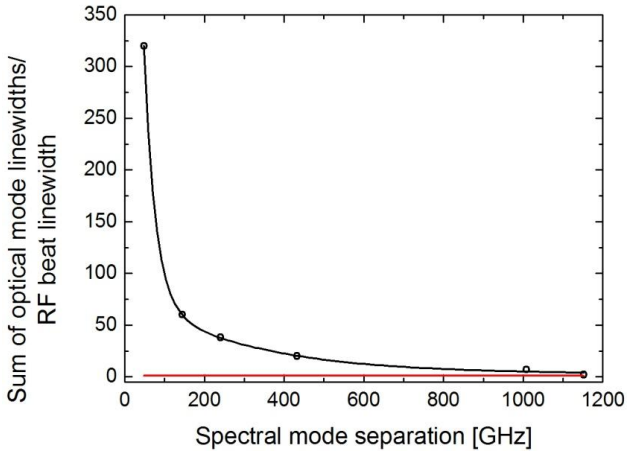

Figure 4-24. Ratio of the sum of the optical linewidths and the RF linewidth (black circles) as a function of increasing spectral mode separation. The red line depicts a unity ratio for non coherent spectral modes

To infer the degree of mode coherence we calculate the ratio of the sum of the optical linewidths and the RF beat-tone linewidth. Using this metric, two mutually incoherent spectral modes would have a ratio of unity, as the RF beat-tone linewidth would be the same as the sum of the optical linewidths of the two spectral modes. In the case where two adjacent modes are measured using the delayed self heterodyne technique (~24 MHz for the sum of two adjacent modes) and RF beat-tone measured using the ESA (~80 kHz linewidth), the ratio yields the typical measured value of ~300. The dual-pump degenerate FWM wavelength

conversion technique used here has a minimum frequency resolution of 320 kHz, implying that the maximum ratio we were able to measure for these passively mode-locked QDash lasers will be ~80. Figure 4-24 shows the calculated ratio of the sum of optical linewidths to RF beat-tone linewidth for the non-adjacent spectral modes of the 48 GHz passively mode-locked QDash laser. The red line depicts unity; a value for which the two spectral modes are incoherent. The experimental data starts with a ratio value of 320 for the adjacent spectral modes (1st harmonic) and reduces to a value of 2.2 for a spectral mode separation of 1488GHz (the 31st harmonic) as the coherence of these passively-locked spectral modes decreases. With a ratio value of 2.2 there is still evidence of mode coherence for this passively mode-locked QDash semiconductor laser even at a mode separation of 1.5THz, however this coherence is considerably weaker than the lower order harmonics.

4.6. Static phase and pulse characteristics

Thus far we have focused our attention in the instantaneous phase or, equivalently, the noise characteristics of the devices under study. We have seen that the instantaneous mode phases are correlated, meaning that some kind of mode locking regime has definitely been established. While this represents a necessary condition, it does not automatically imply the formation of pulses inside the laser cavity. As already explained in Chapter 2, clear pulses will only be observed if the modal static phase difference $\phi_{n+1} - \phi_n$ is constant, i.e., if the group delay (GD) is constant throughout the whole spectral bandwidth, or equivalently, if the group delay dispersion GDD = 0.

In this section, we have systematically measured the group delay and the resulting pulse profile of single section and two section devices as a function of injection current and cavity length [24]. These measurements are the result of a collaborative work between LPN and DCU, Ireland.

We first investigate the 890 μm long single section device. The static phase difference between adjacent modes, up to a zero order term, were measured using the stepped heterodyne technique described in [64], from which the GD, GDD and spectral phase of the electric field have been determined. The experimental setup is the same as in Figure 4-4. The laser output is mixed with an optical local oscillator positioned between two of the laser

modes. The resultant beat signals, namely the beat signal of the oscillator with mode *n*, the beat of the oscillator with mode *n*+1, and the RF tone, are recorded on a real-time oscilloscope. Further signal post-processing will then allow the recovery of the amplitude of the two modes, as well as their phase difference. By stepping the local oscillator across all signal modes we obtained a complete measurement of the laser's output amplitude and phase.

Figure 4-25(a) (red plot) is the measured GD for the 890 μm single section laser when biased at 400 mA as a function of offset frequency, spanning about 50 modes of the corresponding optical spectrum in Figure 4-25(b) (top). An almost linear GD is obtained, the slope of which determines the value of GDD which has been calculated at 1.3 ps^2. Figure 4-25(b) (bottom) shows the corresponding spectral phase (red plot) obtained after integration of the GD curve, exhibiting a parabolic shape.

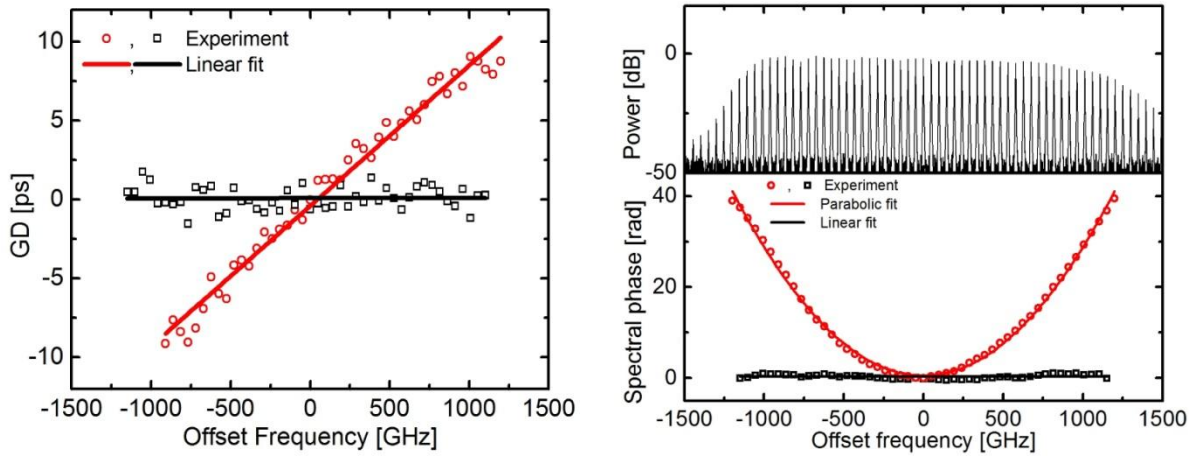

(a) (b)

Figure 4-25. (a) GD of the 890 μm single section laser measured at the laser output (red plot) and after 65 m of SMF (black plot) with corresponding (b) (top) optical spectrum and (b) (bottom) spectral phase at the laser output (red curve) and after 65 m of SMF (black curve) for an injection current of 400 mA

Regardless of the perfect locking of the mode beating frequencies and the low RF linewidths measured in section 4.3, the parabolic spectral phase profile in Figure 4-25(b) (bottom) does not allow for pulse generation. In order to see this, the electric field intensity autocorrelation (AC) was measured directly from the laser by means of a second harmonic generation (SHG) background-free autocorrelator, as seen in the red curve of Figure 4-26(a) showing an almost flat profile indicating the absence of sharp pulses, in agreement with the intensity profile in

Figure 4-26(b) (red curve), which has been reconstructed from the measured power and phase spectra.

The previous measurements have been repeated after inserting 65 m of single mode fiber (SMF) at the laser output introducing -1.3 ps^2 of accumulated dispersion, which would compensate for the laser GDD of 1.3 ps^2. The black curves in Figure 4-25(a) and Figure 4-25(b) show the measured GD and the spectral phase, respectively, after dispersion compensation. As can be noted, the second order term of the spectral phase is now negligible at the fiber end, where the modes now interfere constructively, allowing for perfect pulse generation. This is evidenced by the clean train of pulses in the intensity autocorrelation trace of Figure 4-26(a) (black curve) which has been measured without using any type of optical amplification. In fact, the very narrow pulse widths, measured at 600 fs after deconvolution (assuming a Gaussian pulse shape) and the 40 mW of average output power result in peak powers greater than 1 W, representing the highest peak power values ever obtained from a monolithic semiconductor mode locked laser emitting at 1.55 μm. The electric field intensity profile has once again been reconstructed and plotted in Figure 4-26(b) (black curve) yielding 600 fs pulse widths in agreement with the measured autocorrelation trace, resulting in a TBP of 0.98. This value may seem to be very far from the Fourier transform limit if compared to the usually referred value in the literature of 0.315 corresponding to a $sech^2$ spectral profile. However, the optical spectrum exhibited by these devices is far from having this shape but instead have shown to exhibit very flat topped spectra which may be more appropriately approximated to a rectangular shape, in which case the TBP is 0.88 (cf. Chapter 2). The pulses would still be slightly wider than the Fourier-transform case which we attribute to higher order dispersion (β_3) introduced by the SMF.

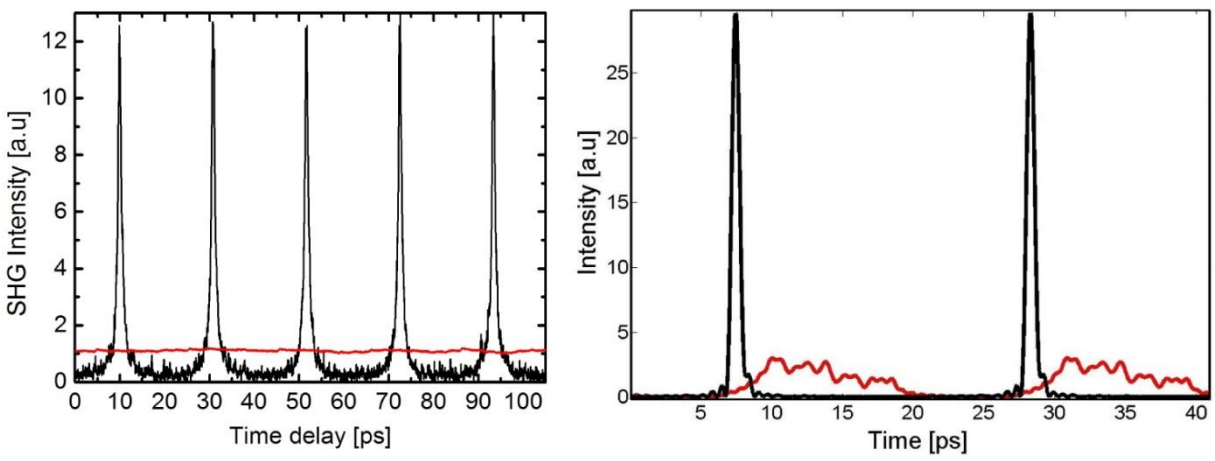

(a) (b)

Figure 4-26. (a) Intensity autocorrelation for the 890 μm laser at the laser output (red curve) and after 65m of SMF (black curve) with corresponding (b) reconstructed field intensity profiles at the laser output (red curve) and after 65 m of SMF (black curve) when driven with 400 mA

Figure 4-27 better illustrates the dependence of the pulse profile on the propagating distance through the SMF. This plot is the result of simulations using the measured amplitude and phase profile of the laser at 400 mA as an input field into a lossless fiber presenting a -20 ps^2/km of group velocity dispersion (GVD). Right at the laser output (z=0), there are no clear pulses due to the high group delay dispersion of the laser field. The fiber negative GVD gradually cancels the positive GDD of the laser during propagation. At z = 65 m, the accumulated GDD in the fiber completely compensates for the laser GDD, at which point the intensity profile consists of a clear train of narrow pulses with high peak power. Further propagation results in a net negative accumulated GDD which is no longer compensated. However, one may expect the re-emergence of pulses if the static phase difference becomes the next multiple of 2π. The propagating distance for this to occur was calculated at 3519 m of propagation, in agreement with simulations as depicted in Figure 4-28. There is also an interesting regime where the phase difference becomes π/M, with M any integer, meaning that RF beatings will be cancelled out every M modes, yielding an artificial repetition frequency of M times the fundamental one. This is simulated in Figure 4-29 for the case of M=10 corresponding to an SMF propagation of 410 m, yielding a repetition frequency of 480 GHz. This was not verified in the laboratory; however, experimental results on QDash lasers have already been reported which confirm these simulations [120].

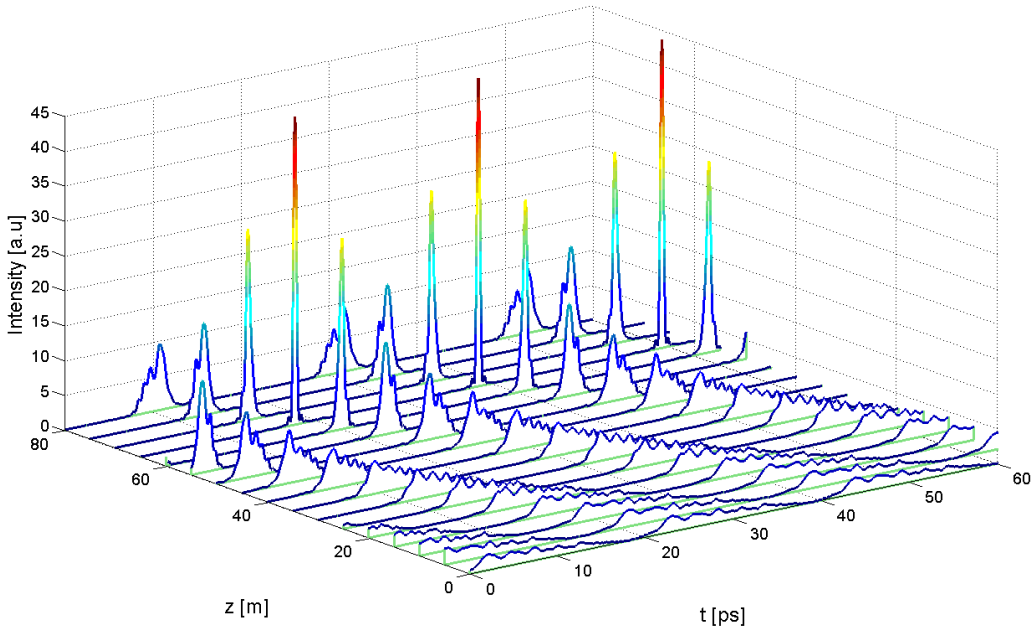

Figure 4-27. Laser field intensity as a function of propagation distance in a SMF for the 890 μm long single section laser for 0 GDD compensation (at 65 m)

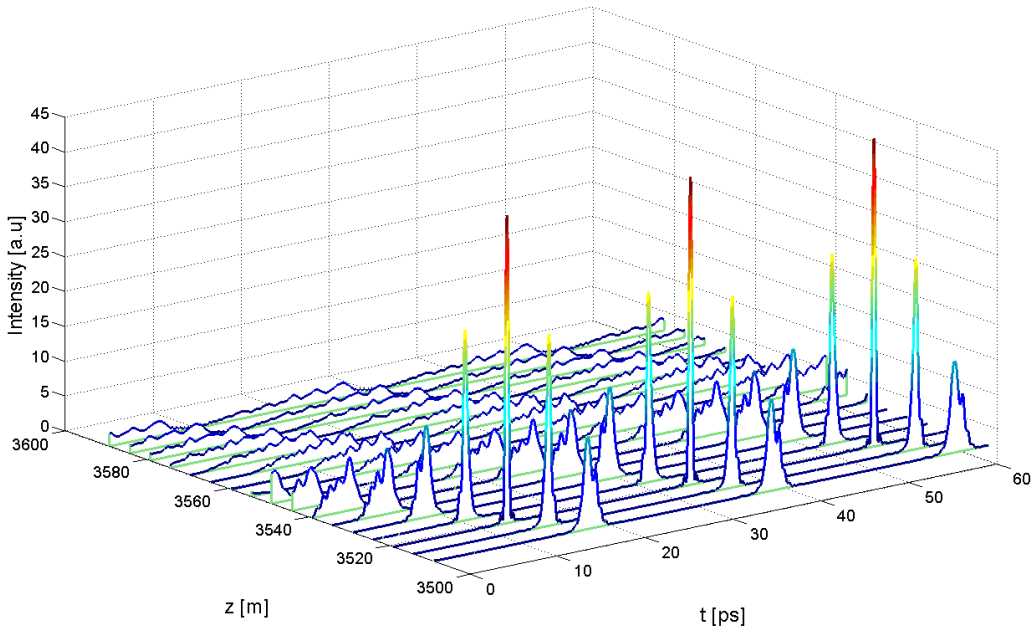

Figure 4-28. Laser field intensity as a function of propagation distance in a SMF for the 890 μm single section laser for -2π GDD compensation

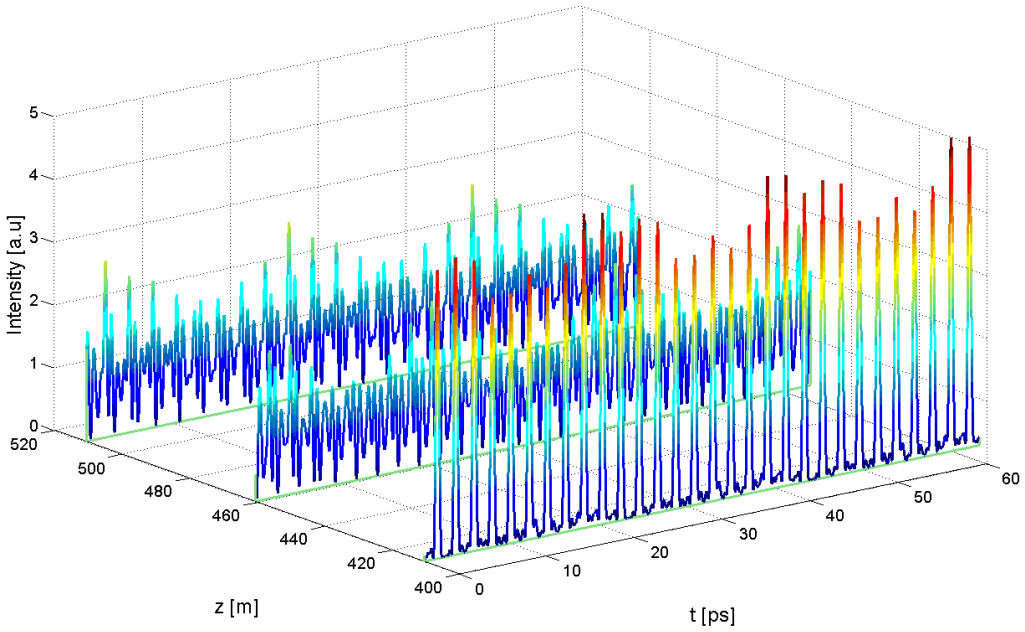

Figure 4-29. Laser field intensity as a function of propagation distance in a SMF for the 890 μm single section laser for -π/10 GDD compensation

In order to see the effect of cavity length on the spectral phase, the same measurements were carried out for the 1820 μm long laser. Figure 4-30(a) is the plot of GD when the laser was biased at 400 mA. Figure 4-30(b) (top) and Figure 4-30(b) (bottom) show respectively the measured power spectrum and spectral phase. The GDD was calculated at 3 ps^2, more than twice that of the 890 μm laser at the same bias current. Once again, this GDD was easily compensated by inserting 150 m of SMF at the laser output, allowing for the formation of 700 fs sharp pulses with a TBP of 0.97.

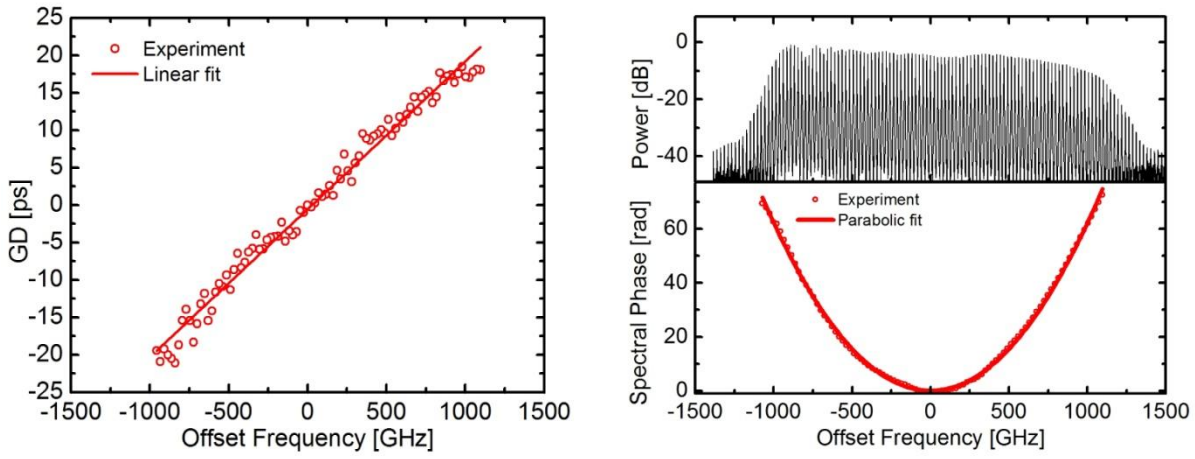

(a) (b)

Figure 4-30. (a) GD of the 1820 μm laser at the laser output with corresponding (b) (top) optical spectrum and (bottom) spectral phase profile when driven with 400 mA

These results are in agreement with the steady state spectral phase obtained in Chapter 2 after numerically solving the coupled mode equations in a nonlinear medium leading to FWM. In the following, we will provide a simpler qualitative analysis of the origin of the parabolic profile of the steady state phases that will also help understanding the next experimental results. Recalling the third ML condition (cf. Chapter 2), we have the relative phase:

$$\Psi(n) = 2\phi_{n+1} - \phi_n - \phi_{n+2} = \Phi_n \qquad \text{for } n \in [1, N-2] \qquad (4.18)$$

We know that Φ_n is actually a contribution from both a linear dispersion and a nonlinear dispersion arising from the FWM effect owing to the third order susceptibility, and can be written as:

$$\Psi(n) = \Phi^L + \Phi^{NL} = \left[\left(2\omega_{n+1} n_{eff\,n+1} - \omega_n n_{eff\,n} - \omega_{n+2} n_{eff\,n+2}\right) L/c\right] + \Phi^{NL} \quad \text{for } n \in [1, N-2] \quad (4.19)$$

Under steady state ML regime we have equal mode spacing independently of any intracavity dispersion due to energy conservation of the FWM process. Consequently Φ^L should be independent of mode number provided we have a constant dispersion in the optical spectral bandwidth. Φ^{NL}, on the other hand, should be mostly bias dependent. The total Φ_n can hence be treated as a constant. Thus, by integrating (4.18) with respect to n one can find:

$$\int \Psi(n)dn = \phi_{n+1} - \phi_n = \Phi n + \alpha \qquad \text{for } n \in [1, N-1] \qquad (4.20)$$

$$\int dn \int \Psi(n)dn = \phi_n = \Phi n^2/2 + \alpha n + \beta \qquad \text{for } n \in [1, N] \qquad (4.21)$$

It can be seen from (4.21) that the result is a quadratic evolution of the static phases ϕ_n as a function of mode number n whenever the value of $\Phi \neq 0$. For perfect pulse generation $\Phi = 2\pi m$, where m is any integer value, and in this case all modes interfere constructively. This is usually the case in standard two-section semiconductor passively MLLs as the absorber locks the static phases of the longitudinal modes by periodically creating a positive net gain window when saturated by the optical field inside the laser cavity. As we have seen, in single section devices $\Phi \neq 0$ but can be made a multiple of 2π after SMF propagation.

By making $d\omega = \omega_r dn$ in (4.20) , (4.21) and by considering only the second order term of the spectral phase ϕ_n, as the first and zero order terms do not affect the shape of $I(t)$, we can write:

$$\frac{d\phi(\omega)}{d\omega} = \Phi\omega/\omega_r^2 \;; \quad \frac{d^2\phi(\omega)}{d\omega^2} = \Phi/\omega_r^2 \qquad (4.22)$$

which are the group delay (GD) and the group delay dispersion (GDD), respectively, associated with the laser electric field inside the cavity, which we can see are clearly dependent on the repetition frequency and consequently to the cavity length.

To experimentally investigate this GDD dependence on cavity length, GDD measurements were performed for the two previously characterized lasers as a function of injection current, the results of which are depicted in Figure 4-31(a).

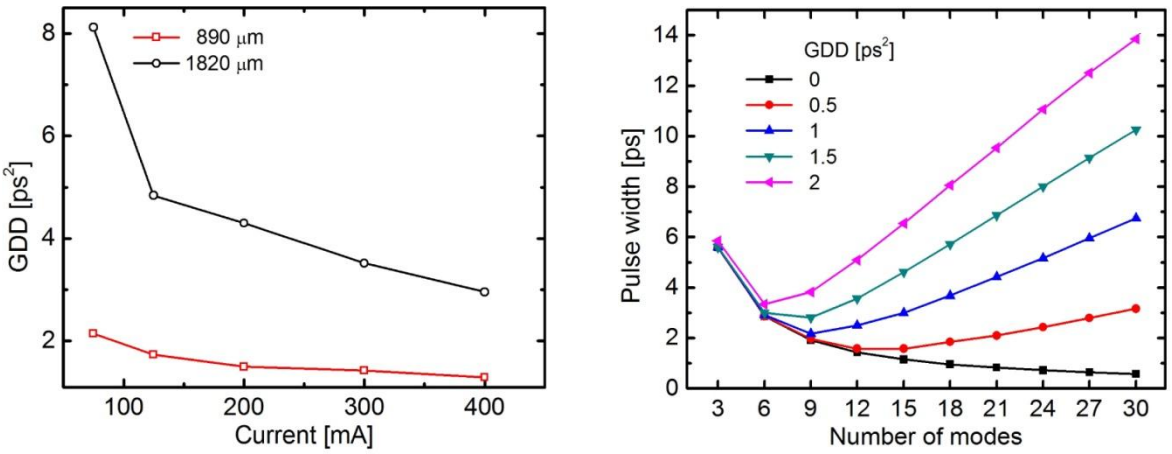

(a) (b)

Figure 4-31. (a) Measured GDD of two single section lasers different cavity lengths. (b) Simulated pulse width as a function of number of modes at -3 dB for different values of GDD for the 890 μm laser

Firstly, the GDD is found to decrease with current, as also reported in [121]. This represents an interesting feature in single section QDash MLLs as it allows for improving the pulse generation while increasing the average output power, contrary to standard two-section QD devices in which the shortest pulses are generally obtained at the lowest injection currents, yielding less average output power and hence a much reduced peak power [8], [122], [123].

It should be noted that if one was able to always compensate for the laser GDD at its output, then one would always observe a clean train of short pulses independently of the injected current. Moreover, the pulse width would always decrease by increasing the applied current, simply owing to the broadening of the optical spectrum (cf. section 2.2.1), which also explains the experimental observations in [124] . This was indeed confirmed experimentally by inserting the right amount of SMF at each value of injection current. In other words, the laser always exhibited mode locking for the whole range of bias conditions, right from above threshold up to saturation. This fact is in agreement with the findings of the previous section showing that, regardless of the RF linewidth broadening at some bias conditions due to feedback instabilities, the mode phase correlation was always preserved.

On the other hand, Figure 4-31(a) shows that the GDD is always smaller for the shorter laser, in agreement with (4.22) stating that for the same value of Φ, a laser with longer cavity will exhibit higher dispersion, which can be intuitively understood as larger modal phase

differences due to a longer propagation round-trip, which explains why the reports on ultra short pulses from single section MLLs almost always corresponded to ultra high repetition frequencies (very short cavity lengths) devices [12], [15], [114]. The value of Φ was found to be slightly different in both lasers and to decrease with injection current from ~0.2 to ~0.1 rad. Despite these relatively small values of Φ, pulses cannot be formed due to the wide spectral widths of the laser emission if no dispersion compensation is performed. Indeed, the larger the spectral width the smaller the value of GDD required for pulse generation. This explains the observation of sharp pulses from single section semiconductor lasers only after filtering a few number of modes from the optical spectrum, as reported in [22], [125], [126]. In order to see this, Figure 4-31(b) illustrates the results of simulations showing the simultaneous effects of GDD and number of modes on pulse width for the 890 μm laser. A stronger dependence of GDD as the number of modes increases is clearly observed. For a small number of modes, the effect of GDD is less important as the mode phases will almost perfectly fit a straight line in which case the modes interfere constructively; however, as the number of modes increases, the modes will begin interfering out of phase due to accumulated dispersion, therefore affecting pulse generation leading to pulse broadening. At 400 mA, the number of modes at -3dB for this laser is ~ 30 from which a GDD=1.3 ps^2 was measured. From Figure 4-31(b), this yields a very broad intensity profile of ~ 9 ps with very low peak powers (as shown in Figure 4-26(b)). In the case of zero GDD or, equivalently, after external dispersion compensation, pulse widths of ~ 600 fs are attainable, in agreement with the experimental results. In this case the pulse width will always decrease when increasing the number of modes as they will perfectly interfere in phase.

Finally, to compare the steady state phase characteristics of the single section devices to that of a classical two-section MLL, the GD and GDD of a two-section laser including a saturable absorber have been measured. The two-section device comes from the same wafer and has exactly the same cavity length as the 48 GHz single section device previously characterized. The saturable absorber section now has a length of 60 μm and the ML regime in this laser is observed when this section is biased in the range between 0.2 and -3V depending on injection current. As in a classical passively MLL, the shortest pulses were obtained for the lowest currents and have been measured down to ~ 1 ps when driven with 70 mA in the gain section and -1.5 V of applied absorber bias, yielding an average power of ~ 4 mW. Under this bias

condition, the GD was measured directly at the laser output as shown in Figure 4-32(a), from which the GDD was estimated at 0.28 ps^2.

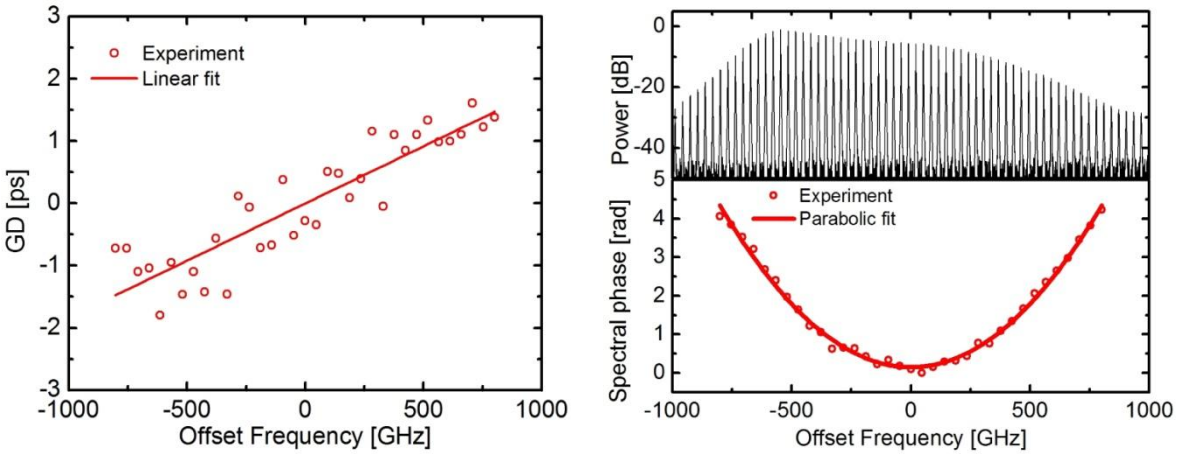

(a) (b)

Figure 4-32. (a) GD of the two-section 890 μm laser measured at the laser output with corresponding (b) (top) optical spectrum and (b) (bottom) spectral phase profile under 70 mA of injection current and -1.5 V of applied reverse bias

As expected, both the GD and GDD were found to be much lower in the two-section device owing to the saturable absorber which periodically phase locks the longitudinal modes. The low GDD value is now evidenced by a clean autocorrelation trace Figure 4-33(a) which is obtained without needing to insert additional SMF for dispersion compensation, and without resorting to optical amplification. The pulse widths were also measured from the reconstructed field intensity (Figure 4-33(b)) and found to be 1.5 ps. The autocorrelation trace yields shorter pulses of 1.2 ps (after deconvolution) as a result of some GDD compensation due to -0.12 ps^2 of accumulated dispersion in our autocorrelation measurement setup. With a spectral width of 9.5 nm, the pulse TBP was calculated at 1.7, but could be reduced to almost the transform limited value by compensating the laser GDD as in the case for the 1-section devices.

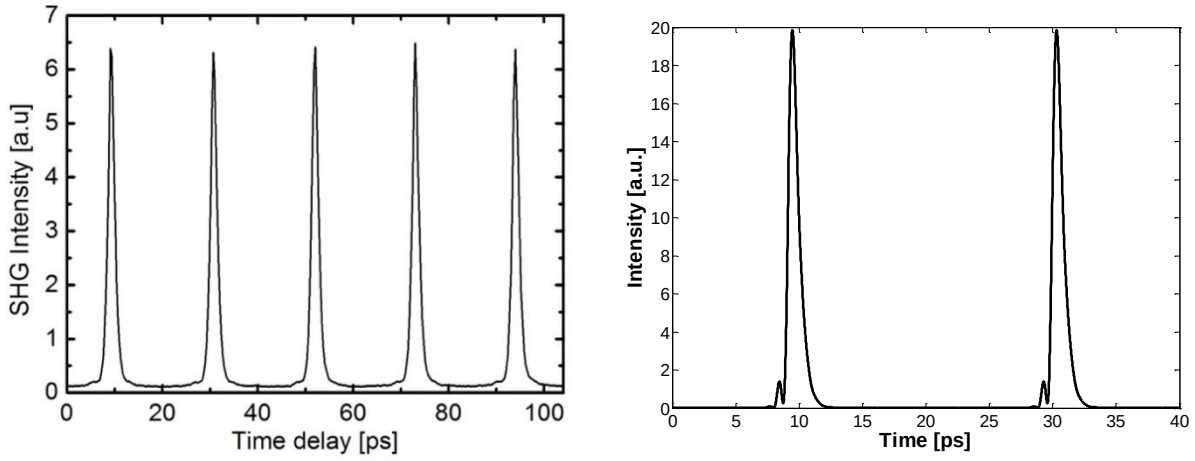

(a) (b)

Figure 4-33. (a) Intensity autocorrelation for the two-section 890 μm laser at the laser output with corresponding (b) reconstructed field intensity profile for a gain current of 70mA and a SA bias of -1.5 V

Figure 4-34 illustrates the effect of fiber propagation on the emitted laser intensity. Contrary to the single section case, one can readily observe pulses right at the output facet. A value of 0.28 ps^2 of GDD is now compensated after propagation through 14 m of SMF, where the pulses reach their maximum peak power and shortest duration.

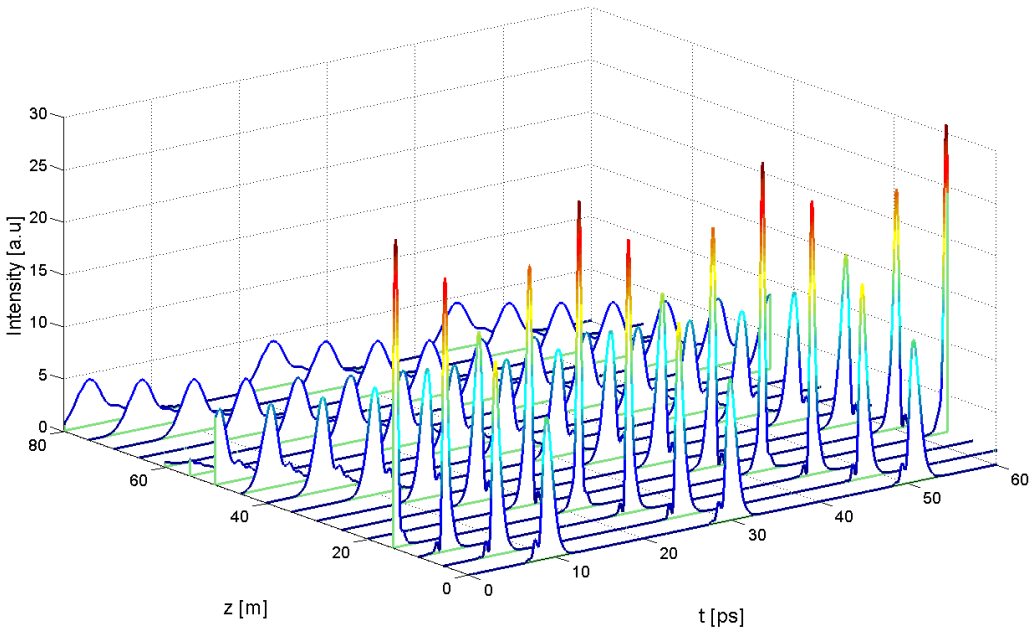

Figure 4-34. Laser field intensity as a function of propagation distance in a SMF for the 890 μm two section laser

The high quality QDash structures of the fabricated devices which led to low threshold currents and high modal gain have allowed two-section mode locking to be achieved at repetition frequencies up to record values of 100 GHz (450 μm cavity length) [127], [128]. The shortest measured AC pulses, together with the lasing spectra are shown in Figure 4-35. In general the minimum pulse width achieved is however slightly higher than for the single section case (after dispersion compensation) due to a narrower bandwidth in the two section lasers owing to the lower bias conditions in which ML takes place in this type of devices.

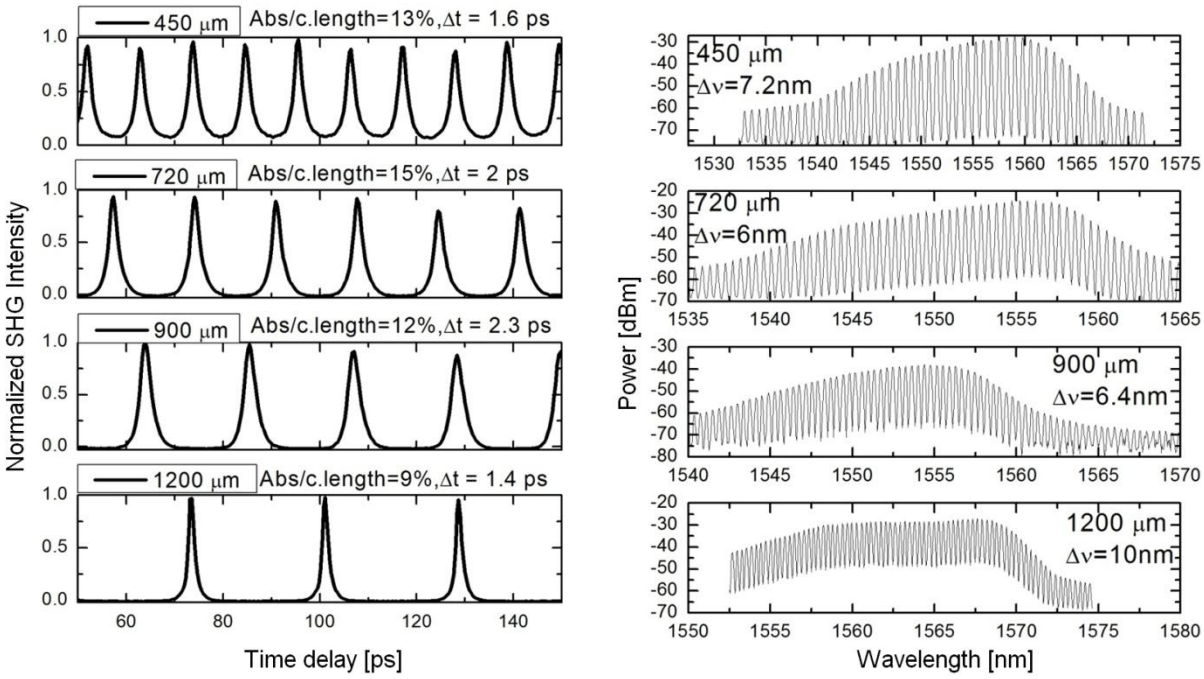

(a) (b)

Figure 4-35. (a) AC trace for the minimum pulse width from different cavity length and absorber to cavity length ratios (Abs/c.length) in two section devices and (b) corresponding optical spectra

In order to systematically investigate the effects of both gain current and absorber bias on the two section devices, the pulse width was estimated by measuring the laser AC intensity. The measurements were carried out on a 17 GHz laser and the results are shown in Figure 4-36. These trends were found to be in general valid for any gain and absorber section lengths. At low SA reverse bias, the SA dynamics are defined by low saturation powers and slow recovery time [6], [75], [80]. At higher SA reverse bias under same gain injection current, the SA can recover faster, resulting in shorter pulses. However, if the SA reverse bias is further increased, the pulses start broadening again while the average output power is very much

reduced due to excess absorption. These observations are in agreement with experimental results for two section QD MLLs, such as those reported in e.g. [8], [122].

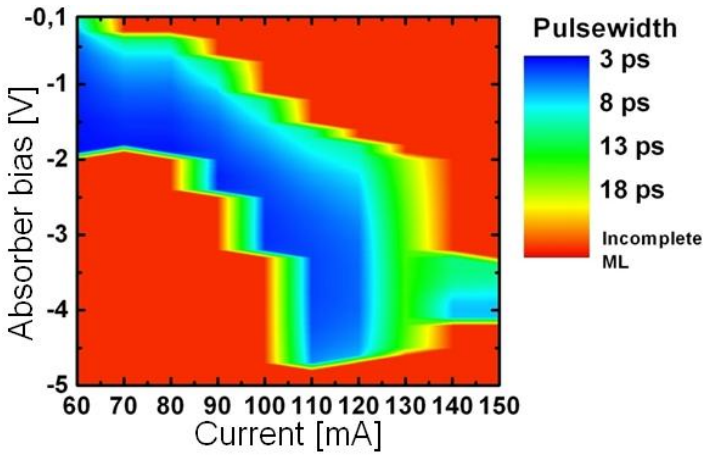

Figure 4-36. Pulse width as a function of bias conditions for a two-section 17 GHz QDash MLL

In conclusion, two-section QDash passively MLLs exhibit a much lower GDD when compared to single section lasers having the same structure and cavity length. However, in order to obtain short pulses, the two-section device needs to be driven with high reverse absorber bias and low injection currents, which results in low average output powers. In addition, biasing the device at low gain currents does not allow to attain a wide spectral bandwidth, which increases with current, hence limiting the generation of shorter pulses. As a consequence, GDD compensated QDash single section MLLs are more advantageous than their two-section counterparts in terms of simultaneously attainable power and pulse width.

4.7. Feedback effect on QDash MLLs

It is well known that optical radiation reflected from optical elements external to the laser cavity can have an effect on the laser performance [129–131]. Indeed, coupling of the laser light beam into the coupling fiber can engender Fresnel reflections from both the near and far fiber ends, as depicted in Figure 4-37. These reflections will be referred to as short and long feedback respectively. Much has been published concerning the effects of feedback in a mode locked laser [123], [132], [133]; however, careful attention must be paid as the distinction between the two different types is seldom made. Indeed, we have identified that

short feedback alone can severely affect the ML behaviour of the QDash lasers under study, significantly obscuring the intrinsic noise properties of the devices and severely degrading system performances. Having its origin on the unavoidable reflections at the coupling fiber facet-air interface, short feedback was found to be very critical as the only practical way to limit it (while preserving a maximum coupling efficiency) was by using commercially available anti-reflection (AR) coated/lensed fibers, which can only reduce the reflectivity down to ~-50 dB. It will be shown that this reflectivity is not sufficient to completely suppress the short feedback effects. Moreover, the specifications for the AR coatings should be taken with caution as they are only valid in a relatively small specific spectral region, which sometimes does not correspond to the spectral range of the lasers under investigation and, as a consequence, some part of it is inevitably always reflected back. The only practical solution to minimize its effects is to intentionally misalign the optical coupling in one or two axes at the expense of a severe reduction in coupled power, representing a great penalty for most foreseen applications. Long feedback effects, on the other hand, are less severe for the mode locking characteristics and were found to be effectively suppressed by inserting an optical isolator.

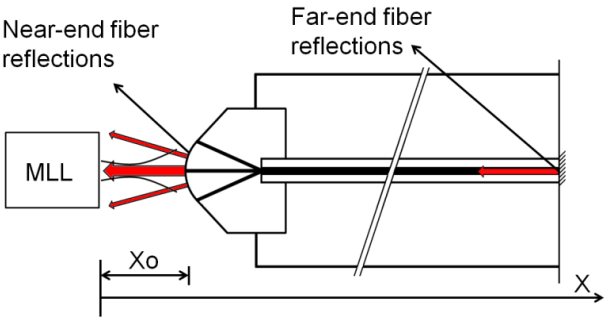

Figure 4-37. Feedback originating from the near and far fiber ends

4.7.1. Short feedback effects

A systematic investigation of the short feedback effects was performed by an analysis of the laser RF spectrum. We have coupled light from the previously characterized 48 GHz single section device when biased at 400 mA into an AR lensed fiber having a -45 dB of reflectivity. The coupling fiber was carefully sliced to an optical isolator (-60 dB) in order to minimize far

end reflections. Detection of the coupled light by a 70 GHz photodiode then allowed for recording the RF spectra measured by an ESA.

Coupling was performed so as to maximize the detected optical power, which typically occurred at Xo~40 μm, from which we obtained 11.6 dBm of coupled power into the fiber. From this point, we increased the separation distance from the laser to the fiber facet in steps of 0.2 μm by using a piezoelectric translator. The RF spectra were recorded as a function of the displacement Δx (x-Xo) up to ~ 3 μm. The corresponding RF linewidth, repetition frequency and RF peak power as a function of Δx are shown in Figure 4-38(a) with some of the measured spectra in Figure 4-38(b).

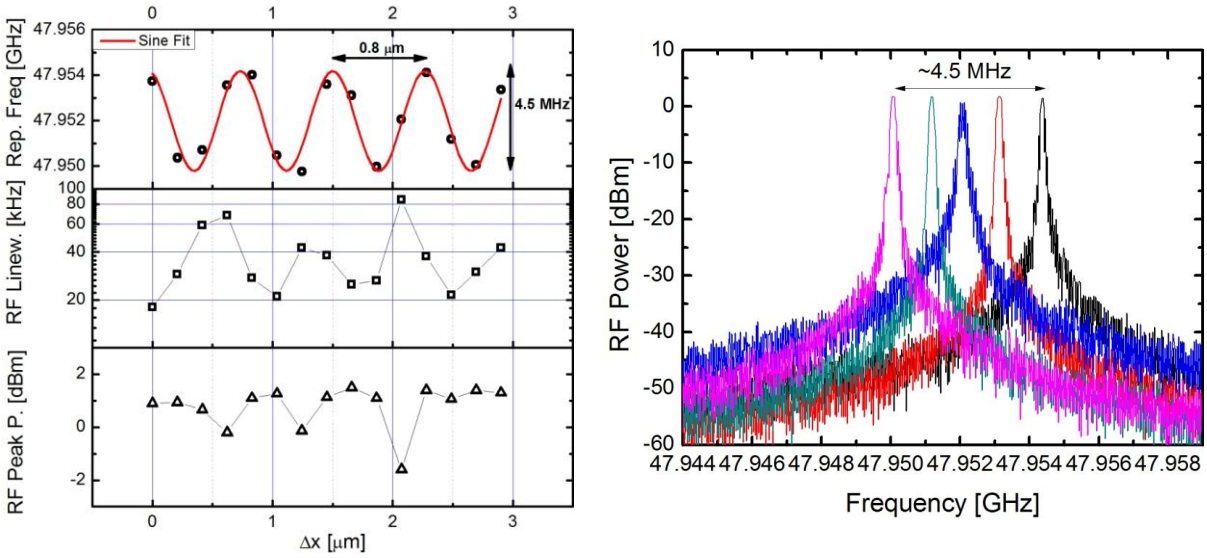

(a) (b)

Figure 4-38. (a) Repetition frequency, RF linewidth and RF peak power as a function of coupling distance displacement starting at 40 μm, (b) measured spectra at different coupling distance positions

The repetition frequency seems to vary almost sinusoidally with a peak to peak excursion of ~ 4.5 MHz and a period of 0.6 μm while the RF linewidth does not show a clear trend, fluctuating around a mean value of ~ 40 kHz with a peak to peak excursion of ~ 80 kHz. It has been observed, however, that there is usually an increase in RF linewidth at repetition frequencies lying in between the extremes, as can be observed in Figure 4-38(b). It is this RF linewidth dependence on the coupling distance at a sub-micron scale which is responsible for the irregular behaviour of linewidth with current as described in section 4.3. Although not

shown here, it was also observed that the same behaviour is exhibited by the optical linewidths. By taking these observations into account, both the RF and the optical linewidths were once again measured as a function of injection current by optimizing the coupling distance in a sub-micron scale so as to obtain the minimum value at each bias condition. The linewidth fluctuations are now much reduced and the optical linewidth trend is now in better agreement with the S-T formula, as shown in Figure 4-39.

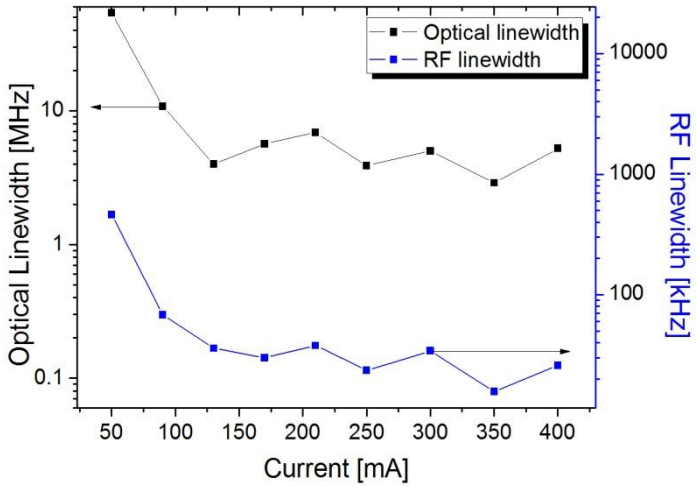

Figure 4-39. Optical and RF linewidth as a function of injection current with short feedback effects minimized

The RF spectra were once again recorded as a function of coupling distance now from a farther point at Xo ~ 150 μm where the coupled power has now decreased down to -8 dBm. This should also translate into a reduction of the short feedback level due to divergence of the optical field. Figure 4-40(a) shows the repetition frequency and RF linewidth excursions, both showing a significant decrease down to 900 kHz and 8 kHz respectively, as can be also seen in Figure 4-40(b). These experimental results suggest that both the repetition frequency excursions and the mean RF linewidth increase with short feedback level.

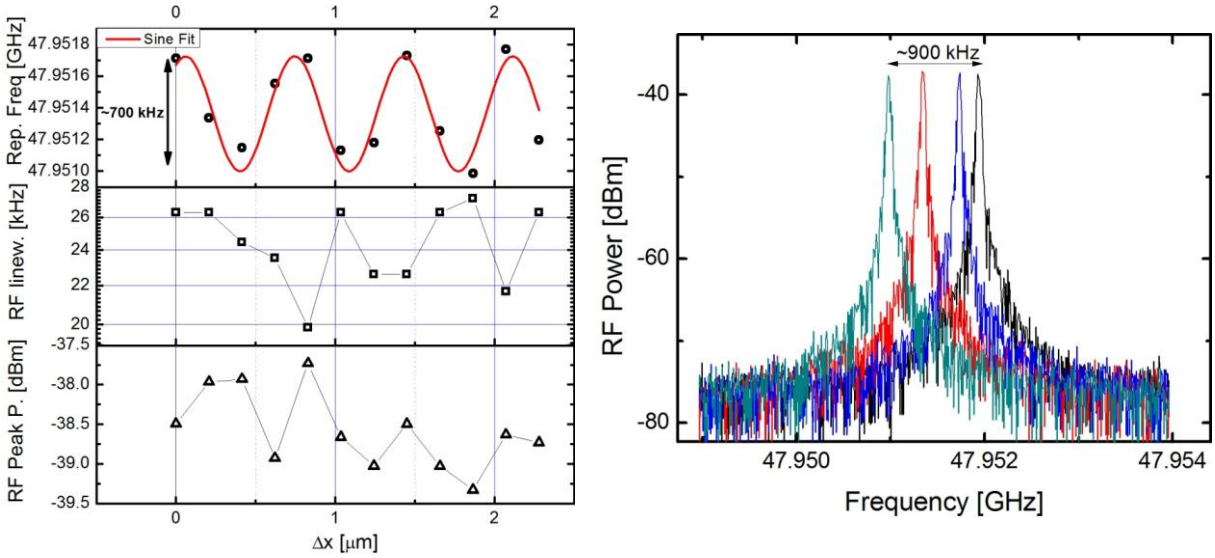

(a) (b)

Figure 4-40. a) Repetition frequency, RF linewidth and RF peak power as a function of coupling distance displacement starting at 150 μm, (b) measured spectra at different coupling distance positions

We are interested now in determining the amount of short feedback that is actually being injected into the laser and what should the maximum allowable level be in order to have stable operation, i.e., a situation corresponding to Figure 4-40, so that the RF linewidth is always kept relatively small independently of Δx. We can translate this into finding the effective reflectivity that would yield a given value of repetition frequency excursion Δf. For this purpose, we have used the very well known transfer matrix approach such as in e.g. [134]. We have used this method for simulating the resonance modes of the laser cold cavity coupled to two external cavities, one corresponding to the short feedback and the second one for the long feedback. Figure 4-41 shows the different cavities with corresponding reflectivities R1 to R4. Of course, this analysis will not take into account the complex laser dynamics nor the effects of the linewidth enhancement factor usually presented in the literature when describing the laser operation under feedback regimes [135–137]. Yet, our simple analysis of the cold cavity coupled to the external ones have proved very useful and in agreement with the experimental observations, independently of the type of laser and or bias conditions used. This fact is also in agreement with feedback investigations on QDash based lasers [138], in which the linewidth enhancement factor was not found to be an important parameter determining the laser feedback sensitivity.

We first take R4=0 (minus infinite in dB) in order to neglect long feedback from the far fiber end. By varying R3 from -80 to -10 dB, we have calculated the optical frequency position of two adjacent modes and the respective laser repetition frequency as a function of distance *x*, as shown in Figure 4-42 for a value of R3=-50dB . From these simulations, the repetition frequency excursion Δf were calculated as a function of R3 and plotted in Figure 4-43

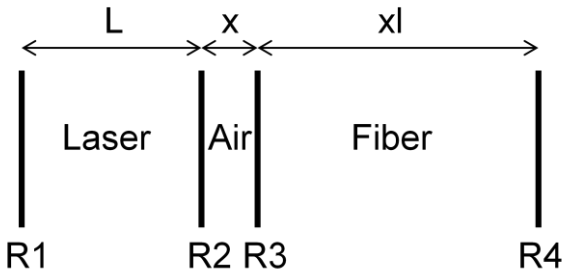

Figure 4-41. Coupled cavities for transfer matrix analysis

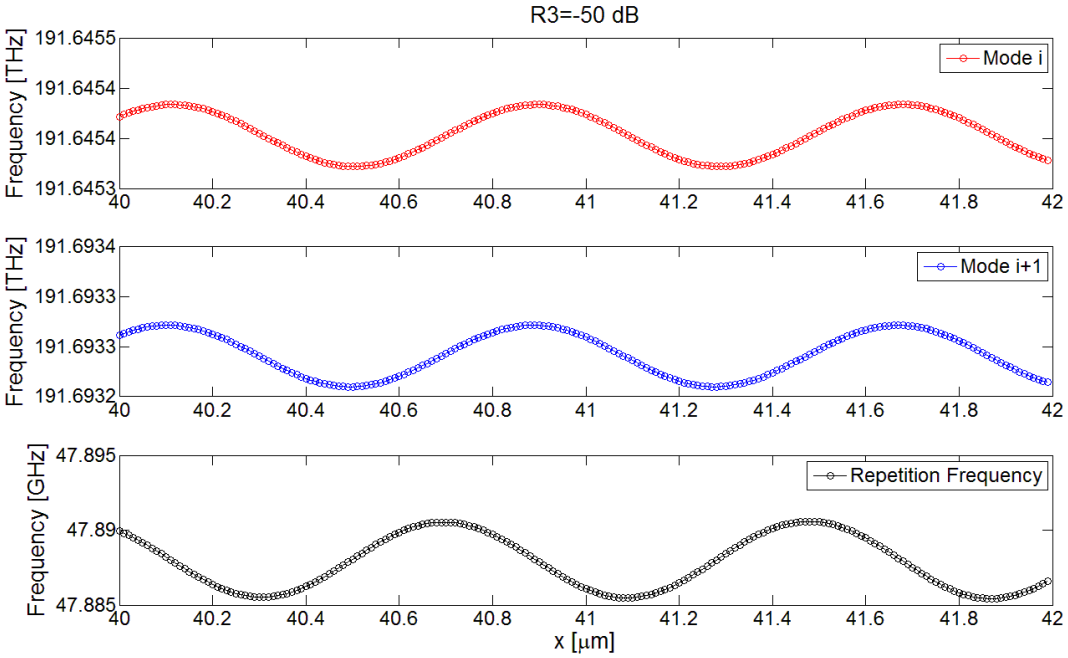

Figure 4-42. Optical mode frequencies and corresponding repetition frequency dependence on coupling distance

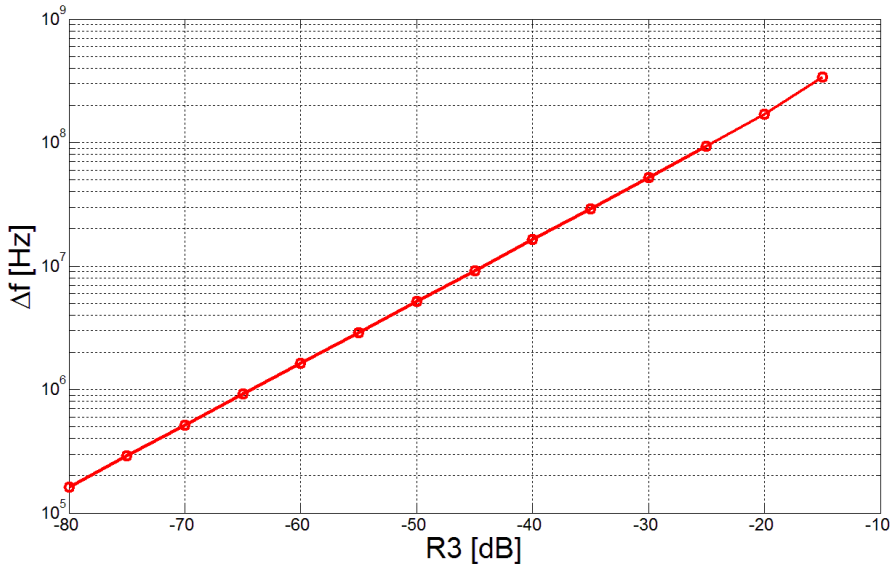

Figure 4-43. Repetition frequency excursions Δf as a function of R3

We can observe an almost sinusoidal dependence of both the cavity mode frequencies and the corresponding repetition frequency with x, in agreement with the previous experimental observations. Interestingly, the repetition frequency excursions Δf were found to vary at a constant rate of 1 dec every 20 dB, as illustrated in Figure 4-43. According to this curve, it may seem that the emitted light from the laser is effectively reflected back with an effective reflectivity of ~-50 dB under optimum coupling conditions (at ~ 40 μm laser-fiber distance), which yields a repetition frequency excursion of ~4.5 MHz, as in Figure 4-38. In order to have a sub MHz Δf, and presumably a better RF linewidth with reduced fluctuations, the effective reflectivity at R3 should be approximately -65 dB or less. It should be noted that this effective reflectivity already includes the losses due to divergence of the optical field, which have been estimated to ~5 dB, in the case of an optimum coupling. This means that the fiber AR coating should be in the order of 60 dB, which was not found in commercially available products. We have nevertheless tested several AR coated coupling fibers from different vendors, some of which claiming a return loss as low as -45 dB. As expected, none of them gave the desired RF spectrum stability with feedback. Only by intentionally decoupling, with the incurred loss in optical power on the order of 20 dB, have we obtained the desired RF spectrum.

After systematic simulations and taking into account the previous considerations, we have fabricated a single section device which is now significantly less sensitive to short feedback perturbations (patent pending). The achieved performance in terms of RF linewidth is now almost 10 times better, as shown in Figure 4-44 , attaining record values for a FP ridge laser of ~ 3 kHz which, in addition, remains constant for any x displacement value of the coupling fiber.

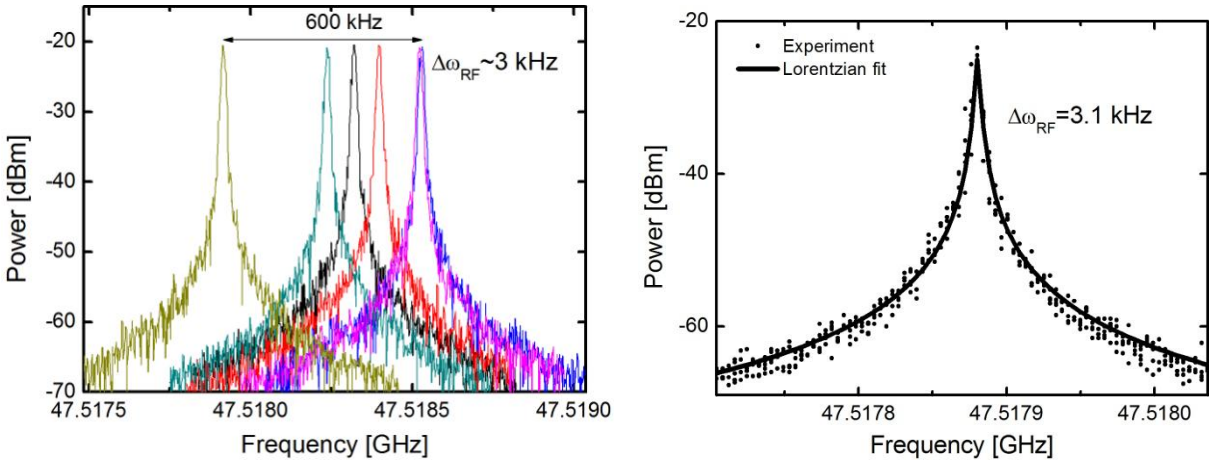

(a) (b)

Figure 4-44. Different RF spectra as a function of coupling distance and (b) high resolution RF spectrum acquisition for the newly designed feedback insensitive laser device

We have already understood the influence of feedback on the repetition frequency of the MLL and used this fact for estimating the maximum allowable level to attain stable operation. We now address the question of why the RF linewidth actually increases due to short feedback. In fact, both the repetition frequency and the RF linewidth vary due to a combined effect of feedback and sub-micron variations of the coupling fiber to laser distance. We attribute these sub-micron variations to environmental acoustic vibrations, i.e. any type of mechanical vibration covering the range of 0-20 kHz. These acoustic vibrations can have amplitudes or peak to peak displacements of up to ~ 2.5 microns [139]. These displacements will modulate the repetition frequency of the laser at a rate corresponding to the noisy acoustic frequencies with a modulation depth which is proportional to the amount of feedback, as already observed. This frequency modulation will then be manifested as a

broadening of the RF spectrum. One may expect that coupling distance fluctuations would result in larger modulation depths near the central repetition frequency while the effects may be much reduced near the frequency limits, in agreement to what is typically observed as in Figure 4-38(b).

4.7.2. Long feedback effects

We considered a fixed long external cavity xl =0.1 m, which is sufficiently long as compared to the 890 μm laser cavity. Long feedback alone did not show to perturb the repetition frequency of the mode locked laser when varying the coupling distance x in a micrometric scale, as illustrated in Figure 4-45 which shows the relative frequency variations (normalized frequency) as a function of coupling distance, from simulations using the transfer matrix approach as before. The figure shows the case corresponding to a typical (using an optical oscillator) R4=-60 dB for two different cases at R3=-45 dB and R3=-infinite. In the first case (R3= -45 dB), the repetition frequency excursions remained the same as without long feedback (R4=minus infinite) in the previous simulations. In the second case, we confirmed that indeed having a finite long feedback alone does not alter the repetition frequency.

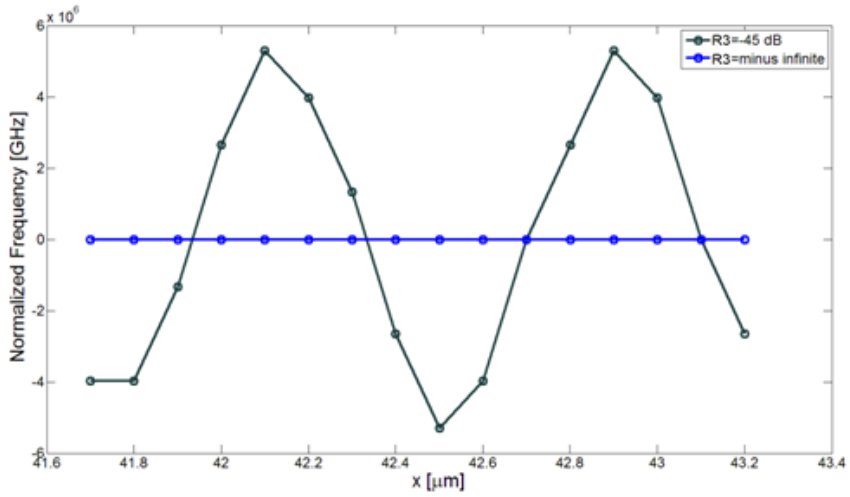

Figure 4-45. Effect of long feedback on the repetition frequency as a function of coupling distance for the case R3=-45dB and R3=minus infinite, for a constant R4=-60dB.

On the other hand, strong and controlled long feedback can be used to stabilize the laser RF spectrum as also reported in a number of papers [123], [133], [140–145]. This fact is illustrated in Figure 4-46, which shows that by including a strong reflectivity R4, with a value

of, e.g., -15 dB, the laser repetition frequency is no longer affected by micrometric changes in the coupling distance x. Of course, the repetition frequency is now sensitive to millimetric changes, and is periodic with a period of 3.1 mm, which corresponds to a roundtrip time in air equal to the roundtrip time of the laser cavity. The repetition frequency excursion is now 1 GHz, corresponding to the fundamental repetition frequency of the fibered external cavity, as depicted in Figure 4-47.

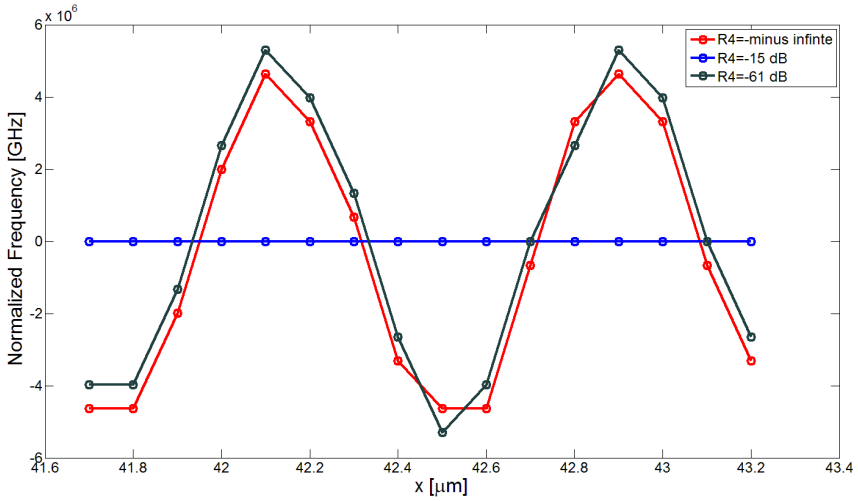

Figure 4-46. Effect of different levels of long feedback on the repetition frequency as a function of coupling distance for a constant R3=-45dB

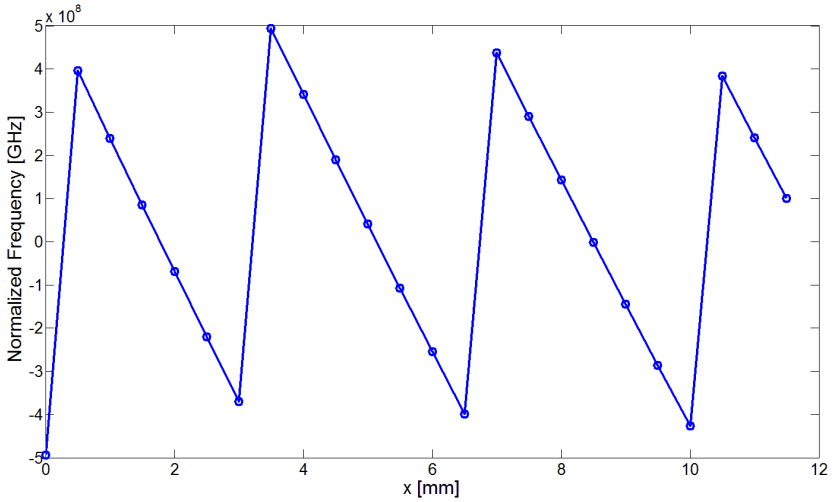

Figure 4-47. Effect of strong long feedback with R4=-15 dB on the repetition frequency as a function of millimetric variations of the coupling distance when R3=-45dB

We have experimentally shown the stabilization of a two section mode locked laser at a repetition frequency of 17 GHz by using this approach. The experimental set-up is illustrated in Figure 4-48 in which the feedback is intentionally introduced by an external mirror with a controlled level achieved by a variable attenuator. The change in cavity length is made in free space by means of a translation stage controlled by a stepped motor.

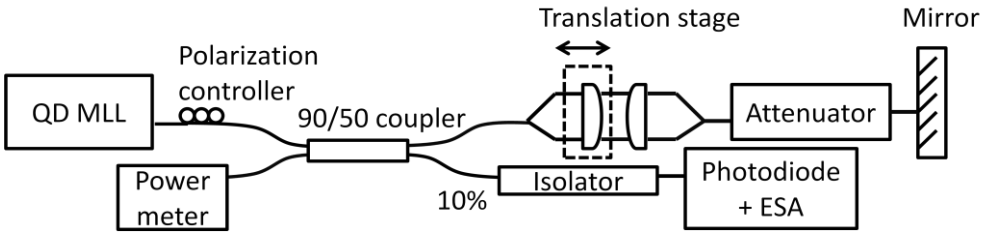

Figure 4-48. Controlled long feedback set-up

For the experiment we used a 2.5 mm (17 GHz) two section laser biased at 120 mA and -1.7 V in the SA section. Figure 4-49 shows the obtained results corresponding to an effective level of feedback (R4) of -24 dB. We obtained the expected repetition frequency trend when changing the external cavity in free space, showing a period of 9 mm for a roundtrip time in air equal to the roundtrip time in the laser cavity. The repetition frequency excursion amounts to about 7 MHz corresponding to the external cavity length of ~ 14 m (amount of fiber from the laser to the mirror). The RF linewidth was also shown to be improved when increasing the feedback level, going from a MHz linewidth down to about 1 kHz for a maximum feedback of -24 dB, as shown in Figure 4-49(b).

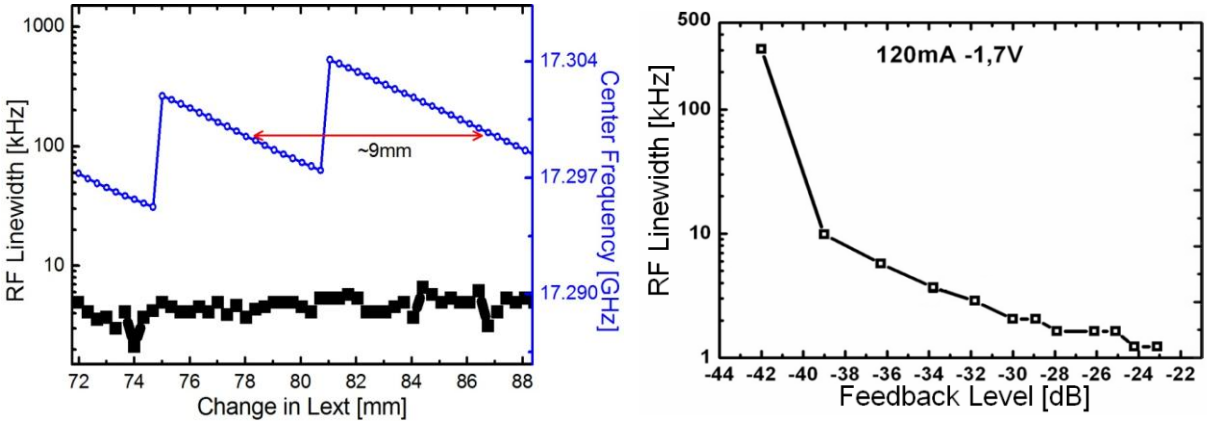

Figure 4-49. RF linewidth and repetition frequency dependence on external cavity length for a long feedback level of -24 dB (b) RF linewidth dependence on long feedback level

In single section lasers, the stabilization of the RF spectrum was also observed; however, the RF linewidth did not exhibit any improvement, probably due to the already narrow intrinsic linewidth of these devices in contrast to the two section case. It should be noted that, although also efficient for stabilizing the RF spectrum, this technique has the inconvenient of introducing external cavity modes which may be very close to the main RF peak and hence may perturb system performance near the RF carrier. These external cavity modes which appear under strong long feedback regime are illustrated in Figure 4-50, showing the RF spectrum for different external cavity lengths for the 890 μm ingle section laser.

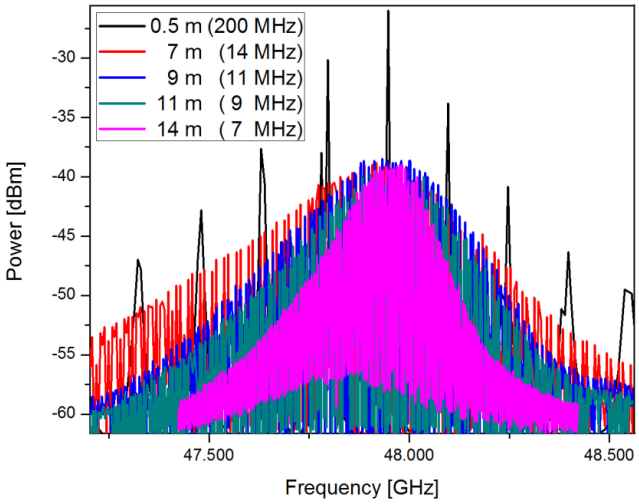

Figure 4-50. RF spectra showing the external cavity modes for a single section 890 μm laser

4.8. Temperature sensitivity of QDash MLLs

Ever since the earlier predictions [7] that the threshold current density of QD based lasers would be relatively independent of temperature due to the 3D confinement of the carriers, there have been lots of research efforts in trying to demonstrate the ultimate temperature insensitive semiconductor laser. Yet, except for very few exceptions [146], this has not in general been accomplished and the threshold current in these devices still exhibits a fast increase with temperature above T~300 K, usually attributed to non radiative recombination mechanisms, similar to the case of quantum well based lasers [147]. This temperature sensitivity is usually quantified by the characteristic temperature T_0 defined as:

$$T_0 = \left[\frac{d\left(\ln\left(I_{th}\right)\right)}{dT} \right]^{-1} \qquad (4.23)$$

Several methods have consequently been proposed in order to achieve higher T_0 values; being p-doping the most commonly used one. Although this technique has proved efficient in obtaining very high values of T_0 in InAs/GaAs QD lasers [148], this usually comes at the expense of higher threshold currents compared to the undoped quantum dot lasers [149].

All of the lasers in this work have been left undoped, consequently only the intrinsic QD behaviour is investigated. In this section we have not limited the study to the temperature influence on the threshold current only, but we have also examined its effects on some of the mode locking properties previously measured at room temperature (~300 K).

The device used for this study was the 890 μm long single section laser. First, the L-I curve as a function of temperature from 15 to 85 C was measured as shown in Figure 4-51(a), from which the corresponding threshold currents were extracted, as depicted in Figure 4-51(b).

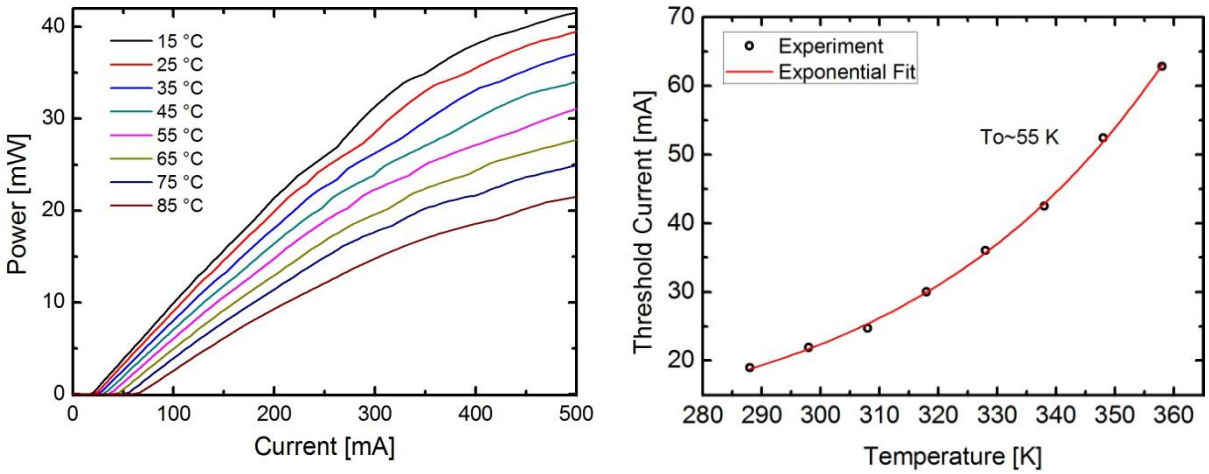

(a) (b)

Figure 4-51. (a) L-I current curves as a function of temperature for the 890 μm long single section laser (b) Threshold current as a function of temperature and T_0 extraction

A T_0 ~ 55 K has been extracted and, although relatively low, this value is in agreement with most reports of undoped QD lasers presenting a T_0 < 70 K [150], which is also similar to that exhibited by quantum well based devices. This poor temperature behaviour of undoped QD

lasers is presumably due to hot carriers populating higher energy states different from the ones used for lasing, therefore, the optical gain required for overcoming the losses is more difficult to attain when increasing temperature. Having deeply confined QD states may help in reducing the temperature sensitivity leading to an increased T_0 in quantum dot based lasers [151].

We have also explored the influence of temperature on the optical spectrum. Figure 4-52(a) shows its FWHM and the corresponding peak wavelength from 15 up to 85 °C. Figure 4-52(b) is the plot of the spectra at 25 and 85 C.

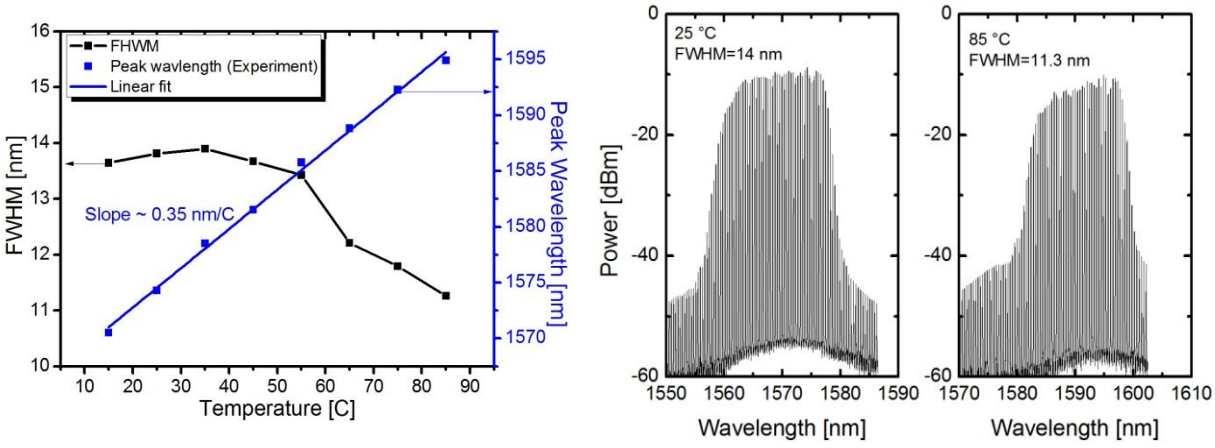

(a) (b)

Figure 4-52. Effect of temperature on the FWHM and peak wavelength of the optical spectrum (b) optical spectra at 25 and 85 C for the 890 μm single section laser

Firstly, a clear red shift is observed with an almost linear dependence of the peak wavelength on temperature at a rate of 0.35 nm/C, a value not surprisingly similar to those reported for quantum well based lasers. Although the previous analysis of hot carriers may rather cause a blue shift, there is also the more important effect of band gap shrinkage due to the increased temperatures, hence, an overall red shift is observed. The FWHM exhibits a slight reduction with temperature probably due to the carrier spread toward energy levels which do not contribute to the main lasing effect. This fact is supported by the intensity increase of the spectrum wings in Figure 4-52(b) measured at 85 C.

Interestingly, the RF spectrum is not severely affected as seen in Figure 4-53 except for a few dB lost in peak power due to a corresponding lost in optical average power. It shows only a

slight increase in the RF linewidth from 13.2 kHz to 15.6 kHz when increasing the temperature from 25 to 85 C accompanied by a ~ -70 MHz shift in the repetition frequency, most likely due to the refractive index *n* dependence of temperature ($dn/dT \sim 10^{-4}\,K^{-1}$ in InP) which translates into an increase in the optical cavity length and consequently into a decrease of 70 MHz of the repetition frequency, in perfect agreement with the experimental results. Mode locking is therefore preserved even at the highest temperatures, representing a major advantage in applications requiring a stable and narrow RF spectrum together with a coolerless operation. Although not investigated as a function of temperature, from the previous results one may expect the pulse widths to be slightly increased (due to the reduction in FWHM of the optical spectrum) while still presenting similar timing jitter characteristics at high temperatures.

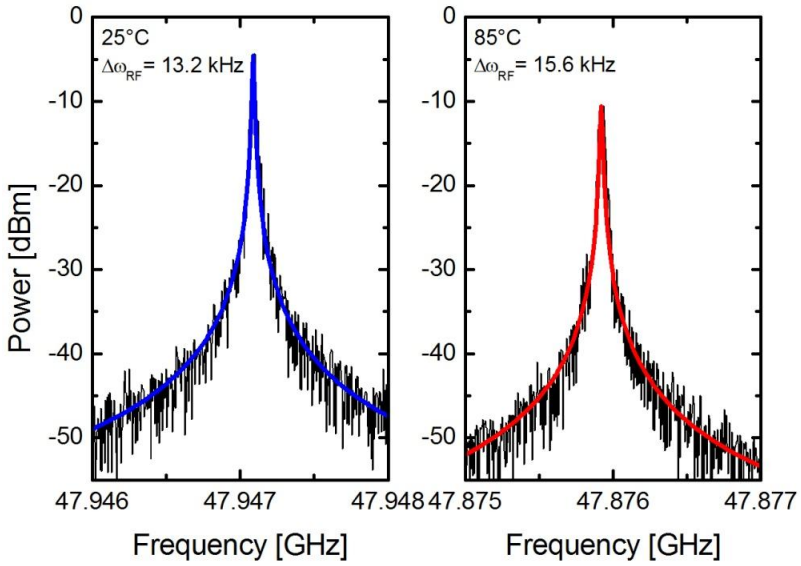

Figure 4-53. Effect of temperature on the RF spectrum at 25 and 85 °C in a single section 890 μm laser

Chapter 5. QDash MLLs for optical communications

By exploiting the knowledge acquired in the previous Chapter on the characteristics of QDash MLLs, we have successfully and efficiently demonstrated the potential of these devices in two different application scenarios in the field of optical communications, namely: broad band wireless access networks and high capacity optical links. This chapter hence presents both a brief review of related state of the art technologies and experimental results showing the high performance of the fabricated devices which, thanks to their exceptionally simple configuration and the low power consuming characteristics, may offer a potentially low cost and environmentally-friendly solution for future implementations of the aforementioned applications.

5.1. QDash MLLs in radio over fiber systems for broad band wireless access

Radio over fiber is a technology in which millimeter wave (30 to 300 GHz) signals are transmitted over an optical fiber link in order to facilitate wireless connections. In the telecommunications arena, RoF technology is emerging as an alternative solution for indoor environments requiring wireless ultra-broadband access. Indeed, the frequency band around 60 GHz offering a 7 GHz license-free bandwidth is a promising candidate for enabling multi Gbps wireless services [152–154]. This would allow to overcoming the bandwidth bottleneck of currently wireless local area network systems of ~100 Mbps, and therefore being able to cope with the ever increasing internet data traffic caused by the fast development of bandwidth consuming services. A number of standards and specifications have recently been defined which make use of the 60 GHz link, including, ECMA 387 wirelessHD, IEEE 802.15.3c and IEEE 802.11ad (release date December 2012), also known as Wigig, confirming the importance of this technology for next generation wireless networks. One

main characteristic of the 60 GHz radio link is the high air loss of about 80 to 85 dB after a few meters of propagation which enables a large frequency reuse factor per indoor environment. As a consequence, a large number of radio access points are required in order to provide full area coverage, hence the necessity of an indoor high capacity network in order to link the different radio access points together and to expand the limited radio coverage [46]. Owing to its large bandwidth, low loss, immunity to electromagnetic interference and future-proof, optical fiber links may therefore efficiently serve as the transport means for distributing wireless signals in future broadband wireless access networks. Figure 5-1 illustrates the main concept of a RoF system for a broadband wireless access implementation in indoor environments. The major elements are the central unit, which enables the conversion from a baseband transmission (fiber to the home FTTH technology) to a RoF transmission scheme, and the remote access points for indoor wireless distribution.

5.1.1. Millimeter wave generation

As already discussed, a RoF implementation requires conversion of a baseband signal into an optical signal as well as conversion to the 60 GHz frequency window for wireless transmission. This is known as frequency up-conversion and involves the generation of a millimeter wave, for which a number of techniques have been reported. It should be noted that substantial progress in technologies based on silicon, such as silicon germanium (SiGe) and baseline complementary metal-oxide semiconductor (CMOS) have recently led to significant improvement in the frequency response of devices based on these technologies which have also demonstrated remarkable integration levels [155–157] , making them potential candidates for low-cost pure-electric millimeter wave generation. There exists, however, several alternative approaches based on optical frequency up conversion which may present some advantages in terms of overall cost and system complexity by centralizing the broadband up-conversion functionalities into a single unit (central unit) instead of realizing direct electrical up conversion at every access point. The main optical up conversion techniques are based on dual or single laser sources and are briefly discussed below.

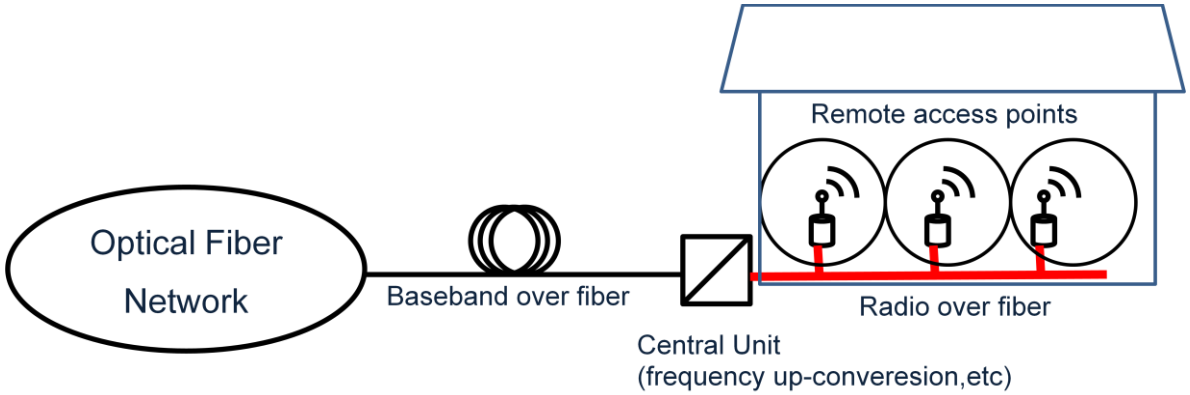

Figure 5-1. RoF system for wireless distribution in indoor environments

Dual laser source schemes:

The outputs of two CW lasers are tuned so that they have a frequency offset (f2-f1) corresponding to the desired millimeter wave frequency. Both CW signals are then mixed and heterodyned in the receiver. One or more of the heterodyning products is the required millimeter wave which is obtained after photodetection with a high speed photodiode, as illustrated in Figure 5-2. This technique, however, can suffer from large frequency drifts and increased phase noise if both laser emissions are incoherent, which is the case if the lasers are independently operated, although this maybe, up to some extent, overcome by applying incoherent demodulation techniques, such as RF self-homodyning [158], optical phase locked loops [159] and optical injection techniques [160] . An advantage of this technique is its insensitivity to dispersion of the optical fiber and consequently to power fading effects, as will be further explained. Other disadvantages include the need of two or more laser sources, therefore a lack of compactness and increased complexity, besides from the poor phase noise performance if left unmanaged.

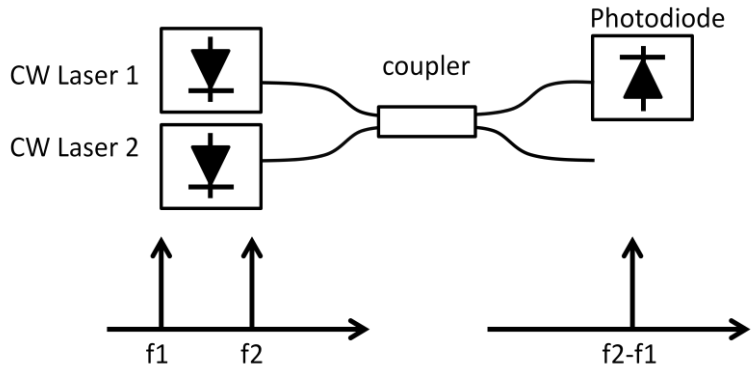

Figure 5-2. Dual laser source scheme for millimeter wave generation

Single laser source schemes:

-External modulation of a CW laser:

Modulation of a CW laser by means of an electro-absorption or a MZ modulator driven by an RF signal at a frequency *fs* can result in the generation of two side bands on either side of the CW optical carrier, which after photodetection by a fast photodiode can yield the desired millimeter wave for RoF transmission at a frequency of *2xfs*, as illustrated in Figure 5-3. The generated millimeter wave has generally low phase noise and exhibits high stability as these characteristics will be determined by the driving external RF signal.

This technique however employs large RF driving powers in order to obtain the required modulation depths. Besides, the modulator can also introduce large amounts of insertion losses, leading to low signal to noise ratios. It is also clear that this scheme does not represent a compact or a low power consumption technique. Several research groups have nevertheless reported on successful RoF transmission by employing this scheme [161], [162].

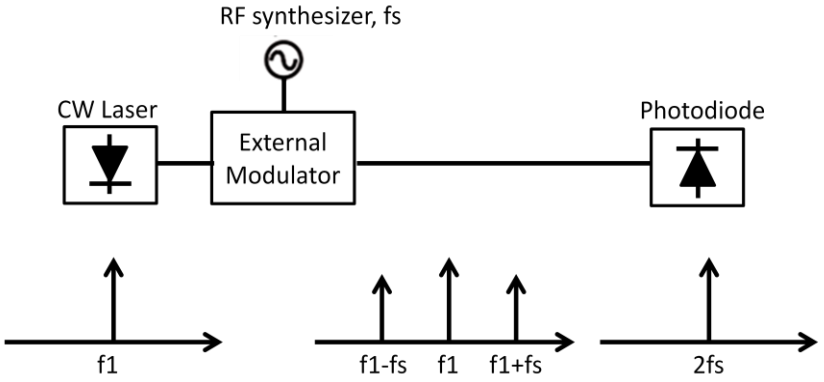

Figure 5-3. Milimmeter wave generation by using an external modulator

-Passively mode locked laser:

A very simple, compact, low cost and low power consumption technique for optical up conversion may be implemented by using a single mode locked laser diode (see Figure 5-4) presenting high performance intensity phase noise characteristics. Particularly, a single section passively QDash based mode locked laser with a repetition frequency of ~ 60 GHz can represent an attractive solution for millimeter wave generation [45], [46] provided it exhibits a stable and narrow RF spectrum. Besides, as will be shown, the QDash MLLs can also exhibit large modulation bandwidths which can enable its direct modulation with the broad band data signals, further simplifying the overall system implementation.

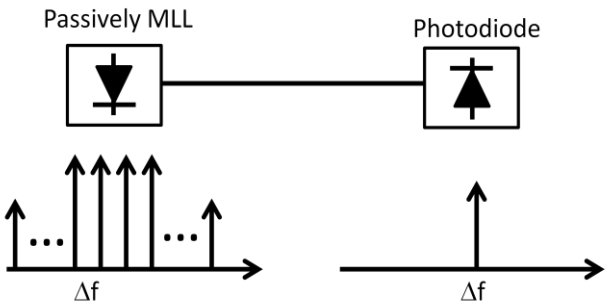

Figure 5-4. Milimmeter wave generation by using a passively MLL

5.1.2. Down link experiments in a RoF system for indoor wireless access networks

We have conducted optical up-conversion experiments and direct modulation for simulating the down-link in a typical RoF indoor environment. These experiments have been carried out in collaboration with Orange Labs, Lannion, within the framework of the French ANR project TELDOT. For this purpose, we have employed the passively mode locked laser approach by using a QDash single section device which was fabricated so as to be insensitive to short feedback reflections. The laser has a cavity length of ~780 μm which results in a repetition frequency of ~55 GHz. The RF spectrum is narrow and stable around a number of bias conditions regardless of mechanical fluctuations or technical vibrations, and it is shown in Figure 5-5(a) for an injection current of 250 mA, exhibiting a corresponding RF linewidth of ~7 kHz. Another important laser characteristic for system cost reduction and simplification would have to be its modulation bandwidth, which will need to be large enough in order to allow for direct modulation without requiring external modulators. The frequency response of the laser exhibits modulation bandwidths in excess of 7 GHz depending on bias conditions as shown in Figure 5-5(b).

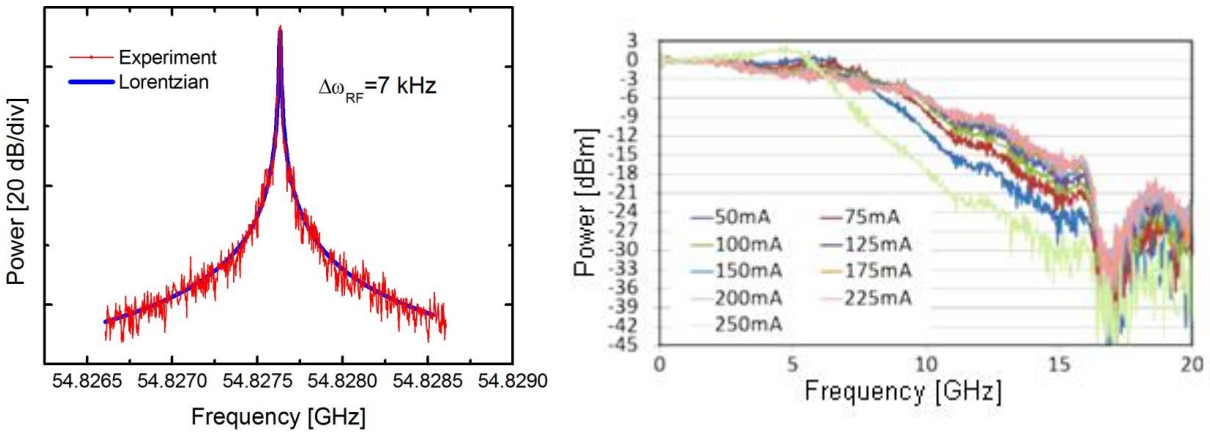

(a) (b)

Figure 5-5. (a) RF spectrum for the 780 μm long laser used for the RoF experiments (b) Frequency response as a function of injection current for assessing the modulation bandwidth

The experimental set-up is presented in Figure 5-6. The test data signal is compliant to the IEEE802.15.3c standard and carries up to 3 Gbps for indoor multimedia applications. We have chosen to use OFDM as the modulation scheme. The OFDM signal is created on a PC

using Matlab with an FFT block size of 512 with 336 data sub carriers. Each sub carrier is modulated in QPSK. The baseband is sampled at 2.59 GHz. A total raw data rate of 3.03 Gbps is achieved for a bandwidth of 1.87 GHz.

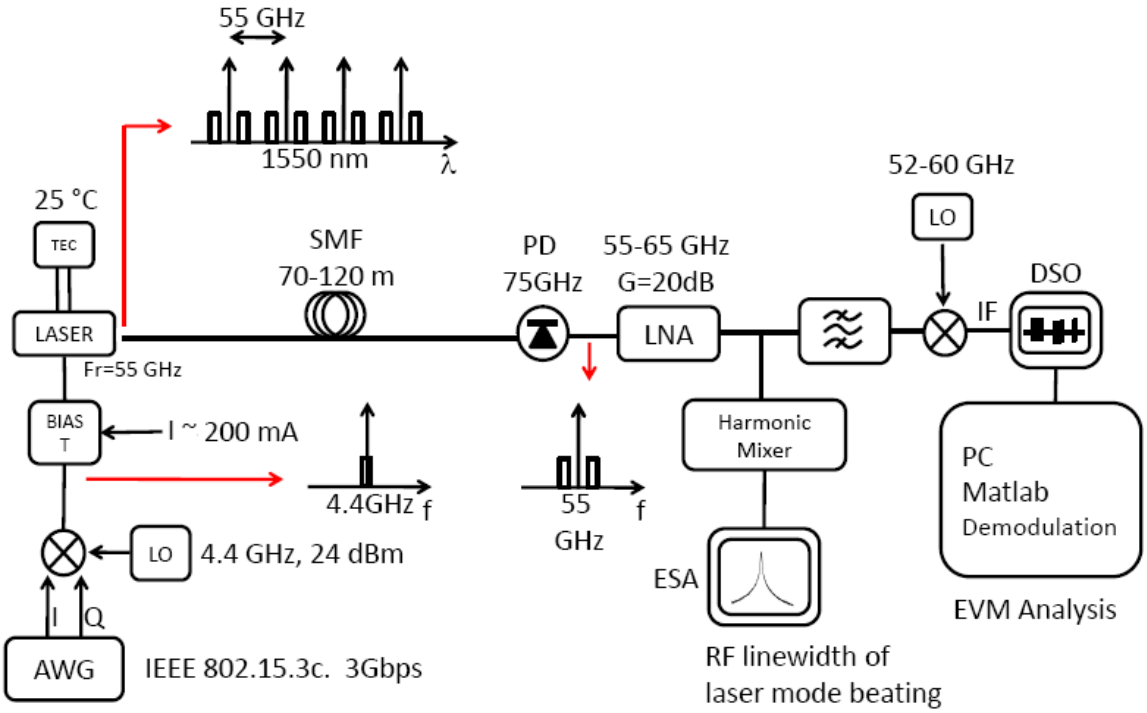

Figure 5-6. Set-up for the RoF transmission experiments

The signal is generated by a 10 GS/s dual output Arbitrary Waveform Generator (AWG) and both outputs (representing both I and Q components) are sent to a RF mixer to generate the radio signal on a 4.5GHz carrier. Direct modulation of the laser when biased at 250 mA was possible owing to the relatively large modulation bandwidth of the device above 7 GHz at this bias current. This modulation bandwidth is sufficient to accommodate the 1.87 GHz baseband data signal centred at 4.5 GHz which was then used for direct modulating the laser via a bias tee. The modulation process generates sidebands at either side of the optical modes separated from 4.4 GHz, as illustrated in Figure 5-6 at the laser output. Transmission through standard single mode fiber is subsequently performed. Typical indoor environments would involve transmission through some 10s up to 100 meters to account for the distance from the central unit to the remote access points. Due to the large spectral width of the laser source (27

modes for a FWHM=12 nm at 250 mA) and the dispersion characteristics of the SMF, propagation through the fiber will result in interference phenomena among the different mode beats leading to fading of the RF power upon photodetection, in the same way pulses emitted from the laser experience broadening and shaping effects as described in Chapter 4. Figure 5-7(a) shows simulations illustrating this effect assuming 27 equalized modes separated by 55 GHz propagating through a lossless fiber with ~-20 ps^2/km of group velocity dispersion. The figure compares the case of the laser presenting a hypothetical GDD=0 and the realistic GDD= 1 ps^2 for the laser used in this experiment.

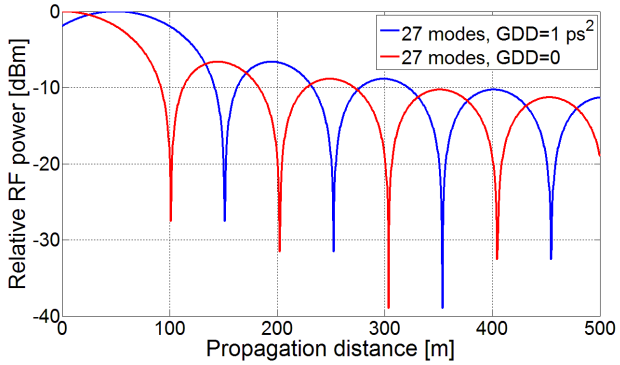

(a)

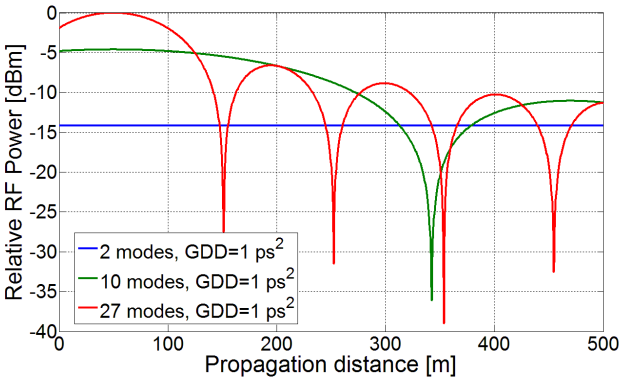

(b)

Figure 5-7. (a) RF power fading effect for a laser exhibiting GDD= 0 and GDD= 1 ps^2 (b) RF power fading effect as a function of number of modes for the same value of GDD= 1 ps^2

The nonzero positive GDD value of the single section devices can be seen as an advantage in this case as it may allow for the recovery of the maximum RF power at the remote access

points after the required propagation distance of a few 10s of meters (50 m in this case) as shown in Figure 5-7(a).

It should be noted that the fading effect may completely be overcome by limiting the number of modes propagating across the fiber, as illustrated in Figure 5-7(b). This can be achieved monolithically by introducing a DBR section or by including an external element acting as an optical filter for reducing the number of propagating modes. Yet an easier solution would be to simply take into account the GDD of the laser and using the right amount of SMF, which may be combined with dispersion shifted fiber (DSF) for extending the propagating distance beyond 100 m if necessary, in other words, by simple dispersion management of the RoF system.

By taking into account the laser GDD so as to maximize the RF power at the access point, the modulated optical signal is sent through 50 m of SMF after which is detected by a 75 GHz bandwidth photodiode. Following photodetection, two up-converted copies of the original data signal centered at 4.4 GHz are available: the first one at ~50 GHz (55-4.4 GHz) and the second one at ~ 60 GHz (55+4.4 GHz), together with a very strong RF peak at ~55 GHz corresponding to the laser intensity spectrum without modulation. The RF signals are then amplified by means of a 20 dB low noise amplifier (LNA). In order to obtain a proper up-converted signal, only the upper modulation sideband is recovered by means of a band-pass (57-62 GHz) filter. At this point the up-converted radio signal centered at 60 GHz is ready for broadcasting into the air.

In order to assess the quality of this signal, we performed its down-conversion to ~5 GHz using a mixer fed with a local oscillator (LO) at 55 GHz. The intermediate frequency signal is then captured by a 40 GS/s Digital Sampling Oscilloscope and demodulated “offline” on a PC running Matlab. Its error vector EVM is computed, which measures the noise variance of the signal in the constellation diagram with respect to that corresponding to an ideal transmitter, hence quantifying the performance of the actual transmitter. The best results are displayed in Figure 5-8, which were obtained for bias currents around 250 mA showing a mean EVM value of 12% with a signal to noise ratio (SNR) of 25 dB demonstrating successful demodulation of the up-converted data. The EVM value was found to be directly correlated to the value of the RF linewidth, being the worst at the lowest injection currents

corresponding to the widest RF spectra, hence the importance this laser parameter and the need for minimizing the effects of optical feedback.

Although similar performances yielding EVM values ~11% have already been reported by using the same approach [46], a number of improvements have been introduced with the introduction of the feedback insensitive device. Indeed, early experiments making use of conventional FP QDash lasers were very much affected by short feedback effects, as described in Chapter 4. This resulted in an increased phase noise of the millimeter wave carrier which exhibited, at the lowest, a few 10s of kHz of RF linewidth. Moreover, the narrowest linewidths, and consequently the best overall system performance, were usually obtained at the expense of intentionally misaligning the laser to fiber coupling so as to minimize the feedback effects, resulting in significant RF power loss and the need of an EDFA at the laser output. In our experiments, we did not require amplification of the modulated signal, which represents an important advantage in terms of costs and practical system considerations. Besides, owing to the insensitivity to feedback reflections, the generated carrier was at all times stable without exhibiting significant frequency drifts. Despite these significant improvements, the obtained EVMs were not found to decrease compared to previous experiments, as could have been expected. We attribute this result to the external RF components in the experimental set-up which were limiting the minimum value of achievable EVM, as was later confirmed by back-to-back experiments using all-electronic up-conversion yielding an EVM of 11%, setting a lower limit in the minimum achievable EVM by using the optical up conversion technique.

Among future perspectives for this application is the growth optimization of the QDash active layers in order to further increase the differential gain so as to achieve higher modulation bandwidths, allowing for 10 Gbps data rates for ultra-broadband wireless access.

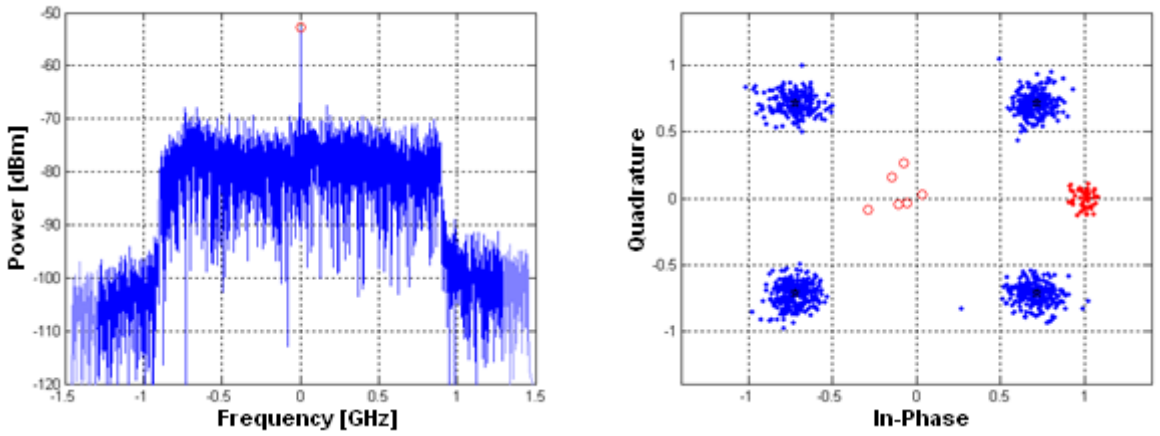

(a) (b)

Figure 5-8. (a) Spectrum of the demodulated signal and (b) corresponding constellation diagram for EVM estimation

5.2. QDash passively MLLs in OFDM superchannel systems for high capacity optical networks

5.2.1. OFDM superchannels

The current maximum capacity of long-haul transmission systems of around 1 Tbps is not sufficient to cope with the increased data traffic caused by the fast development of bandwidth consuming services. In today's systems, wavelength division multiplexing (WDM) is used to allow a single optical fiber to carry multiple independent channels at different wavelengths. However, the inefficient modulation formats and the unused gap between different channels in currently WDM systems do not allow for efficient use of the available bandwidth in optical fibers. In order to prevent the need to install new fiber cables (which is extremely costly) it is necessary to develop novel and spectrally efficient transmission schemes which can increase the capacity of installed fiber systems to meet the increased bandwidth demand. Recently, the use of optical OFDM based superchannels has emerged as a promising technology offering a much higher spectral efficiency and a better tolerance to transmission impairments like dispersion.

There are currently two approaches for generating OFDM based superchannels. One is to generate individual OFDM signals by all electronics means by employing digital signal processing (DSP) techniques, and then use the generated OFDM signals for individually

modulating a set of CW lasers or (as we will propose) a single mode locked laser comprising a set of *N* longitudinal modes or sub-channels, equally separated and power equalized (frequency comb), as depicted in Figure 5-9. Depending on the reception scheme, this approach may be referred to as direct detection OFDM (DD-OFDM) or coherent OFDM (CO-OFDM). A second approach for OFDM based superchannels consists in generating the OFDM signal in an analogue fashion in the optical domain; hence it is referred to as all optical OFDM (AO-OFDM). In this case a set of CW lasers or a laser generating a frequency comb is once again necessary, this time for directly generating the orthogonal subcarriers that will be individually QAM (quadrature amplitude modulation) modulated and subsequently combined for creating the optical OFDM signal, as illustrated in Figure 5-10.

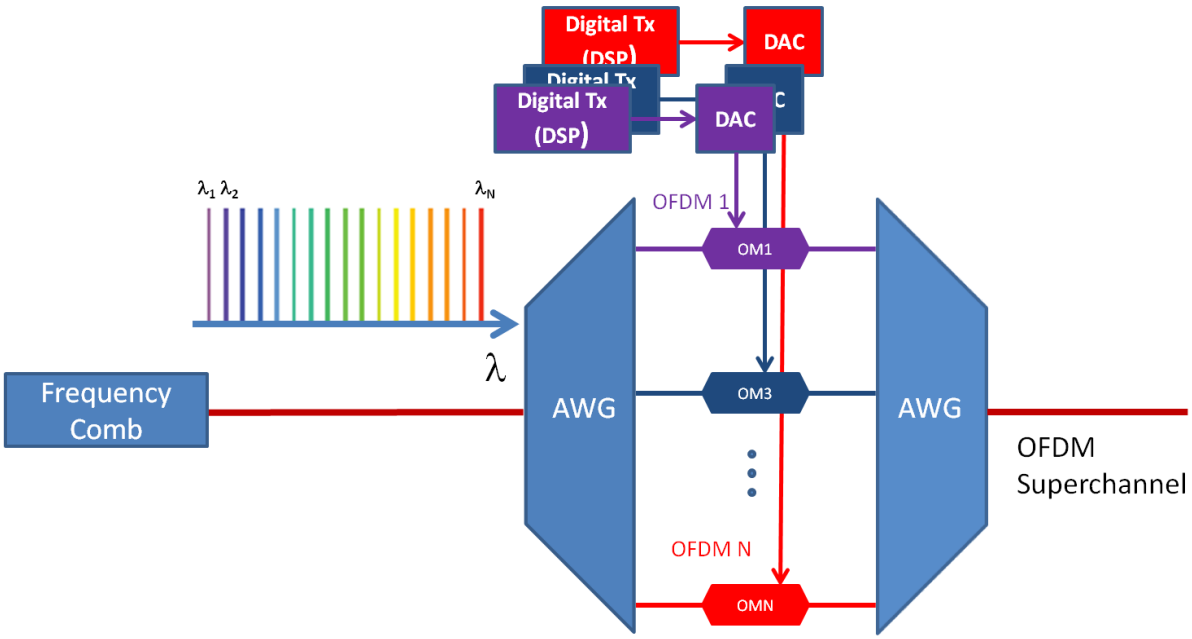

Figure 5-9. OFDM transceiver based on digital signal processing for OFDM superchannel transmission

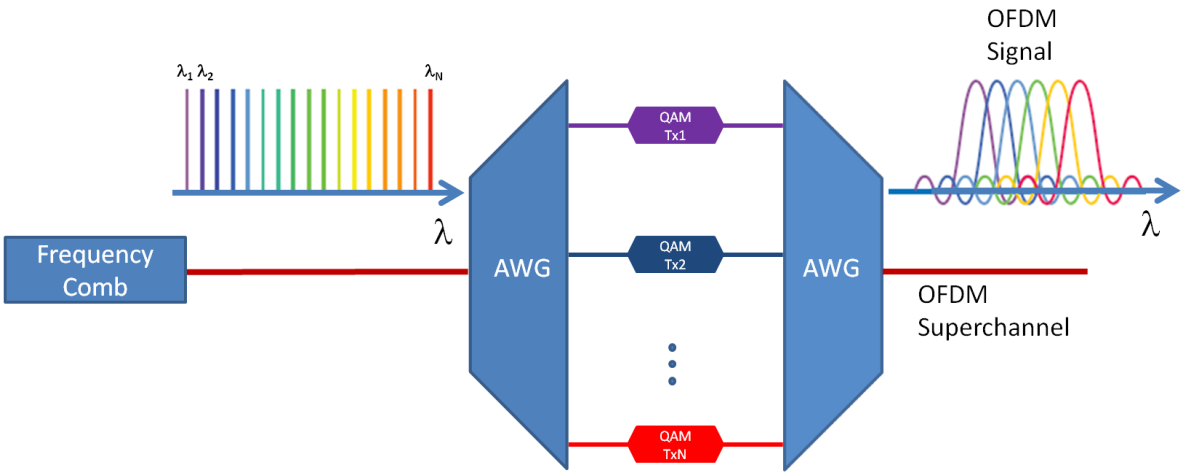

Figure 5-10. All optical OFDM transceiver for OFDM superchannel transmission

Ultra-high bit rates in excess of 1 Tbps have already been demonstrated by several groups [29], [32], [38], [163] by using both approaches. In any case, a key enabler for this technology will be a low cost technique for generating the aforementioned equally spaced sub-channels, which are also required to be large in number, power equalized and optionally, for coherent detection, with low phase noise or narrow optical linewidths. Among the techniques for achieving this are the use of a bank of single wavelength lasers [163], cascaded electro-optic modulators [32], single-side-band modulators based on recirculating frequency shifters [38] and mode locked lasers [29]. These techniques have proved, however, to present a number of drawbacks. For instance, the use of independent single wavelength lasers requires accurate control of each of the emission wavelengths in order to achieve precise sub-channel separations. In [163], a record transmission rate of 101.7 Tbps was achieved, but this involved the use of 370 independent lasers (370 sub-channels), each requiring independent power sources and temperature controllers to overcome temperature instabilities, making the system extremely expensive. Modulating a single wavelength laser can result in the generation of a number of sub-channels; however, modulation-based techniques suffer from stability problems due to the nonlinearity and DC bias of the modulator while only providing a relatively small number of sub-channels. A single MLL, on the other hand, provides inherently frequency-locked sub-channels that are perfectly equidistant to each other without the need for external modulators [29], making it a more

appealing technique in terms of simplicity, stability and cost. Current implementations based on MLLs however, make use of solid state lasers which are only able to offer a reduced number of sub-channels due to the limited available bandwidth in this type of MLL, requiring additional techniques and system components to further increase the number of sub-channels. This was the case in [29], where the authors were required to perform additional amplification and to use highly nonlinear fibres in order to increase the overall bandwidth of the optical frequency comb from 3 nm (~400 GHz) to 15 nm (~2 THz). However, besides the additional complexity and costs introduced, this spectral broadening technique also results in an irregular shape of the spectrum which forces the use of an optical equalizer, or filtering device, in order to adjust the power of each sub-channel to the same value. In order to avoid these added difficulties, we propose the use of a single QDash based MLL. As we have seen in Chapter 4, these devices have proved to exhibit a very flat spectrum of up to ~15 nm width without the need of any form of modulation or external equalization. Besides from providing wider bandwidths, QDash MLLs are also much more compact, less power consuming and easy to fabricate, making them attractive for sub-channel generators in future OFDM based superchannel systems [164].

5.2.2. DD-OFDM experiments for high capacity superchannels

These experiments have been carried out in collaboration with DCU, in Dublin, Ireland, within the framework of the EGIDE Ulysses project. The previously characterized 48GHz QDash laser in the single section configuration was used for implementing DD-OFDM. The choice for a direct detection scheme was the relatively large optical phase noise of the QDash lasing modes which were determined not to be amenable with a coherent scheme. One disadvantage encountered when applying DD-OFDM is the requirement of a guard band between the optical carrier and the OFDM sidebands in order to avoid chromatic dispersion induced power fading upon direct photodetection if standard double side band modulation is used [165], in a similar way the mode beats interfere destructively as already described in the previous section . This guard band will hence reduce the overall spectral efficiency of the system. One technique to overcome this downside is by implementing single side band (SSB) modulation in which case the use of a guard band is no longer needed [166]. We have therefore used OFDM in a single-side band direct detection OFDM transmission experiments using an approach similar to [166]. The SSB OFDM signal which consisted of 74 subcarriers

each encoded with 16QAM, was modulated onto 33 significant modes (those comprised in the FWHM spectral width of the optical spectrum as seen in Figure 5-11) of the 48GHz laser comprising a spectral bandwidth of ~1.5THz, when biased at 300 mA. Of course, in a more realistic experiment, each of the lasing modes should be individually modulated as shown in Figure 5-9. The experiment is however useful for demonstrating a first proof of concept of the proposed system. The setup is shown in Figure 5-11 where the spectral modes of the QDash laser were encoded with the OFDM data using a dual-drive MZ modulator and transmitted across 25 km of SMF, where it was received and digital signal processing (DSP) was performed offline using Matlab after individually filtering the corresponding mode for analysis. The plot in Figure 5-12 shows the received constellation diagrams for one spectral mode (at 1558.55nm) before and after transmission. The error-vector magnitude (EVM) of the back-to-back data was 11% and after 25km SMF transmission was 13.4%, and the calculated bit error rates (BER) for both cases were below the necessary $1x10^{-3}$ threshold for systems employing forward error correction (FEC) of 7%.

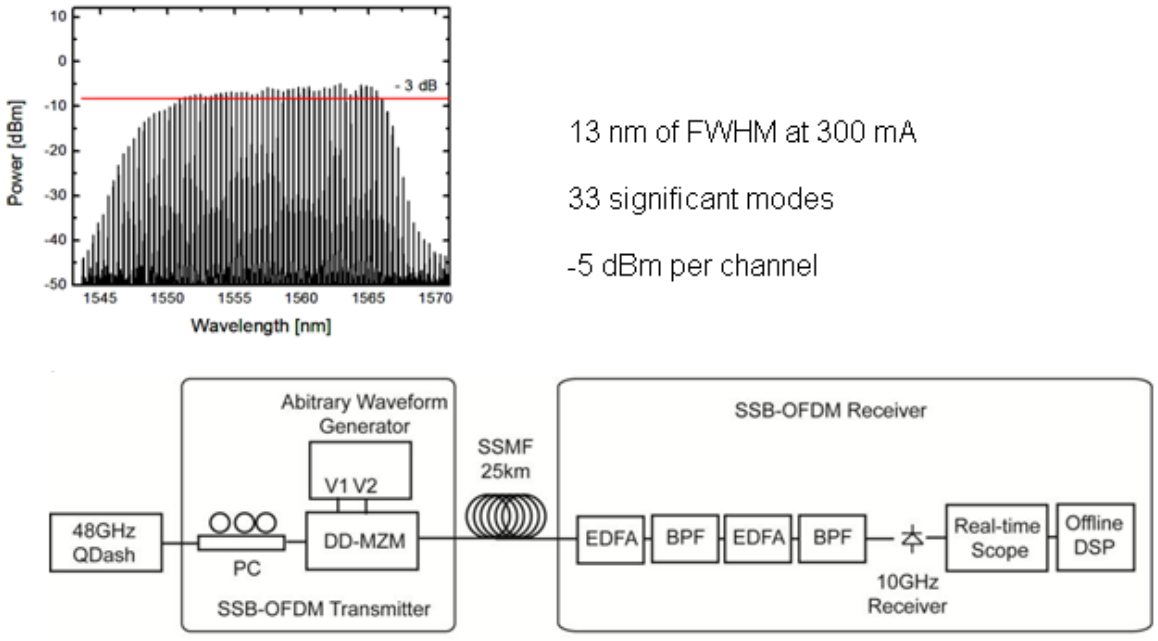

.

Figure 5-11. Spectrum characteristics of the laser used for the OFDM transmission experiments and experimental set-up

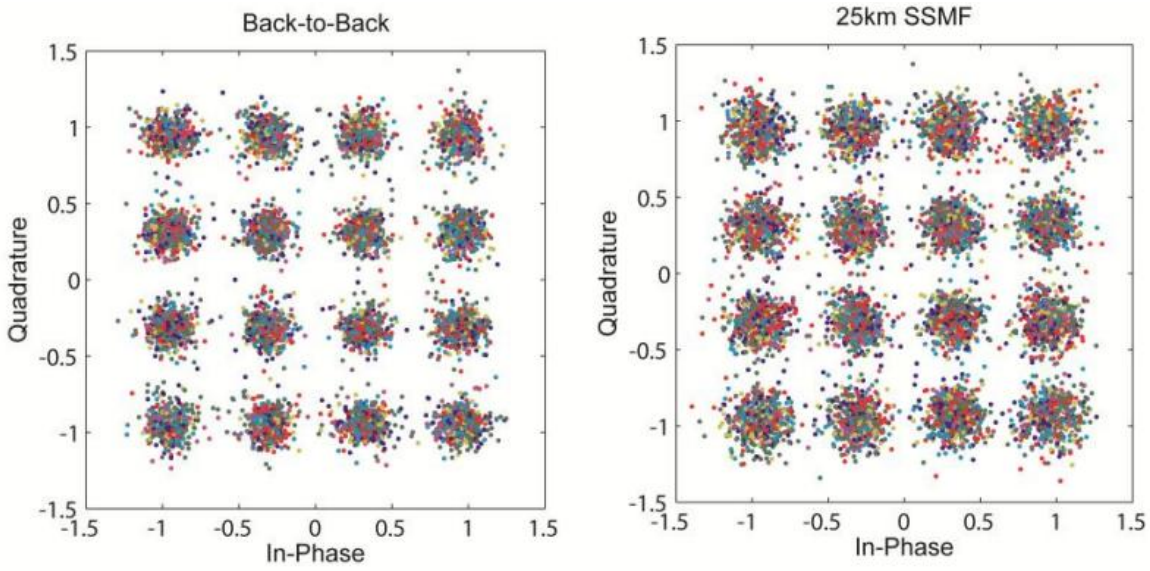

Figure 5-12. Constellation diagrams for (left) back-to-back and (right) after 25 km of SMF transmission experiments using the DD-OFDM approach

Table 5 shows the performance corresponding to three modes of the optical spectrum: at the edges and at the middle. Usually, the performance is degraded toward the edges due to a lower power per mode and probably due to enhanced optical phase noise, as described in Chapter 4. The per-mode data rate after overhead was 10Gbps, which corresponded to an aggregate throughput of 0.33 Tbps (33 x 10Gbps).

Mode	**Back to back**		**25 km**	
(nm)	**EVM (%)**	**BER**	**EVM (%)**	**BER**
1553.55	10.96	4.9E-4	13.41	9.3E-4
1559.34	9.8	9.E-5	12.7	8E-4
1566.00	10.66	4.6E-4	13.66	1.3E-3

Table 5. System performance corresponding to three different modes comparing back-to-back and 25 km transmission experiments over SMF

The previous experiments have successfully shown the feasibility of using a single section QDash passively mode locked laser as a single chip multiple carrier source for effectively transmitting OFDM modulated signals in a bandwidth comprising its optical spectrum FWHM of ~1.5 THz. Nevertheless, the achieved spectral efficiency of about 0.22 bit/s/Hz (0.33Tbps/1.5THz) is still very low compared to the highest value reported for a superchannel implementation of 11 bit/s/Hz [163]. The spectral efficiency may however be increased in a number of ways. Indeed, this can be achieved by using a lower repetition rate device of ~ 10 GHz, which is in theory possible as the 10 Gbps signal occupies a bandwidth of only 3 GHz per channel. The aggregate throughput could hence increase by a factor 5 from 0.33 Tbps up to ~ 1.65 Tbps (165 x 10Gbps) owing to an increase in the number of longitudinal modes (c.f. Chapter 4). Polarization division multiplexing techniques could also be applied in order to increase by a factor 2 the total aggregate throughput, resulting in a final spectral efficiency of ~ 2.2 bit/s/Hz (0.22 x 5 x 2), a value which is very close to those typically found in state of the art superchannel demonstrations. Further improvements of the current implementation are also possible. Indeed, system performance was found to be mostly dependent on the optical signal to noise ratio (OSNR) associated to each of the lasing modes. It is widely known that the SNR is affected by the relative intensity noise (RIN) due to carrier and photon density fluctuations, which is enhanced in this type of experiments due to mode partition effects as the intensity fluctuations of individual modes are greater than those of the total laser intensity. Moreover, the RIN can be further enhanced by chaotic feedback effects [167]. Although the feedback effects on RIN are usually considered negligible for short external cavity lengths (short feedback) [167], recent experiments on QDash MLLs have proven to be severely affected due to reflections from the coupling fiber in a periodic fashion, in the same way the RF linewidth is affected as described in Chapter 4. This suggests the possibility of an improvement in the RIN characteristics and overall system performance by using a feedback insensitive device, like the one used for the RoF experiments in the previous section. These experiments are currently under way and the results will be reported elsewhere. Another means to stabilize the free running devices is by CW and dual-mode injection locking which has already proven to effectively stabilize two section devices [168–170], suggesting a RIN reduction of the lasing modes. Yet another solution to improve the OSNR is by increasing the total laser output power, hence increasing the individual power levels and the OSNR associated to each lasing mode which may additionally lead to reduced

optical linewidths. Remarkable results have already demonstrated the achievement of optical powers up to 120 mW per facet by using asymmetrical cladding waveguide designs [25] in a QDash based mode locked laser, while at the same time achieving good ML characteristics, although at the expense of higher threshold currents.

Chapter 6. Conclusions

This thesis has reported on InAs/InP quantum dash based mode locked lasers emitting in the 1.55 μm telecommunication window. Optimization of the growing conditions allowed for the achievement of relatively high QDash densities per stacked layer and a reduced level of inhomogeneous broadening. This allowed us to fabricate and to process final devices exhibiting good quality static characteristics, such as relatively low threshold currents and high modal gain. This enabled the mode locking regime in a wide range of cavity lengths both in the single and the standard two section configurations, which allowed us to carry out systematic characterization experiments in order to gain further insight into the ML behaviour of these devices. Identification and control of the main physical phenomena limiting device performance such as dispersion and feedback instabilities, allowed unprecedented demonstrations of record peak power, pulse duration, RF linewidth and repetition frequencies in both types of passive mode locking configurations.

An analysis of the ML characteristics of single section QDash based lasers and a comparison with two-section devices has been presented. Spectral phase measurements in the single section lasers were in agreement with simulation results from the proposed model in Chapter 2 which considered the nonlinear four wave mixing mechanism as the main responsible for the mode locking regime in this type of devices. The ML behaviour in the two section lasers was found to be governed by the interplay between gain and loss saturation effects in each of the laser sections, leading to experimental observations which were generally in agreement with those typically reported for the more mature QD MLLs based on the InAs/GaAs material system.

The GDD in the single-section devices was found to affect pulse generation but it proved to be easily compensated in order to efficiently use the wide spectral bandwidth attainable in these laser structures in order to achieve sub-picoseconds pulses. Particularly, the GDD was found to decrease with injection current, favouring the formation of pulses while increasing

the average output power and generally reducing the RF linewidth, representing an advantage as compared to the classical two-section ML devices in which the shortest pulses are generally obtained at the lowest injection currents and under high reverse absorber bias, resulting in lower average output powers and usually higher RF linewidths. Another interesting finding was the reduction of GDD with cavity length implying that ML pulses are more easily generated at higher repetition rates, which explains why most of the reports on single section mode locking usually corresponded to ultra high repetition frequency devices.

We have observed that the RF linewidth can in general attain very narrow values down to ~kHz values, which are usually narrower than those obtained in QW based devices or in the two-section counterparts. This was attributed to a lower optical linewidth of the QD/Dash devices as it was experimentally demonstrated that the optical phase noise was effectively correlated to the laser intensity phase noise. One of the reasons leading to this characteristic was related to a higher population inversion factor of the ground state in QDash. Indeed, the spontaneous emission rate reduces when increasing the inversion of the gain medium so that operating the laser far above threshold my lead to a higher ratio of stimulated to spontaneous emission, therefore reducing the noise characteristics. A lower confinement factor also leads to a higher inversion of the gain medium, which can also explain the reduced optical linewidth, and hence the RF linewidth of the QDash devices. Additionally, the reduced confinement factor may also result in a lower amount of coupled spontaneous emission into the lasing mode as had already been pointed out in previous studies. We have identified that the intrinsically narrow RF linewidth of the QDash lasers can nevertheless be severely degraded due to unwanted optical feedback.

Systematic experiments and simple transfer matrix simulations have allowed to identify and further gain understanding of the feedback problem that was severely affecting system performance. This has allowed us to develop an original, simple, and monolithic solution that was proved efficient for almost completely suppressing any unwanted feedback effects (patent pending).

A theoretical analysis of the optical and intensity spectra of semiconductor lasers under passive mode locking was also presented. This has allowed simple analytical relations to be established between the mode linewidths, RF linewidths, and timing jitter. The use of these

relations was proven to be particularly interesting at high repetition frequencies where direct measurement of the RF and timing jitter is limited by the photodiode and the electronics instrumentation bandwidth. The analytical results have been experimentally validated for single section QDash passively MLLs at repetition frequencies of up to 130 GHz. As the presented theory was based on a phenomenological approach, the results can be applied regardless the MLL configuration.

Finally, we have successfully demonstrated the potential of these devices in two application scenarios in the field of optical communications, namely: broad band wireless access networks and high capacity optical links. For the first case, we have shown the potential of single section QDash lasers for indoor RoF applications in the ~60 GHz band, at multi Gbps transmission rates. For the second application, we have effectively conducted direct detection OFDM transmission experiments which allowed for a proof of concept of an OFDM superchannel implementation for future Tbps high capacity optical networks.

There is still room for performance improvement of the QDash mode locked lasers, such as output power optimization by using flared waveguide configurations and monolithic GDD compensation for ultra short pulse generation directly from the laser output in the single section devices. Growth optimization using p-doping may result in a further increase of the differential gain in order to achieve higher modulation bandwidths, enabling higher data rates for applications involving direct modulating the laser. Additionally, p-doping may also lead to an increase of the laser characteristic temperature, which in the undoped devices remains relatively low and comparable to that exhibited by conventional QW lasers. Other types of applications can also be explored, such as terahertz generation for spectroscopy and sensing, owing to the relatively high output powers and ultra high repetition frequencies attainable in the QDash devices. Emerging technologies for micron-scale cross sectional imaging of biological tissues such as optical coherence tomography (OCT) may also benefit from the broad lasing emission properties of the QDash MLLs in the 1500 nm region.

Appendix A: Derivation of the electric field and the electric field intensity spectra under ML regime

A.1 Electric field (optical) spectrum:

The complex electric field in a semiconductor laser can be generally written as (c.f. Chapter2):

$$E(t)=\left[\sum_{n=1}^{N}E_n e^{j\left[\omega_n t+\theta_n(t)+\phi_n\right]}\right]+c.c$$

Under ML regime, equation 2.5 holds, and the instantaneous modal phase relation can be written as:

$$\theta_n(t)=\theta_c(t)+(n-n_c)\Delta\theta(t)$$

for $n=1$ to N, and with n_c a given mode number with corresponding phase noise $\theta_c(t)$. The complex electric field then becomes:

$$E(t)=\left[\sum_{n=1}^{N}E_n e^{j\left[\omega_n t+\theta_c(t)+(n-n_c)\Delta\theta(t)+\phi_n\right]}\right]+c.c$$

with $\Delta t_r(t)=\Delta\theta(t)/\omega_r$ being the timing fluctuations in the pulse position, commonly referred to as timing jitter. We consider only the effects of phase fluctuations induced by quantum noise. It has been experimentally shown in two section QW [57] and single section QDash passively MLLs [117] through cross correlation measurements, that the variance of $\Delta t_r(t)$ grows linearly with time, which implies that timing jitter undergoes a random walk.

By the central limit theorem, $\Delta t_r(t)$ is normally distributed at large t, therefore it can be described by a Gaussian random walk with zero mean and variance $\left\langle \left| \Delta t_r(t+T_0) - \Delta t_r(T_0) \right|^2 \right\rangle = D|t|$, with D a diffusion coefficient. Substituting $\Delta\theta(t) = \omega_r \Delta t_r(t)$ in (4.4) yields:

$$E(t) = \left[\sum_{n=1}^{N} E_n e^{j\left[\omega_n t + \theta_c(t) + \omega_r (n - n_c)\Delta t_r(t) + \phi_n\right]} \right] + c.c$$

The phase fluctuations in each mode, and therefore $\theta_c(t)$, are affected by amplified spontaneous emission noise and hence undergo a random walk process [50] with $\mathrm{var}\left(\theta_c(t)\right) = \Delta\omega_{\theta_c}|t|$, with $\Delta\omega_{\theta_c}$ a diffusion constant. The optical spectrum $\left|E(\omega)\right|^2$ can be calculated by the Wiener–Khinchin theorem, i.e., by taking the electric field autocorrelation function $R(\tau)$ and Fourier transforming the result:

$$\left|E(\omega)\right|^2 = \int_{-\infty}^{\infty} R(\tau) e^{-j\omega\tau} d\tau$$

Where:

$$\begin{aligned}
R(\tau) &= \left\langle E^*(t) E(t+\tau) \right\rangle \\
&= \left\langle \sum_{n=1}^{N} E_n e^{-j\left[\omega_n t + \theta_c(t) + \omega_r (n - n_c)\Delta t_r(t) + \phi_n\right]} \sum_{n=1}^{N} E_n e^{j\left[\omega_n (t+\tau) + \theta_c(t+\tau) + \omega_r (n - n_c)\Delta t_r(t+\tau) + \phi_n\right]} \right\rangle \\
&= \left\langle \sum_{n=1}^{N} {E_n}^2 e^{j\omega_n \tau} e^{j\left[\left(\theta_c(t+\tau) - \theta_c(t)\right) + \omega_r (n - n_c)\left(\Delta t_r(t+\tau) - \Delta t_r(t)\right)\right]} \right\rangle \\
&= \sum_{n=1}^{N} {E_n}^2 e^{j\omega_n \tau} \left\langle e^{j\left[\left(\theta_c(t+\tau) - \theta_c(t)\right) + \omega_r (n - n_c)\left(\Delta t_r(t+\tau) - \Delta t_r(t)\right)\right]} \right\rangle \\
&= \sum_{n=1}^{N} {E_n}^2 e^{j\omega_n \tau} \times e^{-\frac{1}{2}\left[\mathrm{var}\left(\theta_c(\tau)\right) + \mathrm{var}\left(\omega_r (n - n_c)\left(\Delta t_r(t+\tau) - \Delta t_r(t)\right)\right) + 2\,\mathrm{cov}\left(\theta_c(\tau), \omega_r (n - n_c)\left(\Delta t_r(t+\tau) - \Delta t_r(t)\right)\right)\right]}
\end{aligned}$$

in which $\langle . \rangle$ denotes expectation values. In obtaining $R(\tau)$ we have used the property that for a given zero mean Gaussian distributed variable Θ, $\left\langle e^{j\Theta} \right\rangle = e^{-\frac{1}{2}\mathrm{var}(\Theta)}$.

On the other hand and due to the random walk nature of the random processes involved, we have the following variance (var) and covariance (cov) components:

$$\mathrm{var}\left(\theta_c(\tau)\right) = \Delta\omega_{\theta_c}|\tau|$$
$$\mathrm{var}\left(\omega_r(n-n_c)\Delta t_r(\tau)\right) = \omega_r{}^2(n-n_c)^2 D|\tau|$$
$$\mathrm{cov}\left(\theta_c(\tau), \omega_r(n-n_c)\Delta t_r(\tau)\right) = \omega_r(n-n_c)\gamma_{\theta_c,\Delta t_r}|\tau|$$

with $\gamma_{\theta_c,\Delta t_r}$ a term related to the correlation between both processes θ_c and Δt_r, which is equal to zero if they are uncorrelated.

Hence, we can finally write:

$$R(\tau) = \sum_{n=1}^{N} E_n{}^2 e^{j\omega_n\tau} e^{-\frac{1}{2}\left[\Delta\omega_{\theta_c}+\omega_r{}^2(n-n_c)^2 D+2\omega_r(n-n_c)\gamma_{\theta_c,\Delta t_r}\right]|\tau|}$$

Thus:

$$\left|E(\omega)\right|^2 = \int_{-\infty}^{\infty} R(\tau) e^{-j\omega\tau} d\tau = \int_{-\infty}^{\infty} \sum_{n=1}^{N} E_n^2 e^{j\omega_n\tau} e^{-\frac{1}{2}\left[\Delta\omega_{\theta_c}+\omega_r{}^2(n-n_c)^2 D+2\omega_r(n-n_c)\gamma_{\theta_c,\Delta t_r}\right]|\tau|} e^{-j\omega\tau} d\tau$$

In the above expression, we can identify a decaying exponential function whose Fourier transform is a corresponding Lorentzian. The term $e^{j\omega_n\tau}$ will only shift the optical spectrum to the angular frequency ω_n. Hence:

$$\left|E(\omega)\right|^2 = \sum_{n=1}^{N} E_n^2 \left\{\left[\frac{1}{2}\Delta\omega_{\theta_c} + \frac{1}{2}\omega_r{}^2(n-n_c)^2 D + \omega_r(n-n_c)\gamma_{\theta_c,\Delta t_r}\right]^2 + (\omega-\omega_n)^2\right\}^{-1}$$

Consequently, the optical spectrum consists of N Lorentzian lines centered at ω_n with full width at half maximum (FWHM) linewidths:

$$\Delta\omega_n = \Delta\omega_{min} + \omega_r^2(n-n_{min})^2 D$$

with $n_{min} = n_c - \gamma_{\theta_c,\Delta t_r}/\omega_r D$, and $\Delta\omega_{min} = \Delta\omega_{\theta_c} - \gamma^2_{\theta_c,\Delta t_r}/D$.

A.2 Electric field intensity spectrum (RF spectrum)

The electric field intensity under ML regime can be written (c.f. Chapter 2) as:

$$I(t) \propto \sum_{m=1}^{N-1} \sum_{l=1}^{N-m} 2E_{m+l} E_l \cos\left[m\omega_r \left(t + \Delta t_r(t) \right) + \left(\phi_{m+l} - \phi_l \right) \right]$$

$$I(t) \propto \left[\sum_{m=1}^{N-1} \sum_{l=1}^{N-m} 2E_{m+l} E_l \times e^{j\left[m\omega_r \left(t+\Delta t_r(t) \right) + \left(\phi_{m+l} - \phi_l \right) \right]} \right] + c.c$$

In an analagous manner, its spectrum can be calculated by using the Wiener–Khinchin theorem:

$$\left| I(\omega) \right|^2 \propto \int_{-\infty}^{\infty} R_I(\tau) e^{-j\omega\tau} d\tau$$

where:

$$\begin{aligned} R_I(\tau) &= \left\langle I^*(t) I(t+\tau) \right\rangle \\ &= \left\langle \begin{array}{l} \sum_{m=1}^{N-1} \sum_{l=1}^{N-m} 2E_{m+l} E_l \times e^{-j\left[m\omega_r \left(t+\Delta t_r(t) \right) + \left(\phi_{m+l} - \phi_l \right) \right]} \times \\ \sum_{m=1}^{N-1} \sum_{l=1}^{N-m} 2E_{m+l} E_l \times e^{j\left[m\omega_r \left(t+\tau+\Delta t_r(t+\tau) \right) + \left(\phi_{m+l} - \phi_l \right) \right]} \end{array} \right\rangle \\ &= \left\langle \sum_{m=1}^{N-1} \sum_{l=1}^{N-m} 2E_{m+l} E_l \times e^{jm\omega_r \tau} \times e^{j\left[m\omega_r \left(\Delta t_r(t+\tau) - \Delta t_r(t) \right) \right]} \right\rangle \end{aligned}$$

Following the same calculations as previously and by taking into account the same statistics for the timing jitter $\Delta t_r(t)$, we find:

$$\begin{aligned} R_I(\tau) &= \sum_{m=1}^{N-1} \sum_{l=1}^{N-m} 2E_{m+l} E_l \times e^{jm\omega_r \tau} \times e^{-\frac{1}{2}\left[\mathrm{var}\left(m\omega_r \Delta t_r(t) \right) \right]} \\ &= \sum_{m=1}^{N-1} \sum_{l=1}^{N-m} 2E_{m+l} E_l \times e^{jm\omega_r \tau} \times e^{-\frac{1}{2}\left[(m\omega_r)^2 D|\tau| \right]} \end{aligned}$$

Hence:

$$\left|I(\omega)\right|^2 \propto \int_{-\infty}^{\infty} \sum_{m=1}^{N-1} \sum_{l=1}^{N-m} 2E_{m+l}E_l \times e^{jm\omega_r\tau} \times e^{-\frac{1}{2}\left[(m\omega_r)^2 D|\tau|\right]} e^{-j\omega\tau} d\tau$$

$$= \sum_{m=1}^{N-1} \sum_{l=1}^{N-m} 2E_{m+l}E_l \left[\frac{1}{2}(m\omega_r)^2 D + (\omega - m\omega_r)^2\right]^{-1}$$

Consequently, the RF spectrum consists of a sum of $N-m$ Lorentzian lines centered at $m\omega_r$ for $m=1$ to $N-1$. At any given value of m, each line will have identical FWHM linewidths given by:

$$\Delta\omega_{RF_m} = m^2\omega_r^2 D = m^2 \Delta\omega_{RF_1}$$

with $\Delta\omega_{RF_1} = \omega_r^2 D$.

A.3 Relationship between the optical and the RF spectra and timing jitter extraction

A relation between both the mode linewidths (in the optical spectrum) and those of their beatings (in the RF spectrum) can be established. From the previous results we have:

$$\Delta\omega_n = \Delta\omega_{min} + \omega_r^2 (n - n_{min})^2 D$$

$$\Delta\omega_{RF_m} = m^2\omega_r^2 D = m^2 \Delta\omega_{RF_1}$$

which can be combined to yield:

$$\Delta\omega_n = \Delta\omega_{min} + \frac{\Delta\omega_{RF_m}}{m^2}(n - n_{min})^2$$

or equivalently:

$$\Delta\omega_n = \Delta\omega_{min} + \Delta\omega_{RF_1}(n - n_{min})^2$$

Finally, a relationship between the mode linewidths and the timing jitter can be established. Indeed, a parabolic fit $\Delta\omega_n = \Delta\omega_{min} + \omega_r^2 \left(n - n_{min}\right)^2 D$ can be made if a collection of linewidths $\Delta\omega_n$ from the optical spectrum are known, from which the value of the timing jitter diffusion constant *D* can be extracted. Hence, the pulse to pulse σ_{pp} and the pulse to clock timing jitter σ_{pc} (c.f. Chapters 2 and 4), can be straightforwardly calculated to yield:

$$\sigma_{pp} = \sqrt{DT_r}, \quad \sigma_{pc} = \sqrt{\int_{\omega_1}^{\omega_2} \frac{D}{\omega^2} \frac{d\omega}{2\pi}}$$

List of publications

Journal Contributions

R. Rosales, K. Merghem, C. Calo, A. Martinez, Geraud Bowmans, I. Krestnikov, and A. Ramdane, "Optical pulse generation in single section InAs/GaAs quantum dot edge emitting lasers under continuous wave operation," *Applied Physics Letters*, vol. 101, 23, (in-print).

E. Sooudi, C. de Dios, J. G. McInerney, G. Huyet, F. Lelarge, K. Merghem, **R. Rosales**, A. Martinez, A. Ramdane, and S. P. Hegarty, "A Novel Scheme For Two-Level Stabilization of Semiconductor Mode-Locked Lasers Using Simultaneous Optical Injection and Optical Feedback," *IEEE Journal of Quantum Electronics* (submitted).

E. Sooudi, S. Sygletos, A. D. Ellis, G. Huyet, J. G. McInerney, F. Lelarge, K. Merghem, **R. Rosales**, A. Martinez, A. Ramdane, and S. P. Hegarty, "Optical Frequency Comb Generation Using Dual-Mode Injection-Locking of Quantum-Dash Mode-Locked Lasers: Properties and Applications," *IEEE Journal of Quantum Electronics*, vol. 48, no. 10, pp. 1327 –1338, Oct. 2012.

R. Watts, **R. Rosales**, F. Lelarge, A. Ramdane, and L. Barry, "Mode coherence measurements across a 1.5 THz spectral bandwidth of a passively mode-locked quantum dash laser," *Opt. Lett.*, vol. 37, no. 9, pp. 1499–1501, May 2012.

R. Rosales, K. Merghem, A. Martinez, F. Lelarge, A. Accard, and A. Ramdane, "Timing jitter from the optical spectrum in semiconductor passively mode locked lasers," *Opt. Express*, vol. 20, no. 8, pp. 9151–9160, Apr. 2012.

R. Rosales, S. G. Murdoch, R. T. Watts, K. Merghem, A. Martinez, F. Lelarge, A. Accard, L. P. Barry, and A. Ramdane, "High performance mode locking characteristics of single section quantum dash lasers," *Optics Express*, vol. 20, no. 8, p. 8649, Mar. 2012.

E. Sooudi, G. Huyet, J. G. McInerney, F. Lelarge, K. Merghem, **R. Rosales**, A. Martinez, A. Ramdane, and S. P. Hegarty, "Injection-Locking Properties of InAs/InP-Based Mode-Locked Quantum-Dash Lasers at 21 GHz," *IEEE Photonics Technology Letters*, vol. 23, no. 20, pp. 1544 –1546, Oct. 2011.

R. Rosales, K. Merghem, A. Martinez, A. Akrout, J.-P. Tourrenc, A. Accard, F. Lelarge, and A. Ramdane, "InAs/InP Quantum-Dot Passively Mode-Locked Lasers for 1.55 mm Applications," *IEEE Journal of Selected Topics in Quantum Electronics*, vol. 17, no. 5, pp. 1292–1301, Sep. 2011.

K. Merghem, **R. Rosales**, S. Azouigui, A. Akrout, A. Martinez, F. Lelarge, G.-H. Duan, G. Aubin, and A. Ramdane, "Low noise performance of passively mode locked quantum-dash-based lasers under external optical feedback," *Applied Physics Letters*, vol. 95, no. 13, pp. 131111–131111–3, Sep. 2009.

International Conferences

R. Rosales, R. T. Watts, K Merghem, C Calò, A Martinez, L P Barry, A Ramdane, "Quantum dash mode locked lasers as optical sources for OFDM superchannels," in *38th European Conference on Optical Communications (ECOC)*, Amsterdam, The Netherlands, 2012 (invited).

R. Rosales, R. T. Watts, C Browning, K Merghem, C Calò, A Martinez, L P Barry, A Ramdane, "Quantum dot mode locked lasers for OFDM applications," in *International Nano-Optoelectronics Workshop (iNOW)*, Berkeley-Stanford, (CA), USA, 2012. (invited)

R. Rosales, R. Watts, K. Merghem, C. Calo, A. Martinez, A. Accard, F. Lelarge, L.P. Barry, A. Ramdane, "Quantum dot mode locked lasers for coherent frequency comb generation," in *15th International Conference on Lasers Optics (L0)*, St. Petersburg, Russia, 2012. (invited)

R. Rosales, B. Charbonnier, K. Merghem, A. Martinez, Lelarge, and A. Ramdane, "InAs/InP Quantum Dash based mode locked lasers for 60 GHz radio over fiber applications," in *Compound Semiconductor Week (CSW/IPRM), 2012 Conference on Indium Phosphide and Related Materials*, Santa Barbara, CA (USA), 2012. (oral)

K. Merghem, **R. Rosales**, S. Azouigui, Q. Zou, A. Martinez, A. Accard, F. Lelarge, A. Ramdane, "InAs/InP quantum dot based lasers and effect of optical feedback," in *SPIE, Novel In-Plane Semiconductor Lasers XI,* San Francisco, (CA), USA 2012. (oral)

R. Rosales, K. Merghem, A. Martinez, A. Accard, F. Lelarge, and A. Ramdane, "Timing Jitter Measurements of a 130 GHz Passively Mode Locked QDash Laser from its Optical Spectrum," in *CLEO: Science and Innovations,* San Jose (CA), USA, 2012, p. CW1N.6. (oral)

R. Watts, **R. Rosales**, S. Murdoch, F. Lelarge, A. Ramdane, and L. Barry, "QDash semiconductor mode-locked lasers as compact subchannel comb for optical OFDM superchannel systems," in *CLEO: Science and Innovations,* 2012, p. CM1I.5 (oral)

E. Sooudi, C. De Dios Fernandez, G. Huyet, J. G. McInerney, F. Lelarge, **R. Rosales**, K. Merghem, A. Martinez, A. Ramdane, and S. P. Hegarty, "All Optical Passive Stabilization of a Two-Section InAs/InP Based Quantum-Dash Mode-Locked Laser with Simultaneous CW

Injection-Locking and Selective Optical Feedback," in *CLEO: QELS-Fundamental Science*, 2012, p. JW2A.84. (poster)

R. Rosales, K. Merghem, A. Akrout, A. Martinez, and A. Ramdane, "Low noise quantum dot based mode locked lasers and applications," in *International Nano-Optoelectronics Workshop (iNOW)*, Wurzburg, Germany, 2011. (oral)

R. Rosales, K. Merghem, A. Martinez, A. Accard, F. Lelarge, and A. Ramdane, "High repetition rate two-section InAs/InP quantum-dash passively mode locked lasers," in *Compound Semiconductor Week (CSW/IPRM), 2011 and 23rd International Conference on Indium Phosphide and Related Materials*, Berlin, Germany, 2011, pp. 1 –4. **(awarded Best Student Paper by the IEEE Photonics Society)** (oral)

K. Merghem, **R. Rosales**, A. Martinez, G. Patriarche, A. Ramdane, N. Chimot, F. van Dijk, Y. Moustapha-Rabault, F. Poingt, and F. Lelarge, "Improvement of modal gain of InAs/InP quantum-dash lasers," in *Compound Semiconductor Week (CSW/IPRM), 2011 and 23rd International Conference on Indium Phosphide and Related Materials*, Berlin, Germany, 2011, pp. 1 –4. (oral)

R. Rosales, K. Merghem, A. Martinez, A. Accard, F. Lelarge, and A. Ramdane, "Two-section InAs/InP Quantum-Dash Passively Mode Locked Lasers," in *CLEO:2011 - Laser Applications to Photonic Applications*, Baltimore (MD), USA, 2011, p. CThG2. (oral)

R. Rosales, K. Merghem, S. Azouigui, A. Martinez, F. Lelarge, F. Van Dijk, G. Aubin, and A. Ramdane, "Effect of Optical Feedback on 17-GHz Quantum Dash Based Mode Locked Lasers," in *CLEO: Science and Innovations*, San Jose, (CA), USA, 2010, p. JTuD94. (poster)

K. Merghem, **R. Rosales**, S. Azouigui, A. Martinez, F. Van Dijk, G. Aubin, and A. Ramdane, "Coherence collapse in monolithic quantum-dash-based passive mode-locked lasers," in *SPIE, Semiconductor Lasers and Laser Dynamics*, Brussels, Belgium, 2010. (oral)

National Conferences

R. Rosales, B. Charbonnier, K. Merghem, A. Martinez, F. Van Diijk, et A. Ramdane, "Lasers à blocage de modes à base de batonnets quantiques InAs/InP pour la radio sur fibre à 60 GHz," in *Journées Nationales d'Optique Guidée (JNOG)*, Lyon, France, 2012. (présentation orale)

R. Rosales, K. Merghem, A. Martinez, et A. Ramdane, "Génération d'impulsions à une fréquence de répétition de 100 GHz à l'aide de lasers a verrouillage de modes passif à base de bâtonnets quantiques émettant à 1,55 mm," in *Journées Nationales d'Optique Guidée (JNOG)*, Marseille, France, 2011. (oral)

R. Rosales, K. Merghem, A. Martinez, et A. Ramdane, "Evaluation de la gigue temporelle de lasers à verrouillage de modes à haute fréquence de répétition à partir du spectre optique" in *Journées Nationales d'Optique Guidée (JNOG)*, Besancon, France, 2010. (oral)

R. Rosales, K. Merghem, S. Azouigui, A. Akrout , A. Martinez, F. Lelarge, G.-H. Duan, G. Aubin, et A. Ramdane, "Stabilisation d'un Laser Monolithique à blocage de modes passif à base de bâtonnets quantiques a l'aide d'une rétroaction optique externe," in *Journées Nationales d'Optique Guidée (JNOG)*, Lille, France, 2009. (oral)

References

[1] D. Bimberg, N. Kirstaedter, N. N. Ledentsov, Z. I. Alferov, P. S. Kop'ev, and V. M. Ustinov, "InGaAs-GaAs quantum-dot lasers," *IEEE Journal of Selected Topics in Quantum Electronics*, vol. 3, no. 2, pp. 196 –205, Apr. 1997.

[2] X. Huang, A. Stintz, H. Li, L. F. Lester, J. Cheng, and K. J. Malloy, "Passive mode-locking in 1.3 μm two-section InAs quantum dot lasers," *Applied Physics Letters*, vol. 78, no. 19, pp. 2825–2827, May 2001.

[3] M. Asada, Y. Miyamoto, and Y. Suematsu, "Gain and the threshold of three-dimensional quantum-box lasers," *IEEE Journal of Quantum Electronics*, vol. 22, no. 9, pp. 1915 – 1921, Sep. 1986.

[4] M. Willatzen, T. Tanaka, Y. Arakawa, and J. Singh, "Polarization dependence of optoelectronic properties in quantum dots and quantum wires-consequences of valence-band mixing," *IEEE Journal of Quantum Electronics*, vol. 30, no. 3, pp. 640 –653, Mar. 1994.

[5] E. U. Rafailov, M. A. Cataluna, and W. Sibbett, "Mode-locked quantum-dot lasers," *Nature Photonics*, vol. 1, no. 7, pp. 395–401, 2007.

[6] D. B. Malins, A. Gomez-Iglesias, S. J. White, W. Sibbett, A. Miller, and E. U. Rafailov, "Ultrafast electroabsorption dynamics in an InAs quantum dot saturable absorber at 1.3 μm," *Applied Physics Letters*, vol. 89, no. 17, pp. 171111–171111–3, Oct. 2006.

[7] Y. Arakawa and H. Sakaki, "Multidimensional quantum well laser and temperature dependence of its threshold current," *Applied Physics Letters*, vol. 40, no. 11, pp. 939–941, Jun. 1982.

[8] M. G. Thompson, A. R. Rae, M. Xia, R. V. Penty, and I. H. White, "InGaAs Quantum-Dot Mode-Locked Laser Diodes," *IEEE Journal of Selected Topics in Quantum Electronics*, vol. 15, no. 3, pp. 661 –672, Jun. 2009.

[9] R. H. Wang, A. Stintz, P. M. Varangis, T. C. Newell, H. Li, K. J. Malloy, and L. F. Lester, "Room-temperature operation of InAs quantum-dash lasers on InP [001]," *IEEE Photonics Technology Letters*, vol. 13, no. 8, pp. 767 –769, Aug. 2001.

[10] R. Schwertberger, D. Gold, J. P. Reithmaier, and A. Forchel, "Long-wavelength InP-based quantum-dash lasers," *IEEE Photonics Technology Letters*, vol. 14, no. 6, pp. 735 –737, Jun. 2002.

[11] F. Lelarge, B. Dagens, J. Renaudier, R. Brenot, A. Accard, F. van Dijk, D. Make, O. L. Gouezigou, J.-G. Provost, F. Poingt, J. Landreau, O. Drisse, E. Derouin, B. Rousseau, F. Pommereau, and G.-H. Duan, "Recent Advances on InAs/InP Quantum Dash Based Semiconductor Lasers and Optical Amplifiers Operating at 1.55 mm," *IEEE Journal of Selected Topics in Quantum Electronics*, vol. 13, no. 1, pp. 111 –124, Feb. 2007.

[12] Z. G. Lu, J. R. Liu, S. Raymond, P. J. Poole, P. J. Barrios, and D. Poitras, "312-fs pulse generation from a passive C-band InAs/InP quantum dot mode-locked laser," *Opt Express*, vol. 16, no. 14, pp. 10835–10840, Jul. 2008.

[13] M. J. R. Heck, E. A. J. M. Bente, B. Smalbrugge, Y.-S. Oei, M. K. Smit, S. Anantathanasarn, and R. Nötzel, "Observation of Q-switching and mode-locking in two-section InAs/InP (100) quantum dot lasers around 1.55 ?m," *Opt. Express*, vol. 15, no. 25, pp. 16292–16301, Dec. 2007.

[14] J. Renaudier, R. Brenot, B. Dagens, F. Lelarge, B. Rousseau, F. Poingt, O. Legouezigou, F. Pommereau, A. Accard, P. Gallion, and G.-H. Duan, "45 GHz self-pulsation with narrow linewidth in quantum dot Fabry-Perot semiconductor lasers at 1.5 mu;m," *Electronics Letters*, vol. 41, no. 18, pp. 1007 – 1008, Sep. 2005.

[15] C. Gosset, K. Merghem, A. Martinez, G. Moreau, G. Patriarche, G. Aubin, A. Ramdane, J. Landreau, and F. Lelarge, "Subpicosecond pulse generation at 134 GHz using a quantum-dash-based Fabry-Perot laser emitting at 1.56 μm," *Applied Physics Letters*, vol. 88, no. 24, pp. 241105–241105–3, Jun. 2006.

[16] M. J. R. Heck, A. Renault, E. A. J. M. Bente, Y.-S. Oei, M. K. Smit, K. S. E. Eikema, W. Ubachs, S. Anantathanasarn, and R. Notzel, "Passively Mode-Locked 4.6 and 10.5 GHz Quantum Dot Laser Diodes Around 1.55 mm With Large Operating Regime," *IEEE Journal of Selected Topics in Quantum Electronics*, vol. 15, no. 3, pp. 634 –643, Jun. 2009.

[17] L. Hou, M. Haji, J. Akbar, B. Qiu, and A. C. Bryce, "Low divergence angle and low jitter 40 GHz AlGaInAs/InP 1.55mm mode-locked lasers," *Opt. Lett.*, vol. 36, no. 6, pp. 966–968, Mar. 2011.

[18] K. Merghem, A. Akrout, A. Martinez, G. Moreau, J.-P. Tourrenc, F. Lelarge, F. Van Dijk, G.-H. Duan, G. Aubin, and A. Ramdane, "Short pulse generation using a passively mode locked single InGaAsP/InP quantum well laser," *Opt. Express*, vol. 16, no. 14, pp. 10675–10683, Jul. 2008.

[19] J. J. Plant, J. T. Gopinath, B. Chann, D. J. Ripin, R. K. Huang, and P. W. Juodawlkis, "250 mW, 1.5μm monolithic passively mode-locked slab-coupled optical waveguide laser," *Optics Letters*, vol. 31, no. 2, p. 223, 2006.

[20] C.-Y. Lin, Y.-C. Xin, Y. Li, F. L. Chiragh, and L. F. Lester, "Cavity design and characteristics of monolithic long-wavelength InAs/InP quantum dash passively mode-locked lasers," *Opt. Express*, vol. 17, no. 22, pp. 19739–19748, Oct. 2009.

[21] R. Rosales, K. Merghem, A. Martinez, A. Akrout, J.-P. Tourrenc, A. Accard, F. Lelarge, and A. Ramdane, "InAs/InP Quantum-Dot Passively Mode-Locked Lasers for 1.55 mm Applications," *IEEE Journal of Selected Topics in Quantum Electronics*, vol. 17, no. 5, pp. 1292–1301, Sep. 2011.

[22] K. Sato, "Optical pulse generation using fabry-Pe acute;rot lasers under continuous-wave operation," *IEEE Journal of Selected Topics in Quantum Electronics*, vol. 9, no. 5, pp. 1288 – 1293, Oct. 2003.

[23] Y. Nomura, S. Ochi, N. Tomita, K. Akiyama, T. Isu, T. Takiguchi, and H. Higuchi, "Mode locking in Fabry-Perot semiconductor lasers," *Phys. Rev. A*, vol. 65, no. 4, p. 043807, Mar. 2002.

[24] R. Rosales, S. G. Murdoch, R. T. Watts, K. Merghem, A. Martinez, F. Lelarge, A. Accard, L. P. Barry, and A. Ramdane, "High performance mode locking characteristics of single section quantum dash lasers," *Optics Express*, vol. 20, no. 8, p. 8649, Mar. 2012.

[25] M. Faugeron, M. Tran, F. Lelarge, M. Chtioui, Y. Robert, E. Vinet, A. Enard, J. Jacquet, and F. Van Dijk, "High Power Mode Locked Quantum Dash 1.5 ?m Laser With Asymmetrical Cladding," in *CLEO: QELS-Fundamental Science*, 2012, p. JW2A.85.

[26] G. Carpintero, M. G. Thompson, R. V. Penty, and I. H. White, "Low Noise Performance of Passively Mode-Locked 10-GHz Quantum-Dot Laser Diode," *IEEE Photonics Technology Letters*, vol. 21, no. 6, pp. 389 –391, Mar. 2009.

[27] E. U. Rafailov, M. A. Cataluna, W. Sibbett, N. D. Il'inskaya, Y. M. Zadiranov, A. E. Zhukov, V. M. Ustinov, D. A. Livshits, A. R. Kovsh, and N. N. Ledentsov, "High-power picosecond and femtosecond pulse generation from a two-section mode-locked quantum-dot laser," *Applied Physics Letters*, vol. 87, no. 8, pp. 081107–081107–3, Aug. 2005.

[28] D. Nikitichev, Y. Ding, M. Cataluna, E. Rafailov, L. Drzewietzki, S. Breuer, W. Elsaesser, M. Rossetti, P. Bardella, T. Xu, I. Montrosset, I. Krestnikov, D. Livshits, M. Ruiz, M. Tran, Y. Robert, and M. Krakowski, "High peak power and sub-picosecond Fourier-limited pulse generation from passively mode-locked monolithic two-section gain-guided tapered InGaAs quantum-dot lasers," *Laser Physics*, vol. 22, no. 4, pp. 715–724, 2012.

[29] D. Hillerkuss, R. Schmogrow, T. Schellinger, M. Jordan, M. Winter, G. Huber, T. Vallaitis, R. Bonk, P. Kleinow, F. Frey, M. Roeger, S. Koenig, A. Ludwig, A. Marculescu, J. Li, M. Hoh, M. Dreschmann, J. Meyer, S. B. Ezra, N. Narkiss, B. Nebendahl, F. Parmigiani, P. Petropoulos, B. Resan, A. Oehler, K. Weingarten, T. Ellermeyer, J. Lutz, M. Moeller, M. Huebner, J. Becker, C. Koos, W. Freude, and J. Leuthold, "26 Tbit s-1 line-rate super-channel transmission utilizing all-optical fast Fourier transform processing," *Nature Photonics*, vol. 5, no. 6, pp. 364–371, 2011.

[30] L. K. Oxenløwe, "Optical communications: Single-laser super-channel," *Nature Photonics*, vol. 5, no. 6, pp. 329–331, 2011.

[31] S. Chandrasekhar and X. Liu, "DSP-enabled OFDM superchannel transmission," in *Signal Processing in Photonic Communications*, 2012, p. SpTu2A.1.

[32] X. Liu, S. Chandrasekhar, X. Chen, P. Winzer, Y. Pan, B. Zhu, T. Taunay, M. Fishteyn, M. Yan, J. M. Fini, E. Monberg, and F. Dimarcello, "1.12-Tb/s 32-QAM-OFDM Superchannel with 8.6-b/s/Hz Intrachannel Spectral Efficiency and Space-Division Multiplexing with 60-b/s/Hz Aggregate Spectral Efficiency," in *37th European Conference and Exposition on Optical Communications*, 2011, p. Th.13.B.1.

[33] D. Zou and I. B. Djordjevic, "Beyond 1Tb/s Superchannel Optical Transmission based on Polarization Multiplexed Coded-OFDM over 2300 km of SSMF," in *Signal Processing in Photonic Communications*, 2012, p. SpTu2A.6.

[34] J. Li, M. Sjödin, M. Karlsson, and P. A. Andrekson, "Building up low-complexity spectrally-efficient Terabit superchannels by receiver-side duobinary shaping," *Opt. Express*, vol. 20, no. 9, pp. 10271–10282, Apr. 2012.

[35] Z. He, I. Djordjevic, W. Liu, M. Luo, Q. Yang, Z. Yang, S. Yu, B. Huang, N. Chi, and W. Shieh, "Comparison of Various Bandwidth-Efficient LDPC Coding Schemes for Tb/s Superchannel Long-haul Transmission," in *National Fiber Optic Engineers Conference*, 2012, p. JW2A.43.

[36] M. Jinno, K. Yonenaga, H. Takara, K. Shibahara, S. Yamanaka, T. Ono, T. Kawai, M. Tomizawa, and Y. Miyamoto, "Demonstration of Translucent Elastic Optical Network Based on Virtualized Elastic Regenerator," in *National Fiber Optic Engineers Conference*, 2012, p. PDP5B.6.

[37] Q. Yang, "Experimental Demonstration of Tb/s Optical Transport Network Based on CO-OFDM Superchannel with Heterogeneous ROADM Nodes Supporting Single-Fiber Bidirectional Communications," in *National Fiber Optic Engineers Conference*, 2012, p. JTh2A.47.

[38] J. Yu, Z. Dong, and N. Chi, "Generation, Transmission and Coherent Detection of 11.2 Tb/s (112x100Gb/s) Single Source Optical OFDM Superchannel," in *Optical Fiber Communication Conference*, 2011, p. PDPA6.

[39] Y.-K. Huang, E. Ip, P. N. Ji, Y. Shao, T. Wang, Y. Aono, Y. Yano, and T. Tajima, "Terabit/s Optical Superchannel with Flexible Modulation Format for Dynamic Distance/Route Transmission," in *Optical Fiber Communication Conference*, 2012, p. OM3H.4.
[40] W.-R. Peng, I. Morita, H. Takahashi, and T. Tsuritani, "Transmission of High-Speed (> 100 Gb/s) Direct-Detection Optical OFDM Superchannel," *J. Lightwave Technol.*, vol. 30, no. 12, pp. 2025–2034, Jun. 2012.
[41] X. Chen, A. Li, J. Ye, A. Al Amin, and W. Shieh, "Reception of mode-division multiplexed superchannel via few-mode compatible optical add/drop multiplexer," *Opt. Express*, vol. 20, no. 13, pp. 14302–14307, Jun. 2012.
[42] H. Griesser, K. Grobe, and J.-P. Elbers, "Quaternary Duobinary Modulation for Superchannels with Sub-Nyquist Subcarrier Spacing," in *Optical Fiber Communication Conference*, 2012, p. OTh1B.4.
[43] C. Zhang, J. Duan, J. Li, W. Hu, H. Li, H. Wu, and Z. Chen, "Bidirectional 60-GHz radio-over-fiber systems with downstream OFDMA and wavelength reuse upstream SC-FDMA," *Opt. Express*, vol. 18, no. 18, pp. 19429–19437, Aug. 2010.
[44] M.-K. Hong, Y.-Y. Won, and S.-K. Han, "Gigabit radio-over-fiber link for convergedbaseband and millimeter-wave band signaltransmission using cascaded injection-lockedFabry-Pérot laser diodes," *Opt. Express*, vol. 17, no. 10, pp. 7844–7852, May 2009.
[45] F. van Dijk, B. Charbonnier, S. Constant, A. Enard, S. Fedderwitz, S. Formont, I. F. Lealman, F. Lecoche, F. Lelarge, D. Moodie, L. Ponnampalam, C. Renaud, M. J. Robertson, A. J. Seeds, A. Sto&#x0308 andhr, and M. Weiss, "Quantum dash mode-locked lasers for millimeter wave signal generation and transmission," in *IEEE Photonics Society, 2010 23rd Annual Meeting of the*, 2010, pp. 187 –188.
[46] B. Charbonnier, F. Lecoche, M. Weis, A. Stohr, F. van Dijk, A. Enard, F. Blache, M. Goix, F. Mallecot, D. G. Moodie, A. Borghesani, and C. W. Ford, "Ultra-wideband radio-over-fiber techniques and networks," *IEEE Xplore*, 21-Mar-2010. [Online]. Available: http://ieeexplore.com/xpl/articleDetails.jsp?reload=true&arnumber=5465494. [Accessed: 23-Aug-2012].
[47] M. Sargent Iii, M. O. Scully, and W. E. Lamb Jr, *Laser Physics*. Westview Press, 1978.
[48] Q. An, P. Jin, Z. C. Wang, X. K. Li, and Z. G. Wang, "The Effect of Double-Pass Gain on the Performances of a Quantum-Dot Superluminescent Diode Integrated With a Semiconductor Optical Amplifier," *Journal of Lightwave Technology*, vol. 30, no. 16, pp. 2684 –2688, Aug. 2012.
[49] B. W. Tilma, Y. Jiao, J. Kotani, B. Smalbrugge, H. P. M. M. Ambrosius, P. J. Thijs, X. J. M. Leijtens, R. Notzel, M. K. Smit, and E. A. J. M. Bente, "Integrated Tunable Quantum-Dot Laser for Optical Coherence Tomography in the 1.7 mm Wavelength Region," *IEEE Journal of Quantum Electronics*, vol. 48, no. 2, pp. 87 –98, Feb. 2012.
[50] H. A. Haus and A. Mecozzi, "Noise of mode-locked lasers," *IEEE Journal of Quantum Electronics*, vol. 29, no. 3, pp. 983 –996, Mar. 1993.
[51] J. Reid, D. T. Cassidy, and R. T. Menzies, "Linewidth measurements of tunable diode lasers using heterodyne and etalon techniques," *Appl. Opt.*, vol. 21, no. 21, pp. 3961–3965, Nov. 1982.

[52] T. Okoshi, K. Kikuchi, and A. Nakayama, "Novel method for high resolution measurement of laser output spectrum," *Electronics Letters*, vol. 16, no. 16, pp. 630 – 631, 1980.
[53] E. Bava, G. Galzerano, and C. Svelto, "Frequency-noise sensitivity and amplitude-noise immunity of discriminators based on fringe-side Fabry-Perot cavities," *IEEE Transactions on Ultrasonics, Ferroelectrics and Frequency Control*, vol. 49, no. 8, pp. 1150 –1159, Aug. 2002.
[54] A. J. Lowery, "Amplified-spontaneous noise limit of optical OFDM lightwave systems," *Optics Express*, vol. 16, no. 2, p. 860, 2008.
[55] D. Linde, "Characterization of the noise in continuously operating mode-locked lasers," *Applied Physics B Photophysics and Laser Chemistry*, vol. 39, no. 4, pp. 201–217, Apr. 1986.
[56] D. Eliyahu, R. A. Salvatore, and A. Yariv, "Effect of noise on the power spectrum of passively mode-locked lasers," *J. Opt. Soc. Am. B*, vol. 14, no. 1, pp. 167–174, Jan. 1997.
[57] L. A. Jiang, S. T. Wong, M. E. Grein, E. P. Ippen, and H. A. Haus, "Measuring timing jitter with optical cross correlations," *IEEE Journal of Quantum Electronics*, vol. 38, no. 8, pp. 1047 – 1052, Aug. 2002.
[58] R. Trebino and D. J. Kane, "Using phase retrieval to measure the intensity and phase of ultrashort pulses: frequency-resolved optical gating," *J. Opt. Soc. Am. A*, vol. 10, no. 5, pp. 1101–1111, May 1993.
[59] C. Iaconis and I. A. Walmsley, "Spectral phase interferometry for direct electric-field reconstruction of ultrashort optical pulses," *Opt. Lett.*, vol. 23, no. 10, pp. 792–794, May 1998.
[60] P. Kockaert, M. Peeters, S. Coen, P. Emplit, M. Haelterman, and O. Deparis, "Simple amplitude and phase measuring technique for ultrahigh-repetition-rate lasers," *IEEE Photonics Technology Letters*, vol. 12, no. 2, pp. 187 –189, Feb. 2000.
[61] M. Kwakernaak, R. Schreieck, A. Neiger, H. Jackel, E. Gini, and W. Vogt, "Spectral phase measurement of mode-locked diode laser pulses by beating sidebands generated by electrooptical mixing," *IEEE Photonics Technology Letters*, vol. 12, no. 12, pp. 1677 – 1679, Dec. 2000.
[62] Z. Jiang, D. E. Leaird, and A. M. Weiner, "Optical arbitrary waveform generation and characterization using spectral line-by-line control," *Journal of Lightwave Technology*, vol. 24, no. 7, pp. 2487 – 2494, Jul. 2006.
[63] C. Gosset, K. Merghem, G. Moreau, A. Martinez, G. Aubin, J.-L. Oudar, A. Ramdane, and F. Lelarge, "Phase-amplitude characterization of a high-repetition-rate quantum dash passively mode-locked laser," *Opt. Lett.*, vol. 31, no. 12, pp. 1848–1850, Jun. 2006.
[64] D. A. Reid, S. G. Murdoch, and L. P. Barry, "Stepped-heterodyne optical complex spectrum analyzer," *Opt. Express*, vol. 18, no. 19, pp. 19724–19731, 2010.
[65] I. Kang and C. Dorrer, "Method of optical pulse characterization using sinusoidal optical phase modulations," *Opt. Lett.*, vol. 32, no. 17, pp. 2538–2540, Sep. 2007.
[66] G. P. Agrawal and N. A. Olsson, "Self-phase modulation and spectral broadening of optical pulses in semiconductor laser amplifiers," *IEEE Journal of Quantum Electronics*, vol. 25, no. 11, pp. 2297 –2306, Nov. 1989.
[67] C. Henry, "Theory of the linewidth of semiconductor lasers," *IEEE Journal of Quantum Electronics*, vol. 18, no. 2, pp. 259 – 264, Feb. 1982.

[68] H. Haus, "Theory of mode locking with a slow saturable absorber," *IEEE Journal of Quantum Electronics*, vol. 11, no. 9, pp. 736 – 746, Sep. 1975.
[69] R. G. M. P. Koumans and R. Van Roijen, "Theory for passive mode-locking in semiconductor laser structures including the effects of self-phase modulation, dispersion, and pulse collisions," *IEEE Journal of Quantum Electronics*, vol. 32, no. 3, pp. 478–492, Mar. 1996.
[70] H. A. Haus, "Mode-locking of lasers," *IEEE Journal of Selected Topics in Quantum Electronics*, vol. 6, no. 6, pp. 1173 –1185, Dec. 2000.
[71] E. A. Avrutin, J. H. Marsh, and E. L. Portnoi, "Monolithic and multi-gigahertz mode-locked semiconductor lasers: constructions, experiments, models and applications," *Optoelectronics, IEE Proceedings* -, vol. 147, no. 4, pp. 251 –278, Aug. 2000.
[72] E. A. Avrutin, J. M. Arnold, and J. H. Marsh, "Dynamic modal analysis of monolithic mode-locked semiconductor lasers," *IEEE Journal of Selected Topics in Quantum Electronics*, vol. 9, no. 3, pp. 844 – 856, Jun. 2003.
[73] A. G. Vladimirov*, D. Turaev, and G. Kozyreff, "Delay differential equations for mode-locked semiconductorlasers," *Opt. Lett.*, vol. 29, no. 11, pp. 1221–1223, Jun. 2004.
[74] A. G. Vladimirov and D. Turaev, "Model for passive mode locking in semiconductor lasers," *Phys. Rev. A*, vol. 72, no. 3, p. 033808, Sep. 2005.
[75] E. A. Viktorov, P. Mandel, A. G. Vladimirov, and U. Bandelow, "Model for mode locking in quantum dot lasers," *Applied Physics Letters*, vol. 88, no. 20, pp. 201102–201102–3, May 2006.
[76] M. Radziunas, A. G. Vladimirov, E. A. Viktorov, G. Fiol, H. Schmeckebier, and D. Bimberg, "Pulse Broadening in Quantum-Dot Mode-Locked Semiconductor Lasers: Simulation, Analysis, and Experiments," *IEEE Journal of Quantum Electronics*, vol. 47, no. 7, pp. 935–943, Jul. 2011.
[77] A. G. Vladimirov, U. Bandelow, G. Fiol, D. Arsenijevi?, M. Kleinert, D. Bimberg, A. Pimenov, and D. Rachinskii, "Dynamical regimes in a monolithic passively mode-locked quantum dot laser," *J. Opt. Soc. Am. B*, vol. 27, no. 10, pp. 2102–2109, Oct. 2010.
[78] M. Rossetti, P. Bardella, and I. Montrosset, "Time-Domain Travelling-Wave Model for Quantum Dot Passively Mode-Locked Lasers," *IEEE Journal of Quantum Electronics*, vol. 47, no. 2, pp. 139 –150, Feb. 2011.
[79] P. Borri, W. Langbein, J. M. Hvam, F. Heinrichsdorff, M.-H. Mao, and D. Bimberg, "Ultrafast gain dynamics in InAs-InGaAs quantum-dot amplifiers," *IEEE Photonics Technology Letters*, vol. 12, no. 6, pp. 594 –596, Jun. 2000.
[80] T. Piwonski, J. Pulka, G. Madden, G. Huyet, J. Houlihan, E. A. Viktorov, T. Erneux, and P. Mandel, "Intradot dynamics of InAs quantum dot based electroabsorbers," *Applied Physics Letters*, vol. 94, p. 3504, Mar. 2009.
[81] L. F. Tiemeijer, P. I. Kuindersma, P. J. A. Thijs, and G. L. J. Rikken, "Passive FM locking in InGaAsP semiconductor lasers," *IEEE Journal of Quantum Electronics*, vol. 25, no. 6, pp. 1385 –1392, Jun. 1989.
[82] G. P. Agrawal, "Population pulsations and nondegenerate four-wave mixing in semiconductor lasers and amplifiers," *J. Opt. Soc. Am. B*, vol. 5, no. 1, pp. 147–159, Jan. 1988.
[83] J. Renaudier, G.-H. Duan, P. Landais, and P. Gallion, "Phase Correlation and Linewidth Reduction of 40 GHz Self-Pulsation in Distributed Bragg Reflector Semiconductor Lasers," *IEEE Journal of Quantum Electronics*, vol. 43, no. 2, pp. 147 – 156, Feb. 2007.

[84] Y. R. Shen, *The Principles of Nonlinear Optics*, 1st ed. Wiley-Interscience, 1984.
[85] A. Uskov, J. Mørk, J. Mark, M. C. Tatham, and G. Sherlock, "Terahertz four-wave mixing in semiconductor optical amplifiers: Experiment and theory," *Applied Physics Letters*, vol. 65, no. 8, pp. 944–946, Aug. 1994.
[86] A. Capua, S. O'duill, V. Mikhelashvili, G. Eisenstein, J. P. Reithmaier, A. Somers, and A. Forchel, "Cross talk free multi channel processing of 10 Gbit/s data via four wave mixing in a 1550 nm InAs/InP quantum dash amplifier," *Opt. Express*, vol. 16, no. 23, pp. 19072–19077, Nov. 2008.
[87] A. Bilenca, R. Alizon, V. Mikhelashhvili, D. Dahan, G. Eisenstein, R. Schwertberger, D. Gold, J. P. Reithmaier, and A. Forchel, "Broad-band wavelength conversion based on cross-gain modulation and four-wave mixing in InAs-InP quantum-dash semiconductor optical amplifiers operating at 1550 nm," *IEEE Photonics Technology Letters*, vol. 15, no. 4, pp. 563 –565, Apr. 2003.
[88] T. Akiyama, O. Wada, H. Kuwatsuka, T. Simoyama, Y. Nakata, K. Mukai, M. Sugawara, and H. Ishikawa, "Nonlinear processes responsible for nondegenerate four-wave mixing in quantum-dot optical amplifiers," *Applied Physics Letters*, vol. 77, no. 12, pp. 1753–1755, Sep. 2000.
[89] T. W. Berg and J. Mork, "Theoretical analysis of four wave mixing in quantum dot optical amplifiers," in *Conference on Lasers and Electro-Optics, 2003. CLEO '03*, 2003, p. 3 pp.
[90] G. P. Agrawal and N. K. Dutta, *Semiconductor Lasers, 2nd Edition*, 2nd ed. Van Nostrand Reinhold, 1993.
[91] P. Runge, R. Elschner, and K. Petermann, "Chromatic Dispersion in InGaAsP Semiconductor Optical Amplifiers," *IEEE Journal of Quantum Electronics*, vol. 46, no. 5, pp. 644 –649, May 2010.
[92] S. M. Kim, Y. Wang, M. Keever, and J. S. Harris, "High-frequency modulation characteristics of 1.3- mu;m InGaAs quantum dot lasers," *IEEE Photonics Technology Letters*, vol. 16, no. 2, pp. 377 –379, Feb. 2004.
[93] P. Borri, W. Langbein, J. Mørk, J. Hvam, F. Heinrichsdorff, M.-H. Mao, and D. Bimberg, "Dephasing in InAs/GaAs quantum dots," *Physical Review B*, vol. 60, no. 11, pp. 7784–7787, Sep. 1999.
[94] P. Bhattacharya and Z. Mi, "Quantum-Dot Optoelectronic Devices," *Proceedings of the IEEE*, vol. 95, no. 9, pp. 1723 –1740, Sep. 2007.
[95] D. Bimberg, M. Grundmann, F. Heinrichsdorff, N. N. Ledentsov, V. M. Ustinov, A. E. Zhukov, A. R. Kovsh, M. V. Maximov, Y. M. Shernyakov, B. V. Volovik, A. F. Tsatsul'nikov, P. S. Kop'ev, and Z. I. Alferov, "Quantum dot lasers: breakthrough in optoelectronics," *Thin Solid Films*, vol. 367, no. 1–2, pp. 235–249, May 2000.
[96] K. Yvind, D. Larsson, L. J. Christiansen, C. Angelo, L. K. Oxenlwe, J. Mrk, D. Birkedal, J. M. Hvam, and J. Hanberg, "Low-jitter and high-power 40-GHz all-active mode-locked lasers," *IEEE Photonics Technology Letters*, vol. 16, no. 4, pp. 975 –977, Apr. 2004.
[97] K. Merghem, R. Rosales, A. Martinez, G. Patriarche, A. Ramdane, N. Chimot, F. van Dijk, Y. Moustapha-Rabault, F. Poingt, and F. Lelarge, "Improvement of modal gain of InAs/InP quantum-dash lasers," in *Compound Semiconductor Week (CSW/IPRM), 2011 and 23rd International Conference on Indium Phosphide and Related Materials*, 2011, pp. 1 –4.

[98] C. Gilfert, V. Ivanov, N. Oehl, M. Yacob, and J. P. Reithmaier, "High gain 1.55 μm diode lasers based on InAs quantum dot like active regions," *Applied Physics Letters*, vol. 98, no. 20, pp. 201102–201102–3, May 2011.
[99] J. A. Fleck, J. R. Morris, and M. D. Feit, "Time-dependent propagation of high energy laser beams through the atmosphere," *Applied Physics*, vol. 10, no. 2, pp. 129–160, Jun. 1976.
[100] J. Z. Wilcox, S. Ou, J. J. Yang, M. Jansen, and G. L. Peterson, "Dependence of emission wavelength on cavity length and facet reflectivities in multiple quantum well semiconductor lasers," *Applied Physics Letters*, vol. 54, no. 22, pp. 2174 –2176, May 1989.
[101] W. Elsasser and E. Gobel, "Multimode effects in the spectral linewidth of semiconductor lasers," *IEEE Journal of Quantum Electronics*, vol. 21, no. 6, pp. 687 – 692, Jun. 1985.
[102] T. Habruseva, G. Huyet, and S. P. Hegarty, "Dynamics of Quantum-Dot Mode-Locked Lasers With Optical Injection," *IEEE Journal of Selected Topics in Quantum Electronics*, vol. 17, no. 5, pp. 1272 –1279, Oct. 2011.
[103] F. X. Kartner, *Few-cycle Laser Pulse Generation and its Applications*, 1st ed. Springer, 2004.
[104] T. Habruseva, S. O'Donoghue, N. Rebrova, F. Kéfélian, S. P. Hegarty, and G. Huyet, "Optical linewidth of a passively mode-locked semiconductor laser," *Opt. Lett.*, vol. 34, no. 21, pp. 3307–3309, Nov. 2009.
[105] R. Paschotta, A. Schlatter, S. C. Zeller, H. R. Telle, and U. Keller, "Optical phase noise and carrier-envelope offset noise of mode-locked lasers," *Applied Physics B*, vol. 82, no. 2, pp. 265–273, Dec. 2005.
[106] P. Martin, E. M. Skouri, L. Chusseau, C. Alibert, and H. Bissessur, "Accurate refractive index measurements of doped and undoped InP by a grating coupling technique," *Applied Physics Letters*, vol. 67, no. 7, pp. 881 –883, Aug. 1995.
[107] J. Mulet and J. Moerk, "On the mechanisms governing the repetition rate of mode-locked semiconductor lasers," in *Conference on Lasers and Electro-Optics, 2004. (CLEO)*, 2004, vol. 1, p. 2 pp. vol.1.
[108] A. Martinez, J.-G. Provost, G. Aubin, R. Brenot, J. Landreau, F. Lelarge, and A. Ramdane, "Slow and fast light in quantum dot based semiconductor optical amplifiers," *Comptes Rendus Physique*, vol. 10, no. 10, pp. 1000–1007, Dec. 2009.
[109] F. Kefelian, S. O'Donoghue, M. T. Todaro, J. G. McInerney, and G. Huyet, "RF Linewidth in Monolithic Passively Mode-Locked Semiconductor Laser," *IEEE Photonics Technology Letters*, vol. 20, no. 16, pp. 1405 –1407, Aug. 2008.
[110] M. J. Ablowitz, B. Ilan, and S. T. Cundiff, "Noise-induced linewidth in frequency combs," *Opt. Lett.*, vol. 31, no. 12, pp. 1875–1877, Jun. 2006.
[111] R. Paschotta, "Noise of mode-locked lasers (Part II): timing jitter and other fluctuations," *Applied Physics B: Lasers and Optics*, vol. 79, no. 2, pp. 163–173, 2004.
[112] J. K. Wahlstrand, J. T. Willits, C. R. Menyuk, and S. T. Cundiff, "The quantum-limited comb lineshape ofa mode-locked laser: Fundamental limitson frequency uncertainty," *Opt. Express*, vol. 16, no. 23, pp. 18624–18630, Nov. 2008.
[113] Y. Takushima, "Linewidth of mode combs of passively and actively mode-locked semiconductor laser diodes," 2004, vol. 5595, pp. 213–227.
[114] K. Merghem, A. Akrout, A. Martinez, G. Aubin, A. Ramdane, F. Lelarge, and G.-H. Duan, "Pulse generation at 346 GHz using a passively mode locked quantum-dash-based

laser at 1.55 μm," *Applied Physics Letters*, vol. 94, no. 2, pp. 021107–021107–3, Jan. 2009.

[115] R. Rosales, K. Merghem, A. Martinez, F. Lelarge, A. Accard, and A. Ramdane, "Timing jitter from the optical spectrum in semiconductor passively mode locked lasers," *Opt. Express*, vol. 20, no. 8, pp. 9151–9160, Apr. 2012.

[116] R. Rosales, K. Merghem, A. Martinez, A. Accard, F. Lelarge, and A. Ramdane, "Timing Jitter Measurements of a 130 GHz Passively Mode Locked QDash Laser from its Optical Spectrum," in *CLEO: Science and Innovations*, 2012, p. CW1N.6.

[117] J. P. Tourrenc, A. Akrout, K. Merghem, A. Martinez, F. Lelarge, A. Shen, G. H. Duan, and A. Ramdane, "Experimental investigation of the timing jitter in self-pulsating quantum-dash lasers operating at 155 μm," *Optics Express*, vol. 16, no. 22, p. 17706, Oct. 2008.

[118] A. Demir, A. Mehrotra, and J. Roychowdhury, "Phase noise in oscillators: a unifying theory and numerical methods for characterization," *IEEE Transactions on Circuits and Systems I: Fundamental Theory and Applications*, vol. 47, no. 5, pp. 655 –674, May 2000.

[119] R. Watts, R. Rosales, F. Lelarge, A. Ramdane, and L. Barry, "Mode coherence measurements across a 1.5 THz spectral bandwidth of a passively mode-locked quantum dash laser," *Opt. Lett.*, vol. 37, no. 9, pp. 1499–1501, May 2012.

[120] M. Xia, C. H. Kwok, M. G. Thompson, R. V. Penty, I. H. White, F. van Dijk, A. Enard, F. Lelarge, and G.-H. Duan, "270GHz, 580fs optical pulse generation from a single-section quantum-dash Fabry-P #x00E9;rot laser using frequency multiplication," in *Conference on Lasers and Electro-Optics, 2009 and 2009 Conference on Quantum electronics and Laser Science Conference. CLEO/QELS 2009*, 2009, pp. 1 –2.

[121] S. G. Murdoch, R. T. Watts, Y. Q. Xu, R. Maldonado-Basilio, J. Parra-Cetina, S. Latkowski, P. Landais, and L. P. Barry, "Spectral amplitude and phase measurement of a 40 GHz free-running quantum-dash modelocked laser diode," *Opt. Express*, vol. 19, no. 14, pp. 13628–13635, Jul. 2011.

[122] H. Schmeckebier, G. Fiol, C. Meuer, D. Arsenijević, and D. Bimberg, "Complete pulse characterization of quantum dot mode-locked lasers suitable for optical communication up to 160 Gbit/s," *Opt Express*, vol. 18, no. 4, pp. 3415–3425, Feb. 2010.

[123] K. Merghem, R. Rosales, S. Azouigui, A. Akrout, A. Martinez, F. Lelarge, G.-H. Duan, G. Aubin, and A. Ramdane, "Low noise performance of passively mode locked quantum-dash-based lasers under external optical feedback," *Applied Physics Letters*, vol. 95, no. 13, pp. 131111–131111–3, Sep. 2009.

[124] R. Maldonado-Basilio, J. Parra-Cetina, S. Latkowski, and P. Landais, "Timing-jitter, optical, and mode-beating linewidths analysis on subpicosecond optical pulses generated by a quantum-dash passively mode-locked semiconductor laser," *Opt. Lett.*, vol. 35, no. 8, pp. 1184–1186, Apr. 2010.

[125] K. Merghem, C. Gosset, A. Martinez, G. Moreau, F. Lelarge, G. Aubin, and A. Ramdane, "Effect of spectrum filtering on the performances of Quantum-Dash mode-locked lasers emitting at 1.55 μm," in *CLEO/Europe and IQEC 2007 Conference Digest*, 2007, p. CB13_5.

[126] A. Akrout, A. Shen, F. Lelarge, F. Pommereau, H. Gariah, F. Blache, G. H. Duan, and A. Ramdane, "Spectrum filtering and pulse compression of Quantum-Dash mode-locked lasers emitting at 1.55 #x03BC;m," in *34th European Conference on Optical Communication, 2008. ECOC 2008*, 2008, pp. 1 –2.

[127] R. Rosales, K. Merghem, A. Martinez, A. Accard, F. Lelarge, and A. Ramdane, "High repetition rate two-section InAs/InP quantum-dash passively mode locked lasers," in *Compound Semiconductor Week (CSW/IPRM), 2011 and 23rd International Conference on Indium Phosphide and Related Materials*, 2011, pp. 1 –4.
[128] R. Rosales, K. Merghem, A. Martinez, A. Accard, F. Lelarge, and A. Ramdane, "Two-section InAs/InP Quantum-Dash Passively Mode Locked Lasers," in *CLEO:2011 - Laser Applications to Photonic Applications*, 2011, p. CThG2.
[129] C. Henry and R. Kazarinov, "Instability of semiconductor lasers due to optical feedback from distant reflectors," *IEEE Journal of Quantum Electronics*, vol. 22, no. 2, pp. 294 – 301, Feb. 1986.
[130] G. R. Gray, D. Huang, and G. P. Agrawal, "Chaotic dynamics of semiconductor lasers with phase-conjugate feedback," *Phys. Rev. A*, vol. 49, no. 3, pp. 2096–2105, Mar. 1994.
[131] G. P. Agrawal and C. H. Henry, "Modulation performance of a semiconductor laser coupled to an external high-Q resonator," *IEEE Journal of Quantum Electronics*, vol. 24, no. 2, pp. 134 –142, Feb. 1988.
[132] F. Grillot, C.-Y. Lin, N. A. Naderi, M. Pochet, and L. F. Lester, "Optical feedback instabilities in a monolithic InAs/GaAs quantum dot passively mode-locked laser," *Applied Physics Letters*, vol. 94, no. 15, pp. 153503–153503–3, Apr. 2009.
[133] C.-Y. Lin, F. Grillot, N. A. Naderi, Y. Li, and L. F. Lester, "rf linewidth reduction in a quantum dot passively mode-locked laser subject to external optical feedback," *Applied Physics Letters*, vol. 96, no. 5, pp. 051118–051118–3, Feb. 2010.
[134] M. C. Troparevsky, A. S. Sabau, A. R. Lupini, and Z. Zhang, "Transfer-matrix formalism for the calculation of optical response in multilayer systems: from coherent to incoherent interference," *Opt. Express*, vol. 18, no. 24, pp. 24715–24721, Nov. 2010.
[135] K. Petermann and N. Schunk, "Laser diode characteristics with external optical feedback," in *Optical Communication, 1988. (ECOC 88). Fourteenth European Conference on (Conf. Publ. No.292)*, 1988, pp. 353 –359 vol.1.
[136] O. Carroll, I. O'Driscoll, S. P. Hegarty, G. Huyet, J. Houlihan, E. A. Viktorov, and P. Mandel, "Feedback induced instabilities in a quantum dot semiconductor laser," *Opt. Express*, vol. 14, no. 22, pp. 10831–10837, Oct. 2006.
[137] F. Grillot and N. Dubey, "Influence of the linewidth enhancement factor on the modulation response of a nanostructure-based semiconductor laser operating under external optical feedback," 2011, p. 79330E–79330E–13.
[138] S. Azouigui, B. Kelleher, S. P. Hegarty, G. Huyet, B. Dagens, F. Lelarge, A. Accard, D. Make, O. Le Gouezigou, K. Merghem, A. Martinez, Q. Zou, and A. Ramdane, "Coherence collapse and low-frequency fluctuations in quantum-dash based lasers emitting at 1.57 ?m," *Opt. Express*, vol. 15, no. 21, pp. 14155–14162, Oct. 2007.
[139] THORLABS, "Tutorial: Sources of vibration." [Online]. Available: http://www.thorlabs.com/tutorials/Tables2.cfm. [Accessed: 28-Jul-2012].
[140] O. Solgaard and K. Y. Lau, "Optical feedback stabilization of the intensity oscillations in ultrahigh-frequency passively modelocked monolithic quantum-well lasers," *IEEE Photonics Technology Letters*, vol. 5, no. 11, pp. 1264 –1267, Nov. 1993.
[141] M. Haji, L. Hou, A. E. Kelly, J. Akbar, J. H. Marsh, J. M. Arnold, and C. N. Ironside, "Ultralow 192 Hz RF linewidth optoelectronic oscillator based on the optical feedback of mode-locked laser diodes," in *CLEO: Science and Innovations*, 2012, p. CW1N.4.

[142] S. Breuer, W. Elsaer, J. G. McInerney, K. Yvind, J. Pozo, E. A. J. M. Bente, M. Yousefi, A. Villafranca, N. Vogiatzis, and J. Rorison, "Investigations of Repetition Rate Stability of a Mode-Locked Quantum Dot Semiconductor Laser in an Auxiliary Optical Fiber Cavity," *IEEE Journal of Quantum Electronics*, vol. 46, no. 2, pp. 150 –157, Feb. 2010.

[143] R. Rosales, K. Merghem, S. Azouigui, A. Martinez, F. Lelarge, F. Van Dijk, G. Aubin, and A. Ramdane, "Effect of Optical Feedback on 17-GHz Quantum Dash Based Mode Locked Lasers," in *Conference on Lasers and Electro-Optics*, 2010, p. JTuD94.

[144] K. Merghem, R. Rosales, S. Azouigui, Q. Zou, A. Martinez, A. Accard, F. Lelarge, and A. Ramdane, "InAs/InP quantum dot based lasers and effect of optical feedback," 2012, p. 82770D–82770D–7.

[145] K. Merghem, R. Rosales, S. Azouigui, A. Martinez, F. Van Dijk, G. Aubin, and A. Ramdane, "Coherence collapse in monolithic quantum-dash-based passive mode-locked lasers," 2010, pp. 772018–772018–5.

[146] A. Salhi, G. Raino, L. Fortunato, V. Tasco, G. Visimberga, L. Martiradonna, M. T. Todaro, M. De Giorgi, R. Cingolani, A. Trampert, M. De Vittorio, and A. Passaseo, "Enhanced Performances of Quantum Dot Lasers Operating at 1.3 mm," *IEEE Journal of Selected Topics in Quantum Electronics*, vol. 14, no. 4, pp. 1188–1196, Jul. 2008.

[147] K. Hild, S. J. Sweeney, S. Wright, D. A. Lock, S. R. Jin, I. P. Marko, S. R. Johnson, S. A. Chaparro, S.-Q. Yu, and Y.-H. Zhang, "Carrier recombination in 1.3 μm GaAsSb/GaAs quantum well lasers," *Applied Physics Letters*, vol. 89, no. 17, pp. 173509–173509–3, Oct. 2006.

[148] S. Fathpour, Z. Mi, P. Bhattacharya, A. R. Kovsh, S. S. Mikhrin, I. L. Krestnikov, A. V. Kozhukhov, and N. N. Ledentsov, "The role of Auger recombination in the temperature-dependent output characteristics (T0=∞) of p-doped 1.3 μm quantum dot lasers," *Applied Physics Letters*, vol. 85, no. 22, pp. 5164–5166, Nov. 2004.

[149] I. P. Marko, N. F. Massé, S. J. Sweeney, A. D. Andreev, A. R. Adams, N. Hatori, and M. Sugawara, "Carrier transport and recombination in p-doped and intrinsic 1.3 μm InAs/GaAs quantum-dot lasers," *Applied Physics Letters*, vol. 87, no. 21, pp. 211114–211114–3, Nov. 2005.

[150] I. P. Marko, A. R. Adams, S. J. Sweeney, D. J. Mowbray, M. S. Skolnick, H. Y. Liu, and K. M. Groom, "Recombination and loss mechanisms in low-threshold InAs-GaAs 1.3-/spl mu/m quantum-dot lasers," *IEEE Journal of Selected Topics in Quantum Electronics*, vol. 11, no. 5, pp. 1041–1047, Sep. 2005.

[151] T. W. Berg, J. Mørk, and J. M. Hvam, "Gain dynamics and saturation in semiconductor quantum dot amplifiers," *New Journal of Physics*, vol. 6, pp. 178–178, Nov. 2004.

[152] B. Razavi, "Gadgets Gab at 60 Ghz," *IEEE Spectrum*, vol. 45, no. 2, pp. 46 –58, Feb. 2008.

[153] A. Chowdhury, H.-C. Chien, Y.-T. Hsueh, and G.-K. Chang, "Advanced System Technologies and Field Demonstration for In-Building Optical-Wireless Network With Integrated Broadband Services," *J. Lightwave Technol.*, vol. 27, no. 12, pp. 1920–1927, Jun. 2009.

[154] M. Huchard, M. Weiss, A. Pizzinat, S. Meyer, P. Guignard, and B. Charbonnier, "Ultra-Broadband Wireless Home Network Based on 60-GHz WPAN Cells Interconnected via RoF," *J. Lightwave Technol.*, vol. 26, no. 15, pp. 2364–2372, Aug. 2008.

[155] H.-R. Chuang, L.-K. Yeh, P.-C. Kuo, K.-H. Tsai, and H.-L. Yue, "A 60-GHz Millimeter-Wave CMOS Integrated On-Chip Antenna and Bandpass Filter," *IEEE Transactions on Electron Devices*, vol. 58, no. 7, pp. 1837 –1845, Jul. 2011.
[156] H.-L. Yue, Y.-H. Chuang, and H.-R. Chuang, "60-GHz CMOS integrated on-chip Yagi antenna and balun bandpass filter in 90-nm CMOS technology," in *2012 6th European Conference on Antennas and Propagation (EUCAP)*, 2012, pp. 3546 –3548.
[157] S. Emami, R. F. Wiser, E. Ali, M. G. Forbes, M. Q. Gordon, X. Guan, S. Lo, P. T. McElwee, J. Parker, J. R. Tani, J. M. Gilbert, and C. H. Doan, "A 60GHz CMOS phased-array transceiver pair for multi-Gb/s wireless communications," in *Solid-State Circuits Conference Digest of Technical Papers (ISSCC), 2011 IEEE International*, 2011, pp. 164 –166.
[158] A. H. M. R. Islam, M. Bakaul, A. Nirmalathas, and G. E. Town, "Simplification of millimeter-wave radio-over-fiber system employing heterodyning of uncorrelated optical carriers and self-homodyning of RF signal at the receiver," *Opt. Express*, vol. 20, no. 5, pp. 5707–5724, Feb. 2012.
[159] H. R. Rideout, J. S. Seregelyi, S. Paquet, and J. Yao, "Discriminator-Aided Optical Phase-Lock Loop Incorporating a Frequency Down-Conversion Module," *IEEE Photonics Technology Letters*, vol. 18, no. 22, pp. 2344 –2346, Nov. 2006.
[160] A. Ng'oma, D. Fortusini, D. Parekh, W. Yang, M. Sauer, S. Benjamin, W. Hofmann, M. C. Amann, and C. J. Chang-Hasnain, "Performance of a Multi-Gb/s 60 GHz Radio Over Fiber System Employing a Directly Modulated Optically Injection-Locked VCSEL," *Journal of Lightwave Technology*, vol. 28, no. 16, pp. 2436 –2444, Aug. 2010.
[161] C.-T. Lin, J. Chen, W.-J. Jiang, L.-Y. W. He, P.-T. Shih, C.-H. Ho, and S. Chi, "Ultra-high data-rate 60 GHz radio-over-fiber systems employing optical frequency multiplication and adaptive OFDM formats," in *Optical Fiber Communication Conference and Exposition (OFC/NFOEC), 2011 and the National Fiber Optic Engineers Conference*, 2011, pp. 1 –3.
[162] C.-T. Lin, A. Ng'oma, W.-Y. Lee, C.-C. Wei, C.-Y. Wang, T.-H. Lu, J. Chen, W.-J. Jiang, and C.-H. Ho, "2 × 2 MIMO radio-over-fiber system at 60 GHz employing frequency domain equalization," *Opt. Express*, vol. 20, no. 1, pp. 562–567, Jan. 2012.
[163] D. Qian, M.-F. Huang, E. Ip, Y.-K. Huang, Y. Shao, J. Hu, and T. Wang, "101.7-Tb/s (370×294-Gb/s) PDM-128QAM-OFDM Transmission over 3×55-km SSMF using Pilot-based Phase Noise Mitigation," in *National Fiber Optic Engineers Conference*, 2011, p. PDPB5.
[164] R. Watts, R. Rosales, S. Murdoch, F. Lelarge, A. Ramdane, and L. Barry, "QDash semiconductor mode-locked lasers as compact subchannel comb for optical OFDM superchannel systems," in *CLEO: Science and Innovations*, 2012, p. CM1I.5.
[165] A. Lowery and J. Armstrong, "Orthogonal-frequency-division multiplexing for dispersion compensation of long-haul optical systems," *Opt. Express*, vol. 14, no. 6, pp. 2079–2084, Mar. 2006.
[166] Z. Xu, M. O?Sullivan, and R. Hui, "OFDM system implementation using compatible SSB modulation with a dual-electrode MZM," *Opt. Lett.*, vol. 35, no. 8, pp. 1221–1223, Apr. 2010.
[167] A. T. Ryan, G. P. Agrawal, G. R. Gray, and E. C. Gage, "Optical-feedback-induced chaos and its control in multimode semiconductor lasers," *IEEE Journal of Quantum Electronics*, vol. 30, no. 3, pp. 668 –679, Mar. 1994.

[168] E. Sooudi, G. Huyet, J. G. McInerney, F. Lelarge, K. Merghem, R. Rosales, A. Martinez, A. Ramdane, and S. P. Hegarty, "Injection-Locking Properties of InAs/InP-Based Mode-Locked Quantum-Dash Lasers at 21 GHz," *IEEE Photonics Technology Letters*, vol. 23, no. 20, pp. 1544 –1546, Oct. 2011.

[169] E. Sooudi, S. Sygletos, A. D. Ellis, G. Huyet, J. G. McInerney, F. Lelarge, K. Merghem, R. Rosales, A. Martinez, A. Ramdane, and S. P. Hegarty, "Optical Frequency Comb Generation Using Dual-Mode Injection-Locking of Quantum-Dash Mode-Locked Lasers: Properties and Applications," *IEEE Journal of Quantum Electronics*, vol. 48, no. 10, pp. 1327 –1338, Oct. 2012.

[170] E. Sooudi, C. De Dios Fernandez, G. Huyet, J. G. McInerney, F. Lelarge, R. Rosales, K. Merghem, A. Martinez, A. Ramdane, and S. P. Hegarty, "All Optical Passive Stabilization of a Two-Section InAs/InP Based Quantum-Dash Mode-Locked Laser with Simultaneous CW Injection-Locking and Selective Optical Feedback," in *CLEO: QELS-Fundamental Science*, 2012, p. JW2A.84.